



**Pile à combustible à céramique protonique : élaboration
et caractérisation. Étude de l'électrolyte
BaZr_{0.8}Zr_{0.2}O_{3-d} par spectroscopie d'impédance
électrochimique**

Mélanie François

► **To cite this version:**

Mélanie François. Pile à combustible à céramique protonique : élaboration et caractérisation. Étude de l'électrolyte BaZr_{0.8}Zr_{0.2}O_{3-d} par spectroscopie d'impédance électrochimique. Matériaux. Université Bourgogne Franche-Comté, 2021. Français. NNT : 2021UBFCK074 . tel-03716067

HAL Id: tel-03716067

<https://theses.hal.science/tel-03716067>

Submitted on 7 Jul 2022

HAL is a multi-disciplinary open access archive for the deposit and dissemination of scientific research documents, whether they are published or not. The documents may come from teaching and research institutions in France or abroad, or from public or private research centers.

L'archive ouverte pluridisciplinaire **HAL**, est destinée au dépôt et à la diffusion de documents scientifiques de niveau recherche, publiés ou non, émanant des établissements d'enseignement et de recherche français ou étrangers, des laboratoires publics ou privés.



**THESE DE DOCTORAT DE L'UNIVERSITE DE
BOURGOGNE FRANCHE-COMTE**

Laboratoire Interdisciplinaire Carnot de Bourgogne



Ecole doctorale n°553
Carnot - Pasteur

Doctorat de Physique / Chimie
Par
Mme Mélanie FRANÇOIS

**Protonic Ceramic Fuel Cell: Elaboration and
characterization. Investigation of the $\text{BaZr}_{0.8}\text{Y}_{0.2}\text{O}_{3-\delta}$
electrolyte by electrochemical impedance spectroscopy**

Defended on December 15, 2021



Jury committee:

Mme Sandrine GAUFFINET
Mr Gilles TAILLADES
Mr Antonio BARBUCCI
Mme Maria-Paola CARPANESE
Mme Sandrine RICOTE
Mr Pascal LENORMAND
Mr Frédéric DEMOISSON
Mr Gilles CABOCHE

Professor, University of Burgundy, France
Professor, University of Montpellier, France
Professor, University of Genoa, Italy
Associate professor, University of Genoa, Italy
Researcher, Colorado School of mines, Golden, CO, USA
Associate professor, University Paul Sabatier, France
Associate professor (HDR), University of Burgundy, France
Professor, University of Burgundy, France

President
Referee
Referee
Examiner
Examiner
Examiner
Co-supervisor
Co-supervisor

« On ne croit savoir que quand on sait peu, avec la science, le doute augmente »

Johann Wolfgang Von Goethe

ACKNOWLEDGEMENTS

Les travaux de recherches présentés dans ce manuscrit ont été réalisés au sein du laboratoire Interdisciplinaire Carnot de Bourgogne (ICB) de l'Université de Bourgogne Franche-Comté à Dijon. Je tiens en premier lieu à remercier les directeurs de l'ICB Messieurs Alain Dereux puis Stéphane Guérin de m'avoir accueillie dans leur laboratoire.

J'adresse également mes remerciements à l'école universitaire de recherche EIPHI (Engineering and Innovation through Physical science, High-technologies, and cross-disciplinary research), la région Bourgogne Franche-Comté et le FEDER (Fond Européen de Développement régional) pour avoir financé ces travaux de thèse dans le cadre du projet Pilot-HY (oPtimisation de cellule de pILe à cOmbustible fonctionnant à l'Hydrogène).

Je souhaite remercier Madame Sandrine Gauffinet, professeur à l'Université de Bourgogne, pour avoir accepté de présider mon jury de thèse. Je suis très reconnaissante envers Monsieur Gilles Taillades, professeur à l'Université de Montpellier, d'avoir accepté d'être rapporteur de ce mémoire et pour l'intérêt porté à ces travaux. I would like to sincerely thank Mister Antonio Barbucci, professor at the University of Genoa, for being my referee and for his interest and enthusiasm concerning this work.

I would also like to thank Madam Sandrine Ricote, researcher at the Colorado School of Mines, and Madam Maria Paola Carpanese, associate professor at the University of Genoa, for the examination of my work and being a part of the jury committee. Je voudrais aussi remercier Monsieur Pascal Lenormand, Maître de conférences à l'Université Paul Sabatier, d'avoir fait partie de la commission d'examen en tant qu'examineur.

J'adresse mes remerciements les plus sincères à mes directeurs de thèse Messieurs Gilles Caboche, Professeur à l'Université de Bourgogne, et Frédéric Demoisson, Maître de conférences dans la même université, pour m'avoir suivie, encadrée et soutenue tout au long de ce travail. J'ai énormément appris à vos côtés au fil de ces trois ans et je vous exprime toute ma gratitude pour le savoir à la fois scientifique et transversal que vous m'avez transmis, pour votre bienveillance, votre enthousiasme et pour la confiance que vous m'avez accordée. Je vous adresse également un très grand merci pour votre soutien et votre très grande réactivité lors des derniers rushes !

Je tiens aussi à remercier l'ensemble des permanents l'équipe de M4OXE, Lionel Combemale, Alice Martin, Ioana Popa, Olivier Politano, Maria-Rosa Ardigo-Besnard, Virgil Optasanu, Tony Montesin et Luc Lavis, pour la bonne ambiance et pour les discussions à la fois scientifiques et amicales.

This work would not have been possible without the great collaboration with the DICCA (Dipartimento di Ingegneria Civile, Chimica e Ambientale) laboratory. I would like to thank again Nello (Antonio Barbucci) and Paola for hosting me and supervising me on site. I would like to thank all the people that helped me during my stays, Rodolfo Botter, Marco Panizza, Massimo Viviani, Davide Clematis, Davide Cademartori and Tony Asensio. Dear Paola, I would like to address you a special thanks for making me discover the how complex but powerful EIS technic. I would also like to thank you for your friendliness and your kindness. Thank you for all your help in my work as in my personal life. Grazie mille a tutti.

Je souhaiterais remercier toutes les personnes qui ont contribué de près ou de loin à ce travail de thèse, Jean-Marc Dachicourt et Marie-Laure Léonard pour leur disponibilité et leur aide sur l'équipement à l'ESIREM, Olivier Heintz pour les caractérisations XPS, Pascal Briois et Mohammad Arab Pour Yazdi (FEMTO-ST) pour leurs conseils et les dépôts PVD, Mohamed Sennour (MINES ParisTech) pour les analyses MET, Morgane Gelin et Solène Valton (RX Solutions) pour les analyses par micro-tomographie et les nombreuses heures passées au traitement des données. Je souhaite aussi remercier Claire-Hélène Brachais, pour sa gentillesse, sa patience et pour m'avoir transmis le goût de l'enseignement. Je voudrais également remercier le personnel administratif, Virginie Bourg et Karine Bernaud, pour leur aide précieuse concernant la bureaucratie. Enfin je voudrais remercier Marie-Claire d'avoir tenu les locaux propres et pour les sympathiques discussions tout au long de ces trois années.

J'en viens maintenant à tous les stagiaires qui ont été impliqués dans ce travail, Florian Didier, Fanf^o (François Maeght), Victoire Lescure, Valentin Perrin, Christophe Hartung et Wafaa Oudjdi. Un merci particulier à Fanf^o, c'était un plaisir de travailler avec toi (et je te remercie aussi pour avoir amené tant de fabuleux fromages et charcuteries lors de nos apéros « bons vivants »). Un autre grand merci à Vicky, pour toute son implication dans ce travail et pour notre grande aventure en Italie. Je te souhaite toute la réussite possible pour ta thèse, prend bien soin du « bébé ».

A mes collègues, les doctorants avec qui j'ai partagé ces années, Maman Laura (merci pour tous les gâteaux et tous nos pique-niques), Bastien, Quentin, Mélanie, Célia et Adrien. Je remercie également les occupants de la salle C116 (qui est devenu plus un garde-manger qu'un bureau), Coco et Nonold. Nonold et sa manie de danser quand il entrait dans la pièce, ses exécrations (« le Norem c'est d'la m**** ») et ses fuites pour aller « draguer les L1 ». Coco, pour nos pétages de câbles contre nos ordis ou nos manips (je ne sais pas qui de nous deux à sortis le plus de jurons lors de ces trois ans), pour les conversions qui semblaient sortir à longueur de journée du bureau (en fait on parle juste tous les deux tout seul...) et pour les débats interminables sur l'origine de la vie, le cosmos et l'humanité en général. Un grand merci à vous deux de m'avoir tant fait rire.

A mes meilleures amies, Marie et Maureen. Merci à Maureen pour m'avoir appris à travailler (je partais de loin) et merci à Marie pour son soutien indéfectible et pour m'avoir toujours encouragée. J'espère pouvoir vous retrouver dans le Sud-Ouest un jour !

A mes piliers, ma famille de dragons et de homards (ce serait bête de pas en profiter) Maman, Marie et Julien. Ma chère Maman, merci beaucoup de m'avoir toujours soutenue et de m'avoir offert la chance de pouvoir de faire des études.

Last but definitely not least, j'adresse mes remerciements à celui sans qui rien de tout cela n'aurait pu arriver, aucun mot ne saurais décrire à tout ce que je te dois, alors je me contenterais de ceci : merci pour tout, Papa.

TABLE OF CONTENTS

ACKNOWLEDGEMENTS	i
TABLE OF CONTENTS	v
LIST OF ABBREVIATIONS	ix
LIST OF FIGURES	xi
LIST OF TABLES	xx
GENERAL INTRODUCTION	1
CHAPTER 1: STATE OF THE ART	5
I. The hydrogen solution.....	5
II. The fuel cell technology	7
II.1. Historic and generalities.....	7
II.2. The different fuel cell technologies.....	8
III. Protonic Ceramic Fuel Cells (PCFC)	10
III.1. Operation mechanism	10
III.2. Protonic conduction	10
III.2.a. Proton incorporation.....	11
III.2.b. Proton migration.....	12
III.3. Constituent materials of PCFC	13
III.3.a. Specifications	13
III.3.b. Electrolyte materials.....	14
III.3.b.i. Perovskite-type materials	14
III.3.b.ii. Other materials	16
III.3.b.iii. Summary	17
III.3.c. Anode materials.....	18
III.3.c.i. Pure electronic conductor	18
III.3.c.ii. Mixed electronic protonic conductor	18
III.3.d. Cathode materials.....	19
III.3.d.i. Mixed electronic-oxygen ion conductor	19
III.3.d.ii. Mixed conductor/protonic conductor composite	20
III.3.d.iii. Mixed protonic-electronic-oxygen ion conductor.....	21
IV. Conclusions and course of the study	22
CHAPTER II: HYDROTHERMAL SYNTHESIS AND CHARACTERIZATION OF THE PROTONIC CERAMIC CONDUCTOR.....	23
I. The hydrothermal route.....	23
I.1. Introduction	23
I.2. Principle of hydrothermal synthesis and water properties.....	26
I.3. Hydrothermal apparatus and synthesis protocols	28
I.3.a. The batch reactor.....	28
I.3.b. The continuous reactor.....	29

II.	Structural characterization of the synthesized materials	31
II.1.	BaZrO ₃ (BZ)	31
II.2.	BaCeO ₃	33
II.3.	Ba(Ce,Zr)O ₃	35
II.4.	Ba(Ce,Zr,Y)O _{3-δ}	36
II.5.	Ba(Zr,Y)O _{3-δ} (BZY)	36
III.	Structural, microstructural and chemical study of BZY	42
III.1.	Characterization of the as-synthesized material.....	42
III.1.a.	X-ray diffraction analysis	42
III.1.b.	Granulometry analysis.....	45
III.1.c.	Microstructural and electron diffraction analysis.....	46
III.1.d.	Bulk chemistry analysis	51
III.1.e.	Surface chemistry analysis	53
III.1.f.	Summary	57
III.2.	Characterization of the annealed material.....	57
III.2.a.	X-ray diffraction analysis	58
III.2.b.	Microstructural and electron diffraction analysis.....	59
III.2.c.	Bulk chemistry analysis.....	63
III.2.d.	Surface chemistry analysis	64
III.2.e.	Summary.....	67
III.3.	Formation mechanism of Ba(Zr,Y)O _{3-δ}	67
III.4.	Adjustment of the synthesis conditions	68
III.4.a.	X-ray diffraction analysis	69
III.4.b.	Bulk chemistry analysis	70
III.4.c.	Summary.....	71
IV.	Conclusion.....	72
CHAPTER III: STUDY OF THE CONDUCTIVITY OF Y-DOPED BARIUM ZIRCONATE		73
I.	Electrochemical impedance spectroscopy: theory and application.....	73
I.1.	Theory of complex impedance spectroscopy	73
I.1.a.	Principle of EIS	73
I.1.b.	Mathematical considerations	74
I.1.c.	Representations of the impedance.....	75
I.1.d.	Exploitation the EIS data	76
I.2.	Application in the PCFC area	78
I.2.a.	Defect chemistry and conduction properties in perovskite	79
I.2.a.i.	Model describing the concentration of defects as a function of the atmosphere	79
I.2.a.ii.	Example of the AB _{0.9} M _{0.1} O _{2.95} system.....	80
I.2.b.	Definition and measurement of the conductivity	82
I.3.	Summary.....	85
II.1.	Sinterability	85

II.1.a. Dilatometry of BZY-c powder.....	86
II.1.b. Dilatometry of BZY-b powder	87
II.2. Determination of the sintering conditions	87
II.3. Preparation of the symmetrical cells	90
II.3.a. Electrolyte part.....	90
II.3.a.i. Structural characterization	90
II.3.a.ii. Microstructural characterization.....	91
II.3.a.iii. Bulk chemistry characterization	92
II.2.b. Electrode part.....	93
III. Study of the conductivity of BZY	93
III.1. Experimental set-up	93
III.2. Measured EIS spectra.....	94
III.2.a. EIS spectra of BZY-com symmetrical cell.....	95
III.2.b. EIS spectra of BZY-c 1000 °C symmetrical cell	101
III.2.c. EIS spectra of BZY-b 1000 °C symmetrical cell	106
III.2.d. Summary	110
III.3. Evolution with the temperature.....	111
III.3.a. Resistance in the bulk and in the grain boundaries	111
III.3.a.i. Arrhenius plot of BZY-com, BZY-c 1000 °C and BZY-b 1000 °C	111
III.3.a.ii. Discussion	114
III.3.b. Total resistance.....	115
III.3.b.i. Arrhenius plot of BZY-com, BZY-c 1000 °C and BZY-b 1000 °C	115
III.3.b.ii. Discussion	116
II.4. Comparison of conductivity of BZY-com, BZY-c 1000 °C and BZY-b 1000 °C samples.....	117
IV. Conclusion.....	118
CHAPTER IV: ELABORATION AND CHARACTERIZATION OF PCFC	121
I. Presentation of the complete cell and elaboration procedures	121
I.1. Specifications.....	121
I.2. Fabrication procedures of the cells	122
II. Fabrication of PCFC half-cells by co-tape casting	125
II.1. Formulation of the slurries and preparation of the green half-cells	125
II.2. Co-sintering of the green half-cells	127
III. Fabrication of PCFC complete cells	131
III.1. Elaboration of anode-AFL by co-tape casting	131
III.2. Deposition of the electrolyte by reactive pulsed DC sputtering	132
III.2.a. Presentation of the device and depositions conditions	132
III.2.b. Characterization of the BZY electrolyte	133
III.3. Deposition of the cathode by spray.....	135
IV. Electrochemical test of the cells	136
IV.1. Study of the reduction of NiO	136

IV.2. Electrochemical impedance spectroscopy of complete PCFC	139
IV.2.a. Theoretical EIS spectra of a complete PCFC	139
IV.2.b. Experimental EIS spectra of a complete PCFC	141
V. Conclusion	143
GENERAL CONCLUSION	145
ANNEX CHAPTER: STUDY OF INTERMEDIATE TEMPERATURE SOFC ...	149
I. Presentation of Sm-doped Ceria.....	149
II.1. Preparation of the symmetrical cell.....	151
II.1.a. Electrolyte part.....	151
II.1.a. Electrode part	152
II.2. Impedance measurements.....	153
III.1. Preparation of the complete cell.....	156
III.2. Impedance measurement.....	157
III.3. Post-mortem characterizations	160
III.3.a. Microstructural Investigations and Bulk Chemistry Analysis.....	160
III.3.b. Structural and Surface Chemistry Analysis.....	163
III.3. Discussion	168
IV. Conclusions	170
ANNEX A: RIETVELD REFINEMENT DATA	171
ANNEX B: DIFFRACTOGRAM OF THE BAF ₂ SAMPLE	175
ANNEX C: XPS LITERATURE SURVEY	177
ANNEX D: BODE PLOTS.....	187
ANNEX E: IMPACT OF THE AFL ON THE ELABORATION PROCESS	199
BIBLIOGRAPHY	201

LIST OF ABBREVIATIONS

AC	Alternative current	MEK	Methyl ethyl ketone
AFL	Anode Fonctuntial Layer	MIEC	Mixed ionic electronic conductor
ASC	Area Specific Capacitance	ORR	Oxygen reduction reaction
ASR	Area Specific Resistance	P	Pressure
B	Bulk	P_{O_2}	Partial pressure of O_2
BBP	Benzylbutyl phthalate	P_{H_2O}	Partial pressure of water vapor
BSCF	$Ba_{0.5}Sr_{0.5}Co_{0.8}Fe_{0.2}O_{3-\delta}$	PSD	Particle Size Distribution
BZY	$Ba_{1\pm y}Zr_{1-x}Y_xO_{3-\delta}$	PCFC	Protonic ceramic fuel cell
BZY20	$BaZr_{0.8}Y_{0.2}O_{3-\delta}$	PEG	Polyethylene glycol
BZY-b	$Ba_{1\pm y}Zr_{1-x}Y_xO_{3-\delta}$ elaborated by the batch process	PEMFC	Proton exchange membrane fuel cell
BZY-b 1000 °C	$Ba_{1\pm y}Zr_{1-x}Y_xO_{3-\delta}$ elaborated by the batch process – annealed at 1000 °C	PLD	Pulsed laser deposition
BZY-c	$Ba_{1\pm y}Zr_{1-x}Y_xO_{3-\delta}$ elaborated by the continuous process	H_i^\bullet or OH_0^\bullet	Proton
BZY-c 1000 °C	$Ba_{1\pm y}Zr_{1-x}Y_xO_{3-\delta}$ elaborated by the continuous process – annealed at 1000 °C	PVB	Polyvinyl butyral
BZY-com	$Ba_{1\pm y}Zr_{1-x}Y_xO_{3-\delta}$ commercial	SDC	$Ce_{0.8}Sm_{0.2}O_{2-\delta}$
DC	Direct current	SEM-EDS	Scanning electron microscopy-energy dispersive X-ray spectroscopy
E_a	Activation energy	SOFC	Solid oxide fuel cell
EIS	Electrochemical impedance spectroscopy	SSR	Solid state reaction
h^\bullet	Electron hole	M'_B	Substitutional cation

List of abbreviations

e'	Electron	T	Temperature
EMF	Electromotive force	TEA	Triethanolamine
EtOH	Ethanol	TEC	Thermal expansion coefficient
FWHM	Full width at half maximum	TEM	Transmission electron microscopy
GB	Grain boundary	TPB	Triple phase boundary
HOR	Hydrogen oxidation reaction	XPS	X-ray photoelectron spectroscopy
ICP-AES	Inductively coupled plasma – atomic emission spectroscopy	XRD	X-ray diffraction
LSCF	$(\text{La}_{0.4}\text{Sr}_{0.6})_{0.95}\text{Co}_{0.2}\text{Fe}_{0.8}\text{O}_{3-\delta}$	YSZ	Yttria stabilized zirconia
O_0^\times	Lattice oxygen		

LIST OF FIGURES

Figure I.1: World energy consumption by fuel [2]	6
Figure I.2: Global energy consumption by fuel and projections up to 2040 [5]	6
Figure I.3: Shares of hydrogen production methods based on the review from [8].....	7
Figure I.4: Number of publications per year in ScienceDirect with "high temperature proton conductors" as keywords (in October 2021)	8
Figure I.5: The different fuel cell technologies (adapted from [15])	9
Figure I.6: Operation mechanism in PCFC	10
Figure I.7: The “charge carrier map” of $\text{BaZr}_{0.8}\text{Y}_{0.2}\text{O}_{3-\delta}$ between 673 and 873 K [24].....	12
Figure I.8: The Grotthus mechanism: rotation and proton transfer [27]	13
Figure I.9: Perovskite crystal structure where the blue spheres represent the A cation, the black sphere the B cation and the red spheres the oxygen anion.	15
Figure I.10: Proton conductivities of various doped oxides calculated from proton concentration and motilities (type of dopant is not indicated) [27]	17
Figure I.11: Reaction at the interface anode/electrolyte/gas for a pure electronic conductor anode material [84].....	18
Figure I.12: Reaction in the volume of the anode for a cermet material [84]	19
Figure I.13: Representation of the ORR in the case of a mixed electronic oxygen ion conductor [84]	20
Figure I.14: Representation of the ORR in the case of a mixed conductor/protonic conductor composite [84].....	21
Figure I.15: Representation of the ORR in the case of a mixed conductor/protonic conductor composite [84].....	21
Figure II.1: 3D phase diagram of a pure material (CC BY-SA 3.0)	26
Figure II.2: Water phase diagram, simplified from [148]	26
Figure II.3: Evolution of the water properties as a function of the temperature at 245 bar [151]	27
Figure II.4: Evolution of inorganics and hydrocarbons solubility at 253 bar depending on the temperature [154]	28
Figure II.5: Schematic and photography of the batch hydrothermal set-up	29
Figure II.6: Schematic and photography of the continuous hydrothermal set-up	30
Figure II.7: X-ray diffractogram of BaZrO_3 synthesized by the batch process at 400°C, the continuous process at 400°C and the continuous process at 500°C	32
Figure II.8: X-ray diffractogram of BaCeO_3 -target obtained powder synthesized by the continuous process at 400 °C and 300 bar.	33
Figure II.9: Williamson and Hall diagram of the CeO_2 phase synthesized by the continuous hydrothermal process at 400 °C and 300 bar	34

Figure II.10: X-ray diffractogram of $\text{BaCe}_{0.9}\text{Zr}_{0.1}\text{O}_{3-\delta}$ and $\text{BaCe}_{0.1}\text{Zr}_{0.9}\text{O}_{3-\delta}$ -target powders synthesized by the continuous process at 400 °C and 300 bar.	35
Figure II.11: X-ray diffractogram of $\text{BaCe}_{0.7}\text{Zr}_{0.1}\text{Y}_{0.2}\text{O}_{3-\delta}$ -target powder synthesized by the continuous process at 400 °C and 300 bar.	36
Figure II.12: X-ray diffractogram of $\text{Ba}(\text{Zr},\text{Y})\text{O}_{3-\delta}$ synthesized by the batch process and the continuous process at 400 °C	37
Figure II.13: Comparison of the lattice parameter of BZY reported in the literature as a function of Y content. More details about the preparation of the sample are given in Table II.6.	38
Figure II.14: X-ray diffractogram of the BZY synthesized by the batch and the continuous process, a) 20 – 80 2θ range diffractogram, b) zoom on the 220 peak	42
Figure II.15: Crystal structure of BZY, a) cubic BZY; b) tetragonal BZY. Ba^{2+} is represented in dark blue, Zr^{4+} and Y^{3+} in light blue and O^{2-} in red. The radii scale is set to 50 % to have an exploded view.	44
Figure II.16: Theoretical X-ray diffractogram of the cubic BZY20	44
Figure II.17: Theoretical X-ray diffractogram of the tetragonal BZY20	45
Figure II.18: Particle size distribution by volume of the BZY-c powder.....	46
Figure II.19: TEM micrograph of the BZY-b powder	47
Figure II.20: Electron diffraction pattern of the 105 nm particles from the BZY-b powder ..	47
Figure II.21: Electron diffraction pattern of the 9 nm particles from the BZY-b powder	49
Figure II.22: TEM micrograph of the BZY-c powder	50
Figure II.23: Electron diffraction pattern of the BZY-c powder.....	50
Figure II.24: SEM micrograph in backscattered electron (BSE) mode of the BZY-c powder, the yellow square represent the area for the SEM-EDS analysis.	52
Figure II.25: a) A-site/B-site ratios and b) $\text{Y}/(\text{Zr} + \text{Y})$ ratios obtained from EDS measurement on the BZY-b and the BZY-c powders and the corresponding number of agglomerates per interval.....	52
Figure II.26: Representation of the binding energy associated with different possible compound reported in the literature. a) Ba $3d_{5/2}$ binding energy; b) C 1s binding energy; c) Zr $3d_{5/2}$ binding energy; d) Y $3d_{5/2}$ core-level spectra and e) O 1s binding energy	54
Figure II.27: XPS windows spectra of the BZY-b and BZY-c powders, a) Ba $3d_{5/2}$ core-level spectra; b) Zr 3d core-level spectra; c) Y 3d core-level spectra and d) C 1s core-level spectra. The colored lines represents the fit of each contribution; the black line, the experimental data data; the grey line, the global fit.....	56
Figure II.28: TGA signal (black) and Differential Thermal Analysis (red) of the BZY-c powder	58
Figure II.29: X-Ray Diffractogram of the BZY-b and BZY-c powders after annealing at 1000 °C for 1 hour; a) 20-80 ° 2θ range, b) zoom on the 200 peak and c) zoom on 220 peak.....	59
Figure II.30: TEM micrograph of the BZY-b 1000 °C powder	60
Figure II.31: Electron diffraction pattern of the BZY-b 1000 °C powder	60
Figure II.32: TEM micrograph of the BZY-c 1000 °C powder	61
Figure II.33: Electron diffraction pattern of the BZY-c 1000 °C powder.....	62

Figure II.34: a) A-site/B-site ratios and b) Y/(Zr + Y) ratios obtained from SEM-EDS measurement on the BZY-b powder before and after annealing at 1000 °C for 1 hour and the corresponding number of agglomerates per interval.....	63
Figure II.35: a) A-site/B-site ratios and b) Y/(Zr + Y) ratios obtained from SEM-EDS measurement on the BZY-c powder before and after annealing at 1000 °C for 1 hour and the corresponding number of agglomerates per interval.....	64
Figure II.36: XPS core-level spectra of the BZY-b and BZY-c powders after annealing at 1000 °C for 1 hour. a) core-level spectra of Ba 3d _{5/2} , b) core-level spectra of C 1s, c) core-level spectra of Zr 3d and d) core-level spectra of Y 3d	66
Figure II.37: Schematic of the plausible mechanism of the formation of BaZrO ₃ in a continuous hydrothermal set-up at 400 °C and 300 bar [213].	68
Figure II.38: suspected formation mechanism of BZY in the continuous hydrothermal set-up at 450 °C and 300 bar.	68
Figure II.39: X-ray diffractogram of B1.5ZY, B2ZY, B3ZY and B4ZY powders synthesized by the continuous process at 400 °C and 300 bar; a) 20-80 ° 2θ range and b) zoom on the 110 peak, the theoretical position of the more intense peak is represented in the figure.....	69
Figure II.40: Williamson and Hall diagram of the BZY phase of the B1.5ZY, B2ZY, B3ZY and B4ZY powders synthesized by the continuous process at 400 °C and 300 bar	70
Figure II.41: a) A-site/B-site ratios and b) Y/(Zr + Y) ratios obtained from SEM-EDS measurement on the B1.5ZY, B2ZY, B3ZY and B4ZY powders and the corresponding number of agglomerates per interval.....	71
Figure III.1: Principle of EIS, applied voltage (top) and measured current (bottom) [222]	74
Figure III.2: Impedance representation, a) Nyquist plot ; b) Bode plot.	75
Figure III.3: a) Nyquist plot of PEMFC operating at 160 °C and b) the corresponding DRT plot [226]. (In this plot, g is noted h_k .).....	78
Figure III.4: Defect concentrations as a function of log (P_{O2}) and log (P_{H2O}) in the case of $MB' = 0.1$. (a) oxide ion vacancies, (b) protons, (c) holes and (d) electrons. Partial pressures are in atm [25].	81
Figure III.5: Schematic representation of $\log \sigma$ as a function of $\log P_{O2}$ for a protonic conductive ceramic (adapted from [236]).	83
Figure III.6: Ionic conductivity of BaCe _{0.9} Gd _{0.1} O _{3-δ} , protonic is shown by the entire symbol, oxygen-ion by the hollow symbol [235]. The conductivity of each species was calculated thanks to the transport number of oxygen.	84
Figure III.7: Dilatometry profile of BZY-c, BZY-c mixed with 1 wt% of ZnO and BZY-c annealed at 1000 °C for 1 hour mixed with . wt% of ZnO. a) $\Delta L/L_0$ as a function of the temperature; b) $d(\Delta L/L_0)/d(T)$ as a function of the temperature.....	86
Figure III.8: Dilatometry profile of BZY-b, BZY-b mixed with 1 wt% of ZnO and BZY-b annealed at 1000 °C for 1 hour mixed with 1 wt% of ZnO. a) $\Delta L/L_0$ as a function of the temperature; b) $d(\Delta L/L_0)/d(T)$ as a function of the temperature.....	87
Figure III.9: Densification rate of BZY-com as a function of the quantity of ZnO at different sintering temperature. The sintering time was set to 5 hours.	88

Figure III.10: SEM-micrograph of the BZY-c raw powder mixed with 1 wt% of ZnO sintered at 1550 °C for 5 hours.	89
Figure III.11: XRD pattern of the BZY-b 1000 °C, BZY-c 1000 °C and BZY-com after sintering at 1550 °C for 5 hour. Each powder was mixed with 1 %wt of ZnO prior to the shaping.	90
Figure III.12: SEM micrograph of a) BZY-com sintered pellet (cross-section), b) BZY-c 1000 °C sintered pellet (surface) and c) BZY-b 1000 °C sintered pellet (surface).....	92
Figure III.13: SEM-EDS measurements of the sintered BZY-b 1000 °C, BZY-c 1000 °C and BZY-com sintered pellets. a) A-site/B-site ratio and b) Y/(Y+Zr) ratio.....	93
Figure III.14: Norecs Probostat set-up, a) schematical representation and b) photography of the device [255].	94
Figure III.15: Nyquist plots of the BZY-com symmetrical cell at a) 250 °C, b) 400 °C, c) 550 °C, and d) 700 °C in wet H ₂ and wet air atmosphere. The frequencies delimiting the different contributions are written on the graph, those in black are for the two spectra.....	97
Figure III.16: Nyquist plots of the BZY-c 1000 °C symmetrical cell at a) 250 °C, b) 400 °C, c) 550 °C, and d) 700 °C in wet H ₂ and wet air atmosphere. The frequencies delimiting the different contributions are written on the graph, those in black are for the two spectra.....	104
Figure III.17: Nyquist plots of the BZY-b 1000 °C symmetrical cell at a) 250 °C, b) 400 °C, c) 550 °C, and d) 700 °C in wet H ₂ and wet air atmosphere. The frequencies delimiting the different contributions are written on the graph, those in black are for the two spectra.....	108
Figure III.18: Typical Nyquist plot of a symmetrical cell at low temperature. The spectrum was simulated by Nova 2.1 software according to the inserted equivalent circuit.	111
Figure III.19: Arrhenius diagram of σ_{AC} calculated from R_B or R_{GB} in wet air and wet H ₂ . a) BZY-com symmetrical cell, b) BZY-c 1000 °C symmetrical cell and c) BZY-b 1000 °C symmetrical cell	113
Figure III.20: Schematic illustration of the space charge layer at the grain boundary [238].	115
Figure III.21: Arrhenius diagram of σ_{AC} calculated from R_{TOT} in wet air and wet H ₂ . a) BZY-com symmetrical cell, b) BZY-c 1000 °C symmetrical cell and c) BZY-b 1000 °C symmetrical cell	116
Figure III.22: Arrhenius diagram of σ_{AC} calculated from R_{TOT} of BZY-com, BZY-c 1000 °C and BZY-b 1000 °C symmetrical cell. a) in wet H ₂ and b) in wet air.....	118
Figure IV.1: Schematical representation of the target PCFC cell	122
Figure IV.2: Schematical representation of the fabrication of PCFC by co-tape casting and spray deposition.....	123
Figure IV.3: Schematical representation of the fabrication of PCFC by co-tape casting, reactive pulsed DC sputtering and spray deposition	123
Figure IV.4: Pictures of a) anode-AFL-electrolyte green tape after the night of drying, view from the anode side and b) two green cells after cutting, anode side on the top and electrolyte side on bottom	126
Figure IV.5: Pictures of the anode-AFL-electrolyte green tape, a) during the punching of the half-cells, b) after cutting	127

Figure IV.6: Dilatometry profile of the BZY-c 1000 °C-NiO pellet. 60% wt NiO/40% wt BZY. a) $\Delta L/L_0$ as a function of the temperature; b) $d(\Delta L/L_0)/dt$ as a function of the temperature .	127
Figure IV.7: X-ray diffractograms of the half-cell sintered at 1550 °C for 5 hours, top: electrolyte side and bottom: anode side	128
Figure IV.8: SEM micrographs of the anode-AFL-electrolyte assembly elaborated by co-tape casting and co-sintering at 1500 °C. a) cross-section, b) cross-section (global view) and c) surface of the electrolyte	129
Figure IV.9: X-ray diffractograms of the half-cell sintered at 1550 °C for 5 hours, top: electrolyte side and bottom: anode side	130
Figure IV.10: SEM micrographs of the anode-AFL-electrolyte assembly elaborated by co-tape casting and co-sintering at 1450 °C.....	130
Figure IV.11: Pictures of sintered anode-AFL assembly elaborated by co-tape casting, a) 1450 °C, b) 1400 °C and c) 1350 °C.....	132
Figure IV.12: SEM micrographs of the anode-AFL substrate elaborated by co-tape casting and co-sintering at 1350 °C. a) cross-section (global view) and b) zoom in the anode layer	132
Figure IV.13: Photographs of the DC sputtering device. a) general view, b) inner chamber	133
Figure IV.14: SEM micrographs of the BZY electrolyte elaborated by reactive pulsed DC sputtering. a) as-deposited, b) after annealing at 1000 °C for 2 hours	134
Figure IV.15: X-ray diffractograms of the BZY electrolyte elaborated by reactive pulsed DC sputtering. a) as-deposited, b) after annealing at 1000 °C for 2 hours. The relative intensity of a non-textured BZY phase calculated using CaRine software is presented at the bottom of the figure.	135
Figure IV.16: SEM micrographs of the cathode layer deposited by spray	136
Figure IV.17: Recorded OCV and H ₂ % in the N ₂ -H ₂ gas mixture during the reduction as a function of the time	137
Figure IV.18: SEM micrograph of the complete cell after reduction	138
Figure IV.19: Tomography micrographs of the complete cell after half-reduction. a) view from the bulk of the anode, b) cross-sectional view of the anode-AFL-electrolyte assembly	138
Figure IV.20: Schematic representation of the reduction of NiO into Ni. The red arrows represent the compressive and tensile forces	139
Figure IV.21: Classical a) Nyquist and b) Bode plot of a complete cell.....	141
Figure IV.22: SEM micrographs of the complete cell after cell operation	142
Figure IV.23: EIS spectra at OCV of a complete cell with 5 µm thick electrolyte deposited by reactive DC sputtering. a) Nyquist plot and b) Bode plot.....	143
Figure 1: a) Fluorite crystal structure and b) oxygen migration path the fluorite structure. The red spheres represent the oxygen ions, the yellow-green the cations and the square the oxygen vacancy [313].	150
Figure 2: Activation energy and total conductivity in air at 400 °C as a function of Sm dopant concentration [319]. The samples consist of an epitaxial thin film of Sm-doped CeO ₂ sandwiched between two Pt electrodes deposited by photolithography. This preparation explains the unusually high conductivity values.....	150
Figure 3: XRD pattern of the SDC pellet sintered at 1215 °C for 3 hours.....	152

Figure 4: SEM micrograph of the SDC pellet sintered at 1215 °C for 3 hours.	152
Figure 5: Nyquist plots of LSCF//SDC//LSCF and Pt//SDC//Pt symmetrical cells at a) 200 °C, b) 325 °C, c) 350 °C, d) 525 °C, e) 550 °C and f) 700 °C in air atmosphere. Some frequencies are written on the graph, the one in black correspond to the two spectra.	154
Figure 6: Arrhenius diagram of the two symmetrical cells in the temperature range 200 – 700 °C. The values reported correspond to the high frequency intercept of the impedance spectra with the x-axis.	155
Figure 7: Electrochemical measurement at 550 °C of the cell sintered at 1380 °C at t = 0, 17 and 40 h. a) Nyquist plots, the numbers reported in the figure indicate the log of the frequency; b) Bode plots and c) evolution of the electrolyte resistance over the time.	158
Figure 8: BSE-SEM surface micrograph and EDX mappings of the cathode–electrolyte interface, a) before and b) after cell testing.	161
Figure 9: Elemental content evolution in the cathode and the electrolyte layers as a function of the distance from the interface, represented as a dashed line, for a) the non-tested sample and b) the tested sample. EDX point measurements were acquired at each cross on the SEM-BSE micrograph inserted at the top of the figures.	163
Figure 10: BSE-SEM micrograph of the cathode–electrolyte interface after selective dissolution of LSCF.	164
Figure 11: Low incidence angle (2°) X-ray diffractogram of the cathode–electrolyte interface after the selective dissolution of LSCF.	165
Figure 12: XPS windows spectra of the tested interface and the reference sample, a) Ce 3d core-level spectra, b) Sm 3d _{5/2} core-level spectra, c) La 3d core-level spectra, d) Sr 3d core-level spectra, e) Fe 2p core-level spectra and f) C 1s core-level spectra.	168
Figure 13: Schematic of the strontium segregation and lanthanum, cerium and samarium diffusion.	169
Figure B.1: XRD pattern of the BaF ₂ single-cristal	175
Figure B.2: β as a function of 2θ plot of the BaF ₂ single-cristal	176
Figure D.1: EIS spectra of BZY-com symmetrical cell at 250 °C. a) Nyquist plot; b) Bode plot in wet air and c) Bode plot in wet H ₂ . The insert in the Nyquist plot exposes a zoom of the high frequencies points.	187
Figure D.2: EIS spectra of BZY-com symmetrical cell at 400 °C. a) Nyquist plot; b) Bode plot in wet air and c) Bode plot in wet H ₂ . The insert in the Nyquist plot exposes a zoom of the high frequencies points.	188
Figure D.3: EIS spectra of BZY-com symmetrical cell at 550 °C. a) Nyquist plot; b) Bode plot in wet air and c) Bode plot in wet H ₂ . The insert in the Nyquist plot exposes a zoom of the high frequencies points.	189
Figure D.4: EIS spectra of BZY-com symmetrical cell at 700 °C. a) Nyquist plot; b) Bode plot in wet air and c) Bode plot in wet H ₂ . The insert in the Nyquist plot exposes a zoom of the high frequencies points.	190
Figure D.5: EIS spectra of BZY-c symmetrical cell at 700 °C. a) Nyquist plot; b) Bode plot in wet air and c) Bode plot in wet H ₂ . The insert in the Nyquist plot exposes a zoom of the high frequencies points.	191

Figure D.6: EIS spectra of BZY-c symmetrical cell at 400 °C. a) Nyquist plot; b) Bode plot in wet air and c) Bode plot in wet H2. The insert in the Nyquist plot exposes a zoom of the high frequencies points.....	192
Figure D.7: EIS spectra of BZY-c symmetrical cell at 550 °C. a) Nyquist plot; b) Bode plot in wet air and c) Bode plot in wet H2. The insert in the Nyquist plot exposes a zoom of the high frequencies points.....	193
Figure D.8: EIS spectra of BZY-c symmetrical cell at 700 °C. a) Nyquist plot; b) Bode plot in wet air and c) Bode plot in wet H2. The insert in the Nyquist plot exposes a zoom of the high frequencies points.....	194
Figure D.9: EIS spectra of BZY-b symmetrical cell at 250 °C. a) Nyquist plot; b) Bode plot in wet air and c) Bode plot in wet H2. The insert in the Nyquist plot exposes a zoom of the high frequencies points.....	195
Figure D.10: EIS spectra of BZY-b symmetrical cell at 400 °C. a) Nyquist plot; b) Bode plot in wet air and c) Bode plot in wet H2. The insert in the Nyquist plot exposes a zoom of the high frequencies points.....	196
Figure D.11: EIS spectra of BZY-b symmetrical cell at 550 °C. a) Nyquist plot; b) Bode plot in wet air and c) Bode plot in wet H2. The insert in the Nyquist plot exposes a zoom of the high frequencies points.....	197
Figure D.12: EIS spectra of BZY-b symmetrical cell at 700 °C. a) Nyquist plot; b) Bode plot in wet air and c) Bode plot in wet H2. The insert in the Nyquist plot exposes a zoom of the high frequencies points.....	198
Figure E.1: Pictures of half-cell after co-sintering, the electrolyte layer is on the top side ...	199

LIST OF TABLES

Table I.1: Specification for each part of elementary cell, adapted from [23], [32], [33].	14
Table II.1: Comparison of advanced oxide powder processes from Yoshimura et al. (2017), Santos et al. (2018) and Lintingre et al. (2016) [145]–[147]	25
Table II.2: Notation of the different compositions.	31
Table II.3: Rietveld refinement of BaZrO ₃ synthesized by the batch process at 400°C, the continuous process at 400°C and the continuous process at 500°C	32
Table II.4: Rietveld refinement of BaCe _{0.9} Zr _{0.1} O _{3-δ} and BaCe _{0.1} Zr _{0.9} O _{3-δ} -target powders synthesized by the continuous process at 400 °C and 300 bar.	35
Table II.5: Rietveld refinement of Ba(Zr,Y)O _{3-δ} synthesized by the batch process and the continuous process at 400 °C	37
Table II.6: Additional informations, mainly synthesis route and eventual sintering treatment, about the lattice parameter of BZY reported in the literature	41
Table II.7: Crystallographic data of cubic BZY20 as inputted in CaRIne Software.	43
Table II.8: Crystallographic data of tetragonal BZY20 as inputted in CaRIne Software	43
Table II.9: Indexation of the electron diffraction pattern of the 116 nm particles in the BZY-b powder.	48
Table II.10: Indexation of the electron diffraction pattern of the 8 nm particles in the BZY-b powder in the hypothesis of a F lattice mode.	49
Table II.11: Indexation of the electron diffraction pattern of the 8 nm particles in the BZY-b powder in the hypothesis of a I lattice mode.	49
Table II.12: Indexation of the electron diffraction pattern of the BZY-c powder.	51
Table II.13: Elemental composition (at%) of the BZY-b and the BZY-c powders obtained by XPS.	53
Table II.14: Rietveld refinement of the BZY-b and BZY-c powders after annealing at 1000 °C for 1 hour	59
Table II.15: Electron diffraction pattern of the BZY-b powder after annealing at 1000 °C for 1 hour.	61
Table II.16: Electron diffraction pattern of the BZY-c powder after annealing at 1000 °C for 1 hour.	62
Table II.17: Elemental composition (at%) of the BZY-b 1000 °C and the BZY-c 1000 °C powders obtained by XPS.	64
Table II.18: Rietveld refinement and analysis of the Williamson and Hall diagram of the BZY-b and BZY-c powders after annealing at 1000 °C for 1 hour	70
Table III.1: Expression and example of R, C, L and CPE element.	77
Table III.2: Refined lattice parameter of the BZY phase and refined phase percentage of the BZY-c, BZY-b and BZY-com pellets.	91
Table III.3: Densification rate of the BZY-c, BZY-b and BZY-com sintered pellets obtained by Archimedean buoyant force.	91

Table III.4: Evolution of the elementary component of the equivalent circuits of the BZY-com symmetrical cell as a function of the temperature in wet H ₂	98
Table III.5: Evolution of the elementary component of the equivalent circuits of the BZY-com symmetrical cell as a function of the temperature in wet air. The values in italic corresponds to the values of the (R ₃ 'Q ₃ ') contribution.	98
Table III.6: ASC values and their possible interpretation, based of the work from Irvine et al. [256] and adapted from various authors [24], [66], [248], [257], [259]–[267].	99
Table III.7: Calculated equivalent capacitance of the (R ₁ Q ₁) and (R ₂ Q ₂) components from Equations III.34-37. R (in Ω) and not ASR (Area Specific Resistance – in Ω.cm ²) was used for the calculation.	100
Table III.8: Calculated ASC of the (RC) components of the BZY-com symmetrical cell depicted in Table III.4 in wet H ₂	100
Table III.9: Calculated ASC of the (RC) components of the BZY-com symmetrical cell depicted in Table III.5 in wet air.	101
Table III.10: Evolution of the elementary component of the equivalent circuit of the BZY-c 1000 °C symmetrical cell as a function of the temperature in wet H ₂	105
Table III.11: Evolution of the elementary component of the equivalent circuit of the BZY-c 1000 °C symmetrical cell as a function of the temperature in wet air.	105
Table III.12: Calculated ASC of the (RC) components of the BZY-c 1000 °C symmetrical cell depicted in Table III.10 in wet H ₂	106
Table III.13: Calculated ASC of the (RC) components of the BZY-c 1000 °C symmetrical cell depicted in Table III.11 in wet air.	106
Table III.14: Evolution of the elementary component of the fitted equivalent circuit of the BZY-b 1000 °C symmetrical cell as a function of the temperature in wet H ₂	109
Table III.15: Evolution of the elementary component of the fitted equivalent circuit of the BZY-b 1000 °C symmetrical cell as a function of the temperature in wet air.	109
Table III.16: Calculated ASC of the (RC) components of the BZY-b 1000 °C symmetrical cell depicted in Table III.14 in wet H ₂	110
Table III.17: Calculated ASC of the (RC) components of the BZY-b 1000 °C symmetrical cell depicted in Table III.15 in wet air.	110
Table III.18: Calculated activation energy of charge carrier transport in the bulk and in the grain boundary in wet air and wet H ₂ for BZY-com, BZY-c 1000 °C and BZY-b 1000 °C and reported activation energy from Sun et. al [273], Babilo et al. [69] and Yamazaki et al. [67].	114
Table III.19: Total conductivity of each sample in wet H ₂ and wet at 300 and 600 °C.....	118
Table IV.1: Comparison of some classical elaboration method of SOFC, adapted from [293], [294]	124
Table IV.2: Quantity used for the first anode, AFL and electrolyte slurry preparation, based on the thesis from Visweshwar Sivasankaran [15].	125
Table IV.3: Optimized quantity of anode, AFL and electrolyte slurries.....	126
Table IV.4: Sputtering deposition parameters of Ba and Zr _{0.8} Y _{0.2} targets	133

Table IV.5: Lattice parameter of BZY and NiO phases before and after annealing at 1000 °C	135
Table IV.6: Quantity used for the cathode ink	135
Table IV.7: Elementary steps involved in PCFC operation. The sense of reaction is given in the fuel cell mode, in electrolyze mode, all the elementary steps occur in the non-spontaneous way. Anode is noted A, cathode, C and electrolyte, E. TPB refers to the triple-phase boundary, ads refers to adsorbed. Adapted from [264], [309], [310].	140
Table 1: Quantity of each component of the LSCF slurry	153
Table 2: Obtained activation energies of SDC conduction on both LSCF//SDC//LSCF and Pt//SDC//Pt sample.....	155
Table 3: Quantities used for slurries preparation.	156
Table 4: Equivalent capacitances for the three contributions, calculated from Hirschorn [269].	158
Table 5: Fitted elements and mean time constants of the three semicircles.....	159
Table 6: Elemental composition (atomic%) of the tested interface, reference SDC and reference LSCF obtained by XPS. Adventitious carbon, cobalt and residual chlorine were removed from the elemental composition. ND (Non Determined).....	165
Table A.1: Structural parameters of the cubic BZ.....	171
Table A.2: Structure parameter of the orthorhombic BaCO ₃	172
Table A.3: Structural parameters of the cubic CeO ₂	172
Table A.4: Structural parameters of the cubic BZY20.....	173
Table A.5: Structural parameters of the monoclinic YO(OH).. ** O2 is the oxygen supporting the hydrogen.	173
Table A.6: Structural parameters of the c monoclinic Y _{0.8} Zr _{0.2} O(OH). ** O2 is the oxygen supporting the hydrogen.....	174
Table A.7: Structural parameters of the cubic Y _{1.6} Zr _{0.4} O _{3.2}	174
Table C.1: Ba 3d literature review	178
Table C.2: Zr 3d literature review	180
Table C.3: Y 3d literature review	183
Table C.4: O 1s literature review	185
Table C.5: C 1s literature review	186

GENERAL INTRODUCTION

With the increasing need for energy and global climate change, it is necessary to find an alternative to fossil fuels (coal, oil, natural gas) and nuclear energy. Indeed, the use of these resources is the major cause of greenhouse gas emissions and polluting gases and, moreover, they are not inexhaustible. Renewable energy production systems such as wind turbines and photovoltaic panels are highly sustainable, however, they operate intermittently. The need for a constant energetic supply has paved the way for the use of hydrogen as an energetic vector.

In an ideal energy cycle, hydrogen is produced by sustainable systems, stored in a tank and used into a fuel cell to fill the lack of electricity as needed. This thesis work focuses on the fuel cell part of the cycle. Nowadays, two fuel cell technologies are more or less mature: the proton exchange membrane fuel cell that operates at low temperature, typically below 200 °C, and the solid oxide fuel cell, based on oxide ion conduction, that operates at a temperature higher than 700 °C. The solid oxide fuel cell presents important advantages such as excellent efficiency, fuel flexibility and the use of non-precious materials but the high operating temperature leads to a strong degradation of the system.

This context is the driving force for the emergence of fuel cell technology which is the subject of this study: the protonic ceramic fuel cell (PCFC). As in solid oxide fuel cells, ceramic materials are the components of PCFC with protons as active ion species. Proton has a lower activation energy than the oxygen ion involved in solid oxide fuel cell, allowing to decrease the working temperature of the system in the 400 – 600 °C range. Moreover, the PCFCs exhibit the same merits as the solid oxide fuel cells in terms of efficiency and fuel flexibility.

The protonic conduction in some oxides has been reported in early 80's and the research on PCFC has begun in 90's. At the Interdisciplinaire Carnot de Bourgogne (ICB) laboratory, work on PCFC started in 2005 with the thesis work of Sandrine Ricote [1]. Despite intensive research around the world, several challenges remain in the PCFC area. One of the most important resides in the highly refractory nature of the conventional electrolyte materials requiring very high synthesis temperatures by the ceramic route and even higher temperatures during the sintering. To answer this problematic, the hydrothermal synthesis allowing to considerably reduce the temperature of synthesis was used in this study. In particular, a hydrothermal device allowing a continuous synthesis and developed at the ICB laboratory since 2003 was employed. This work is a part of the Pilot-HY project (oPtimisation d'une cellule de pILe à cOmbustible foncTionnant à l'HYdrogène), financed by the EIPHI (Engineering and Innovation through Physical Sciences, High-technologies, and crossdIsiplinary research) graduate school, the Bourgogne Franche-Comté region and the Fond Européen de Développement Régional (FEDER).

The thesis manuscript is divided into four main chapters, followed by an annex chapter concerning SOFC at the end of the manuscript.

The first chapter exposes the energy context with a focus on the hydrogen solution. In the second part, the different fuel cell technologies are presented and the PCFC principle is described. In the last part, the different possible materials of each component of an elementary cell (anode, electrolyte and cathode) are presented.

The second chapter focuses on the hydrothermal synthesis of the protonic conductor. The two devices used in this thesis work, the batch and the continuous devices, are described. In the second section, the results concerning the synthesis of the electrolyte material among the Y-doped $\text{BaCeO}_3\text{--BaZrO}_3$ solid solution are shown. The third part displays further characterization (structural, microstructure, compositional and chemical) on the chosen electrolyte material: $\text{BaZr}_{0.8}\text{Y}_{0.2}\text{O}_{3-\delta}$. The same analyses after annealing treatment at 1000 °C to homogenize the powder are presented in the fourth section. Finally, the assumed synthesis mechanism and the optimization of the synthesis procedure is shown in the last section.

The third chapter concerns the electrochemical impedance spectroscopy (EIS) of the protonic conductor. In the first section, the principle of EIS is described. The defect chemistry and the charge carrier species in perovskite protonic conductors are detailed, the definition and the measurement of the conductivity are presented. In the second section, the preparation of the symmetrical cell for the impedance measurement is described. A particular attention to the sintering behavior and the improvement of the sinterability of $\text{BaZr}_{0.8}\text{Y}_{0.2}\text{O}_{3-\delta}$ is given. The third part shows the impedance measurements completed in a wide range of temperature and the evolution of the conductivity on three samples: $\text{BaZr}_{0.8}\text{Y}_{0.2}\text{O}_{3-\delta}$ elaborated by the continuous route, $\text{BaZr}_{0.8}\text{Y}_{0.2}\text{O}_{3-\delta}$ synthesized by the batch process and a commercial $\text{BaZr}_{0.8}\text{Y}_{0.2}\text{O}_{3-\delta}$ as a comparison.

The fourth chapter deals with the elaboration of the PCFC. Two routes are evaluated. After an introduction to present the specification of the cells, the first route consisting of a co-tape casting and co-sintering is presented and characterizations of the elaborated half-cells are exposed. The third section outlines the manufacturing of complete cells by co-tape casting, reactive pulsed DC sputtering and spray deposition in order to improve the performances of the cells. The structure and microstructure at each step of the fabrication are analyzed. In the last section, the performances of the complete cells measured by EIS are presented.

The annex chapter presents results on solid oxide fuel cell with $\text{Ce}_{0.8}\text{Sm}_{0.2}\text{O}_{2-\delta}$ as electrolyte material. The purpose of this study was to work out the electrochemical analysis techniques used to test $\text{BaZr}_{0.8}\text{Y}_{0.2}\text{O}_{3-\delta}$ and PCFCs. In this section, the electrolyte material is presented. Then, impedance measurements on $\text{Ce}_{0.8}\text{Sm}_{0.2}\text{O}_{2-\delta}$ symmetrical cells are exhibited, a comparison of two electrode materials, Pt and $\text{La}_{0.6}\text{Sr}_{0.4}\text{Co}_{0.2}\text{Fe}_{0.8}\text{O}_{3-\delta}$ is given. The last section provides the preparation of SOFC complete cells by co-tape casting and co-sintering, the electrochemical performances and the study of the degradation of the cell.

CHAPTER 1: STATE OF THE ART

The purpose of this first chapter is to describe, firstly, the current energy context and the hydrogen solution. Secondly, the different fuel cell technologies are presented and the operation of Protonic Ceramic Fuel Cell (PCFC) are described. Special attention will be given to the mechanism of protonic diffusion. Finally, the specifications concerning the materials of each constituent of an elementary fuel cell (anode, electrolyte and cathode) are established and the materials matching the specifications are presented.

I. The hydrogen solution

In 2018 and 2019, the society has consumed nearly 14,000 million tons of oil equivalent (TOE), in which 12,000 million tons of oil equivalent were fossil fuels (oil, coal, natural gas) as shown in **Figure I.1** [2]. This represents more than 85% of global energy consumption and generates significant greenhouse gas emissions leading to a rise in global temperature. Even though the worldwide energy consumption decreased by 3.5 % in 2020 due to the global pandemic, the energy consumption started to rise again with a 4.1 % growth in 2021 [3]. According to the estimations of the Intergovernmental Panel on Climate Change (IPCC), global warming is expected to reach 1.5°C between 2030 and 2052 compared to the pre-industrial period if emissions continue to increase at the current rate [4].

Figure I.2 exposes the forecasts concerning energy consumption in the new policies scenario [5]. This scenario takes into account the policy commitment and the plans announced by the countries. As exposed in the figure, the share of renewables increases but the use of fossil fuels is still important and contributes to the rise of greenhouse gases emissions. Furthermore, fossil energies are non-renewable on the scale of a human life, and their depletion will pose significant problems for society. According to statistics from the Engie Group, oil, natural gas and coal reserves are expected to cover 54, 67 and 120 years of current consumption respectively [6]. Therefore, it becomes critical to ensure the energy transition.

Wind turbines and photovoltaic panels are some of the means envisaged. However, these devices generate electricity intermittently and therefore cannot ensure a constant response to the demand. Moreover, the major part of this energy is produced during the day, where the demand is the lowest, thus, a significant part of this energy is lost. One solution to improve efficiency is to store excess energy by the mean of hydrogen. Compared to petrol, hydrogen is an excellent energy carrier, indeed, 1 kg of hydrogen contains 33 kWh of usable energy, whereas gasoline and diesel only hold about 12 kWh/kg [7].

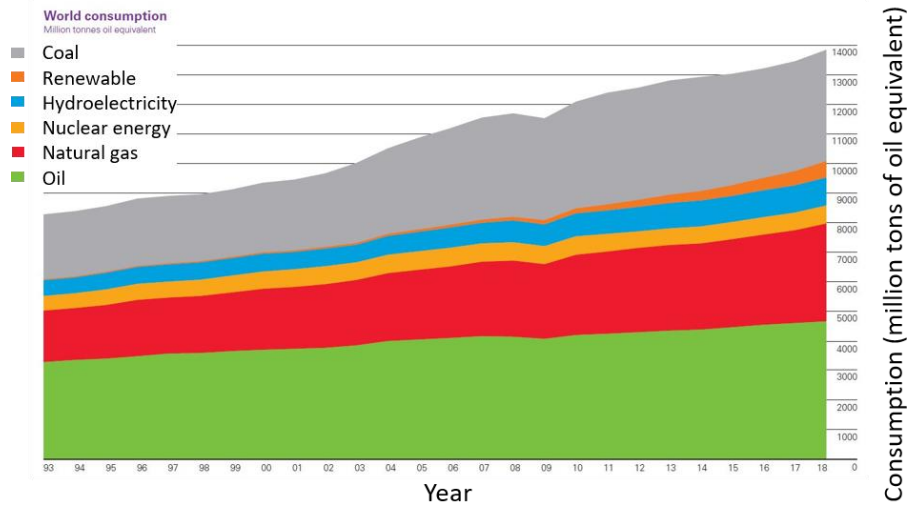


Figure I.1: World energy consumption by fuel [2]

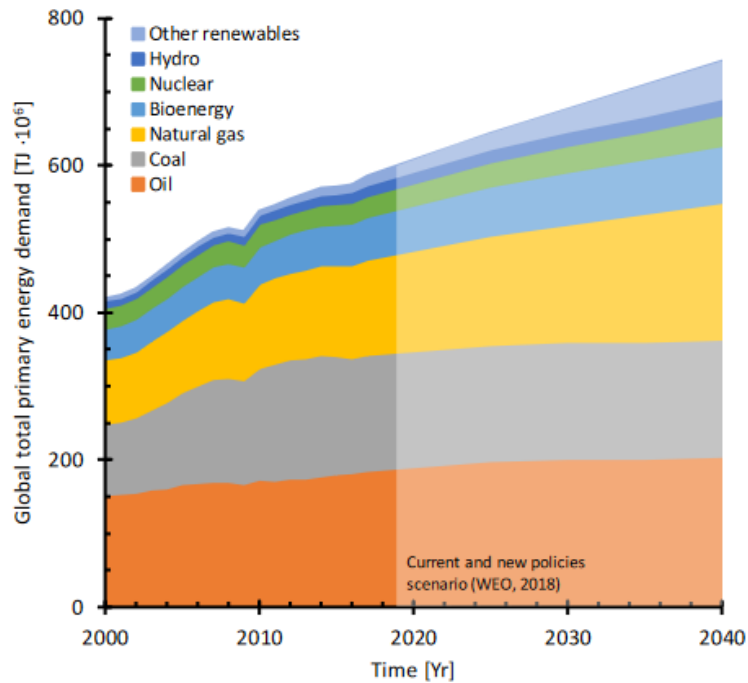


Figure I.2: Global energy consumption by fuel and projections up to 2040 [5]

Hydrogen is not present in its native state on Earth and about 96% of hydrogen is produced from fossil fuel, mainly by hydrocarbon steam reforming [8]. The remaining 4% comes from water electrolysis, a free greenhouse gas emission process [8]. The shares of production methods of hydrogen based on the review from Pinsky et al. are presented in **Figure I.3** [8]. Currently, research focuses on improving the efficiency of electrolysis and, consequently, increasing the part of hydrogen produced by water electrolysis.

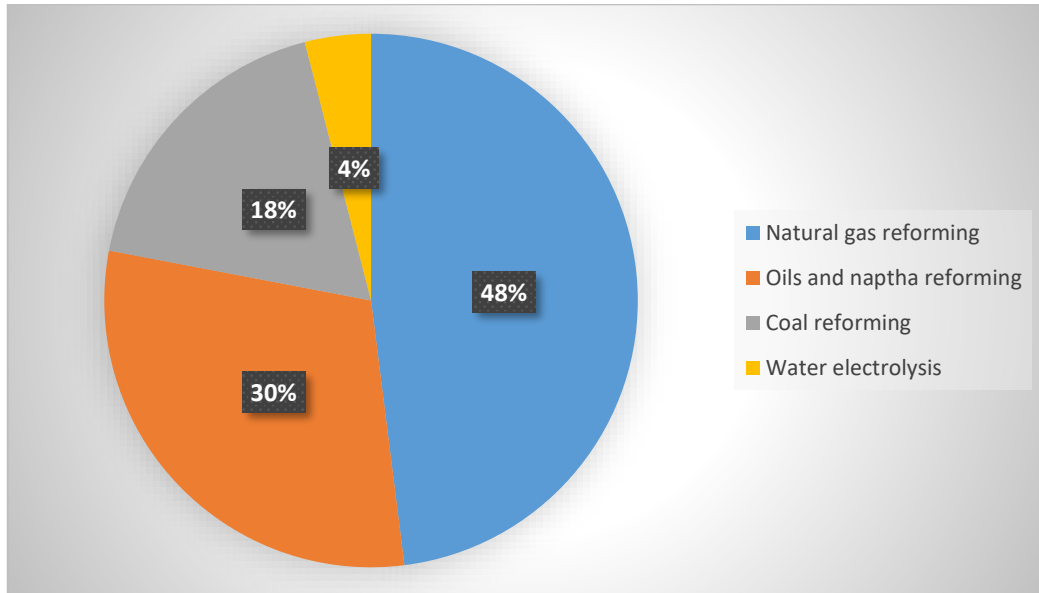


Figure I.3: Shares of hydrogen production methods based on the review from [8]

In an ideal energy cycle, hydrogen could be generated by water electrolysis from wind turbines and photovoltaic panels excess electricity. Produced hydrogen could be stored in a tank and used into a fuel cell to produce electricity when needed. Closed system tests have been conducted in several projects, such as the EOLBUS project in Auxerre, a pilot project involving wind turbine to produce hydrogen by electrolysis and the use of hydrogen into fuel cell electric buses [9] or the Energy Observer, a zero-emission boat combining solar panels, wind turbine, electrolyzer and fuel cell [10].

II. The fuel cell technology

Fuel cells are electrochemical devices that allow the direct conversion of chemical energy into electrical energy through oxidation-reduction reactions. When run on pure H_2 , the only by-products are electrons and water vapor.

II.1. Historic and generalities

In 1839, the English scientist Sir William Grove built the first system producing electricity from gas. It was a hydrogen-oxygen cell with platinum electrodes and sulphuric acid as electrolyte [11]. Grove detected an electric current between the electrodes when he introduced oxygen into one electrode and hydrogen at the other electrode, however, his discovery did not attract much academic interest. The industrial interest in fuel cells is based on the work of Francis Thomas Bacon. In 1953, he produced a prototype Alkaline Fuel Cell, which has served as a model for the fuel cells used in the Apollo space missions [12].

The first Solid Oxide Fuel Cell (SOFC), a fuel cell based on ceramic materials, was developed by Baur and Preis in 1937 [13]. This cell operated at 1000 °C. Since then, a lot of research has been done to lower the working temperature.

The protonic conduction at high temperature in perovskite material was highlighted in 1981 by *Iwahara et al.* [14]. This work has paved the way for a new type of fuel cell: the Protonic Ceramic Fuel Cell (PCFC). These cells use ceramic materials such as SOFCs but work at an intermediate temperature (400-600 °C). As shown in **Figure I.4**, the interest for high temperature proton conductors has continuously increased over the years. Indeed, in 2020, the number of papers containing “high temperature proton conductors” was 1638 on ScienceDirect website.

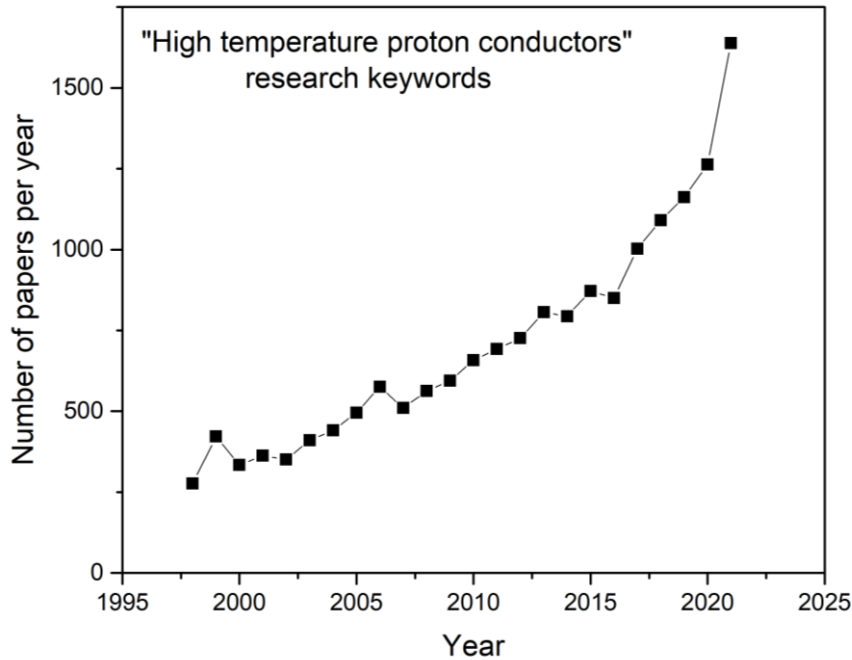


Figure I.4: Number of publications per year in ScienceDirect with "high temperature proton conductors" as keywords (in October 2021)

An elementary fuel cell consists of an anode, where the fuel (e.g., hydrogen) is oxidized, an electrolyte, which allows the passage of ions, and a cathode, where the oxidant (e.g., oxygen from the air) is reduced. As the electrolyte is electrically insulating, the electrons are collected at the electrodes by metal interconnectors, the electrons circulate in an external electrical circuit and thus generate electricity. The elementary cells are assembled one on the other through interconnects to form a "stack". The power of the stack depends on the number of elementary cells.

II.2. The different fuel cell technologies

There are several categories of fuel cells depending on the nature of the electrolyte material, they differ by the type of conducting species and by the working range of temperature. **Figure I.5** summarizes the characteristics of each type of fuel cell.

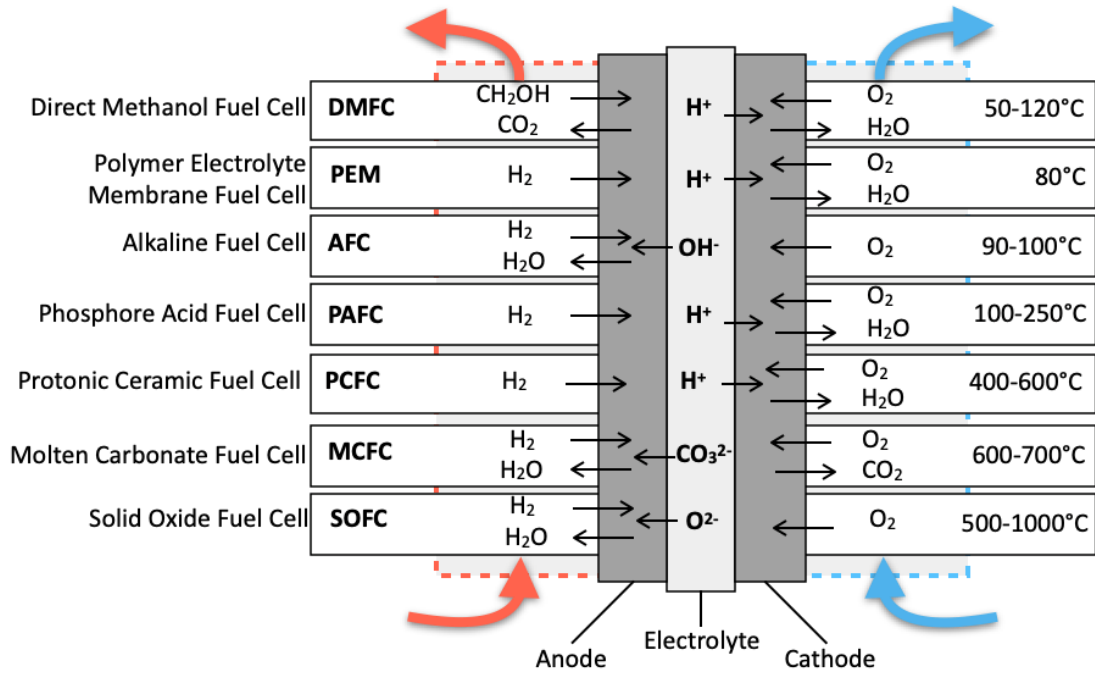


Figure I.5: The different fuel cell technologies (adapted from [15])

The research interest has mainly focused on Solid Oxide Fuel Cell (SOFC) and Proton Exchange Membrane Fuel Cell (PEMFC) for several years [16], [17]. PEMFCs are well advanced types of fuel cells that are suitable for cars and mass transportation. One of the main drawbacks of this system is that PEMFCs have to be fed with ultra-pure hydrogen to avoid carbon monoxide and sulfur poisoning. Commercialized PEMFCs typically use perfluorosulfonic acid (Nafion) as membrane. To maintain optimal performances, the Nafion membrane must be hydrated, for this reason, PEMFCs operate at temperatures below 100°C [18]. However, heat is needed for a good kinetic reaction. In this context, research in PEMFC systems concentrates on increasing the operating temperature of these systems.

In SOFC, the electrolyte material is a ceramic, classically yttrium-doped zirconia or samarium or gadolinium-doped ceria. These systems are promising for stationary applications due to their high efficiency, the possible cogeneration of heat and the ability to use a large variety of fuels, even natural gas [16]. However, the high working temperature (600-1000°C) leads to a strong degradation of the components and requires expensive specific materials for interconnector and sealing parts.

A consensus has thus emerged for the development of Protonic Ceramic Fuel Cell able to operate at intermediate temperatures (in the 400-600 °C temperature range). At these temperatures, the aging of materials is slower, cogeneration of heat is still possible and a high hydrogen purity is not necessary. Furthermore, less expensive standard interconnector materials (like metallic alloys) can be used.

Work on PCFCs at the ICB laboratory started in 2005. The governmental plan to develop hydrogen in France in 2018 has sparked a renewed interest in fuel cell research at the ICB laboratory. This work, financed by the EIPHI graduate school, is a part of the Pilot-HY project, a project funded by the Bourgogne Franche-Comté region and the Fond Européen de

Développement Régional (FEDER) within the framework of the national “Territoires hydrogène” label.

III. Protonic Ceramic Fuel Cells (PCFC)

PCFCs use an intermediate technology between the PEMFC and SOFC. PCFCs are characterized by a proton conductive membrane made of ceramic material.

III.1. Operation mechanism

In Protonic Ceramic Fuel Cell (PCFC), the active species is the proton. The hydrogen gas is oxidized at the anode, releasing protons and electrons. The electrons reach the cathode via an external circuit, generating an electric current. The protons pass through the electrolyte to the cathode. The combination of electrons, protons and oxygen results in the formation of water at the cathode, whereas for a SOFC cell, water vapor is produced at the anode. This operation mechanism is represented in **Figure I.6**.

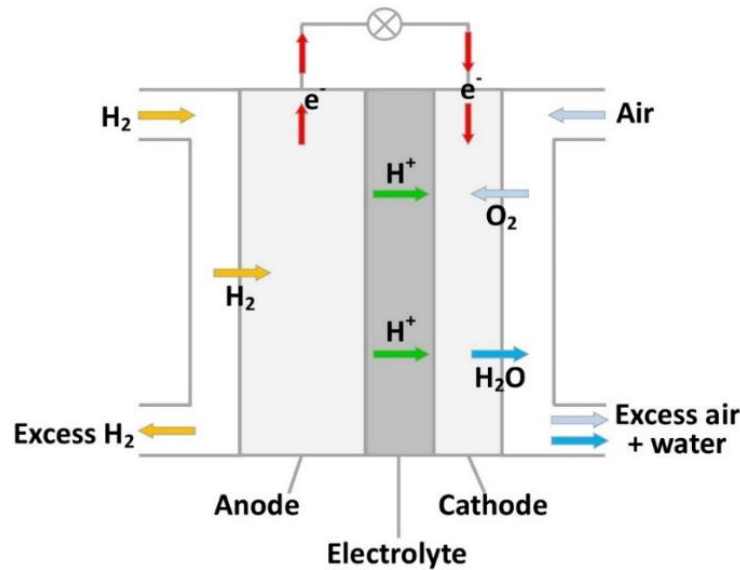


Figure I.6: Operation mechanism in PCFC

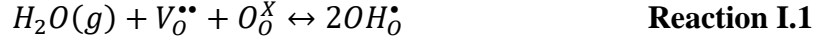
III.2. Protonic conduction

Since the discovery of protonic conduction at high temperatures in cerate and zirconate-based perovskite by *Iwahara et al.* in the early 80s, many applications using this property have been developed [14], [19]. These applications include fuel cells, hydrogen sensors and steam

electrolyzers [20]. The protonic conduction can be decomposed into two steps that will be developed in the following paragraphs: the proton incorporation and the proton migration.

III.2.a. Proton incorporation

Proton species are formed by dissociative adsorption of water vapor in oxygen vacancy as shown in **Reaction I.1** [21].



The water reacts with an oxygen from the lattice leading to the formation of two protonic defects in the form of hydroxyl species. As shown in this reaction, oxygen vacancies play an important role in proton incorporation, they are usually introduced by doping with an element of a lower valence.

When the material is exposed to H₂ containing atmosphere, proton incorporation occurs by following the **Reaction I.2** [22].



This reaction leads to the emergence of electronic conductivity in a reductive atmosphere which is not favorable for the cell performances.

Furthermore, the introduction of oxygen vacancies also leads to oxygen ion conductivity at high temperatures, i.e., when the energy needed for the oxygen ions to jump from their original sites to adjacent vacant sites is low [23].

A study from Nomura and Kageyama has shown that predominant proton conduction appears below 600 °C in the presence of water vapor and/or hydrogen, the predominant oxide-ion conduction happens under dry and low P(O₂) conditions and the predominant hole conduction domain takes place under dry and high P(O₂) conditions [24]. These results are consistent with the studies from Iwahara [19] and Bonanos and Poulsen [25]. **Figure I.7** shows the “charge carrier map” of Y-doped BaZrO₃ from the work of Nomura and Kageyama. To resume, in order to have sufficient protonic conductivity, it is necessary to operate under a humid reducing atmosphere.

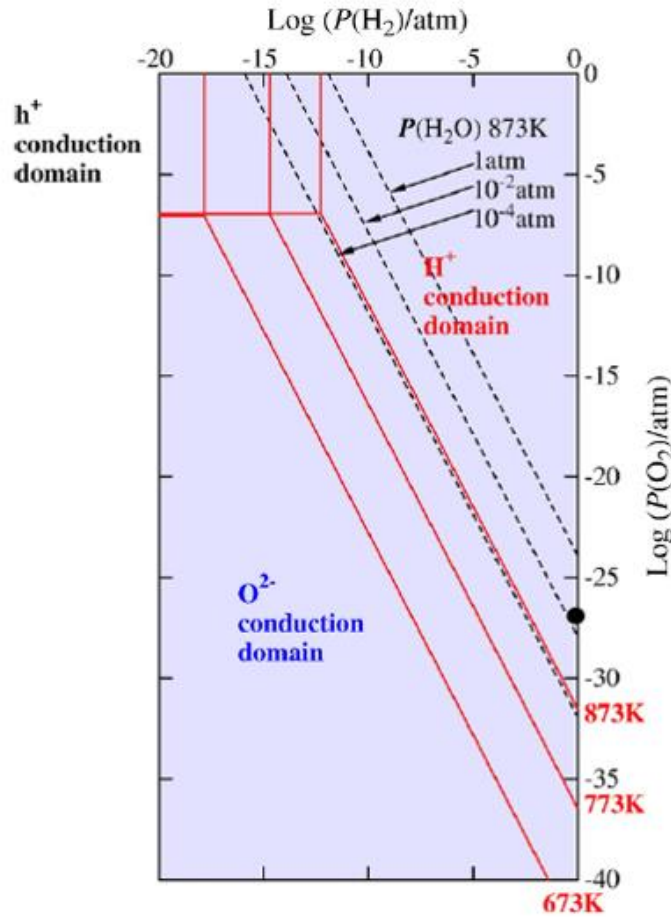


Figure I.7: The “charge carrier map” of $\text{BaZr}_{0.8}\text{Y}_{0.2}\text{O}_{3-\delta}$ between 673 and 873 K [24]

III.2.b. Proton migration

The conductivity depends not only on the number of charge carriers but also on the mobility of the charge carriers. For proton conduction, three relevant conduction mechanisms have been proposed [26]. The first considers that the proton is bound to a mobile ion, e.g., an oxygen ion, to form a mobile OH^- hydroxyl group. The second assumes that the proton is attached to a mobile molecule such as water or ammonia, to form a hydronium ion H_3O^+ or an ammonium ion NH_4^+ . In both cases, the proton then moves through the network via "a vehicle mechanism". The third mechanism considers the proton acceptor site to be a stationary ion in the lattice. In this case, the proton jump from the acceptor site to an adjacent site. This transport model is called the Grotthuss mechanism.

In perovskite oxides, the most common PCFC electrolyte material, the Grotthuss mechanism was confirmed using quantum-MD simulation [27]. The proton, in the form of hydroxyl specie, moves from oxygen ion to oxygen ion following a two-step mechanism:

- the rotation of the proton. This step presents a very low activation energy ($E_a < 0.1$ eV)
- the proton jump to the nearest acceptor site neighbor. This process is considered as the limiting step of proton conduction [28]–[30].

This mechanism is illustrated in **Figure I.8**.

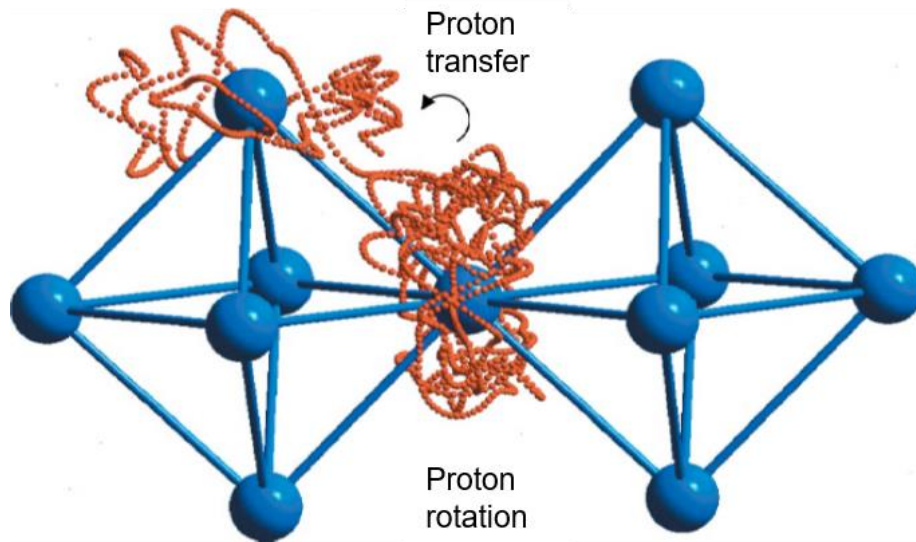


Figure I.8: The Grotthuss mechanism: rotation and proton transfer [27]

III.3. Constituent materials of PCFC

This paragraph describes the material specification for each part of the elementary cell and the possible materials that meet the specifications.

III.3.a. Specifications

Detailed materials specifications for PCFC components are difficult to ascertain as this technology is not yet mature [31]. However, it is possible to draw up the specifications of PCFC components based on that corresponding to the SOFC [23], [32]–[34].

The electrodes must have high electro-catalytic activity regarding the oxidation-reduction reactions, i.e. the oxidation of hydrogen on the anode side and the reduction of oxygen on the cathode side. Their electronic conductivity must be higher than 100 S.cm^{-1} at the operating temperature and a protonic conductivity of $10^{-5} \text{ S.cm}^{-1}$ should be sufficient. The polarization resistance of the electrodes is characterized by the area specific resistance (ASR), and, in order to obtain good electrochemical performance, the ASR of both cathode and anode have to be lower than $0.3 \text{ } \Omega.\text{cm}^2$. The anode has to be stable in a water-containing reductive atmosphere and the cathode has to be stable in a water-containing oxidizing atmosphere. Finally, both electrodes must present a porous microstructure.

The electrolyte has a large impact on fuel cell performance through its contribution to the internal ohmic resistance. For optimum cell performance, the electrolyte has to exhibit a protonic conductivity greater than $10^{-2} \text{ S.cm}^{-1}$ at the operating temperature and has to be an electronic insulator or to present negligible electronic conductivity. The electrolyte must be stable in both water-containing reducing and oxidizing atmosphere and, finally, it must have a dense microstructure to ensure gas separation.

Lastly, the chosen materials must have similar thermal expansion coefficients in order to avoid mechanical stresses during the elaboration and the thermal cycling in operation. They

must also be chemically stable toward the other cell components in order to prevent chemical reactions leading to an insulating phase.

The different specifications of each part of the elementary cell are presented in **Table I.1**.

Element of the cell	Anode	Electrolyte	Cathode
Protonic			
conductivity	$> 10^{-2} \text{ S.cm}^{-1}$	$> 10^{-2} \text{ S.cm}^{-1}$	$> 10^{-2} \text{ S.cm}^{-1}$
between 400 and 600 °C	preferable		preferable
Electronic			
conductivity	$> 100 \text{ S.cm}^{-1}$	Negligible	$> 100 \text{ S.cm}^{-1}$
between 400 and 600 °C			
Area specific resistance (ASR)	$< 0.3 \text{ } \Omega.\text{cm}^2$	$< 0.3 \text{ } \Omega.\text{cm}^2$	$< 0.3 \text{ } \Omega.\text{cm}^2$
Microstructure	Porous	Dense	Porous

Table I.1: Specification for each part of elementary cell, adapted from [23], [32], [33].

The cell interconnects have to separate fuel and oxidant gases in addition to the electrons collection. Then, the cell interconnects must present a good electronic conductivity ($> 100 \text{ S.cm}^{-1}$) and have to be chemically stable against water-containing reducing and oxidizing atmosphere at the operating temperature.

III.3.b. Electrolyte materials

Several materials present protonic conduction in the 400 – 600 °C range. The perovskite-type oxides have attracted the most attention. Some pyrochlore-type, Fergusonic-type and fluorite-type structure have also been considered.

III.3.b.i. Perovskite-type materials

The perovskite is defined by ABO_3 formula. The crystal structure is presented in **Figure I.9**. The substitution of B site by a trivalent element creates the oxygen vacancies required for proton incorporation.

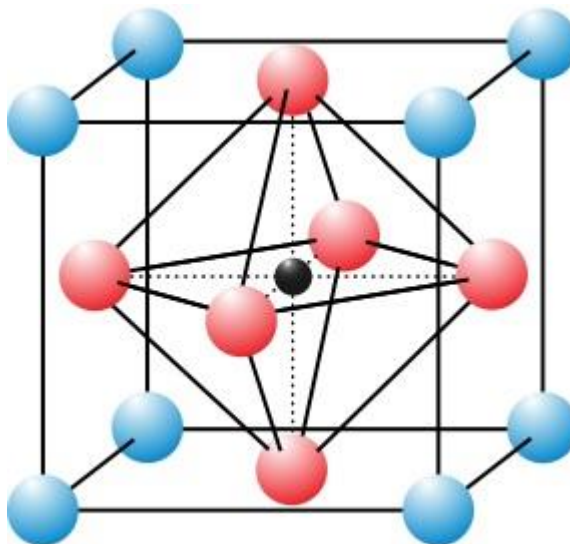


Figure I.9: Perovskite crystal structure where the blue spheres represent the A cation, the black sphere the B cation and the red spheres the oxygen anion.

Acceptor-doped $A^{2+}B^{4+}O_3$ -type perovskites are the most studied electrolyte materials. Research in perovskite-type materials for proton conductors has started with the work of Iwahara *et al.* on $SrCeO_3$ with Ce partially substituted by an aliovalent cation like Yb or Mg [14]. Since then, two major classes of perovskite-type proton conductors have emerged: the cerate-based materials and the zirconate-based materials [17], [35], [36].

$BaCeO_3$ -based oxides are currently the most studied electrolyte material for PCFC [17], [37]–[40]. It is generally reported that doped- $BaCeO_3$ exhibits the highest protonic conductivity among the perovskite-type material [27], [41]–[44]. Several dopants like Y, Nd, Yb, Gd or In have been examined [40], [45]–[47] and Y-doped $BaCeO_3$ appears to be the most promising electrolyte candidate with a protonic conductivity equal or superior to $2 \times 10^{-2} \text{ S.cm}^{-1}$ à 600°C [42], [48]–[50].

However, $BaCeO_3$ -based perovskites exhibit low stability in H_2O and/or CO_2 containing atmosphere which limits their practical application. Indeed, $BaCeO_3$ reacts with water vapor to form barium hydroxide (**Reaction I.3**) and reacts with CO_2 to form barium carbonate (**Reaction I.4**) [41], [43], [51], [52]:



To increase $BaCeO_3$ stability, some researchers have investigated the co-doping by a metallic and a non-metallic element [53], [54]. Wang *et al.* considered the influence of Cl doping on $BaCe_{0.8}Sm_{0.2}O_{3-\delta}$ on stability and protonic conductivity. Even if the stability against CO_2 was improved, they highlighted a drop in the conductivity [55]. Su *et al.* studied F-doped $BaCe_{0.8}Sm_{0.2}O_{3-\delta}$, they succeeded to improved chemical stability and no conductivity loss was observed [56].

Acceptor-doped $BaZrO_3$ is considered as a good electrolyte material, especially with a substitution of 20%mol of yttrium [57]–[59]. Y-doped $BaZrO_3$ presents excellent chemical stability [36], [38], [60]. However, the highly refractive nature of $BaZrO_3$ requires high

sintering temperatures (1600-1700 °C) and long annealing times (>24 h), to achieve dense membranes with large grains [43]. When such high sintering temperatures are used, the stoichiometry of the composition can be changed due to partial vaporization of barium from the perovskite and, for high Ba-losses, a segregation of yttrium oxide (Y₂O₃) at the grain boundaries can be observed, causing the decrease of the total proton conductivity [43].

Doped-BaZrO₃ shows lower total conductivity than BaCeO₃ because of the large grain boundary resistance [38], [43]. Different strategies exist to improve BZY sinterability. The first one is to synthesize ultrafine powder of BZY and the second one is to add sintering aids [38]. For example, Khani *et al.* reached 95% densification on a pellet of BZY10 after sintering at 1500°C by using 10-15nm particles synthesized by hydrogelation of acrylates [61]. Nevertheless, the addition of sintering aid such as ZnO, NiO or CuO remains the most used strategy [62]–[64]. However, the use of NiO and CuO as sintering aid involves electronic conductivity or leads to secondary phase formation [36], [65], [66], then ZnO appears to be the best candidate for sintering aid [62], [67]. In fact, doped-BaZrO₃ exhibit high bulk conductivity ($> 10^{-2}$ S.cm⁻¹ at 600°C) but the grain boundary resistance limits the total protonic conductivity (i.e., the sum of bulk and grain boundary conductivity) [27], [62], [64], [68], [69]. Reported total conductivity values of Y-doped BaZrO₃ differ from 10⁻⁶ to 10⁻² S.cm⁻¹ at 600°C in wet H₂ depending on the sample manufacturing [70].

Finally, the best perovskite-type electrolyte material seems to be an acceptor-doped BaCeO₃–BaZrO₃ solid solution which appears to be a good compromise between protonic conductivity and chemical stability [71]. Shi *et al.* reported a sufficient stability and a protonic conductivity of 9×10^{-3} S.cm⁻¹ at 600°C in wet hydrogen for BaZr_{0.3}Ce_{0.5}Y_{0.2}O_{3-δ} [72]. Other authors highlighted a conductivity higher than $> 10^{-2}$ S.cm⁻¹ at 600°C with no-reactivity during operating condition for BaCe_{0.7}Zr_{0.1}Y_{0.2}O_{3-δ} [71], [73], [74]. Yang *et al.* reported a maximum protonic conductivity of 5×10^{-2} S.cm⁻¹ at 600°C for BaCe_{0.7}Zr_{0.1}Y_{0.1}Yb_{0.1}O_{3-δ} [75].

III.3.b.ii. Other materials

Some pyrochlore-type oxides have also been considered as electrolytes for PCFC. Shimura *et al.* found a protonic conductivity up to 10⁻³ S.cm⁻¹ at 600 °C in a hydrogen-containing atmosphere for Ln₂Zr_{1.8}Y_{0.2}O_{7-δ}, with Ln = La, Nd, Sm and Gd [76]. Eurenus *et al.* investigated the protonic conductivity in Ln_{1.96}Ca_{0.04}Sn₂O_{7-δ} with Ln=La, Sm and Yb and they highlighted a protonic conductivity of 10⁻⁴ S.cm⁻¹ at 600 °C in wet argon for La_{1.96}Ca_{0.04}Sn₂O_{7-δ} [77].

Doped LaNbO₄, with Ferguson-type structure below 500°C and Scheelite-type structure above 500 °C, is considered as an attractive proton conductor material due to its good thermal, chemical and mechanical stability [78]–[80]. A protonic conductivity of 10⁻³ S.cm⁻¹ was found for Ca-doped LaNbO₄ at 800°C [80]. Nonetheless, this conductivity value remains one order of magnitude lower than those attainable in the best perovskite proton conductors.

In a recent study, Zamudio-García *et al.* have explored the protonic conduction of doped $\text{La}_2\text{Ce}_2\text{O}_7$. $\text{La}_2\text{Ce}_2\text{O}_7$ presents a disordered fluorite structure with composition $\text{Ce}_{0.5}\text{La}_{0.5}\text{O}_{2.75}$. This oxide exhibits protonic conductivity in wet atmosphere and the substitution of La^{3+} by an aliovalent element (Na^+ , Ca^{2+} , Sr^{2+} , Ba^{2+}) allows to increase protonic conductivity up to $9 \times 10^{-3} \text{ S.cm}^{-1}$ in wet air at 700°C [81]. However, in a reductive atmosphere, Ce^{4+} is partially reduced in Ce^{3+} involving the consequent formation of electronic charge carriers which limit its application as electrolyte for PCFC [82].

III.3.b.iii. Summary

A review from Kreuer has referenced many different proton-conducting oxides depending on their protonic conductivity as represented in **Figure I.10** [27]. This figure demonstrates that perovskite-type oxides have the highest protonic conduction. This result is in adequacy with several other studies [33], [76], [77], [79], [81]–[83]. Based on this conclusion, this work will focus on perovskite-type electrolyte material.

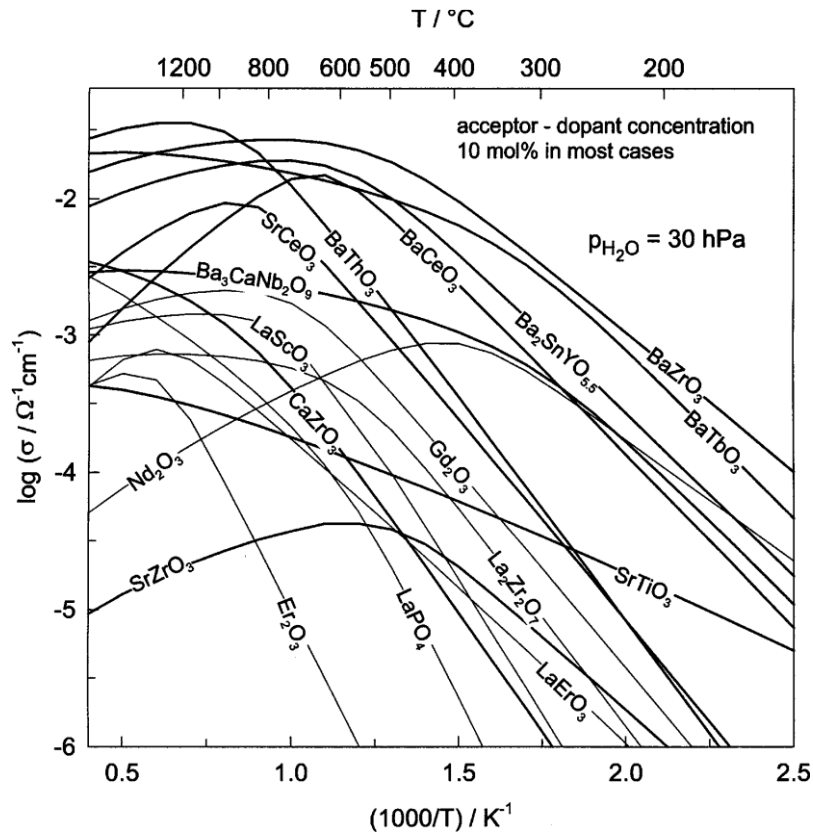


Figure I.10: Proton conductivities of various doped oxides calculated from proton concentration and motilities (type of dopant is not indicated) [27]

III.3.c. Anode materials

As described before, the anode material has to be an electronic conductor and is intended to catalyze the hydrogen oxidation reaction (HOR) according to **Reaction I.5** [84]:



III.3.c.i. Pure electronic conductor

Noble metals like platinum and palladium are well known to catalyze the oxidation reaction of hydrogen [85], [86]. Due to their high price, they have been replaced by transition metals such as nickel and cobalt [86], [87]. Those materials are pure electronic conductors, hence, the metallic material must be in contact with a proton-conducting material and the fuel for the HOR to occur. As shown in **Figure I.11**, this reaction can only take place at the anode/electrolyte/gas interface named the Triple Phase Boundary (TPB). Thus, the use of pure electronic conductor limits the number of reactive and the active volume of the electrode is restricted to the electrode-electrolyte interface.

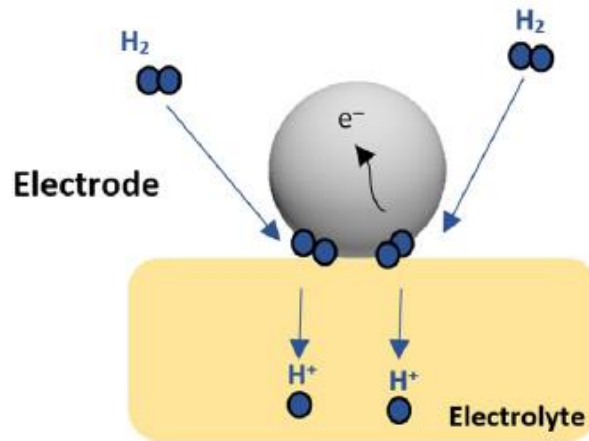


Figure I.11: Reaction at the interface anode/electrolyte/gas for a pure electronic conductor anode material [86]

III.3.c.ii. Mixed electronic protonic conductor

To increase the number of TPBs and thus the performances, the most common strategy is to combine an electronic conductor with a protonic conductor. Usually, the metallic material is mixed with the electrolyte material to form a porous cermet [88]. In that case, the HOR can occur in the volume of the anode as represented in **Figure I.12**.

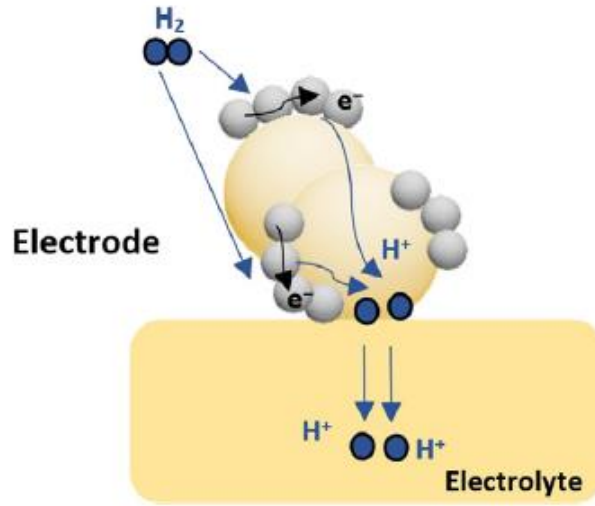
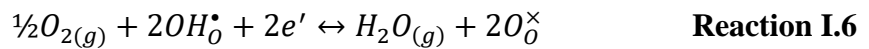


Figure I.12: Reaction in the volume of the anode for a cermet material [86]

Nickel is currently the most chosen material for the metallic component due to its good catalytic activity of the HOR and its good electrical conductivity [74], [89]–[92]. In classical SOFC systems, it is widely reported that nickel exhibits low tolerance to carbon deposition, named coking, and sulfur poisoning in the case of not pure hydrogen at the operating temperature [93]–[98]. However, nickel associated with proton conducting materials like Y or Yb-doped BaZrO₃ shows good tolerance to coking and sulfur poisoning [99]. In fact, the adsorbed water on the perovskite material reacts with adsorbed carbon or sulfur on the Ni surface to form CO and SO₂ respectively [100]. As for SOFC, cobalt-based cermet has also been considered [86]. Cobalt presents a better sulfur tolerance than nickel, but cobalt is not commonly used due to its high cost [101].

III.3.d. Cathode materials

The cathode side is the place of Oxygen Reduction Reaction (ORR) according to **Reaction I.6** [84].



As the water vapor is produced at the cathode side in the fuel cell mode, it is necessary to have a porous microstructure to ensure water vapor evacuation and dioxygen refueling.

III.3.d.i. Mixed electronic-oxygen ion conductor

Mixed ionic-electronic ion conductor (MIEC) material, the usual cathode material in SOFC systems, was also proposed for PCFC [102]. In this case, the simplified ORR mechanism occurs in two steps (**Reaction I.7** and **8**):



These reactions are represented in the **Figure I.13**. The most studied SOFC material, La_{1-x}Sr_xMnO_{3-δ}, was intended for PCFC cathode, but its poor ionic conductivity limits the

performance of the cell [103]. Cobalt-based perovskite such as $\text{La}_{1-x}\text{Sr}_x\text{CoO}_{3-\delta}$ was also proposed but presents the same drawback as $\text{La}_{1-x}\text{Sr}_x\text{MnO}_{3-\delta}$ [45], [46].

The partial substitution of Co by Fe allows to increase the ionic conductivity and $\text{La}_{0.6}\text{Sr}_{0.4}\text{Co}_{0.2}\text{Fe}_{0.8}\text{O}_{3-\delta}$ is widely reported as a promising cathode material [75], [104]–[106]. $\text{Sm}_{0.5}\text{Sr}_{0.5}\text{CoO}_{3-\delta}$ has been proposed due to its high catalytic activity for ORR and its acceptable ionic conductivity [107]–[111]. Extensive research about $\text{Ba}_{0.5}\text{Sr}_{0.5}\text{Co}_{0.8}\text{Fe}_{0.2}\text{O}_{3-\delta}$ is also carried, since this material exhibits high catalytic activity toward ORR, low ARS and acceptable ionic and electronic conductivity [112]–[115].

Finally, these three materials, $\text{La}_{0.6}\text{Sr}_{0.4}\text{Co}_{0.2}\text{Fe}_{0.8}\text{O}_{3-\delta}$, $\text{Sm}_{0.5}\text{Sr}_{0.5}\text{CoO}_{3-\delta}$ and $\text{Ba}_{0.5}\text{Sr}_{0.5}\text{Co}_{0.8}\text{Fe}_{0.2}\text{O}_{3-\delta}$ exhibit the highest catalytic activity for the reduction of dioxygen and, then are the most employed in PCFC area [107], [116], [117].

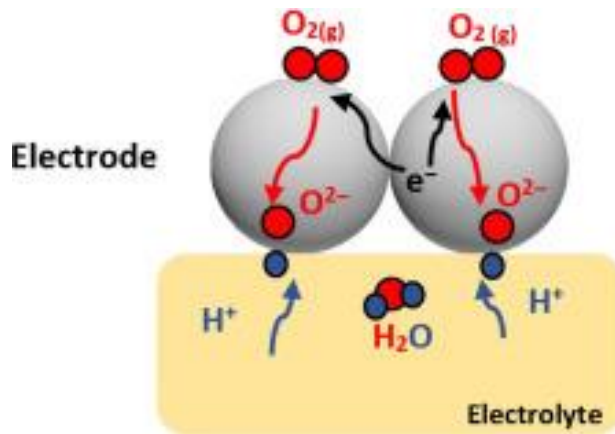


Figure I.13: Representation of the ORR in the case of a mixed electronic oxygen ion conductor [86]

As illustrated in **Figure I.13**, the formation of water can only be carried out at the interface electrode/electrolyte. To enhance the efficiency of ORR by increasing the number of place where **Reaction I.8** can occur, it is necessary to introduce protonic conduction into the cathode material [116].

III.3.d.ii. Mixed conductor/protonic conductor composite

To increase the number of TPB, the most promising method is to employ a composite of MIEC and a protonic conductor (usually the electrolyte material) [45], [46], [75], [104], [111], [118], [119]. In the case of such composite, the ORR occurs in the volume of the cathode as illustrated in **Figure I.14**. Furthermore, the use of a composite cathode allows to reduce the Thermal Expansion Coefficient (TEC) mismatch existing between classical cathode and electrolyte material [120], [121].

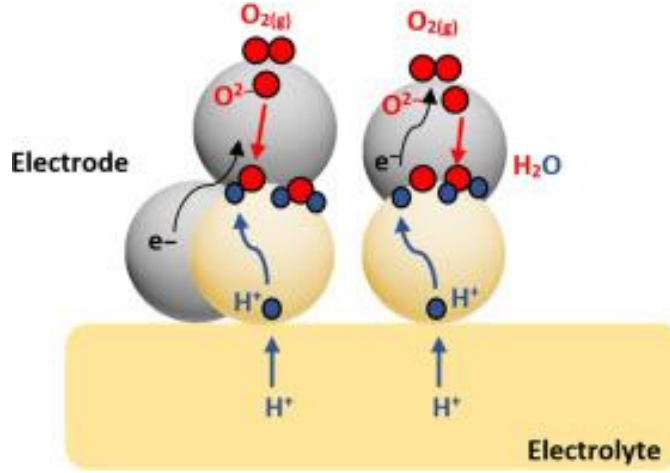


Figure I.14: Representation of the ORR in the case of a mixed conductor/protonic conductor composite [86]

III.3.d.iii. Mixed protonic-electronic-oxygen ion conductor

To promote the ORR in the entire volume of the cathode as illustrated in **Figure I.15**, mixed protonic-electronic-oxygen ion conductors have been developed. Cerate based material such as $\text{BaCe}_{1-x}\text{Yb}_x\text{O}_{3-\delta}$, $\text{BaCe}_{1-x}\text{Bi}_x\text{O}_{3-\delta}$ and $\text{BaCe}_{0.8-y}\text{Pr}_y\text{Gd}_{0.2}\text{O}_{3-\delta}$ have been proposed since they exhibit triple conduction under wet air atmosphere but their poor stability against CO_2 limits their practical application [122], [123]. $\text{NdBa}_{0.5}\text{Sr}_{0.5}\text{Co}_{1.5}\text{Fe}_{0.5}\text{O}_{5+\delta}$ and $\text{BaCo}_{0.4}\text{Fe}_{0.4}\text{Zr}_{0.1}\text{Y}_{0.1}\text{O}_{3-\delta}$ have also been reported as single-phase cathode materials. The cell based on $\text{BaCo}_{0.4}\text{Fe}_{0.4}\text{Zr}_{0.1}\text{Y}_{0.1}\text{O}_{3-\delta}$ using a $\text{BaCe}_{0.7}\text{Zr}_{0.1}\text{Y}_{0.1}\text{Yb}_{0.1}\text{O}_{3-\delta}$ electrolyte exhibited at a peak power density of 0.455 W.cm^{-2} at 500°C without degradation of the performances after 1400 hours [124]. The cell using $\text{BaCe}_{0.7}\text{Zr}_{0.1}\text{Y}_{0.1}\text{Yb}_{0.1}\text{O}_{3-\delta}$ as electrolyte material and $\text{NdBa}_{0.5}\text{Sr}_{0.5}\text{Co}_{1.5}\text{Fe}_{0.5}\text{O}_{5+\delta}$ as cathode material showed at peak power density of 0.69 W.cm^{-2} for 500 hours at 500°C [125].

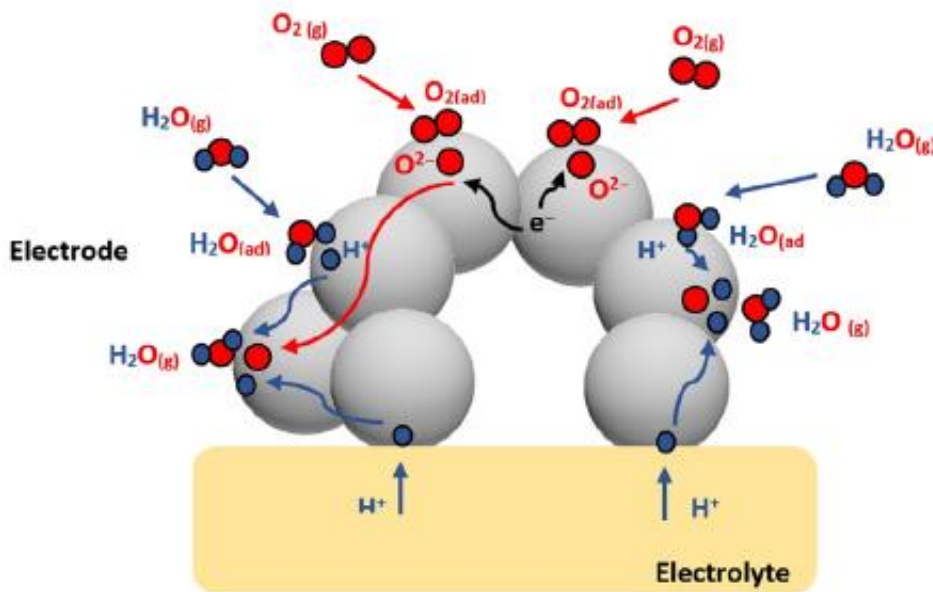


Figure I.15: Representation of the ORR in the case of a mixed conductor/protonic conductor composite [86]

IV. Conclusions and course of the study

Among the various alternative energy production, the use of hydrogen into fuel cell is attracting more and more interest. For a few years now, PCFCs are considered as one of the most promising fuel cell technology. In contrast to SOFCs that operate at a temperature above 600 °C and where the oxygen ions are the charge carriers, PCFCs use protons. Indeed, the lower activation energy of proton diffusion compared to that of the oxygen ion allows to decrease the operating temperature down to the 400–600 °C range.

Among the different high temperature proton conductors that have been presented in this chapter, the perovskite-type oxides and in particular the solid solution of acceptor-doped $\text{BaCeO}_3\text{--BaZrO}_3$ appears to be the most promising electrolyte material in terms of protonic conductivity and chemical stability. In this study, the hydrothermal synthesis of different protonic conductors among the Y-doped $\text{BaCeO}_3\text{--BaZrO}_3$ solid solution has been carried out. The synthesis route and the results will be presented in the second chapter. The electrochemical properties of the chosen electrolyte material have been studied by electrochemical impedance spectroscopy and will be shown in the third chapter.

The anode and cathode materials have also been selected to elaborate complete cells presented in the fourth chapter. Since Ni-electrolyte cermet is well known for SOFC as well as PCFC applications, it is the anode material that will be used in this study. Concerning the cathode material, the choice has felt on a composite $\text{Ba}_{0.5}\text{Sr}_{0.5}\text{Co}_{0.8}\text{Fe}_{0.2}\text{O}_{3-\delta}$ -electrolyte material due to the high catalytic activity of this oxide, its low ASR and its sufficient electronic and oxygen ion conductivity. Even though the triple conducting oxides are highly promising, they were not chosen since they are not commercially available.

CHAPTER II: HYDROTHERMAL SYNTHESIS AND CHARACTERIZATION OF THE PROTONIC CERAMIC CONDUCTOR

The present chapter describes, in the first part the principle of the hydrothermal process. Two variants were evaluated: one by a classical batch hydrothermal device and the other one by a novel continuous hydrothermal device developed at ICB laboratory [126].

The second part presents the different protonic electrolyte candidates among the Y-doped $\text{BaCeO}_3\text{--BaZrO}_3$ solid solution elaborated by the hydrothermal synthesis and their structural analysis.

Lastly, the final section provides further characterizations about $\text{Ba}(\text{Zr},\text{Y})\text{O}_3$, the chosen electrolyte material elaborated the batch and the continuous process. The structure, the microstructure, the composition and the surface chemistry of the as-synthesized powders was analyzed. Furthermore, the same study was carried on the annealed at 1000 °C powder.

The main results of the study of $\text{Ba}(\text{Zr},\text{Y})\text{O}_3$ powder elaborated by the continuous hydrothermal process has been published in *Ceramics International* in 2021 [127].

I. The hydrothermal route

The hydrothermal synthesis initially refers to the geological formation of minerals in the earth's crust thanks to the action of hot and pressurized water [128]. To reproduce these conditions, hydrothermal synthesis is carried out in a close vessel brought at high temperature and high pressure to control the equilibrium reaction and promote the formation of the targeted product [129], [130].

I.1. Introduction

Ceramics materials are commonly elaborated by several methods: solid-state reaction, co-precipitation, sol-gel process, spray drying and hydrothermal route [131]. The solid-state reaction (also called the ceramic route) remains the most used method for elaborating perovskite [65]. It consists of the mixing and grinding of metal oxides, metal carbonates or metal salts followed by a calcination at high temperature [132]. In the case of $\text{BaZr}_{0.8}\text{Y}_{0.2}\text{O}_{3-\delta}$ and $\text{BaCe}_{0.9}\text{Y}_{0.1}\text{O}_{3-\delta}$ preparation, the calcination temperature is 1400 °C [133], [134]. Despite its simplicity, this method presents several limitations, such as the presence of impurities (contamination from ball milling and crucible) and the large grains size obtained with a broad particle size distribution [65], [131].

The need for better purity and finer powders has triggered the development of soft-chemistry processes. The co-precipitation method consists in the dissolution of the starting materials (metal salts) in a common solvent (usually water), followed by precipitation using a precipitating agent (for example NH_4^+) [135]. The resulting precipitate is therefore calcinated in order to obtain the oxide powder. This route provides a satisfying control of the composition and of the particle size [136].

The sol-gel route involves a series of hydrolysis-condensation reactions of metal alkoxides leading to an inorganic network that is annealed to convert it into oxide powder [137], [138]. This process offers a precise control of the chemical composition of the powder and the formation of fine particles [139].

The Pechini method is derivated from the sol-gel route, used for metallic precursors with no hydroxo-stable species. The principle is based on the chelation reaction of the metallic cation followed by the esterification between the chelate and a monomer (usually ethylene glycol) to form a gel [140]. As for the co-precipitation and the sol-gel processes, the Pechini method requires a calcination treatment to obtain an oxide powder.

The spray drying process consists of spraying a precursors solution followed by a rapid drying of the droplets by using a hot gas and a calcination step to obtain the ceramic powder [141], [142]. This method allows to obtain spherical particles with a good control of the particle size and the particle size distribution [143].

The hydrothermal synthesis is defined as a process that uses solubility parameters and heterogeneous reactions in aqueous media at elevated temperature and pressure to directly crystallize inorganic materials from solution [144]–[146]. On the contrary to the other soft chemistry routes, the hydrothermal synthesis does not usually require additional calcination treatment to obtain a crystalline ceramic powder.

Table II.1 lists the advantages and drawbacks of the previous synthesis methods according to Yoshimura et al. [147]. The spray drying characteristics were added according to Santos et al. and Lintingre et al. [148], [149]. Based on this review, the hydrothermal synthesis offers many advantages such as a precise control of the morphology and the size of the particles with a narrow size distribution, a moderate cost and no requirement of additional thermal treatment.

	Solid Reaction	State Co-precipitation	Polymerized complex (*)	Sol-gel	Hydrothermal	Spray drying
Cost	Low-moderate	Moderate	High	High	Moderate	Moderate
State of development	Commercial	Commercial/ demonstration	R&D	R&D	Demonstration	Commercial
Compositional control	Poor	Good	Excellent	Good/Excellent	Good/Excellent	Good
Morphology control	Poor	Moderate	Moderate	Moderate	Good	Moderate
Powder reactivity	Poor	Good	Good	Good	Good	Good
Purity (%)	<99.5	>99.5	>99.9	>99.9	>99.5	N.D.
Calcination step	Yes	Yes	Yes	Yes	No	Yes
Milling step	Yes	Yes	Yes	Yes	No	No

Table II.1: Comparison of advanced oxide powder processes from Yoshimura et al. (2017), Santos et al. (2018) and Lintingre et al. (2016) [147]–[149]

*Polymerized complex refers to the Pechini method; N.D. = not defined

I.2. Principle of hydrothermal synthesis and water properties

The state of matter, liquid, solid and gas, depends on the temperature T , the pressure P and the specific volume V as presented in **Figure II.1**. To simplify the representation, the states of matter are commonly represented on a 2D phase diagram as a function of the T and the P . **Figure II.2** shows the 2D phase diagram of water. The prevalence domain of each state is delimited by the state change curves, joining at the triple point, where the three phases of water are co-existent. The vaporization curve, separating liquid and gas states, stops in a point called the critical point ($T_c = 374\text{ °C}$ and $P_c = 221\text{ bar}$). Above the critical point, water is in its supercritical state and exhibits physicochemical properties intermediate between a liquid and a gas. The hydrothermal synthesis exploits this property and is usually carried out in the supercritical condition.

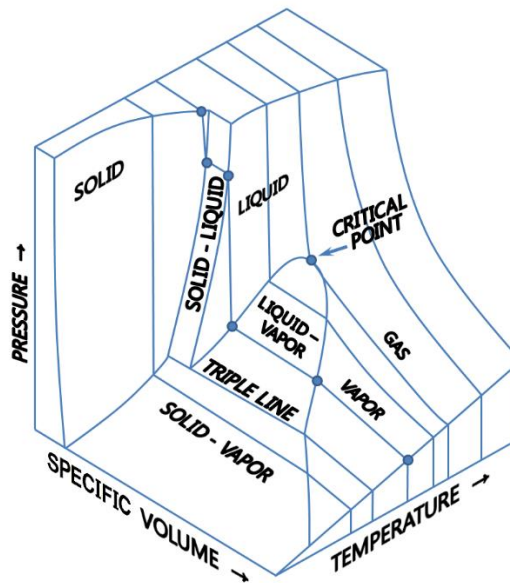


Figure II.1: 3D phase diagram of a pure material (CC BY-SA 3.0)

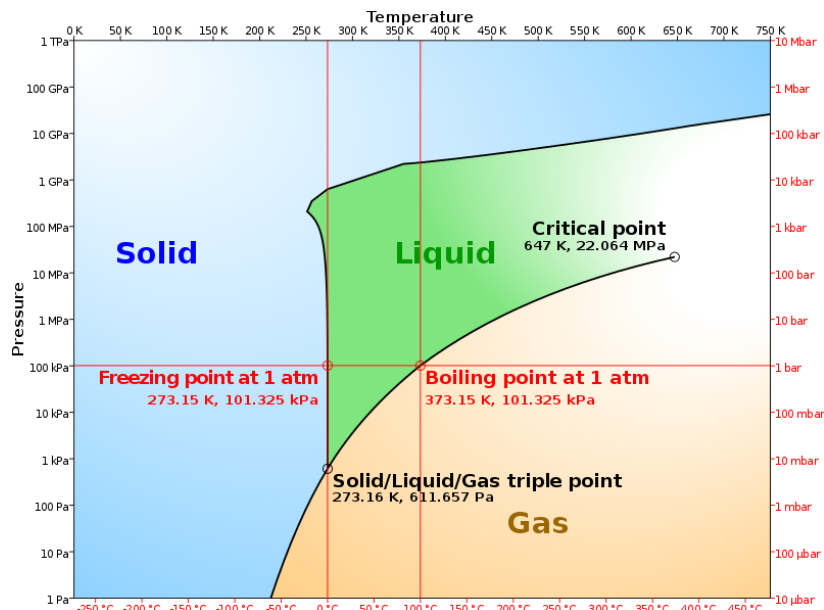


Figure II.2: Water phase diagram, simplified from [150]

Figure II.3 shows the evolution of the water's properties as a function of the temperature at 245 bar. The density drops rapidly near the critical point, reaching a value of 280 kg.m^{-3} at the critical point and stabilizes around 50 kg.m^{-3} at higher T and P [151]. This decrease and the viscosity close to that of the gas after the critical point allow rapid and homogeneous mixing during the hydrothermal synthesis in supercritical conditions. The passage of the critical point is complemented by a fall of the thermal conductivity, which limits the heat exchanges within the reaction environment. The specific heat capacity reaches a maximum at the critical point with a abrupt rise and fall in specific heat capacity around the critical point indicates that the critical point is difficult to cross. At 25°C and 1 bar, the dielectric constant of water is 78 F.m^{-1} , by increasing the temperature, the dielectric constant regularly decreases to 2 F.m^{-1} after the critical point [152].

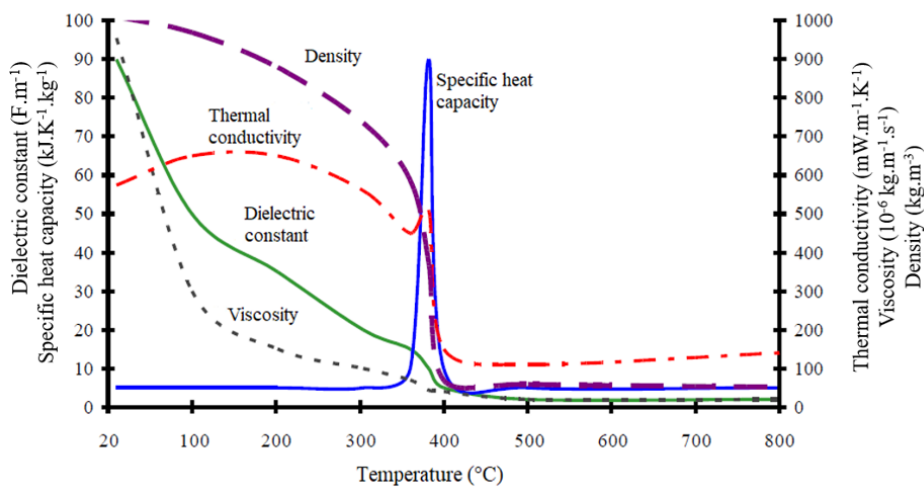


Figure II.3: Evolution of the water properties as a function of the temperature at 245 bar [153]

The dielectric constant is a key parameter of the hydrothermal synthesis since it affects the solubility of the species as it represents the bulk polarity of the solvent [154]. The solubility of the inorganics and hydrocarbons at 253 bar depending on the temperature is presented in **Figure II.4**. Before the critical point, hydrocarbons are insoluble in water while inorganics are soluble. At a temperature higher than 374°C , hydrocarbons become soluble while inorganics become insoluble, leading to the formation of hydroxide nuclei which are immediately dehydrated to form ultrafine particles [155].

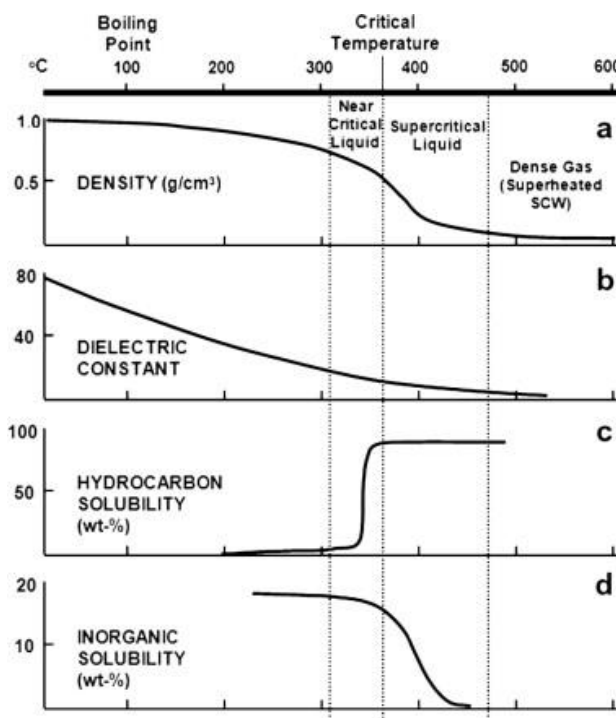


Figure II.4: Evolution of inorganics and hydrocarbons solubility at 253 bar depending on the temperature [156]

The combination of the properties in sub- and supercritical domain presented above makes the hydrothermal synthesis very interesting for several applications, mainly for the extraction, for example, the extraction of caffeine or the processing of inorganic materials, such as perovskite oxides.

I.3. Hydrothermal apparatus and synthesis protocols

Two variants of the process were evaluated, one by a classical batch hydrothermal device and the other one by a continuous hydrothermal device developed at ICB laboratory [157]. The supercritical hydrothermal synthesis of metal oxide particles using a continuous flow reactor was first proposed by Adschiri *et al.* in 1992 [158]. Besides the improved productivity, using a continuous flow involves a short reaction time leading to the possible formation of metastable and highly doped structures [159], [160].

I.3.a. The batch reactor

The batch process can be used for solvothermal synthesis up to 500 °C and 350 bar. Since the couple critical temperature/critical pressure is 374 °C and 221 bar for water, this device is able to work in supercritical conditions. In our experiments, all the syntheses were carried out at 400 °C and 300 bar. $\text{ZrO}(\text{NO}_3)_2 \cdot 6\text{H}_2\text{O}$, $\text{Ba}(\text{NO}_3)_2$, $\text{Ce}(\text{NO}_3)_3 \cdot 6\text{H}_2\text{O}$ and $\text{Y}(\text{NO}_3)_2 \cdot 6\text{H}_2\text{O}$ have been used as precursor materials (purchased from Sigma-Aldrich). 50 mL of metallic precursors in solution at $5 \times 10^{-2} \text{ mol.L}^{-1}$, prepared according to the stoichiometry of the target composition by dissolution in deionized water and homogenized with an ultrasonic rod, is introduced into the reactor. 50 mL of another solution, consisting of sodium hydroxide

at $3 \times 10^{-1} \text{ mol.L}^{-1}$, employed in order to avoid the formation of ZrO_2 , is also introduced into the reactor [161]. The final pH in the reactor is equal to 13. Finally, to complete the working volume of the reactor, which is 150 mL, 50 mL of deionized water is added. The reactor, in Inconel, is sealed by an Inconel seal and eight screws, also in Inconel, tightened to a force of 60 N.m. The reactor is then heated by external resistances to the target temperature. A thermocouple, passing through the reactor, measures the temperature of the solution. By increasing the temperature, and because the reactor is sealed, the pressure also increases. The obtained pressure depends on the temperature and the volume of the solution. A stirring blade ensures the mixing and the homogenization of the solution. After two hours, the conditions (T and P) are reached, meaning the experiment is finished. The reactor is brought back to room temperature by air circulation between the reactor walls and the electric furnace and the solution containing the particles is recovered. **Figure II.5** shows the schematic and the photography of the batch set-up.

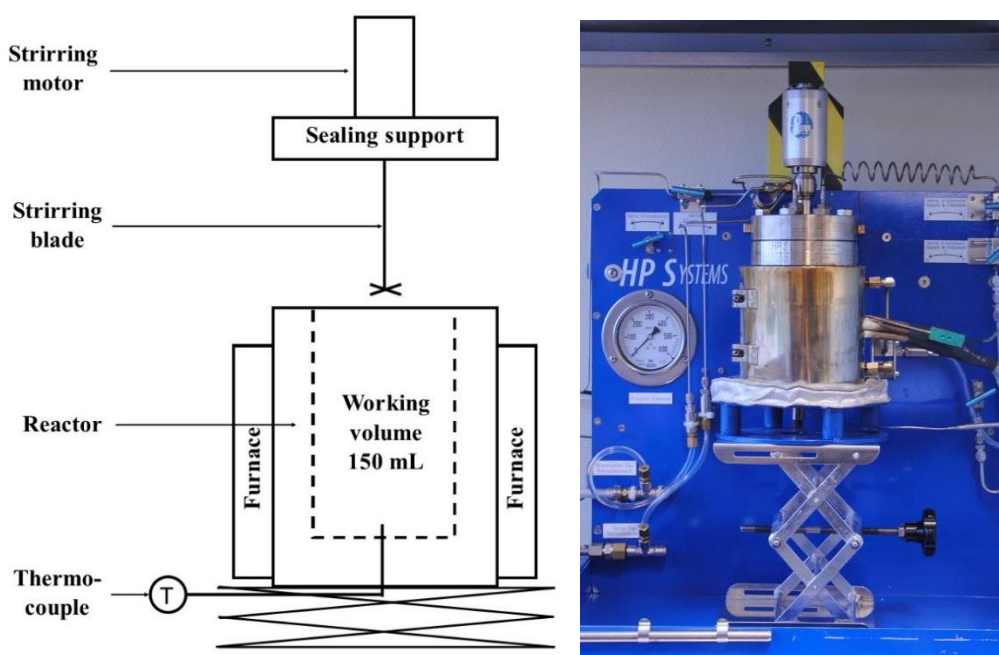


Figure II.5: Schematic and photography of the batch hydrothermal set-up

1.3.b. The continuous reactor

The continuous process can be used up to 600 °C and 350 bar. For the experiments, the syntheses were carried out between 400 °C and 500 °C and at 300 bar. The solution of metallic precursors and the sodium hydroxide solution are prepared by the same method as before. **Figure II.6** shows the scheme of the continuous set-up. Container (a), at the beginning of the process, holds the aqueous solution of metal cations, container (b) holds the solution of sodium hydroxide and the third container (c) holds the distilled water. The reactor consists of a “pipe to pipe” cylinder with a total volume of 25 mL, the inner diameter of the external pipe is 10 mm. Pressurized solutions (a) and (b) are brought to the reactor inlet at room temperature by high-pressure pumps. Pressurized demineralized water is pre-heated and brought counter-currently through the internal pipe of the reactor so that the three solutions meet at the mixing

zone. In the reactor the pH is equal to 13. The resulting solution is evacuated through the external tube, where the reactions leading to the formation of metal oxides take place. The flow rate of the three solutions is set to around 10 mL min^{-1} per solution, the final flow measured at the end of the set-up (after the backpressure regulator) varies between 30 and 35 mL.min^{-1} . The residence time into the reactor under supercritical conditions is of the order of few seconds (determined by Computational Fluid Dynamics calculations) [162]. At the reactor outlet, a cooling system stops the germination and growth stages. A filtration system at the end of the device captures the agglomerated particles to avoid damage to the backpressure regulator. These particles are added to the suspension obtained after the backpressure regulator. The particles sediment at the bottom of the beaker, the surfactant is siphoned off and distilled water is added to wash the particles. This operation is repeated until a neutral pH is obtained. The supernatant water is siphoned off one last time and the suspension is dried in an oven at 80°C for three days to get a powder.

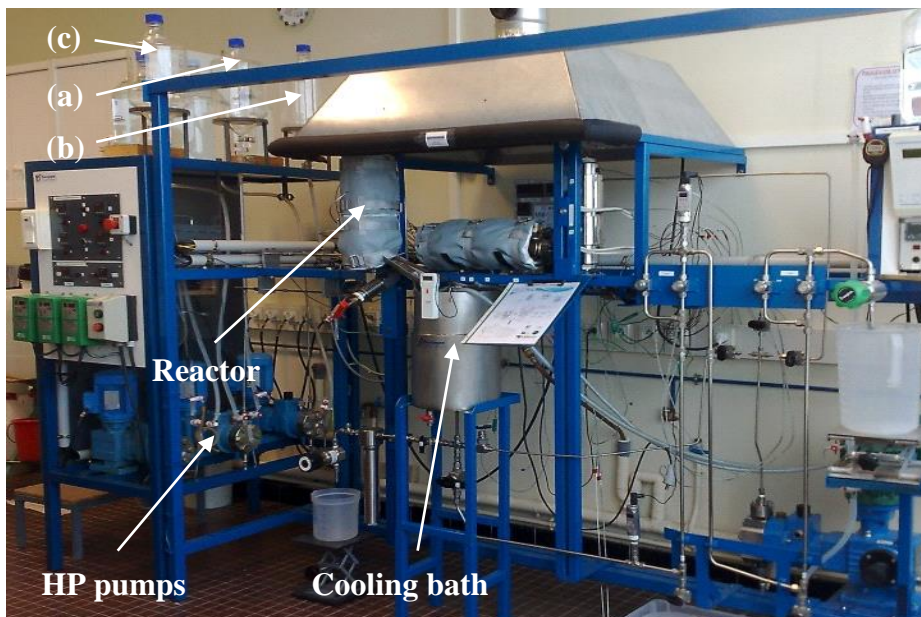
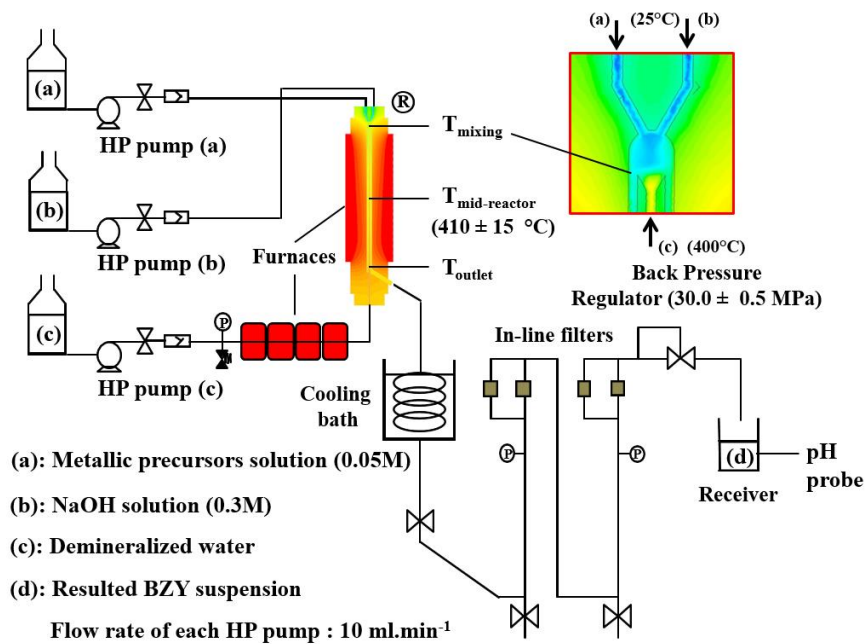


Figure II.6: Schematic and photography of the continuous hydrothermal set-up

II. Structural characterization of the synthesized materials

Based on the review from the first chapter, the target material is $\text{BaCe}_{0.7}\text{Zr}_{0.1}\text{Y}_{0.2}\text{O}_{3-\delta}$. To achieve this objective, different syntheses were carried out: BaZrO_3 , BaCeO_3 , $\text{Ba}(\text{Ce},\text{Zr})\text{O}_3$, $\text{Ba}(\text{Zr},\text{Ce},\text{Y})\text{O}_{3-\delta}$ and $\text{Ba}(\text{Zr},\text{Y})\text{O}_{3-\delta}$. To simplify the notation, each composition is noted as described in **Table II.2**. The synthesized powders are analyzed by X-Ray Diffraction (XRD) to verify the composition, the structure and the lattice parameter. XRD analysis is conducted on Bruker D2 Phaser coupled with linear detector Lynxeye_XE_T using the Cu $K\alpha$ radiation ($\lambda_{K\alpha1} = 1.54056 \text{ \AA}$ and $\lambda_{K\alpha2} = 1.54439 \text{ \AA}$), in the 2θ range from 20 to 80° with steps of 0.02° , the acquisition time of each step was 0.5 second. The XRD patterns were refined using the Rietveld method using Fullprof software (Version 2.0). The crystallographic data and structural parameters of each phase as inputted in the software are presented in **Annex A**.

Composition	Synthesis process	Notation
BaZrO_3	Batch	BZ-b
BaZrO_3	Continuous	BZ-c
BaCeO_3	Continuous	BC-c
$\text{BaCe}_{0.9}\text{Zr}_{0.1}\text{O}_3$	Continuous	BCZ10-c
$\text{BaCe}_{0.1}\text{Zr}_{0.9}\text{O}_3$	Continuous	BCZ90-c
$\text{BaCe}_{0.7}\text{Zr}_{0.1}\text{Y}_{0.2}\text{O}_{3-\delta}$	Continuous	BCZY712-c
$\text{BaZr}_{0.8}\text{Y}_{0.2}\text{O}_{3-\delta}$	Batch	BZY20-b
$\text{BaZr}_{0.8}\text{Y}_{0.2}\text{O}_{3-\delta}$	Continuous	BZY20-c

Table II.2: Notation of the different compositions

II.1. BaZrO_3 (BZ)

The synthesis of BZ by the continuous process was investigated previously at the ICB laboratory by Aimable et al. [161]. BZ powder was synthesized with the continuous hydrothermal process in supercritical water at $400^\circ\text{C} - 300 \text{ bar}$ and $500^\circ\text{C} - 300 \text{ bar}$. In the batch set-up, the conditions were $400^\circ\text{C} - 300 \text{ bar}$. **Figure II.7** shows the diffractograms of the synthesized powders. Two phases were identified. The main phase corresponds to BaZrO_3 which exhibits a cubic perovskite structure with $Pm-3m$ space group. Such high symmetrical structure promotes the excellent stability of this compound [86]. All diffractograms show a secondary phase consisting of BaCO_3 (orthorhombic system, space group $Pnma$). The quantity varies with the synthesis conditions. Many studies focusing on the synthesis of Ba-based perovskite report the presence of BaCO_3 impurity [163]–[166]. BaCO_3 is formed by free Ba^{2+} and CO_2 from the atmosphere [167].

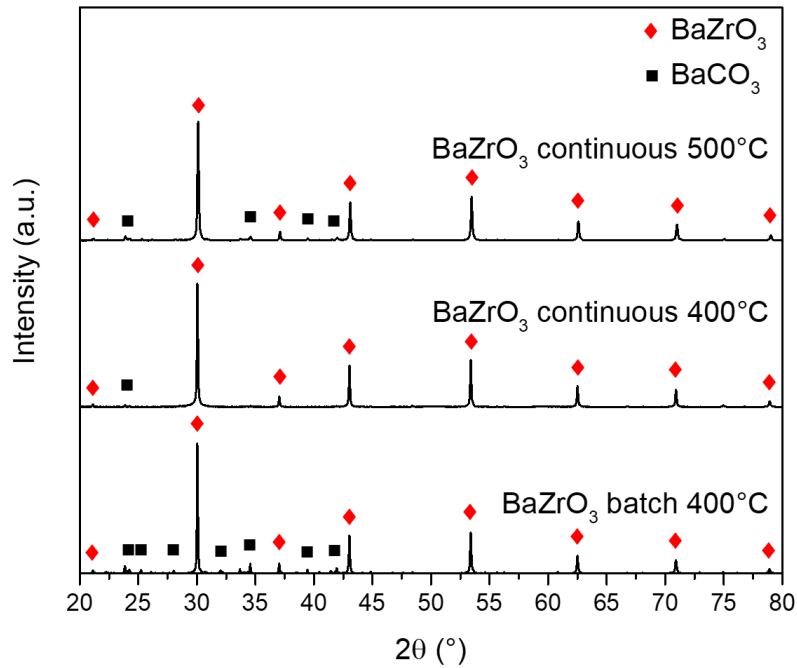


Figure II.7: X-ray diffractogram of BaZrO_3 synthesized by the batch process at 400°C , the continuous process at 400°C and the continuous process at 500°C

Rietveld refinement was performed on the three diffractograms and the results are recorded in **Table II.3**. The refined lattice parameters are $4.193(0)$ Å for BZ-b at 400°C , $4.193(2)$ Å for BZ-c at 400°C and $4.191(0)$ Å for BZ-c at 500°C . The values obtained for the synthesis at 400°C are in perfect agreement with the values obtained by the Nuñez group (4.1930 Å) and the Akbarzadeh group (4.1943 Å) [168], [169]. However, the lattice parameter obtained for the powder synthesized by the continuous process at 500°C is slightly lower than expected, suggesting ions sub-stoichiometry and/or crystal defect.

BZ-c at 400°C contains 1.6 wt% of BaCO_3 while BZ-b at 400°C and BZ-c at 500°C exhibit respectively 11.8 and 6.0 wt% of BaCO_3 . According to these considerations, i.e., composition/crystal defect and amount of BaCO_3 , the synthesis should be conducted at 400°C using the continuous process.

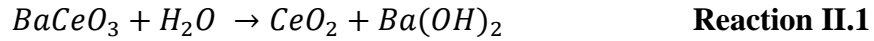
Name	Lattice parameter of the perovskite phase	Wt% of BaZrO_3	Wt% of BaCO_3
BZ-b 400°C	$4.193(0)$ Å	88.2	11.8
BZ-c 400°C	$4.193(2)$ Å	98.4	1.6
BZ-c 500°C	$4.191(0)$ Å	94.0	6.0

Table II.3: Rietveld refinement of BaZrO_3 synthesized by the batch process at 400°C , the continuous process at 400°C and the continuous process at 500°C

II.2. BaCeO₃

The synthesis of BaCeO₃ was attempted in the continuous reactor at 400 °C and 300 bar following a similar protocol as BaZrO₃. **Figure II.8** presents the X-ray diffractogram of the obtained powder. Three phases were detected: one major CeO₂ phase (cubic, Fm-3m), BaCO₃ and BaZrO₃ with respective weight percentages obtained by Rietveld refinement of 95.7, 3.7 and 0.6 wt%. The presence of BaZrO₃ is a contamination due to a remainder of the previous synthesized powder into the set-up.

It has been widely shown that BaCeO₃ is not stable in H₂O and CO₂-containing atmospheres [43], [170], [171]. In an H₂O-containing atmosphere, BaCeO₃ decomposes into CeO₂ and Ba(OH)₂ according to **Reaction II.1** [172]. This chemical degradation is induced by the high basicity of BaCeO₃ [173], [174].



The resultant Ba(OH)₂ reacts with CO₂ from the atmosphere according to **Reaction II.2**:

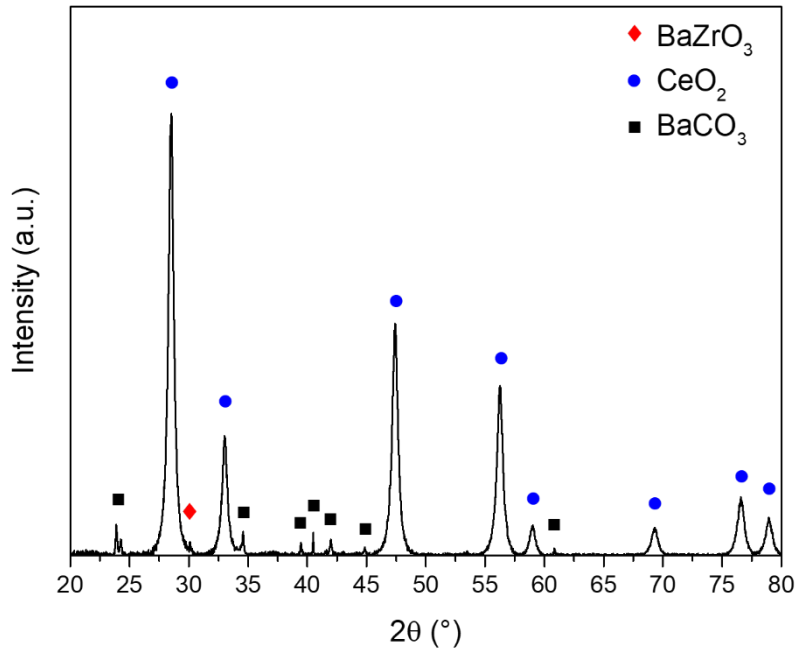
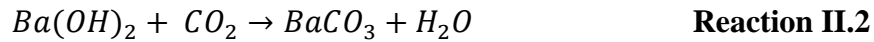


Figure II.8: X-ray diffractogram of BaCeO₃-target obtained powder synthesized by the continuous process at 400 °C and 300 bar.

Moreover, the synthesized CeO₂ material exhibits large diffraction peaks, characteristic of small coherent diffraction domains. The average crystallite size t was estimated by the Williamson and Hall method. In this method, the integral breadth β of the sample is considered as a summation of the breadth due to the particle size broadening β_P and the lattice strain broadening β_L . Since $\beta_P = \frac{\lambda}{t \cos \theta}$ and $\beta_L = 4\xi \tan \theta$, where t represents the apparent crystallite size, λ the X-ray wavelength, θ the Bragg angle and ξ the lattice strain rate, the integral breadth of the sample is defined as showed in **Equation II.1** [175]:

$$\beta = \frac{\lambda}{t \cos \theta} + 4\xi \tan \theta \quad \text{Equation II.1}$$

Then by plotting $\beta \cos \theta$ as a function of $\sin \theta$, the crystallite size can be calculated from the y-intercept corresponding to λ/t and the lattice strain rate from the slope which is 4ξ . In order to obtain the integral breadth β of the sample, it is first necessary to subtract the broadening due to the instrument according to **Equation II.2**:

$$\beta_{\text{sample}} = \beta_{\text{observed}} - \beta_{\text{instrumental}} \quad \text{Equation II.2}$$

To obtain the $\beta_{\text{instrumental}}$, a single-crystal of BaF_2 considered as an infinite crystallite that does not give rise to a widening of peaks, i.e. ($\beta_{\text{sample}} = 0$), was analyzed. The obtained XRD diffractogram is presented in **Annex B**.

The Williamson and Hall diagram of CeO_2 phase is presented in **Figure II.9**. The point at $\sin \theta = 0.49$, i.e., $\theta = 59^\circ$, is not in line with the others due to the slightly asymmetric shape of the diffraction peak and was not taken into account for the linear fit. A negative slope is not expected and is probably related to this diffraction peak, then, the slope can be considered close to zero and the lattice strain broadening can be neglected. The crystallite size calculated using **Equation II.3** is 18 nm, only $\lambda_{\text{K}\alpha 1}$ was taken into account, since the diffraction contribution due to the $\lambda_{\text{K}\alpha 2}$ of Cu was subtracted in the data set. This small crystallite size suggests that the kinetics of CeO_2 precipitation and nucleation is considerably higher than the one of BaCeO_3 , leaving not enough free Ce^{4+} ion for the precipitation of BaCeO_3 .

$$t = \frac{Y\text{-intercept}}{\lambda} \quad \text{Equation II.3}$$

These chemical and kinetics considerations make the hydrothermal synthesis of BaCeO_3 impracticable.

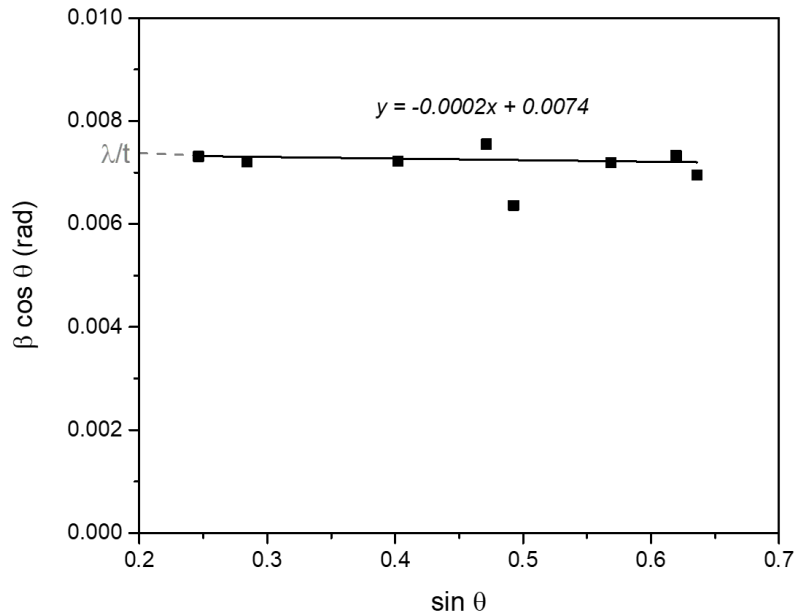


Figure II.9: Williamson and Hall diagram of the CeO_2 phase synthesized by the continuous hydrothermal process at 400°C and 300 bar

II.3. Ba(Ce,Zr)O₃

Solid solution of BaCeO₃-BaZrO₃ has been developed to improve the chemical stability of the compound [71], [170]. High Zr-content highly increases the stability of the compound in detriment to the protonic conductivity. To evaluate the possibility of synthesizing BCZ material, two target compositions were considered: BaCe_{0.9}Zr_{0.1}O_{3-δ} and BaCe_{0.1}Zr_{0.9}O_{3-δ}. The syntheses were carried out at 400 °C and 300 bar. **Figure II.10** shows the X-ray diffractogram of the synthesized powders. The obtained powder for the BaCe_{0.1}Zr_{0.9}O_{3-δ} target exhibits two phases: the major phase consisting of perovskite and a minor ceria phase. Concerning BaCe_{0.9}Zr_{0.1}O_{3-δ} three phases were obtained: perovskite, ceria and BaCO₃.

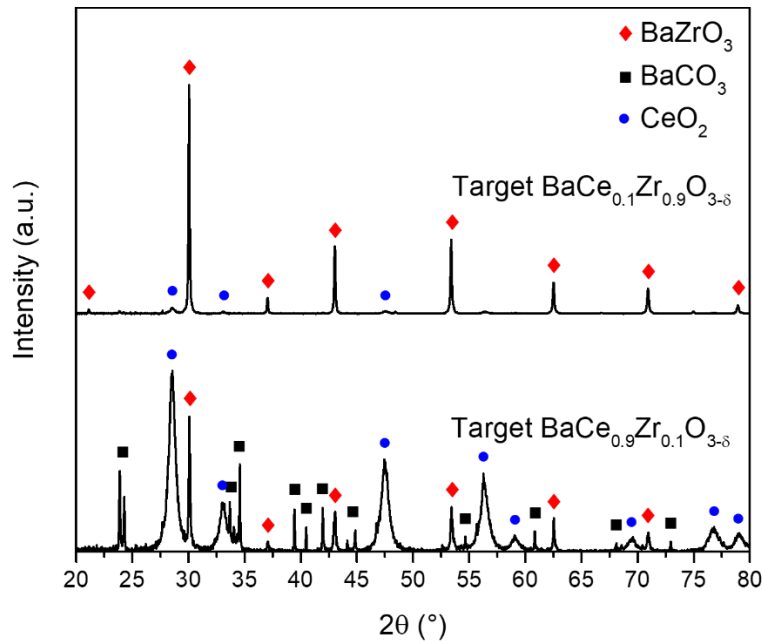


Figure II.10: X-ray diffractogram of BaCe_{0.9}Zr_{0.1}O_{3-δ} and BaCe_{0.1}Zr_{0.9}O_{3-δ}-target powders synthesized by the continuous process at 400 °C and 300 bar.

The results of the Rietveld on these diffractograms are presented in **Table II.4**. The obtained lattice parameter of the perovskite phase is similar to the one of pure BaZrO₃, indicating no substitution of Zr by Ce. Furthermore, as for the synthesis of BaCeO₃, CeO₂ precipitates faster than the perovskite target BaCe_{1-x}Zr_xO_{3-δ} (the width of the peak of CeO₂ is large, indicating a lot of nucleation), making impossible the synthesis of BaCe_{1-x}Zr_xO_{3-δ} by the hydrothermal route.

Name	Lattice parameter of the perovskite phase	Wt% of BaZrO ₃	Wt% of CeO ₂	Wt% of BaCO ₃
BaCe _{0.9} Zr _{0.1} O _{3-δ}	4.192(5) Å	89.7	10.3	0
BaCe _{0.1} Zr _{0.9} O _{3-δ}	4.193(4) Å	11.3	77.7	10.9

Table II.4: Rietveld refinement of BaCe_{0.9}Zr_{0.1}O_{3-δ} and BaCe_{0.1}Zr_{0.9}O_{3-δ}-target powders synthesized by the continuous process at 400 °C and 300 bar.

II.4. Ba(Ce,Zr,Y)O_{3-δ}

The synthesis of BaCe_{0.7}Zr_{0.1}Y_{0.2}O_{3-δ} was attempted, **Figure II.11** gives the X-ray diffractogram of the obtained powder. Three phases were obtained, one major ceria phase, one perovskite and one BaCO₃ with corresponding phase percentages of 80.0, 10.2 and 9.8 % determined by Rietveld refinement. The refined lattice parameter of the ceria phase is 5.400(9) Å, lower than the 5.410(0) Å expected, suggesting a partial substitution of Ce by Y. The refined lattice parameter of the perovskite phase is 4.194(3) Å, corresponding to pure BZ. As before, peaks corresponding to the ceria phase are much larger than those of the perovskite phase, indicating a faster precipitation of Y-doped CeO₂, making the synthesis of BaCe_{0.7}Zr_{0.1}Y_{0.2}O_{3-δ} impossible by the hydrothermal process.

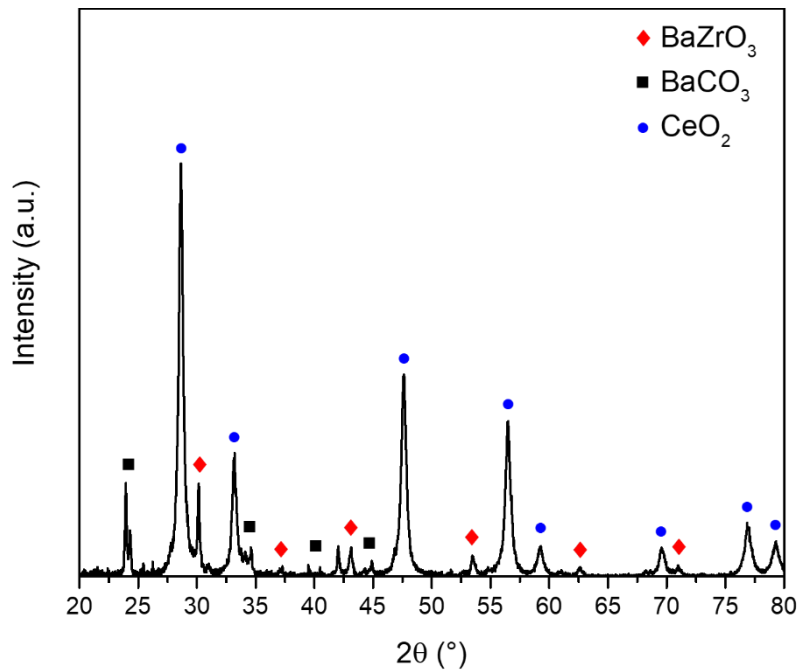


Figure II.11: X-ray diffractogram of BaCe_{0.7}Zr_{0.1}Y_{0.2}O_{3-δ}-target powder synthesized by the continuous process at 400 °C and 300 bar.

II.5. Ba(Zr,Y)O_{3-δ} (BZY)

BaZr_{0.8}Y_{0.2}O_{3-δ} was synthesized at 400 °C and 300 bar by both batch and continuous process. **Figure II.12** shows the obtained X-Ray diffractogram of the synthesized powders. The two diffractograms evidence the presence of three phases: a major phase consisting of perovskite cubic structure with Pm-3m space group, BaCO₃, with an orthorhombic *Pnma* structure, and YO(OH), with a monoclinic *P2₁/m* structure. Rietveld refinement was conducted of the diffractograms and the results are presented in **Table II.5**. The structural parameters inputted in FullProf program are reported in **Annex A**. The obtained lattice parameters are 4.201(5) Å for BZY-c and 4.211(5) Å for BZY-b. The increase of the lattice parameter compared to the one of BaZrO₃ confirms the effective substitution of Zr by Y. Moreover, since

BZY-b exhibits a higher lattice parameter than BZY-c, BZY-b should incorporate more Y than BZY-c.

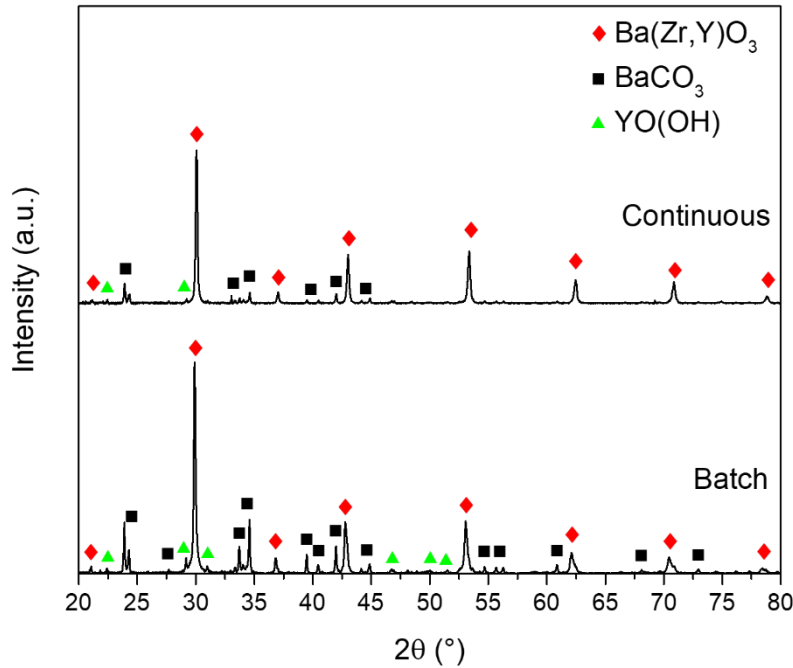


Figure II.12: X-ray diffractogram of $\text{Ba}(\text{Zr},\text{Y})\text{O}_{3-\delta}$ synthesized by the batch process and the continuous process at 400 °C

Name	Lattice parameter of the perovskite phase	Wt% of $\text{Ba}(\text{Zr},\text{Y})\text{O}_{3-\delta}$	Wt% of BaCO_3	Wt% of $\text{YO}(\text{OH})$
$\text{Ba}(\text{Zr},\text{Y})\text{O}_{3-\delta}$ -continuous	4.201(5) Å	86.2	10.6	3.1
$\text{Ba}(\text{Zr},\text{Y})\text{O}_{3-\delta}$ -batch	4.211(5) Å	80.9	13.7	5.4

Table II.5: Rietveld refinement of $\text{Ba}(\text{Zr},\text{Y})\text{O}_{3-\delta}$ synthesized by the batch process and the continuous process at 400 °C

As presented in **Figure II.13**, which displays the reported lattice parameter of different studies as a function of the substitution of Zr by Y, there are significant discrepancies concerning the value of BZY lattice parameter. For example, BZY10 exhibits lattice parameter between 4.198(2) Å and 4.210(1) Å. Information concerning the sample preparation are given in **Table II.6**. The general tendency is that samples prepared by solid-state reaction or sintered at high temperature exhibit larger lattice parameter than sample synthesized at low temperature.

As it can be seen, the lattice parameter is widely related to the preparation method, which can imply distortions and inaccurate composition of the sample. The key factors related to the composition impact on the lattice parameter are the amount of Ba and the substitution rate by Y in both A- and B- site of the perovskite, in fact, Y is an amphoteric species that can substitute for Ba and Zr [176]. Then, in the next section, further characterization of the

synthesized BZY will be presented in order to investigate more precisely the structure of the perovskite phase.

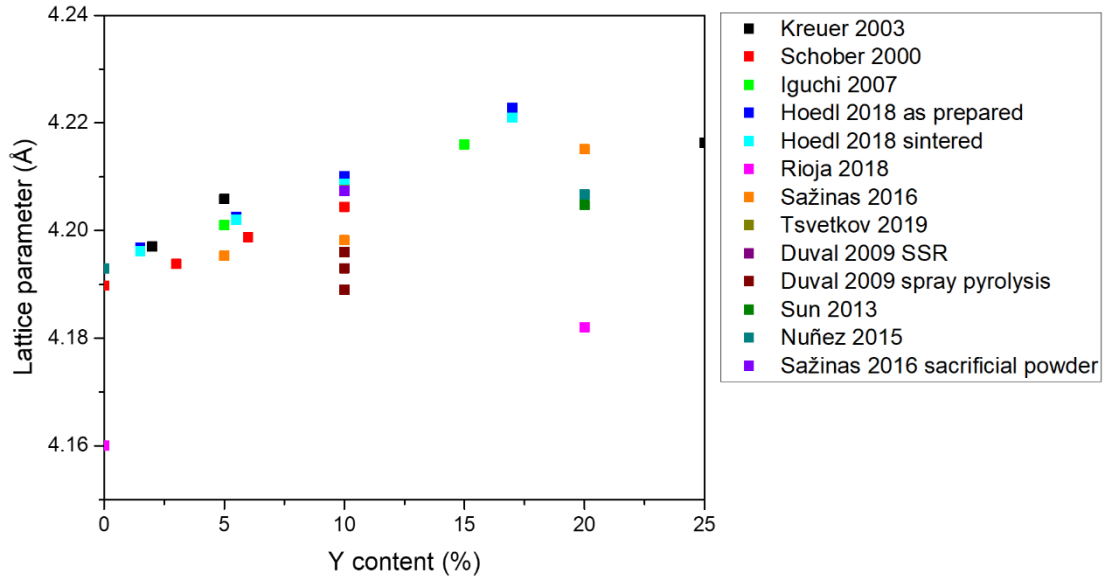


Figure II.13: Comparison of the lattice parameter of BZY reported in the literature as a function of Y content. More details about the preparation of the sample are given in Table II.6.

Study	% Y (%)	a (Å)	Space group	Sample preparation	Sintering	Evaluation of the composition	Ref.
Kreuer 2001	2	4.1971	Pm-3m	SSR* 1250 °C 15 h	1700 °C time not specified	Not specified	[177]
	5	4.2058 a = 4.2151	Pm-3m				
	10	c = 4.2047 a = 4.2317	P4mm				
	15	c = 4.2113 a = 4.2413	P4mm				
	20	c = 4.2259	P4mm				
	25	4.2163	Pm-3m				
Schober 2000	0	4.1898	Pm-3m	SSR* 1250 °C 10 h	1730 °C 30 h	Not specified	[178]
	3	4.1938	Pm-3m				
	6	4.1988	Pm-3m				
Iguchi 2007	5	4.201	Pm-3m	SSR* 1380 °C 3 h	1800 °C 20 h	Florescence X	[179]
	10	4.209	Pm-3m				
	15	4.216	Pm-3m				
Han 2013	Ba _{0.9} Zr _{0.88} Y _{0.12} O _{3-δ}	4.2016	Pm-3m	SSR* 1300 °C 10h	1600 °C 2 × 24 h	STEM-EDS	[180]
	Ba _{0.74} Zr _{0.55} Y _{0.45} O _{3-δ}	4.2109	Pm-3m			STEM-EDS	

	$\text{Ba}_{0.97}\text{Zr}_{0.81}\text{Y}_{0.19}\text{O}_{3-\delta}$	4.223	Pm-3m			ICP-AES	
	$\text{Ba}_{0.9}\text{Zr}_{0.88}\text{Y}_{0.12}\text{O}_{3-\delta} \cdot \text{H}_2\text{O}$	4.2298	Pm-3m			ICP-AES	
Hoedl 2018	1.5	4.1969	Pm-3m	SSR* 1300 °C 8h		SEM-EDS	[181]
	5.5	4.2026	Pm-3m				
	10	4.2101	Pm-3m				
	17	4.2228	Pm-3m				
	1.5	4.1962	Pm-3m		SPS 1600 °C 5 min + 1600 °C 5h		
	5.5	4.202	Pm-3m				
	10	4.2087	Pm-3m				
	17	4.221	Pm-3m				
Rioja 2018	0	4.160	Pm-3m	Modified Pechini method – calcination 1000 °C 6h		Not specified	[182]
	20	4.182	Pm-3m				
Sažinas 2016	0	4.1931	Pm-3m	Spray pyrolysis – calcination 950 °C 12 h	1600 °C 10 h	SEM-EDS	[183]
	5	4.1953	Pm-3m		1600 °C 10 h		
	10	4.1982	Pm-3m		1600 °C 10 h		
	10	4.1982	Pm-3m		1700 °C 10 h		
	10	4.2074	Pm-3m		1600 °C 10 h + sacrificial powder		
	20	4.2151	Pm-3m		1600 °C 10 h		

Tsvetkov 2019	10	4.2075	Pm-3m	Glycerol-nitrate method – 1500 °C 24 h + calcination 1100 °C time not specified	sacrificial powder	Not specified	[184]
Duval 2009	10	4.193	Pm-3m	SSR* 1200 °C 10 h – calcination 1400 °C 10 h		Not specified	[185]
	10	4.196	Pm-3m	Spray pyrolysis – calcination 1200 °C 10 h			
	10	4.189	Pm-3m				
Sun 2013	20	4.2048	Pm-3m	Combustion 1100 °C 6 h		Not specified	[186]
Nuñez 2015	0	4.1930	Pm-3m	Modified Pechini method – calcination 1000 °C 6 h + 1000 °C 48 h		SEM-EDS	[168]
	20	4.2067	Pm-3m				

Table II.6: Additional informations, mainly synthesis route and eventual sintering treatment, about the lattice parameter of BZY reported in the literature

*SSR refers to Solid State Reaction

III. Structural, microstructural and chemical study of BZY

According to the previous section, the initial target composition $\text{BaCe}_{0.7}\text{Zr}_{0.1}\text{Y}_{0.2}\text{O}_{3-\delta}$ is impossible to obtain via hydrothermal synthesis, then, the chosen protonic conductor is $\text{Ba}(\text{Zr},\text{Y})\text{O}_{3-\delta}$.

III.1. Characterization of the as-synthesized material

The synthesized BZY-b and BZY-c powders were further characterized by different methods. The agglomeration state was analyzed via Dynamic Light Scattering. The morphology and the size of particles were evaluated by Transmission Electron Microscopy. The composition was estimated by Scanning Electron Microscopy coupled with Energy Dispersive X-Ray Spectroscopy and the chemical state was studied by X-ray Photoelectron Spectroscopy.

III.1.a. X-ray diffraction analysis

Figure II.14.a presents the full range XRD pattern of the synthesized material obtained by the batch and the continuous process. As a reminder, the obtained lattice parameter are 4.201(5) Å for BZY-c and 4.211(5) Å for BZY-b. The larger lattice parameter of the BZY-b suggests a more important content of Ba and/or Y into the perovskite structure. The diffraction peaks exhibit no preferential direction. However, as presented in **Figure II.14 b**, which displays a zoom on the 200 diffraction peak, the BZY-b peak shows a short shoulder toward higher angle while the BZY-c peaks appear more or less symmetric. Thus, BZY-c should present a cubic perovskite structure, while the asymmetric shape of BZY-b could be related to a composition gradient or a tetragonal distortion [177].

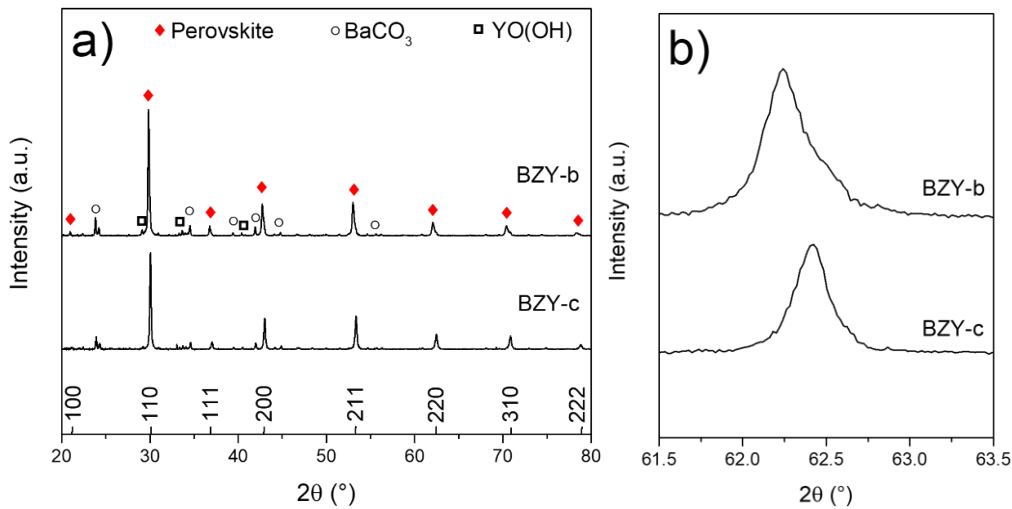


Figure II.14: X-ray diffractogram of the BZY synthesized by the batch and the continuous process, a) 20 – 80 2θ range diffractogram, b) zoom on the 220 peak

In order to investigate the effect of a tetragonal distortion on the X-ray diffractogram, the theoretical diffractogram of the two BZY structures, i.e. cubic and tetragonal, were carried out using CaRIne Crystallography software (Version 3.1). Cubic BZY20 crystallizes in $Pm-3m$ space group. The lattice parameter used in this study is 4.2088 Å. It is an average of the values reported in the work of Sažinas et al., Sun et al. and Nuñez et al. presented in **Table II.6** since those values does not deviate too much from the overall behavior and compatible with the experimental lattice parameter determined for BZY-b and BZY-c [168], [183], [186]. Tetragonal BZY20 crystallizes in $P4mm$ space group, the lattice parameters, taken from the work of Kreuer, are $a = 4.2413$ Å and $c = 4.2259$ Å, the angles are $\alpha = \beta = \gamma = 90^\circ$ [177]. Since the crystal structure of tetragonal BZY is not referenced in the literature, the atomic positions are adapted from the tetragonal BaTiO₃ referenced in the works of Aimi *et al.*, Mahmood *et al.*, Yasuda *et al.* and Wäsche *et al.* [187]–[190]. The crystallographic data of cubic and tetragonal BZY20 inputted in Carine software are given in **Table II.7** and **Table II.8**. As a reminder, the ionic radius of Ti⁴⁺ in an octahedral environment is 0.61 Å lower than the ionic radius of Zr⁴⁺ so that the tetragonal perovskite may be ever more distorted.

Atom	Oxidation state	Ionic radii (Å)	x	y	z	Occupation
Ba	+2	1.61	0	0	0	1
Zr	+4	0.72	0.5	0.5	0.5	0.8
Y	+3	0.90	0.5	0.5	0.5	0.2
O1	-2	1.40	0.5	0.5	0	1
O2	-2	1.40	0.5	0	0.5	1
O3	-2	1.40	0	0.5	0.5	1

Table II.7: Crystallographic data of cubic BZY20 as inputted in CaRIne Software

Atom	Oxidation state	Ionic radii (Å)	x	y	z	Occupation
Ba	+2	1.61	0	0	0	1
Zr	+4	0.72	0.5	0.5	0.522	0.8
Y	+3	0.90	0.5	0.5	0.522	0.2
O1	-2	1.40	0.5	0.5	-0.022	1
O2	-2	1.40	0.5	0	0.488	1
O3	-2	1.40	0	0.5	0.488	1

Table II.8: Crystallographic data of tetragonal BZY20 as inputted in CaRIne Software

Figure II.15 presents the crystal structure of cubic and tetragonal BZY. In both structures, Ba²⁺ ions occupy the edge of the polyhedron. In cubic BZY (**Figure II.15.a**), Zr⁴⁺ and Y³⁺ are in the center of the cube, whereas they deviated toward a higher z value for tetragonal BZY (**Figure II.15.b**). O²⁻ ions are in the middle of each face for cubic BZY and shift in the opposite direction than Zr⁴⁺ and Y³⁺ ions in the tetragonal structure. There is no oxygen ion represented in the (0 0 $\bar{1}$) plan because the center of the ion is out of the elementary cell.

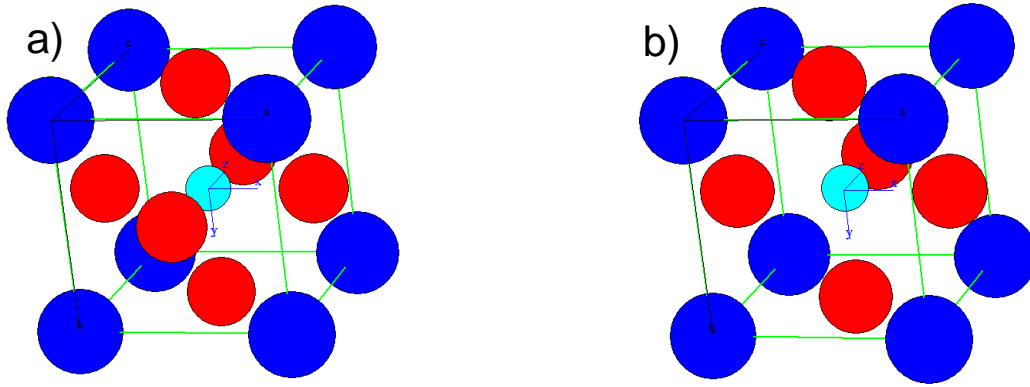


Figure II.15: Crystal structure of BZY, a) cubic BZY; b) tetragonal BZY. Ba^{2+} is represented in dark blue, Zr^{4+} and Y^{3+} in light blue and O^{2-} in red. The radii scale is set to 50 % to have an exploded view.

The theoretical diffractogram is calculated from $2\theta = 20^\circ$ to $2\theta = 80^\circ$ according to the Cu $K\alpha_1$ wavelength ($\lambda = 1.54056 \text{ \AA}$). **Figure II.16** exposes the theoretical diffractogram of the cubic BZY20 phase. All diffraction plans exhibit a single peak, the maximum intensity is obtained for the (110) plan. **Figure II.17** presents the theoretical X-ray diffractogram of the tetragonal BZY20. Except for the (111) and (222) plans, all the diffraction peaks are split in two.

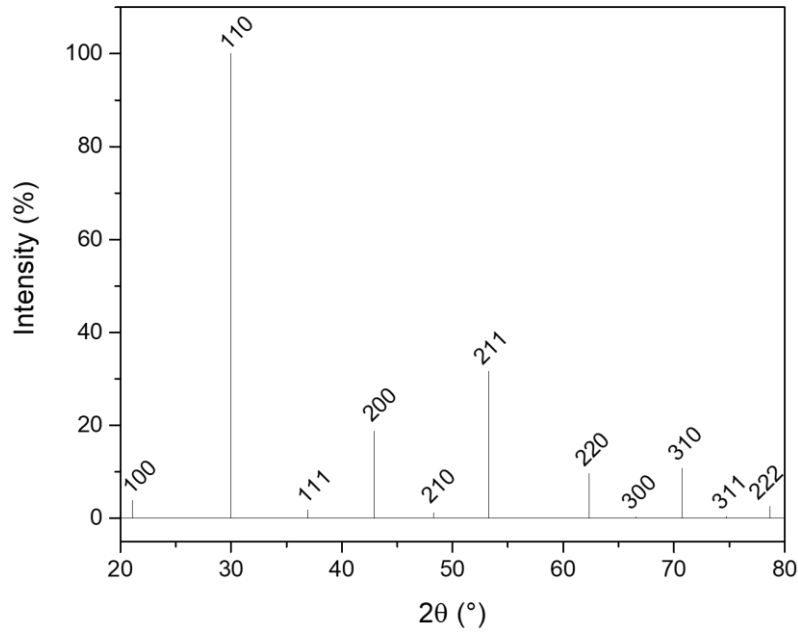


Figure II.16: Theoretical X-ray diffractogram of the cubic BZY20

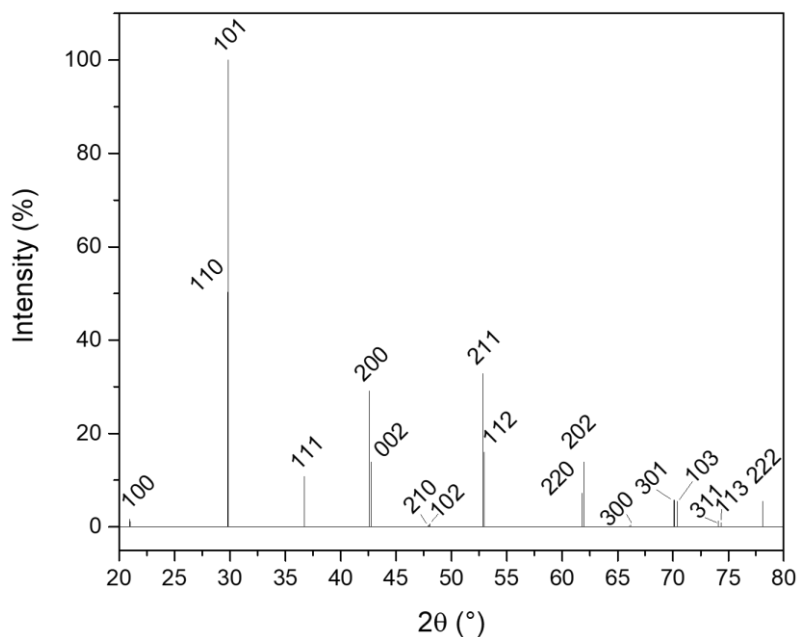


Figure II.17: Theoretical X-ray diffractogram of the tetragonal BZY20

As it can be seen in **Figure II.17**, the (202) diffraction peak, located at higher 2θ than the (220), is supposed to be twice more intense than the (220) peak, then in the tetragonal system, this peak should be asymmetric toward low angle. Since, the BZY-b diffraction peak displays an asymmetry toward high angle, it is assumed that BZY-b exhibits a cubic perovskite structure and a gradient of composition causes the asymmetry.

III.1.b. Granulometry analysis

The particle size distribution (PSD) was evaluated using the Dynamic Light Scattering method using Mie theory calculation with a Malvern Microsizer 2000 laser granulometer. **Figure II.18** shows the volume PSD of the synthesized BZY-c. The volume PSD exhibit a quadrimodal distribution with mean sizes at around 0.1 μm , 1.7 μm , 14 μm and 210 μm . The D10 is the diameter for which 10 % of the distribution has a smaller particle size, D50 is for 50 % and D90 is for 90 %. The obtained D10, D50 and D90 are 0.817 μm , 4.570 μm and 35.73 μm , respectively, suggesting that the elementary grains are highly agglomerated.

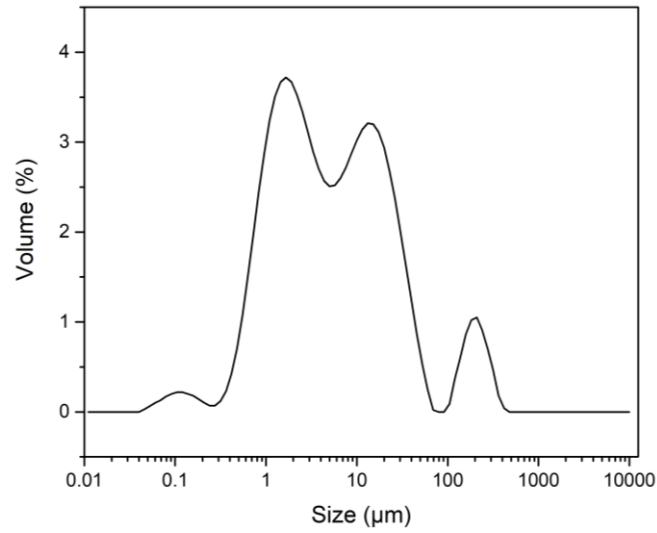


Figure II.18: Particle size distribution by volume of the BZY-c powder

III.1.c. Microstructural and electron diffraction analysis

The microstructural investigations were performed by transmission electron microscopy (TEM) on a ThermoFisher FEI Tecnai F20. The size of the particles was determined with ImageJ software. The interreticular distance corresponding to each electron diffraction ring was calculated by following **Equation II.4**:

$$d_{hkl} = \frac{\lambda R}{D^*} \quad \text{Equation II.4}$$

With d_{hkl} , the interreticular distance; λ , the wavelength of the electron beam; R , the camera length; and D^* , the radius of the diffraction ring. The lattice mode (primitive (P), centered (I), face-centered (F)) was determined by looking at the systematic extinctions: P mode does not present extinctions, the extinction condition in the I mode is $h + k + l = 2n + 1$ and in F mode, the extinction occurs if h , k and l are in different parity.

Figure II.19 shows the TEM micrograph of the BZY-b powder. Two kinds of particles were detected, on the bottom left corner, spherical particles of 9 ± 2 nm (evaluation on 34 particles) are highly agglomerated in clusters, the other particles are 105 ± 25 nm (evaluation on 102 particles) and are agglomerated in rosary shape.

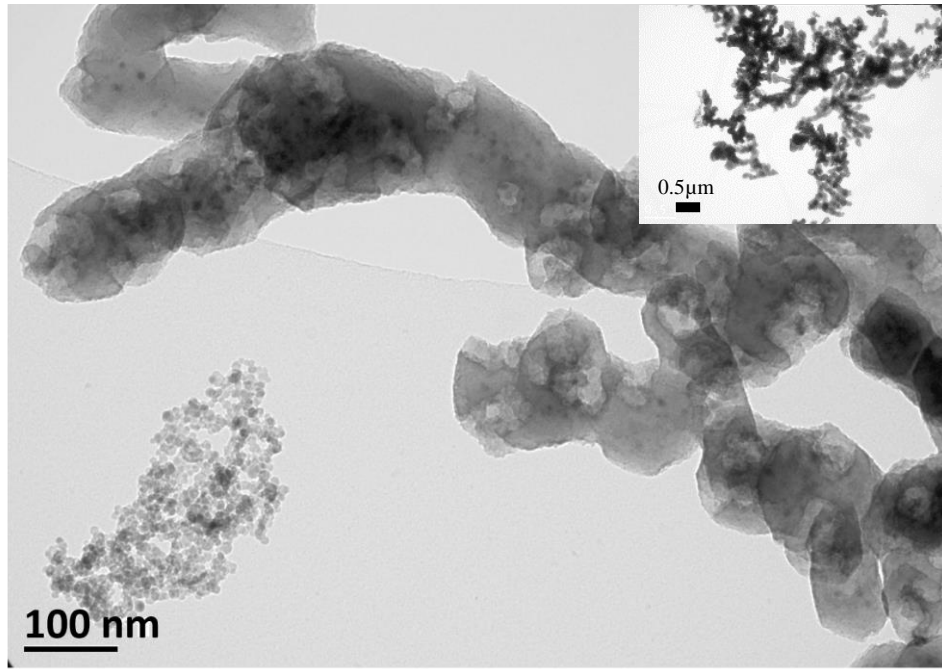


Figure II.19: TEM micrograph of the BZY-b powder

The electron diffraction patterns of the 105 nm particles is presented in **Figure II.20**. The pattern exhibits characteristic diffraction spots of a polycrystalline sample, the indexation is presented in **Table II.9**. The crystal structure corresponds to a primitive mode with an average lattice parameter of 4.21(5) Å. The first ring was not taken into account for the calculation of the lattice parameter since it overlaps with the one of the small particles. The obtained lattice parameter is in line with the 4.211(5) Å of BZY-b obtained by XRD, then the 105 nm particles were attributed to BZY. No additional spot was highlighted out of the rings, confirming that BZY-b does not present a tetragonal distortion.

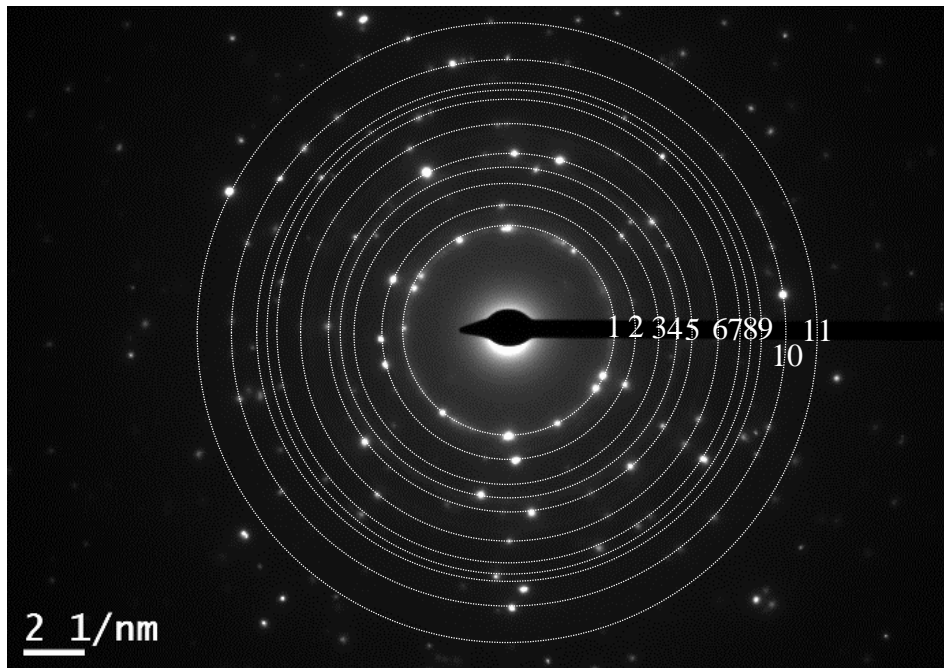


Figure II.20: Electron diffraction pattern of the 105 nm particles from the BZY-b powder

Ring	d_{hkl}	h	k	l	Lattice parameter (Å)
1	3.02(4)	1	1	0	4.27(7)
2	2.43(3)	1	1	1	4.21(4)
3	2.10(7)	2	0	0	4.21(5)
4	1.88(6)	2	1	0	4.21(8)
5	1.71(9)	2	1	1	4.21(2)
6	1.49(1)	2	2	0	4.21(6)
7	1.33(2)	3	1	0	4.21(3)
8	1.27(2)	3	1	1	4.21(8)
9	1.21(7)	2	2	2	4.21(4)
10	1.12(7)	3	2	1	4.21(8)
11	0.99(3)	4	1	1	4.21(4)

Table II.9: Indexation of the electron diffraction pattern of the 116 nm particles in the BZY-b powder.

Figure II.21 exhibits the electron diffraction pattern of the 9 nm particles. The complete rings are a classical feature of a polycrystalline sample with a high number of particles.

Two crystal structures can be deduced from this diffraction pattern. The more obvious indexation (**Table II.10**) evidences a face-centered system (mode F) with a 5.19(7) Å lattice parameter corresponding to yttria-stabilized zirconia (YSZ) with 17 % of yttrium. However, YO(OH) was highlighted by XRD, then, it can be assumed that a Y-based oxide is obtained. Indeed, oxyhydroxides are not stables in the TEM environment (high voltage electron beam) and lead to oxide species [191], [192]. **Table II.11** presents the indexation of the diffraction pattern in the hypothesis of a centered lattice mode (mode I). The indexed hkl reflection fit perfectly with the more intense diffraction peaks of the ICDD data 04-008-2591 corresponding to $Y_{1.8}Zr_{0.2}O_{3+\delta}$ (space group Ia-3). The obtained lattice parameter is 10.39(4) Å, a bit lower than the 10.5652 Å of $Y_{1.8}Zr_{0.2}O_{3+\delta}$ reported in ICDD data, suggesting more incorporation of Zr^{4+} . In order to get an idea of the content of Zr^{4+} , the Vegard's Law was applied, the obtained composition is $Y_{1.6}Zr_{0.4}O_{3+\delta}$.

According to the XRD result and the thermal behavior of the two synthesized BZY powders that will be seen in the section, this second assumption is the most probable.

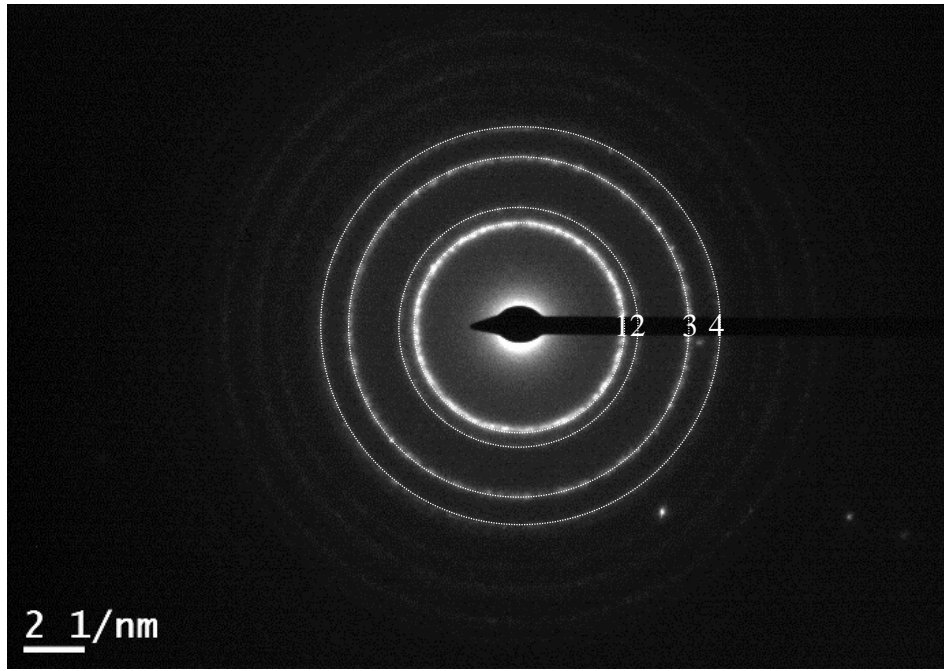


Figure II.21: Electron diffraction pattern of the 9 nm particles from the BZY-b powder

Ring	d_{hkl}	h	k	l	Lattice parameter (Å)
1	3.00(0)	1	1	1	5.19(6)
2	2.60(0)	2	0	0	5.20(0)
3	1.83(5)	2	2	0	5.19(1)
4	1.56(8)	3	1	1	5.20(0)

Table II.10: Indexation of the electron diffraction pattern of the 8 nm particles in the BZY-b powder in the hypothesis of a *F* lattice mode.

Ring	d_{hkl}	h	k	l	Lattice parameter (Å)
1	3.00(0)	2	2	2	10.39(2)
2	2.60(0)	4	0	0	10.40(0)
3	1.83(5)	4	4	0	10.38(2)
4	1.56(8)	6	2	2	10.40(0)

Table II.11: Indexation of the electron diffraction pattern of the 8 nm particles in the BZY-b powder in the hypothesis of a *I* lattice mode.

Figure II.22 shows the TEM micrograph of the BZY-c powder. As suggested by the PSD analysis, the particles with a nearly spherical morphology are agglomerated. The particle size varies from 10 nm to 315 nm on this micrograph, with a median value of 48 nm (evaluation on 50 particles). As for the powder synthesized by the batch process, particles of 9 nm are surrounding the bigger particles. **Figure II.23** exhibits the electron diffraction pattern of the powder, it corresponds to a polycrystalline sample. Indexation of the rings is exposed in **Table II.12**. It is a primitive lattice mode with a lattice parameter of 4.20(6) Å, quite in line with the 4.201(5) Å obtained by XRD. The ring 2, which overlaps with the 222 plan of Zr-

doped Y_2O_3 , was not considered for the calculation. As for the BZY-b and in agreement with the XRD peak shape, no spot was detected out from the rings, suggesting that BZY-c crystallizes in a cubic perovskite lattice.

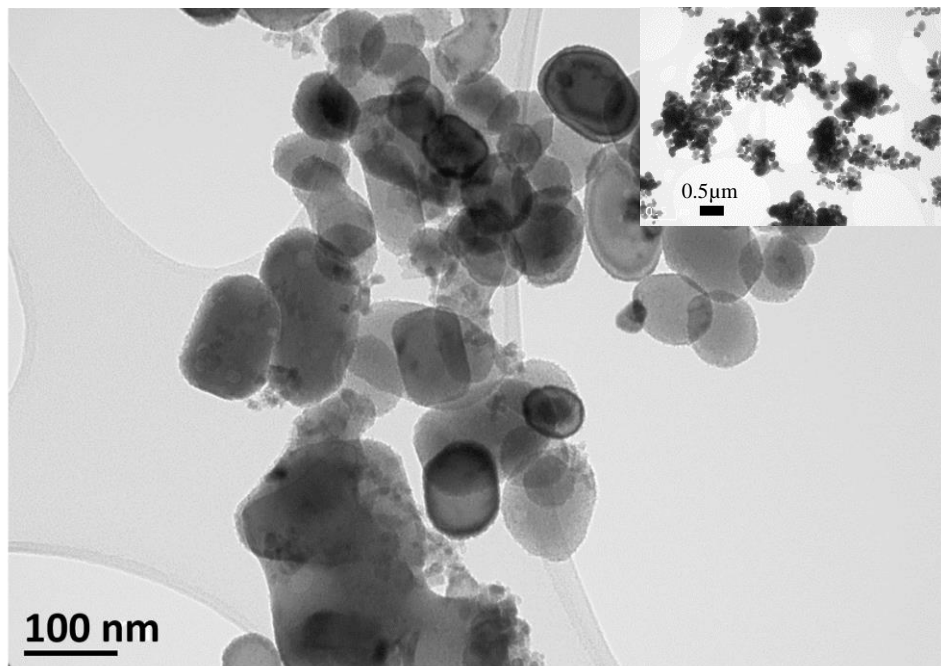


Figure II.22: TEM micrograph of the BZY-c powder

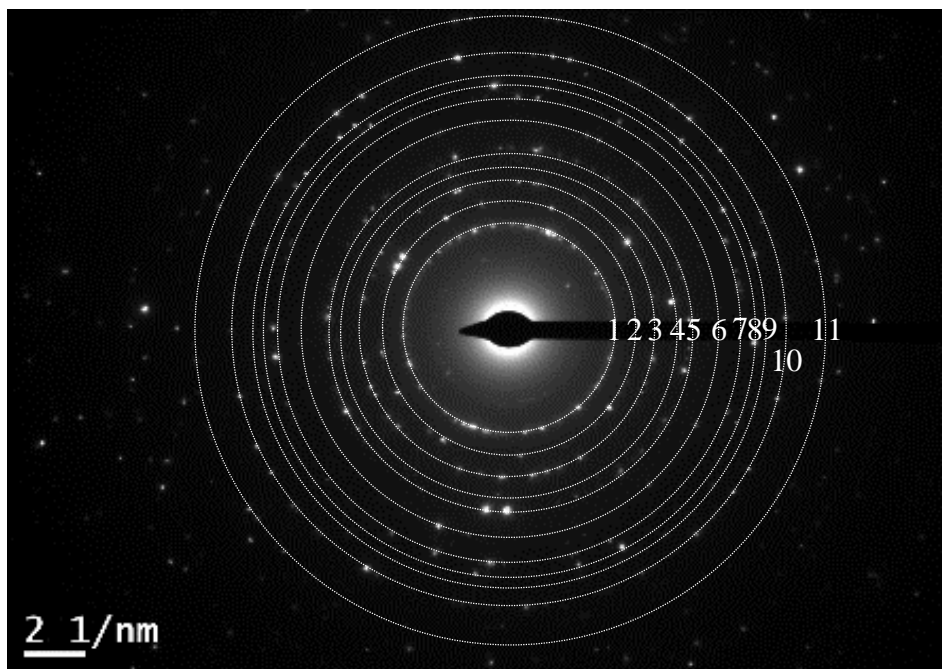


Figure II.23: Electron diffraction pattern of the BZY-c powder.

Ring	d_{hkl}	h	k	l	Lattice parameter (Å)
1	4.21(5)	1	0	0	4.21(5)
2	2.98(6)	1	1	0	4.22(3)
3	2.43(0)	1	1	1	4.20(9)
4	2.10(3)	2	0	0	4.20(6)
5	1.87(9)	2	1	0	4.20(1)
6	1.71(9)	2	1	1	4.21(2)
7	1.48(6)	2	2	0	4.20(3)
8	1.33(0)	3	1	0	4.20(7)
9	1.26(8)	3	1	1	4.20(7)
10	1.21(3)	2	2	2	4.20(3)
11	1.12(3)	3	2	1	4.20(3)

Table II.12: Indexation of the electron diffraction pattern of the BZY-c powder.

III.1.d. Bulk chemistry analysis

The chemical composition of the BZY grains in the powder was investigated through Scanning Electron Microscopy-Energy Dispersive X-Ray Spectroscopy (SEM-EDS). The fluorescence X and the Inductively Coupled Plasma – Atomic Emission Spectroscopy (ICP-AES) techniques were put aside since they give a global information of each element of a certain quantity of powder. The SEM is a Hitachi SU1510 coupled with a Bruker XFlash6I10 energy-dispersive X-ray analyzer. The voltage was set to 15 kV, the working distance to 15 ± 0.5 mm. The detected elements are Ba, Zr, Y, O and C. The collected peaks for EDS quantification corrected by the ZAF method (atomic number (Z) effect, self-absorption (A) effect and fluorescence (F) effect) were the L-series of Ba, Zr and Y and the K-series of O. EDS investigations were conducted on 16 different agglomerates with an area of measurement from $5 \mu\text{m} \times 5 \mu\text{m}$.

BaCO_3 was easily excluded from the analysis since it has a specific morphology of needle, as highlighted in **Figure II.24**. Due to the 10 nm size of the oxyhydroxy species, and since they surround the BZY particles, $(\text{Y,Zr})\text{O}(\text{OH})$ cannot be excluded from the analysis. For the ratio exposed below, Ba atoms are supposed to occupy the A-site of the perovskite while Zr and Y occupy the B-site.

Figure II.25 shows a) the A-site/B-site ratios and b) the $\text{Y}/(\text{Zr} + \text{Y})$ ratios for the BZY-b and the BZY-c powders and the corresponding number of agglomerates per interval. The BZY-c powder exhibits a wide range of A-site/B-site ratio, from 0.70 to 1.33, with a strong tendency for the Ba-deficient composition, the obtained average value is 0.93 ± 0.17 . The A-site/B-site ratio of the BZY-b is less widespread and varies from 0.67 to 1.09 with an average value of 0.88 ± 0.13 .

The $Y/(Zr + Y)$ ratio values of the BZY-c powder cover an interval of 0.08–0.25 with an average value of 0.14 ± 0.03 , this ratio is lower than the expected 0.20. BZY-b exhibits higher values from 0.18 to 0.32 and presents an average value of 0.27 ± 0.04 .

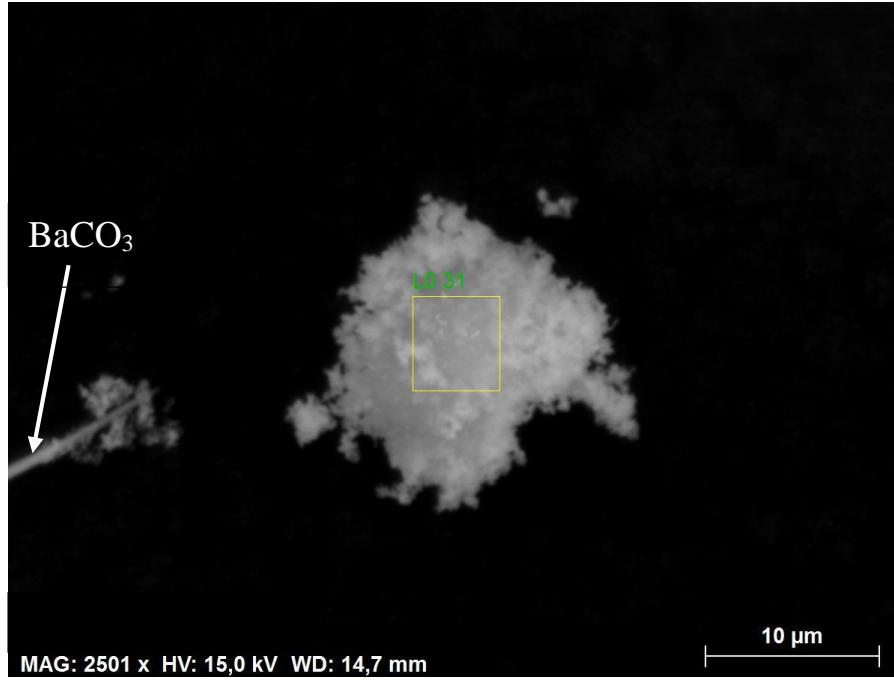


Figure II.24: SEM micrograph in backscattered electron (BSE) mode of the BZY-c powder, the yellow square represent the area for the SEM-EDS analysis.

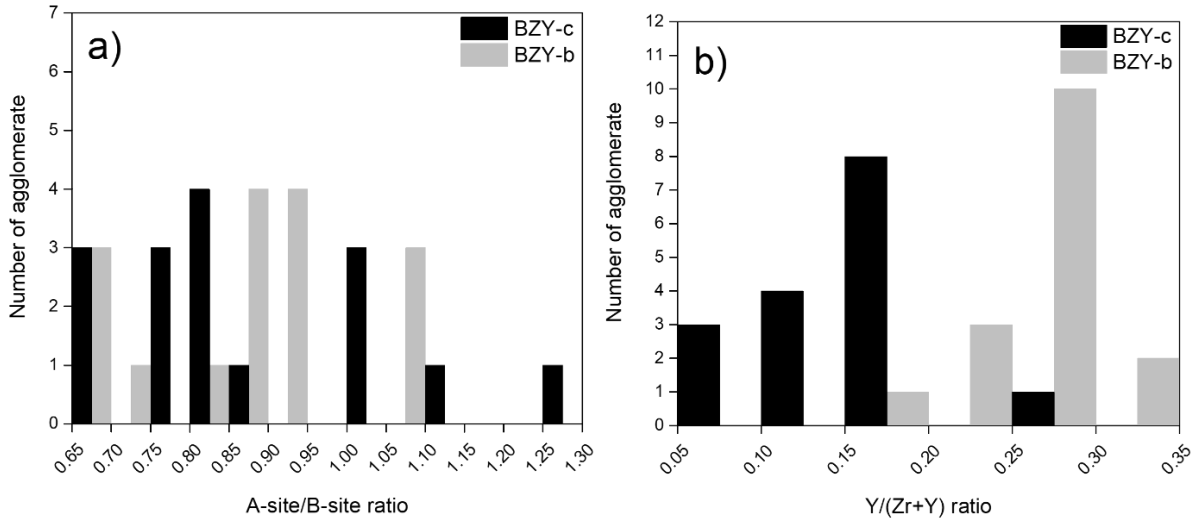


Figure II.25: a) A-site/B-site ratios and b) $Y/(Zr + Y)$ ratios obtained from EDS measurement on the BZY-b and the BZY-c powders and the corresponding number of agglomerates per interval.

III.1.e. Surface chemistry analysis

The surface chemistry of the BZY-b and the BZY-c powder was investigated by X-Ray Photoelectron Spectroscopy (XPS). XPS was carried out on an XPS PHI 5000 VersaProbe with a monochromatized Al K α 1 source (1486.7 eV). All the binding energies were calibrated from the C 1s of the adventitious carbon (C–C and C–H bonds) peak at 284.8 eV. Casa XPS software (Version 2.3.23) was used for data processing. The analyzed area is a circular disk of 200 μ m in diameter, the penetration depth is 20 nm.

The surface element composition is exposed in **Table II.13**. BZY powder presents an unexpectedly low amount of Y in comparison with the ratio obtained by SEM-EDS, the ratio Y/(Zr + Y) is only 0.17 for the BZY-b powder and 0.14 for the BZY-c powder, this value is in line with the one obtained in the previous section. The obtained A-site/B-site are 0.73 and 0.39 for BZY-b and BZY-c respectively, suggesting that the BZY-c is highly covered by (Y,Zr)O(OH).

Sample	Barium	Zirconium	Yttrium	Oxygen	Carbon
BZY-b	11.3	12.8	2.6	62.3	11.0
BZY-c	6.8	14.8	2.5	58.4	15.2

Table II.13: Elemental composition (at%) of the BZY-b and the BZY-c powders obtained by XPS.

To facilitate the interpretation of the XPS spectra, a plot representing the different possible contribution and their associated binding energy founded in the literature was constructed. The plot of each element is presented in **Figure II.26**. The details about the XPS spectra (preparation of the sample, precise binding energy and shape of the XPS spectra) are presented in **Annex C**.

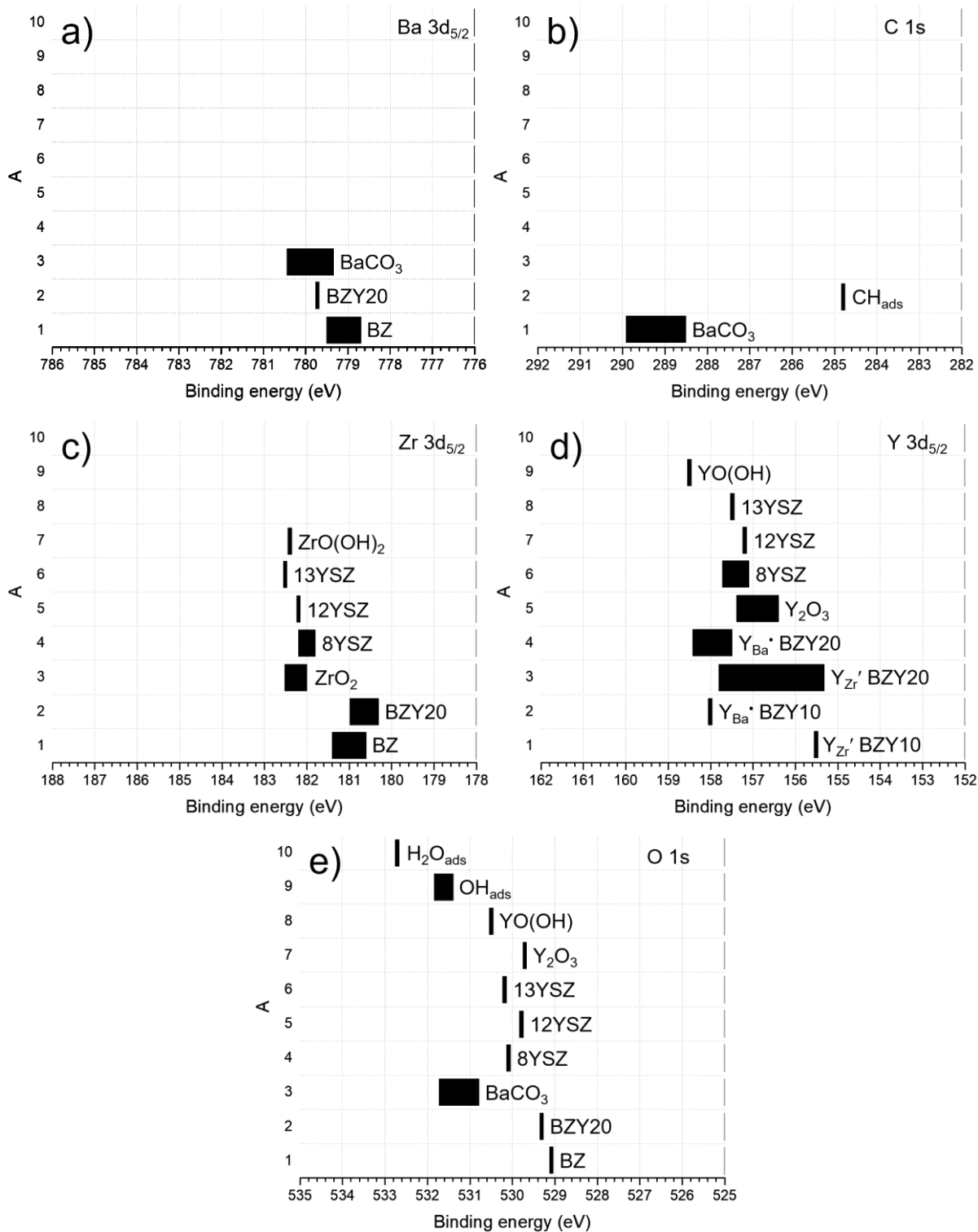


Figure II.26: Representation of the binding energy associated with different possible compound reported in the literature. a) Ba 3d_{5/2} binding energy; b) C 1s binding energy; c) Zr 3d_{5/2} binding energy; d) Y 3d_{5/2} core-level spectra and e) O 1s binding energy

The XPS window spectra of the two BZY powders are presented in **Figure II.27**. The Ba 3d_{5/2}, shown in **Figure II.27.a**, exhibits an asymmetric peak which can be fitted with two contributions. The main peak, situated at 779.2 eV for BZY-b and 779.5 eV for BZY-c, corresponds to Ba from the perovskite phase [186], [193], [194]. The studies diverge about the origin of the asymmetric peak of Ba 3d_{5/2} in perovskite structure. Some explains that the

asymmetric shape of the peak may be due to terminal Ba-O bonds [194], [195], some other to the distortion of the lattice implemented by oxygen vacancies [196] and finally, it can correspond to BaCO₃ [197]–[200]. According to Ba spectra of the annealed powders that will be presented in the next section, this contribution was assigned to terminal Ba-O bond and the Ba from BaCO₃ contribution overlap with the Ba from BZY contribution.

Figure II.27.b exhibits the C 1s core-level spectra of the two powders. Both spectra present three contributions, two overlapped peaks between 287 and 283 eV characteristic of adventitious carbon, namely C-C and C-H bonds, and one contribution at 289.2 eV for BZY-b and 289.6 eV for BZY-c corresponding to C in BaCO₃ [197]–[201]. In agreement with the XRD analysis, BZY-b presents more BaCO₃ than BZY-c, the % of the area are respectively 59.6 %, corresponding to 6.6 at%, and 17.8 %, corresponding to 2.7 at%.

The Zr 3d core-level spectra is presented in **Figure II.27.c**. The spectra can be fitted with two contributions (each contribution give rise to one 3d_{5/2} peak and one 3d_{3/2} peak). The contribution situated at 181.0 ± 0.1 eV for the 3d_{5/2} level and 183.4 ± 0.2 eV for the 3d_{3/2} level correspond to Zr_{Zr}^x from BZY [186], [193], [194], [202]. In the BZY-b sample, this contribution is the more important, it equals to 58.8 % of the area and 7.5 at% of the detected elements. In the BZY-c sample, the second contribution, situated at 182.1 ± 0.1 eV (3d_{5/2}) and 184.5 ± 0.1 eV (3d_{3/2}) is the more important as it occupy 87.1 % of the area, corresponding to 12.9 at% of the sample. According to **Figure II.26**, this contribution can be assigned to ZrO₂, YSZ or ZrO(OH)₂ [197], [203]–[207]. From the XRD analysis, the oxyhydroxide specie is the most probable.

Figure II.27.d displays the Y 3d core-level spectra of the two samples. Each spectrum can be fitted with one contribution, situated at 156.7 eV (3d_{5/2}) and 158.8 eV (3d_{3/2}) in the BZY-b powder and 157.8 eV (3d_{5/2}) and 159.9 (3d_{3/2}) for the BZY-c sample. According to the literature survey plotted in **Figure II.26**, the BZY-b contribution may correspond to Y_{Zr}['] from BZY or to Y₂O₃ [176], [197], [202], [208]. The BZY-c contribution should be assigned to Y_{Zr}['] from BZY or Y_{Ba}^{*} from BZY [176], [186], [202]. The second contribution at 158.4 eV (3d_{5/2}) and 160.5 ± 0.1 eV (3d_{3/2}) in the two spectra may correspond to the oxyhydroxide specie. In agreement with the core-level spectra of Zr, the proportion of oxyhydroxide species is more important in the BZY-c powder than in the BZY-b powder.

The O 1s spectra of the BZY-b and the BZY-c powders are presented in **Figure II.27.e**. Three contributions fits well the spectra. The first contribution, situated at 529.0 ± 0.1 eV, is assigned to O from BZY [193], [202]. It represents 41.6 % of the area for BZY-b and only 9.2 % of the area for BZY-c. The second contribution, at 530.0 ± 0.1 eV, can be assigned to YSZ or Y₂O₃ [203], [205], [206], [208]. However, according to the precedent assignments and the acceptable shift (about 0.5 eV) with the reported value for YO(OH), this second contribution is attribution to the oxygen from of oxyhydroxide species [209]. The third contribution, at 531.4 ± 0.3 eV, corresponds to BaCO₃ [198]–[201].

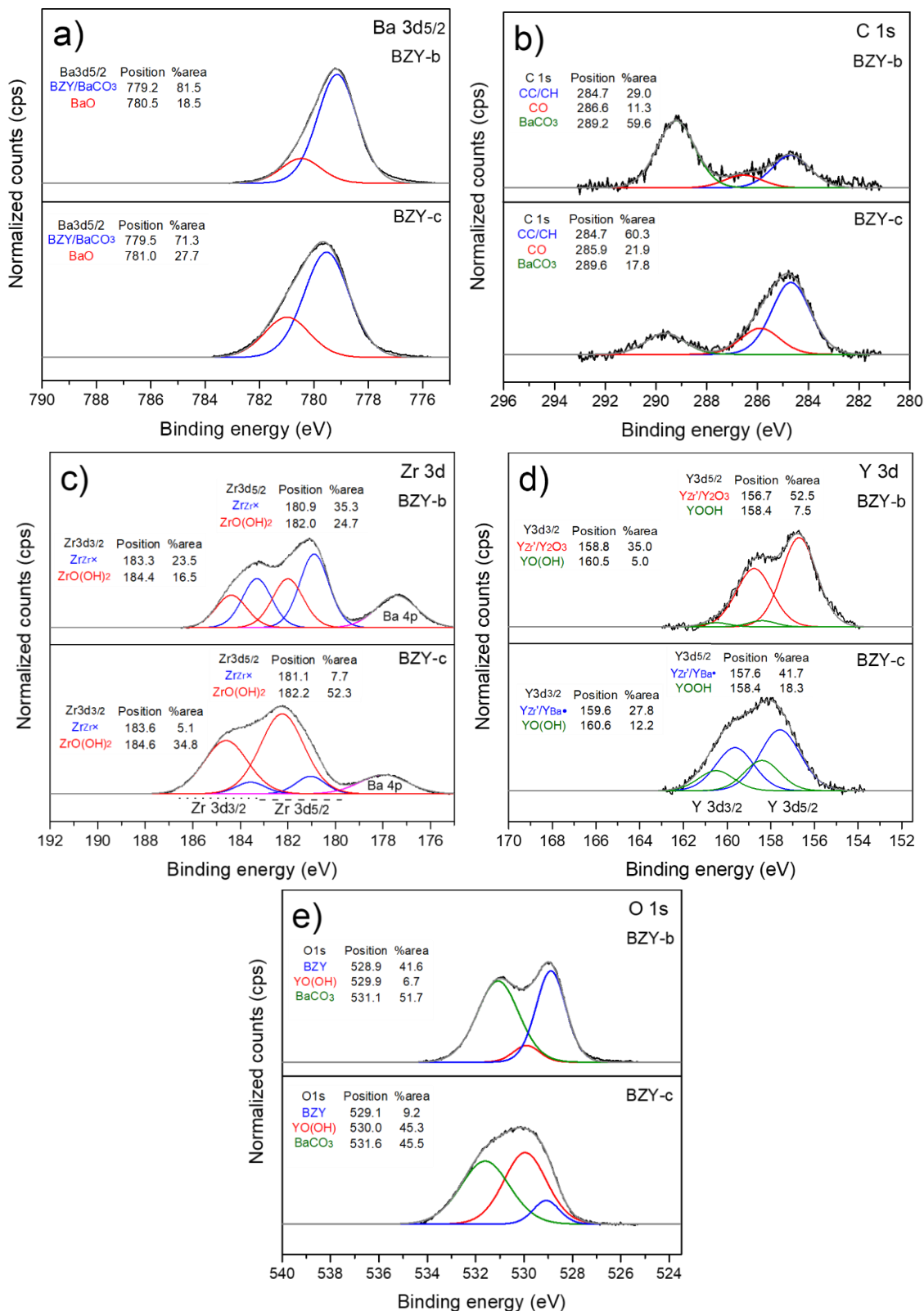


Figure II.27: XPS windows spectra of the BZY-b and BZY-c powders, a) Ba 3d_{5/2} core-level spectra; b) Zr 3d core-level spectra; c) Y 3d core-level spectra and d) C 1s core-level spectra. The colored lines represents the fit of each contribution; the black line, the experimental data; the grey line, the global fit.

III.1.f. Summary

BZY20 was synthesized by hydrothermal route in supercritical condition ($T = 400\text{ }^{\circ}\text{C}$ and $P = 300\text{ bar}$). Two different set-ups were employed, the continuous and the batch process. In both routes, the final product consists in a white powder, mainly containing a BZY exhibiting a cubic perovskite structure (space group $Pm-3m$). The two secondary phases formed during the synthesis are BaCO_3 (space group $Pnma$) and $(\text{Y,Zr})\text{O}(\text{OH})$ (space group $P2_1/m$).

The perovskite structure presents a Ba-deficiency in BZY-b and BZY-c, the A-site/B-site ratio are respectively 0.88 and 0.93. The BZY-b perovskite integrates a higher content of Y than the BZY-c, indeed, the $\text{Y}/(\text{Y}+\text{Zr})$ ratio is 0.27 while it is only 0.14 for BZY-c. The higher lattice parameter of BZY-b obtained from XRD is consistent with the higher content of Y in the BZY-b than in the BZY-c powder.

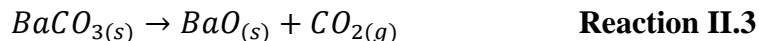
Particles are 116 nm in diameter for BZY-b and 48 nm for BZY-c. The smaller particle size in the continuous process is explained by the shorter residence time into the reactor: few seconds against two hours.

The surface chemistry analyses indicate that each element is present in at least two chemical state. The Ba core-level spectra is similar for the BZY elaborated by batch and continuous process. The BZY-c powder exhibits a higher content of oxyhydroxide species at its surface than the BZY-b, this statement is observed in both Y and Zr core-level spectra.

To summarize, the BZY-b powder accepts a higher content of Y but a higher Ba-deficiency. In contrast, BZY-c shows less Ba deficiency but a smaller content of Y.

III.2. Characterization of the annealed material

In order to homogenize and stabilize the crystal structure, a thermal treatment was carried out on the two powders. To fix the temperature of the annealing treatment, thermogravimetric analysis (TA Instruments Q600 SDT) was performed on the as-synthesized powder. **Figure II.28** shows the profile obtained for the BZY-c powder. 27.11 mg was set in a platinum crucible and analyzed in air atmosphere from ambient temperature to $1500\text{ }^{\circ}\text{C}$ with a heating ramp of $10\text{ }^{\circ}\text{C}\cdot\text{min}^{-1}$. The weight loss and the temperature limiting the different domains were evaluated via the TA Universal Analysis 4.5 software. Four weight losses are highlighted, noted as (I), (II), (III) and (IV). The first occurs from ambient temperature to $238\text{ }^{\circ}\text{C}$ and corresponds to the loss of adsorbed water. The second degradation occurs from $238\text{ }^{\circ}\text{C}$ to $607\text{ }^{\circ}\text{C}$, with a maximum exothermic peak at $391\text{ }^{\circ}\text{C}$ and is attributed to the transformation of $(\text{Y,Zr})\text{O}(\text{OH})$ in oxide specie $[\text{210}]-[\text{212}]$. The third decomposition in the $607 - 1034\text{ }^{\circ}\text{C}$ range corresponds to the decomposition of BaCO_3 according to **Reaction II.3** [213], [214]. The last decomposition step occurring from $1034\text{ }^{\circ}\text{C}$ to $1166\text{ }^{\circ}\text{C}$ corresponds to BaO vaporization.



According to these considerations, the annealing treatment of the powder is performed at $1000\text{ }^{\circ}\text{C}$ in order to decompose BaCO_3 impurity and compensate Ba vacancies in the perovskite structure by incorporating BaO.

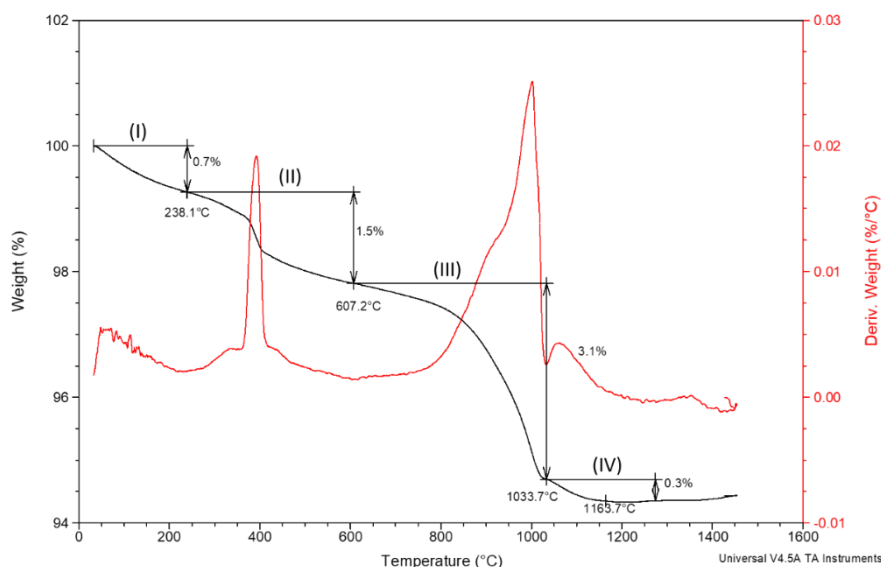


Figure II.28: TGA signal (black) and Differential Thermal Analysis (red) of the BZY-c powder

III.2.a. X-ray diffraction analysis

BZY-b and BZY-c powders were annealed at 1000 °C for 1 hour in air atmosphere, the heating and cooling ramps were 3 °C/min. **Figure II.29.a** gives the 20 – 80 ° 2θ range diffractogram of the two powders. The major phase obtained in both samples is a perovskite phase corresponding to BZY. As suggested by the TGA analysis, the (Y,Zr)O(OH) has changed in Zr-doped Y₂O₃ (space group *Ia-3*) and BaCO₃ has been decomposed. **Figure II.29.b** exposes the zoom on the (200) peak, while **Figure II.29.c** shows the zoom on the (220) peak. As exposed in the previous section, those two peaks are widely split in the tetragonal system. The BZY-c 1000 °C peaks are almost symmetric, characteristic of a cubic perovskite lattice. The BZY-b 1000 °C peak is asymmetric. However, it is not characteristic of a tetragonal distortion. Thus, the asymmetric shape of the diffraction peak of the BZY-b 1000 °C is presumably due to a gradient of composition and the annealed BZY-b powder exhibits a cubic system.

The two patterns were refined by the Rietveld method and the result is shown in **Table II.14**, the crystallographic data of the two phases are described in **Annex A**. The proportion of each phase is in the same order in the two samples, 93.1 wt% and 94.2 wt% of BZY-b and BZY-c against 6.9 wt% and 5.8 wt% of Zr-doped Y₂O₃ respectively. The thermal treatment increases the lattice parameter, from 4.211(5) Å to 4.215(2) Å for BZY-b and from 4.201(5) Å to 4.206(5) Å for BZY-c. This rise could be assigned to the incorporation of BaO inside the perovskite lattice.

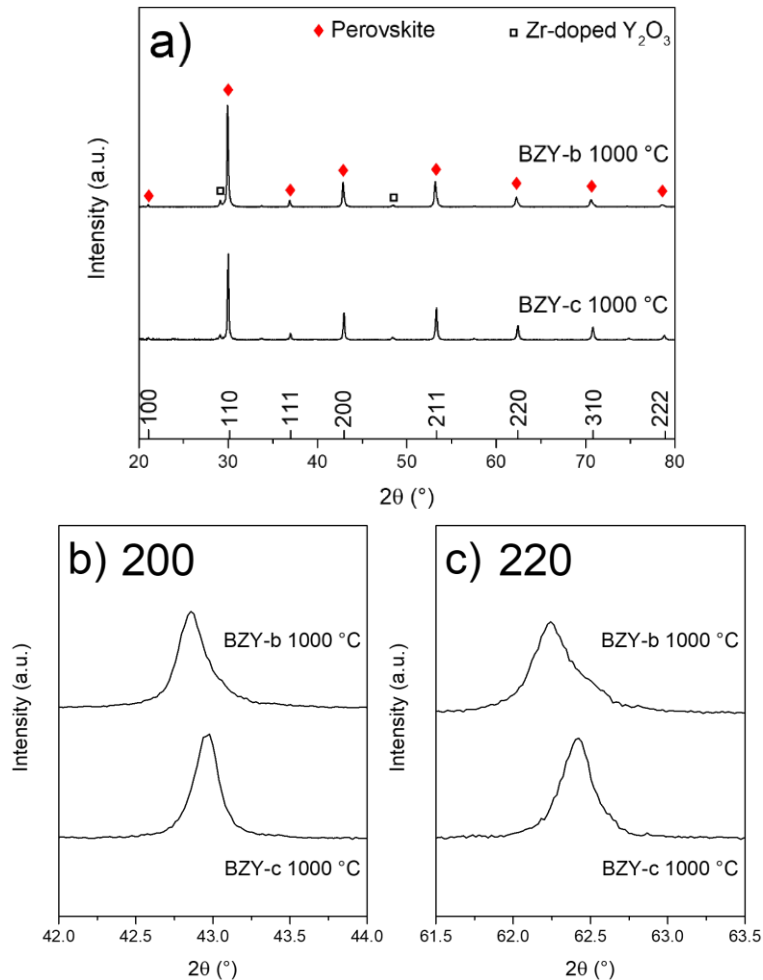


Figure II.29: X-Ray Diffractogram of the BZY-b and BZY-c powders after annealing at 1000 °C for 1 hour; a) 20-80 ° 2θ range, b) zoom on the 200 peak and c) zoom on 220 peak

Sample	Lattice parameter of BZY (wt%)	Wt% of BZY	Wt% of Zr-doped Y ₂ O ₃
BZY-b 1000 °C	4.215(2) Å	93.1	6.9
BZY-c 1000 °C	4.206(5) Å	94.2	5.8

Table II.14: Rietveld refinement of the BZY-b and BZY-c powders after annealing at 1000 °C for 1 hour

III.2.b. Microstructural and electron diffraction analysis

The two annealed powders were examined by TEM. **Figure II.30** shows the TEM micrograph of the annealed BZY-b powder. Spherical particles are still agglomerated in rosary shape, a strong heterogeneity of contrast is observed in the micrograph. The particle size increases the thermal treatment, it was evaluated on 102 particles and is 153 ± 42 nm, as a reminder, the average particle size of the raw powder was 105 ± 25 nm. The agglomerates of the 9 nm particles appearing in the raw BZY-b powder are no longer visible on this micrograph. However, on the electron diffraction pattern (**Figure II.31**), the very intense ring of the (222)

plan of the Zr-doped Y_2O_3 is present (it overlaps with the ring corresponding to the plan (110) of BZY). Therefore, it can be assumed that Zr-doped Y_2O_3 is still present on the surface of BZY, leading to the contrast heterogeneities in **Figure II.30**.

Indexation of the electron diffraction pattern is exposed in **Table II.15**. It is a primitive lattice mode with a lattice parameter of $4.21(7) \text{ \AA}$, corresponding well to the lattice parameter of $4.21(5) \text{ \AA}$ obtained by XRD. The ring 2, which overlaps with the (222) plan of Zr-doped Y_2O_3 , was not considered for the calculation.

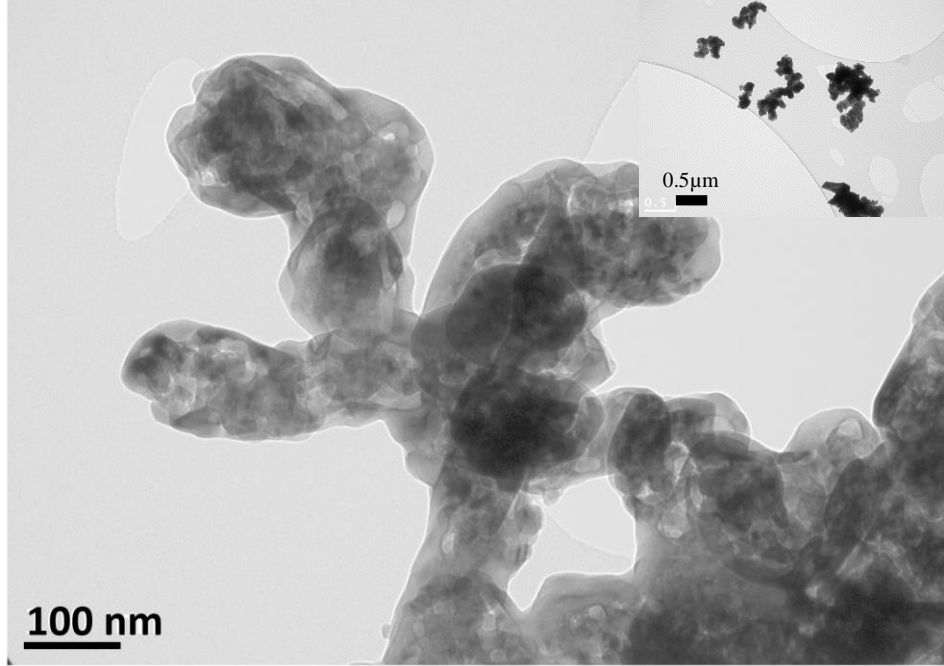


Figure II.30: TEM micrograph of the BZY-b 1000 °C powder

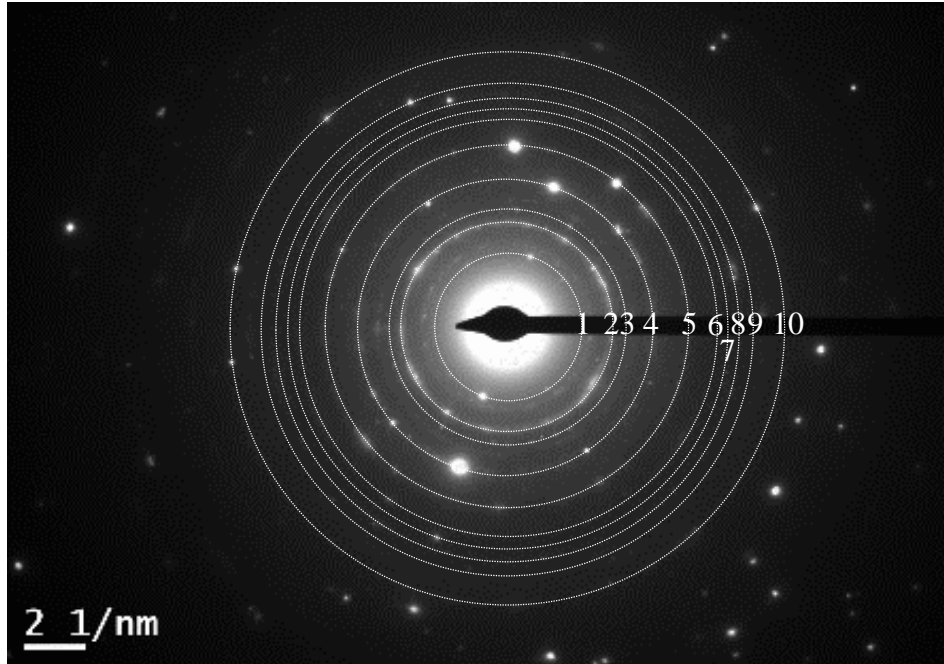


Figure II.31: Electron diffraction pattern of the BZY-b 1000 °C powder

Ring	d_{hkl}	h	k	l	Lattice parameter (Å)
1	4.21(5)	1	0	0	4.21(5)
2	2.98(6)	1	1	0	4.22(3)
3	2.63(1)	1	1	1	4.55(8)
4	2.10(7)	2	0	0	4.21(5)
5	1.71(9)	2	1	1	4.21(2)
6	1.49(5)	2	2	0	4.22(9)
7	1.40(5)	3	0	0	4.21(5)
8	1.33(2)	3	1	0	4.21(3)
9	1.27(0)	3	1	1	4.21(2)
10	1.12(7)	3	2	1	4.21(8)

Table II.15: Electron diffraction pattern of the BZY-b powder after annealing at 1000 °C for 1 hour.

The TEM micrograph of the BZY-c powder after the annealing treatment is exposed in **Figure II.32**. Particles are spherical and agglomerated, the surface appears less heterogeneous than the BZY-b 1000 °C powder. The particle size was evaluated on 104 particles and is 174 ± 61 nm. The small particles of Zr-doped Y_2O_3 are not visible on the micrographs. However, on the electron diffraction pattern presented in **Figure II.33**, the ring corresponding to the (222) plane of Zr-doped Y_2O_3 is present but exhibits a very low intensity. The indexation of the diffraction pattern is shown in **Table II.16**. It consists in a primitive group with a lattice parameter of 4.21(0) Å corresponding to BZY. The value of the lattice parameter is in agreement with the 4.20(7) Å determined by XRD.

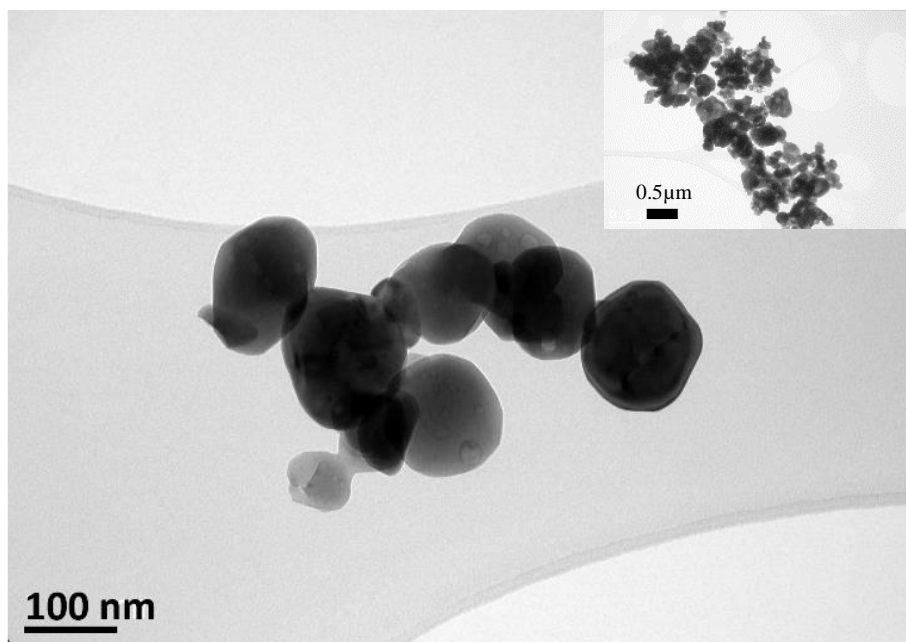


Figure II.32: TEM micrograph of the BZY-c 1000 °C powder

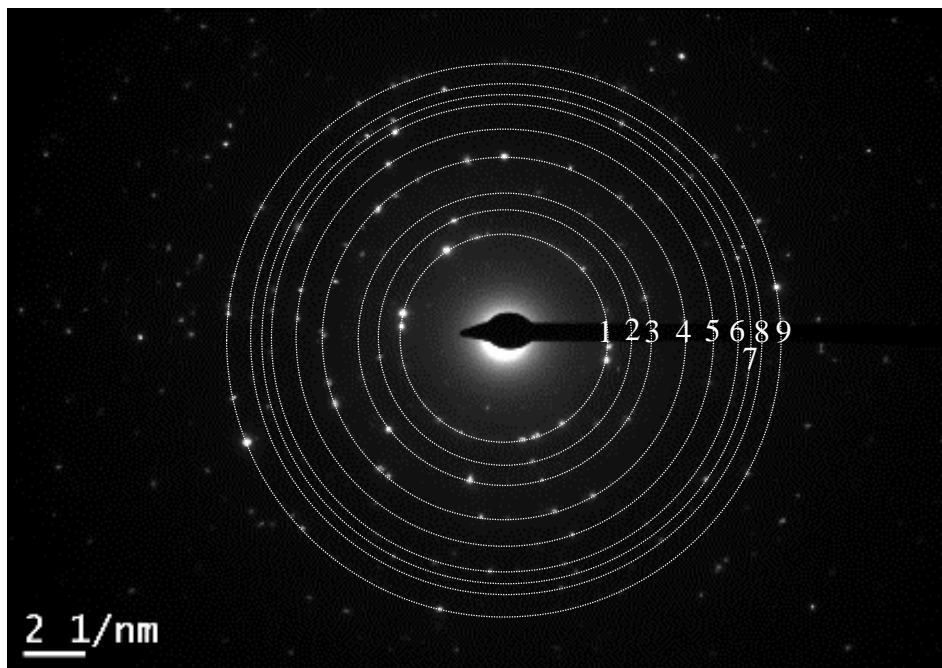


Figure II.33: Electron diffraction pattern of the BZY-c 1000 °C powder

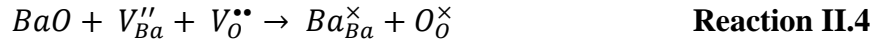
Ring	d_{hkl}	h	k	l	Lattice parameter (Å)
1	2.97(7)	1	1	0	4.21(0)
2	2.43(0)	1	1	1	4.20(9)
3	2.10(3)	2	0	0	4.20(6)
4	1.71(6)	2	1	1	4.20(4)
5	1.48(8)	2	2	0	4.21(0)
6	1.33(2)	3	1	0	4.21(3)
7	1.26(8)	3	1	1	4.20(7)
8	1.21(8)	2	2	2	4.22(0)
9	1.12(6)	3	2	1	4.21(3)
10	2.97(7)	1	1	0	4.21(0)

Table II.16: Electron diffraction pattern of the BZY-c powder after annealing at 1000 °C for 1 hour.

III.2.c. Bulk chemistry analysis

As for the raw powders, the chemical composition of BZY-b and BZY-c after the annealing treatment was investigated through SEM-EDS. Only Ba, Zr, Y, C and O elements were detected. The analysis was performed on 16 agglomerates with an area of measurement from $20\ \mu\text{m} \times 20\ \mu\text{m}$. As previously, Ba is supposed to belong to the A-site of the perovskite and Zr and Y occupy the B-site.

Figure II.34 shows a) the A-site/B-site ratios and b) the $Y/(Zr + Y)$ ratios of the BZY-b powder before and after annealing at $1000\ ^\circ\text{C}$ for 1 hour and the corresponding number of agglomerates per interval. After the annealing treatment, the distribution of A-site/B-site ratio is narrower, passing from the 0.67-1.09 range to the 0.88-1.09 with an average value at 0.96 ± 0.06 . This increase of the low-value limit attests the compensation of Ba-vacancies by BaO during the thermal treatment. The integration of BaO in the BZY structure is described in Kröger-Vink notation in **Reaction II.4**.



$Y/(Zr + Y)$ ratio exhibits slightly lower values after annealing than the raw powder. The interval was 0.17-0.32 before annealing and is 0.17-0.27 after, with an average value at 0.24 ± 0.03 . Finally, the average composition of the annealed BZY-b is $\text{Ba}_{0.96}\text{Zr}_{0.76}\text{Y}_{0.24}\text{O}_{3-\delta}$. This result is in perfect agreement with the determined lattice parameter.

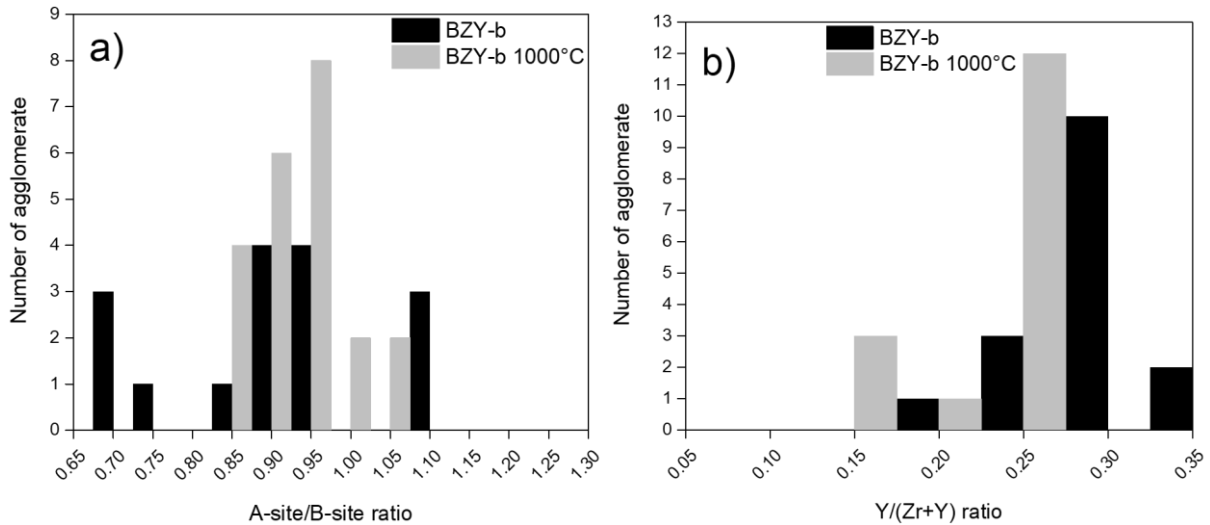


Figure II.34: a) A-site/B-site ratios and b) $Y/(Zr + Y)$ ratios obtained from SEM-EDS measurement on the BZY-b powder before and after annealing at $1000\ ^\circ\text{C}$ for 1 hour and the corresponding number of agglomerates per interval.

The SEM-EDX investigation on the BZY-c powder before and after thermal treatment is shown in **Figure II.35**. As for the batch powder, the annealing treatment allows to narrowing the interval of A-site/B-site value. The initial range was 0.70-1.33 and is 0.92-1.09 after the annealing treatment, with an average value of 1.01 ± 0.04 . The $Y/(Zr+Y)$ distribution has the same profile before and after annealing. Values are also in the same order, from 0.08 to 0.25 before the thermal treatment and from 0.07 to 0.24 after annealing, with an average value of

0.14 ± 0.04 . This thermal treatment is efficient to homogenize of the composition, indeed the average composition of the raw powder was $\text{Ba}_{0.93}\text{Zr}_{0.86}\text{Y}_{0.14}\text{O}_{3-\delta}$ and $\text{Ba}_{1.01}\text{Zr}_{0.85}\text{Y}_{0.15}\text{O}_{3-\delta}$ is the average composition after the thermal treatment.

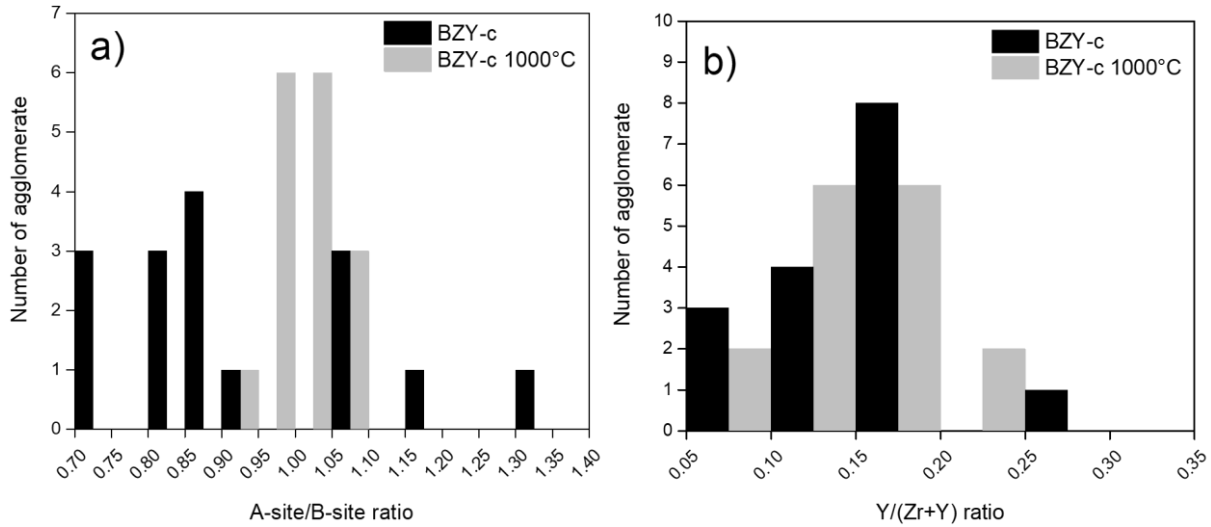


Figure II.35: a) A-site/B-site ratios and b) $\text{Y}/(\text{Zr} + \text{Y})$ ratios obtained from SEM-EDS measurement on the BZY-c powder before and after annealing at 1000 °C for 1 hour and the corresponding number of agglomerates per interval.

III.2.d. Surface chemistry analysis

The surface chemistry of the BZY-b and the BZY-c powder was investigated by XPS after the annealing thermal treatment at 1000 °C for 1 hour. The binding energy of each element window was calibrated from the C 1s of the adventitious carbon (C–C and C–H bonds) peak at 284.8 eV. The elemental composition of the surface of each powder determined by XPS is presented in **Table II.17**. The content of carbon and oxygen are similar to those determined for the raw powder. The $\text{Y}/(\text{Zr} + \text{Y})$ ratio is 0.22 for the BZY-b 1000 °C powder, larger than the one determined by EDS, and 0.17 for the BZY-c 1000 °C powder. This value is in line with the EDS analysis. The A-site/B-site ratio is 0.97 and 0.91 for BZY-b 1000 °C and BZY-c 1000 °C respectively. These values are much larger than for the as-synthesized powders, agreeing well with the Ba uptake during the thermal treatment statement highlighted in the previous paragraph.

Sample	Barium	Zirconium	Yttrium	Oxygen	Carbon
BZY-b 1000 °C	14.3	11.5	3.2	60.5	10.4
BZY-c 1000 °C	11.8	10.7	2.2	57.3	15.7

Table II.17: Elemental composition (at%) of the BZY-b 1000 °C and the BZY-c 1000 °C powders obtained by XPS.

The XPS window spectra of each element for the two BZY powders annealed at 1000 °C for 1 hour are presented in **Figure II.36**. The Ba 3d_{5/2} (**Figure 36.a**) spectra are similar to those

of the raw powder. The main peak at 779.2 ± 0.2 eV corresponds to Ba from BZY and possibly Ba from BaCO_3 [186], [193], [194], [197]–[200]. The peak at 780.6 ± 0.2 eV is attributed to Ba-O terminal bonds [194], [195].

The C 1s core-level spectra displayed in **Figure II.36.b** can be deconvoluted in three contributions, the same as before the annealing treatment, for each spectrum. In comparison with the as-synthesized powder, the BZY-c 1000 °C shows more C from BaCO_3 content, suggesting a surface carbonation of the sample. The calculated content is 4.8 at% after annealing treatment while it was 2.7 at% in the as-synthesized powder. The BZY-b 1000 °C C 1s spectra are very similar before and after the thermal treatment.

The Zr 3d core-level spectra are presented in **Figure II.36.c**. As for the raw powder, the spectra can be fitted with two contributions. The contribution situated at 181.0 ± 0.1 eV for the $3d_{5/2}$ level and 183.4 ± 0.1 eV for the $3d_{3/2}$ level correspond to $\text{Zr}_{\text{Zr}}^{\times}$ from BZY [186], [193], [194], [202]. It should be noticed that in both powders, the proportion of Zr from BZY has highly increased in comparison with the as-synthesized powder. According to the XRD experiments, the second contribution at 182.2 ± 0.1 eV ($3d_{5/2}$) and 184.6 ± 0.1 eV ($3d_{3/2}$) could correspond to surface YSZ [203]–[206]. No literature data was found for Zr-doped Y_2O_3 but the energy of the chemical bonding Y–O–Zr is supposed to be nearly the same in Zr-doped Y_2O_3 than YSZ, then this contribution was assigned to Zr-doped Y_2O_3 .

The Y 3d core spectra are depicted in **Figure II.36.d** are different than from the as-synthesized spectra and present two contributions in each sample. The contribution at 157.8 ± 0.1 eV ($3d_{5/2}$) and 159.9 ± 0.1 eV ($3d_{3/2}$) could reasonably be assigned to Y_{Zr}' from BZY while the 155.9 ± 0.1 eV ($3d_{5/2}$) and 158.6 ± 0.1 eV ($3d_{3/2}$) peaks could be assigned to $\text{Y}_{\text{Ba}}^{\bullet}$ [183], [202]. The atomic percent of $\text{Y}_{\text{Ba}}^{\bullet}$ calculated from the area of the peaks and the surface composition of the sample are 1.5 at% for BZY-b 1000 °C and 0.15 at% for BZY-c 1000 °C. The contribution of YSZ and so Y from Zr-doped Y_2O_3 overlaps with the one of Y_{Zr}' , then, it was impossible to deconvolute the two signals.

The O 1s spectra of the BZY-b 1000 °C and the BZY-c 1000 °C powders are presented in **Figure II.36.e**. They are quite similar to those of the as-synthesized powder and can be fitted with three contributions corresponding to BZY (at 528.9 ± 0.1 eV), Zr-doped Y_2O_3 (at 530.0 ± 0.1 eV) and BaCO_3 (at 531.2 ± 0.1 eV) according to the literature survey displayed in **Figure II.26**. For this assignation, the YSZ contribution was replaced by Zr-doped Y_2O_3 according to the XRD indexation.

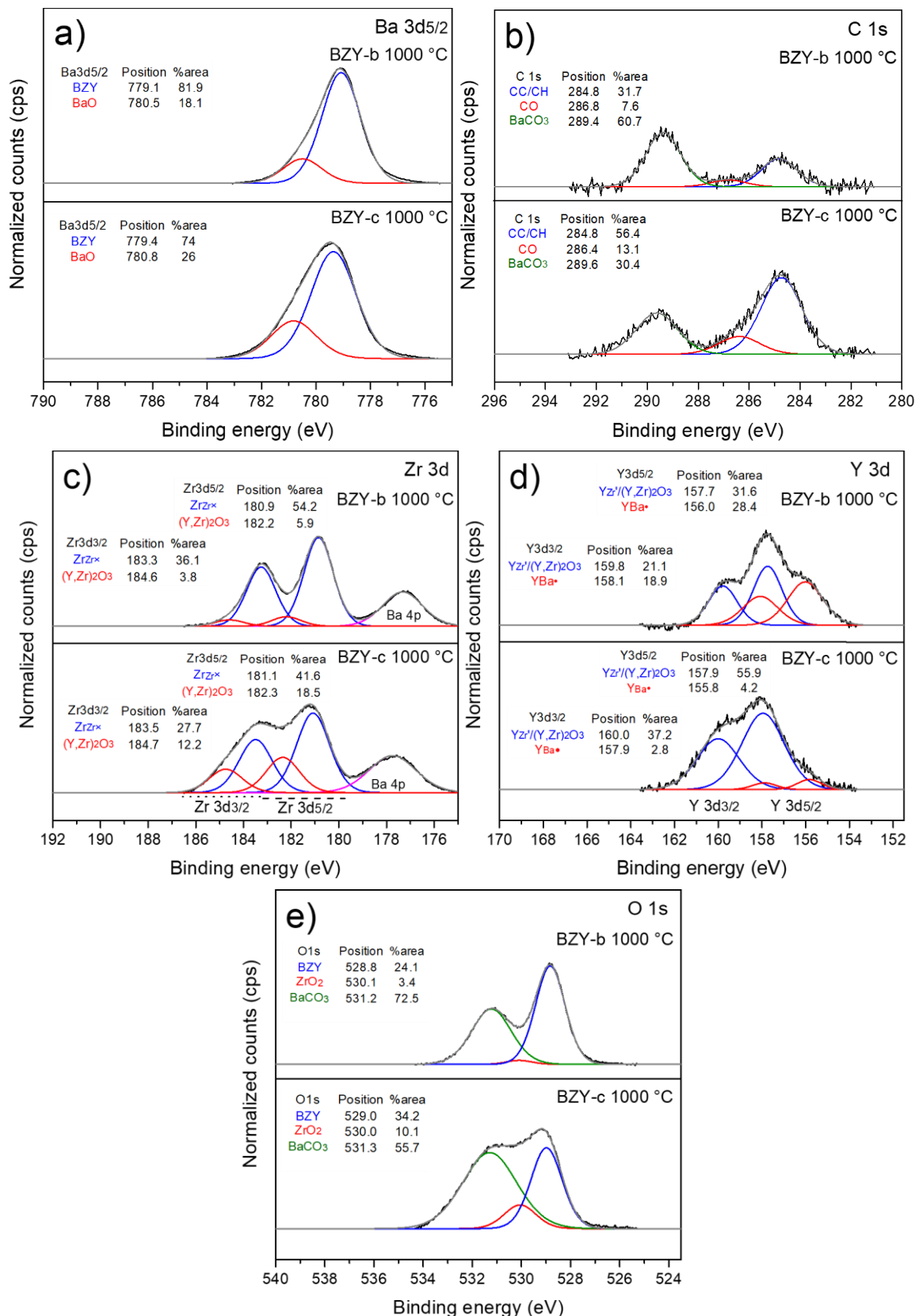
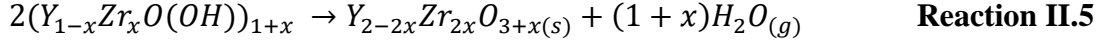


Figure II.36: XPS core-level spectra of the BZY-b and BZY-c powders after annealing at 1000 °C for 1 hour. a) core-level spectra of Ba 3d_{5/2}, b) core-level spectra of C 1s, c) core-level spectra of Zr 3d and d) core-level spectra of Y 3d

III.2.e. Summary

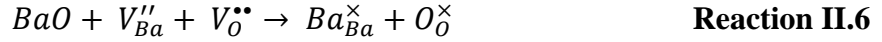
The annealing treatment at 1000 °C for 1 hour allows to homogenize the structure of the BZY powder. Several reactions occur during this thermal treatment. Firstly, the oxyhydroxide species is converted into oxide according to **Reaction II.5**.



In a second step, BaCO₃ decomposes in BaO and CO₂ according to **Reaction II.3**.



Finally, the resulting BaO incorporates the lattice of BZY following **Reaction II.6**.



This compensation of Ba-deficiency results in an increase of the cubic lattice parameter. BZY-b pass from 4.211(5) Å to 4.215(2) Å after the thermal treatment and BZY-c pass from 4.201(5) Å to 4.206(5) Å, the amount of Y_{1-x}Zr_xO_{3+δ} is about 6.4 %wt in the two powders. The incorporation of Ba is also highlighted by SEM-EDS measurement, the final compositions are Ba_{0.96}Zr_{0.76}Y_{0.24}O_{3-δ} for BZY-b and Ba_{1.01}Zr_{0.85}Y_{0.15}O_{3-δ} for BZY-c.

The resulting powder consists in spherical grains of about 119 nm for BZY-b and 138nm for BZY-c, agglomerated in cluster. The surface chemistry analysis via XPS evidenced that the thermal treatment does not affect the Ba, C and O chemical bonding. Zr 3d spectra suggested that less impurity (Zr-doped Y₂O₃) is present after the annealing treatment. Y 3d core-level spectra highlight the presence of Y in the two cationic sites of the perovskite. Furthermore, the substitution of A-site by Y is 10 times more important in the BZY-b 1000 °C than in the BZY-c 1000 °C.

Even though this thermal treatment is useful for the elimination of BaCO₃ and the compensation of the Ba-deficiency in the crystal structure, it does not solve the problem of the Y- and Zr-based impurity. Then, in the last part of this chapter, a study about avoiding the formation of (YO(OH))_{1-x}(ZrO(OH)₂)_x will be presented.

III.3. Formation mechanism of Ba(Zr,Y)O_{3-δ}

Another group, Yoko et al., studied the formation mechanism of BaZrO₃ in supercritical water. **Figure II.37** presents the schematic of the plausible mechanism of the formation of BaZrO₃ in a continuous hydrothermal set-up at 400 °C and 300 bar [215]. They suspected the formation of Ba-deficient particles with a ZrO(OH)₂ shell at the early stage of the precipitation followed by an uptake of Ba²⁺ up to Ba/Zr=1. In 2016, the same group used in situ X-ray diffraction to study and support the previous mechanism [216].

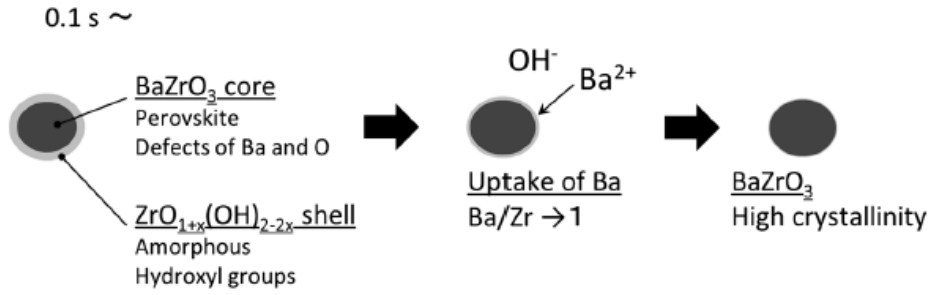


Figure II.37: Schematic of the plausible mechanism of the formation of BaZrO_3 in a continuous hydrothermal set-up at 400 °C and 300 bar [215].

The formation mechanism of BZY, adapted from Yoko et al., is presented in **Figure II.38**. It consists of the formation of $(\text{YO}(\text{OH}))_{1-x}(\text{ZrO}(\text{OH})_2)_x$ shell surrounding a $\text{Ba}_{1-x}(\text{Zr}, \text{Y})\text{O}_{3-\delta}$ core. In a second step, Ba^{2+} , Zr^{4+} and Y^{3+} are incorporated from the solution to the shell while Ba^{2+} is uptake in the core. In the last step, the separation of the core and the shell occurs. During the drying of the powder, free Ba^{2+} form BaO which is carbonate into BaCO_3 .

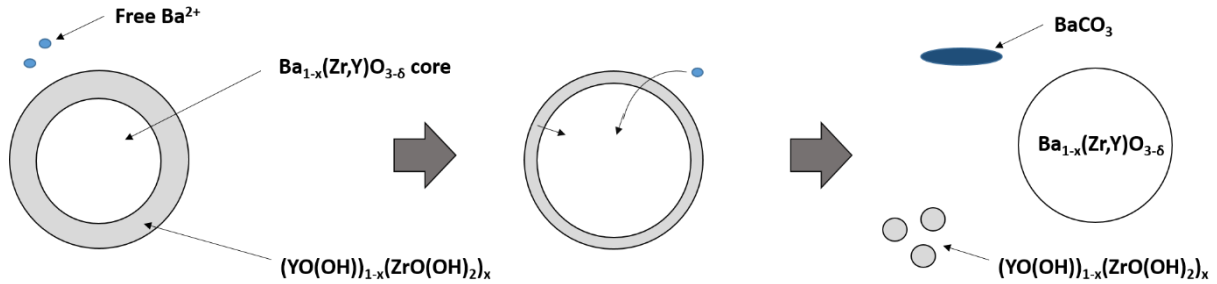


Figure II.38: suspected formation mechanism of BZY in the continuous hydrothermal set-up at 450 °C and 300 bar.

III.4. Adjustment of the synthesis conditions

In a study from 2010, Yamazaki et al. studied the phase behavior of Ba-deficient BZY synthesized by the sol-gel route [217]. They demonstrated that, by considering the $\text{Ba}_{1-x}\text{Zr}_{0.8}\text{Y}_{0.2}\text{O}_{3-\delta}$ formula:

- if $x < 0.06$, then BZY is obtained as a single phase and the sub-stoichiometry is compensated by incorporating Y in the A-site.
- if $0.08 < x < 0.2$, then $(\text{Y}, \text{Zr})_2\text{O}_3$ is formed as secondary phase.
- if $0.2 < x < 0.3$, two secondaries phases are formed: $(\text{Y}, \text{Zr})_2\text{O}_3$ and $(\text{Zr}, \text{Y})\text{O}_2$
- if $0.3 < x < 0.4$, then the secondary phase consists of $(\text{Zr}, \text{Y})\text{O}_2$.

It can then be assumed that, by avoiding the Ba-deficiencies, the $(\text{Y}, \text{Zr})\text{O}(\text{OH})$ compound will not be formed. In order to prevent obtaining Ba-deficiencies, an over-stoichiometry of $\text{Ba}(\text{NO}_3)_2$ is used during the hydrothermal synthesis. Different compositions were tested: a ratio $\text{Ba}(\text{NO}_3)_2/(\text{ZrO}(\text{NO}_3)_2 \cdot 6\text{H}_2\text{O} + \text{Y}(\text{NO}_3)_3 \cdot 6\text{H}_2\text{O})$ equal to 1.5, noted B1.5ZY, the same ratio equal to 2, noted B2ZY, the ratio equal to 3, noted B3ZY and the ratio equal to

4, noted B4ZY. The synthesis were carried out in the continuous set-up in the same conditions as before, i.e., $T = 400\text{ }^{\circ}\text{C}$, $P = 300\text{ bar}$ and $\text{pH} = 13$.

III.4.a. X-ray diffraction analysis

The XRD patterns of B1.5ZY, B2ZY-c, B3ZY-c, B4ZY-c are shown in **Figure II.39.a**. Two phases are obtained, the major phase corresponds to cubic BZY and impurity is only consisting of BaCO_3 . As shown in **Figure II.X.39.b**, where a zoom on the 110 peak is shown, there is no trace of the oxyhydroxide species.

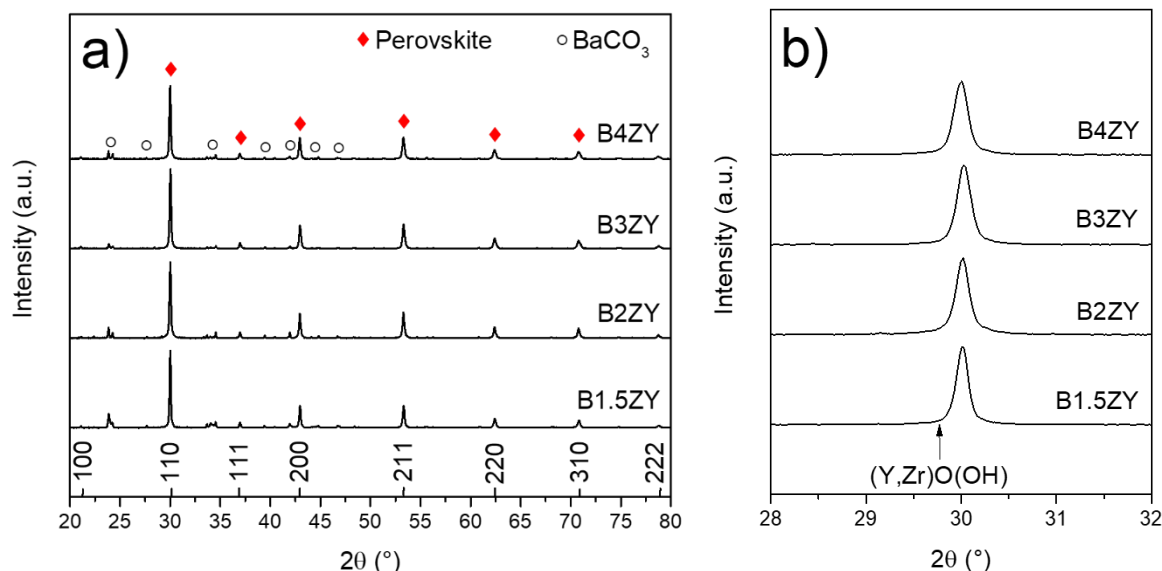


Figure II.39: X-ray diffractogram of B1.5ZY, B2ZY, B3ZY and B4ZY powders synthesized by the continuous process at $400\text{ }^{\circ}\text{C}$ and 300 bar; a) $20\text{--}80\text{ }^{\circ} 2\theta$ range and b) zoom on the 110 peak, the theoretical position of the more intense peak is represented in the figure

Rietveld refinement was conducted on the four diffractograms and the refined lattice parameter of the BZY phase and phase percentage is shown in **Table II.18**. The particle size of the BZY phase was determined with the William and Hall method, the obtained Williamson and Hall diagram is presented in **Figure II.40**. The structural parameters inputted in FullProf program are reported in **Annex A**. The refined lattice parameter is very close to each other, varying from $4.207(9)\text{ \AA}$ for B1.5ZY to $4.205(1)\text{ \AA}$ for B3ZY. In a general manner, the lattice parameter of the BZY phase decrease with the augmentation of the initial $[\text{Ba}]/([\text{Zr}]+[\text{Y}])$ ratio, suggesting a less important incorporation of Ba and/or Y into the structure. The percentage of BaCO_3 is maximum for the B1.5ZY powder with 23.3 wt%, on the contrary, B3ZY exhibits only 7.9 wt% of BaCO_3 . The crystallite size, that can be assimilated to the particle size in the raw powder, is 63 nm for B1.5ZY, 49 nm for B2ZY and increase up to 120 nm for B4ZY.

Name	Lattice parameter of the perovskite phase	Crystallite size of the perovskite phase	Microstrain (%)	Wt% of Ba(Zr,Y)O _{3-δ}	Wt% of BaCO ₃
B1.5ZY	4.207(9) Å	65 nm	0.09	76.7	23.3
B2ZY	4.206(0) Å	57 nm	0.10	85.2	14.8
B3ZY	4.205(1) Å	77 nm	0.16	92.1	7.9
B4ZY	4.207(3) Å	75 nm	0.16	87.5	12.5

Table II.18: Rietveld refinement and analysis of the Williamson and Hall diagram of the BZY-b and BZY-c powders after annealing at 1000 °C for 1 hour

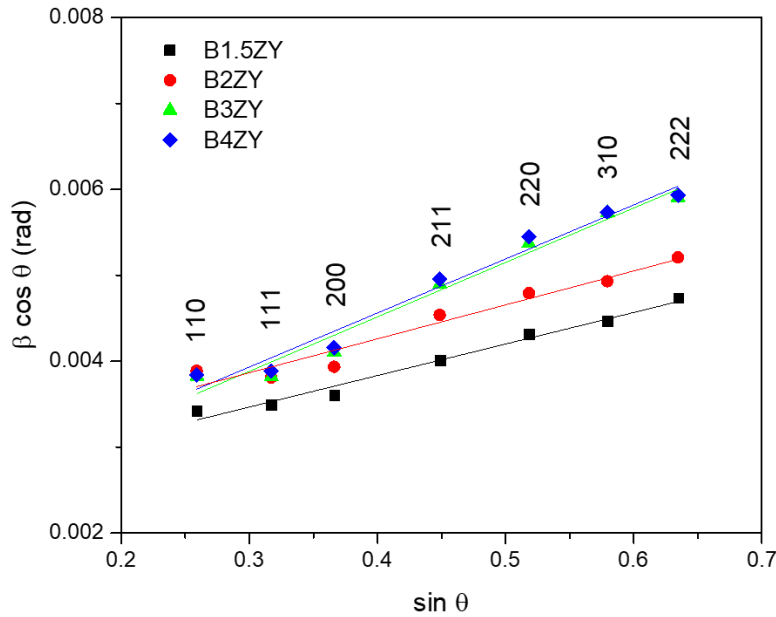


Figure II.40: Williamson and Hall diagram of the BZY phase of the B1.5ZY, B2ZY, B3ZY and B4ZY powders synthesized by the continuous process at 400 °C and 300 bar

III.4.b. Bulk chemistry analysis

In order to determine the composition, SEM-EDS was performed on the B1.5ZY, B2ZY, B3ZY and B4ZY powders. The area of measurement was 10 μm \times 10 μm on the 20 analyses. Only Ba, Zr, Y, C and O elements were detected. As previously, Ba is supposed to belong to the A-site of the perovskite and Zr and Y occupy the B-site.

The number of agglomerate per A-site/B-site ratio interval is represented on **Figure II.41.a**. As suggested by the XRD, the higher is the initial amount of Ba, the lower is the amount of Ba in the perovskite. Values vary from 0.94 to 1.26 with an average value of 1.13 ± 0.07 for B1.5ZY, from 0.94 to 1.13 with an average value of 1.03 ± 0.05 for B2ZY, from 0.85 to 1.08 with an average value of 0.95 ± 0.06 for B3ZY and from 0.83 to 1.01 with an average value of 0.91 ± 0.05 for B4ZY. Furthermore, in comparison with the SEM-EDS analysis of the BZY-b and BZY-c powder (**Figure II.25**), the deviation of the values is more narrow.

The Y/(Zr+Y) ratios of each powder are shown in **Figure II.41.b**. Always in agreement with the XRD analysis, the more the initial [Ba]/([Zr]+[Y]) ratio increases, the less the yttrium enter the structure. For B1.5ZY, the Y/(Zr+Y) ratio varies from 0.14 to 0.25 with an average value of 0.21 ± 0.04 , from 0.14 to 0.26 with an average value of 0.19 ± 0.04 for B2ZY, from 0.13 to 0.22 with an average value of 0.17 ± 0.03 for B3ZY and from 0.10 to 0.29 with an average value of 0.16 ± 0.05 for B4ZY.

Consequently to these results, the chemical composition of the perovskite phase of B1.5ZY can be written as $\text{Ba}_{1.13}\text{Zr}_{0.79}\text{Y}_{0.21}\text{O}_{3-\delta}$, B2ZY as $\text{Ba}_{1.03}\text{Zr}_{0.81}\text{Y}_{0.19}\text{O}_{3-\delta}$, B3ZY as $\text{Ba}_{0.95}\text{Zr}_{0.83}\text{Y}_{0.17}\text{O}_{3-\delta}$ and B4ZY as $\text{Ba}_{0.91}\text{Zr}_{0.84}\text{Y}_{0.16}\text{O}_{3-\delta}$.

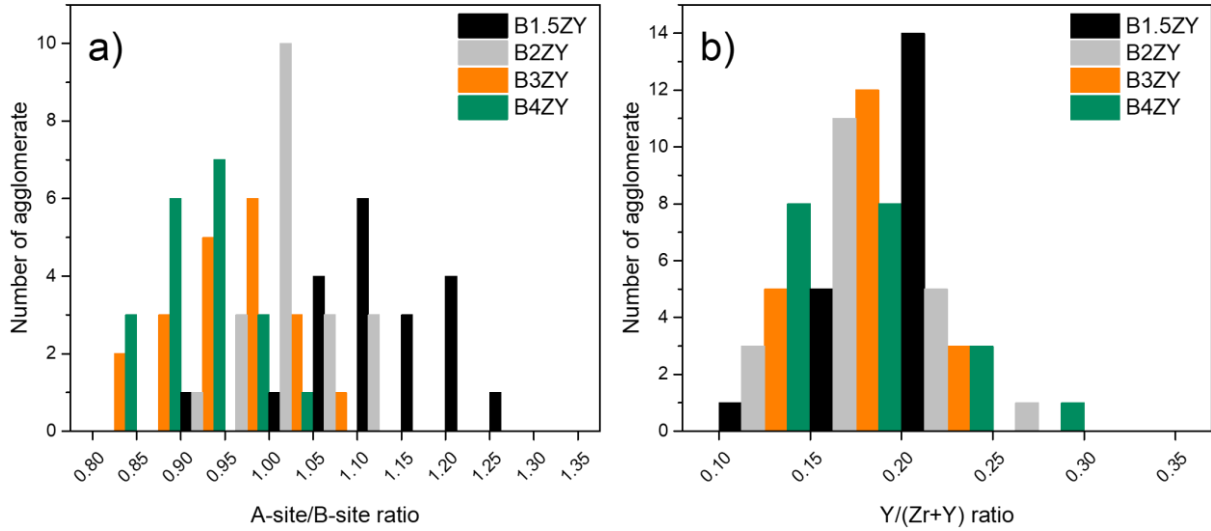


Figure II.41: a) A-site/B-site ratios and b) Y/(Zr + Y) ratios obtained from SEM-EDS measurement on the B1.5ZY, B2ZY, B3ZY and B4ZY powders and the corresponding number of agglomerates per interval.

III.4.c. Summary

The increase of the initial quantity of Ba^{2+} allows to avoid the formation of the (Y,Zr)O(OH) species. The only impurity detected in the powder consists of BaCO_3 , formed consequently to the carbonation of free Ba^{2+} at the end the synthesis. Among the four $\text{Ba}(\text{NO}_3)_2/(\text{ZrO}(\text{NO}_3)_2 \cdot 6\text{H}_2\text{O} + \text{Y}(\text{NO}_3)_3 \cdot 6\text{H}_2\text{O})$ ratio tested (1.5, 2, 3 and 4), 2 appears to be the more optimal. Indeed, the ratio equal to 3 and 4 allows the synthesis of Ba-deficient perovskite. The Ba-deficient structure hinders the incorporation of Y into the structure. The powder synthesized with the 1.5 ratio, does not present Ba-deficiency, on the contrary, the BZY phase exhibits an over-stoichiometry of Ba. The content of Y was found to be close to the expected 20 %. Finally, the powder synthesized with the 2 ratio presents a composition very close the target one: $\text{Ba}_{1.03}\text{Zr}_{0.81}\text{Y}_{0.19}\text{O}_{3-\delta}$ and should be the chosen experimental condition.

IV. Conclusion

The Ce-containing compounds among the Y-doped $\text{BaCeO}_3\text{--BaZrO}_3$ solid solution is impossible to obtain by the hydrothermal route using water as solvent. On the one hand, BaCeO_3 -based oxides are not stable in water containing atmosphere. On the other hand, the fast nucleation of CeO_2 in hydrothermal conditions hinders the formation of BaCeO_3 -based compounds. For these reasons, only the synthesis of the BaZrO_3 and $\text{Ba}(\text{Zr},\text{Y})\text{O}_{3-\delta}$ (BZY) were carried out. As seen in the first chapter, BaZrO_3 does not exhibit high protonic conductivity, then BZY is the chosen protonic conductor.

BZY was synthesized by batch and continuous devices in supercritical conditions ($T = 400\text{ }^\circ\text{C}$ and $P = 300\text{ bar}$) using a stoichiometric quantity of precursors. In both routes, the synthesis led to the formation of three different phases: one major BZY phase and BaCO_3 and $(\text{Y},\text{Zr})\text{O}(\text{OH})$ as impurities. The content of these secondary phases was similar regardless of the synthesis process (about BaCO_3 12 wt% of and 4 wt% of $(\text{Y},\text{Zr})\text{O}(\text{OH})$). The lattice parameter determined by X-ray diffraction and electron diffraction and the EDS analyses indicates a highest incorporation of Y in the BZY powder elaborated by the batch process than in the powder elaborated in the continuous device. The same observation is made for the Ba incorporation: the BZY-batch powder contains more Ba than the BZY-continuous powder. The surface chemistry analyses support these considerations. From the microstructural point of view, both BZY powders present a spherical morphology. In agreement with the residence time in the two processes, the BZY-continuous powder has a smaller grain size (about 50 nm) than the BZY-batch powder (100 nm).

The annealing treatment at $1000\text{ }^\circ\text{C}$ for 1 hour is beneficial for the two powders. First, the decomposition of the BaCO_3 secondary phase leads to the compensation of Ba-deficiency in the BZY structure. It results in an increase in the lattice parameter and it is confirmed by the EDS measurements. The determined average composition is $\text{Ba}_{0.96}\text{Zr}_{0.76}\text{Y}_{0.24}\text{O}_{3-\delta}$ for BZY-b and $\text{Ba}_{1.01}\text{Zr}_{0.85}\text{Y}_{0.15}\text{O}_{3-\delta}$ for BZY-c. In parallel, the $(\text{Y},\text{Zr})\text{O}(\text{OH})$ reacts to form Zr-doped Y_2O_3 oxide. The presence of this oxide could be detrimental to the conductivity properties [218]. The thermal treatment slightly increases the particle size, an average value of 153 nm was calculated for BZY-batch $1000\text{ }^\circ\text{C}$ and 173 nm for BZY-continuous $1000\text{ }^\circ\text{C}$. XPS surface chemistry indicates the partial substitution of the Ba by Y. The phenomenon is much more evident in the BZY-batch $1000\text{ }^\circ\text{C}$ powder than in the BZY-continuous $1000\text{ }^\circ\text{C}$ powder.

Finally, by optimizing the precursor quantity, a $\text{Ba}_{1.03}\text{Zr}_{0.81}\text{Y}_{0.19}\text{O}_{3-\delta}$ composition is obtained for the initial ratio $[\text{Ba}]/([\text{Zr}]+[\text{Y}])$ of two. In addition, in such synthesis conditions, no trace of $(\text{Y},\text{Zr})\text{O}(\text{OH})$ impurity was found. In agreement with Yamazaki et al., it is due to the absence of Ba-deficiency [217].

CHAPTER III: STUDY OF THE CONDUCTIVITY OF Y-DOPED BARIUM ZIRCONATE

The present chapter describes in the first part the electrochemical impedance spectroscopy technique, from its principle to the exploitation of the data. The defect chemistry and the charge carrier species in perovskite protonic conductors will be detailed. Finally, the definition and the measurement of the conductivity is presented.

In the second section, the sintering behavior of BZY and the preparation of the BZY samples for the conductivity measurement is exposed.

The third part shows the EIS measurements from 200 to 700 °C conducted on the samples: the BZY elaborated by the continuous route, the BZY synthesized by the batch process and a commercial BZY will be studied as a comparison. Finally, the thermal behavior of the conductivity of the three materials is presented and discussed.

I. Electrochemical impedance spectroscopy: theory and application

The Electrochemical Impedance Spectroscopy (EIS), also known as complex impedance spectroscopy, is one the most powerful analysis method for characterizing electrochemical devices [219], [220]. Indeed, this method allows to distinguish and separate the response from any layer that can be polarized (electrolyte, electrodes and even interfaces) and is widely applied to study the conductivity and characterize fuel cells [221].

I.1. Theory of complex impedance spectroscopy

This first part aims to give an overview of EIS: the principle of the experiment, the mathematical definition of the complex impedance, the construction of the EIS spectra, the different representations of the data and, finally, the interpretation of the EIS spectra.

I.1.a. Principle of EIS

The principle of EIS consists in applying a small quantity of sinusoidal voltage to perturb a system and measuring the system's response (an oscillating current with a specific amplitude and shift) as illustrated in **Figure III.1** [219]. Each layer (electrolyte, electrodes and interfaces) will be polarized in a unique way under an applied voltage. The rate of change of the polarized region when the voltage is reversed is characteristic of the type of interface/layer and allows to separate the different contributions [222]. For example, the oxygen reduction

reaction at the cathode side involves slow electrochemical phenomena, while the diffusion of a charged species toward the bulk of a conductor material occurs very fast [223].

In practice, a potentiostat measures the impedance, that is to say, the dependence between the applied sinusoidal voltage and the recorded current wave. A spectrum is then built point by point by measuring this signal at different frequencies. In the fuel cell area, the typical amplitude of voltage is in the 10 – 50 mV range and the frequency varies from 10^6 to 10^{-2} Hz.

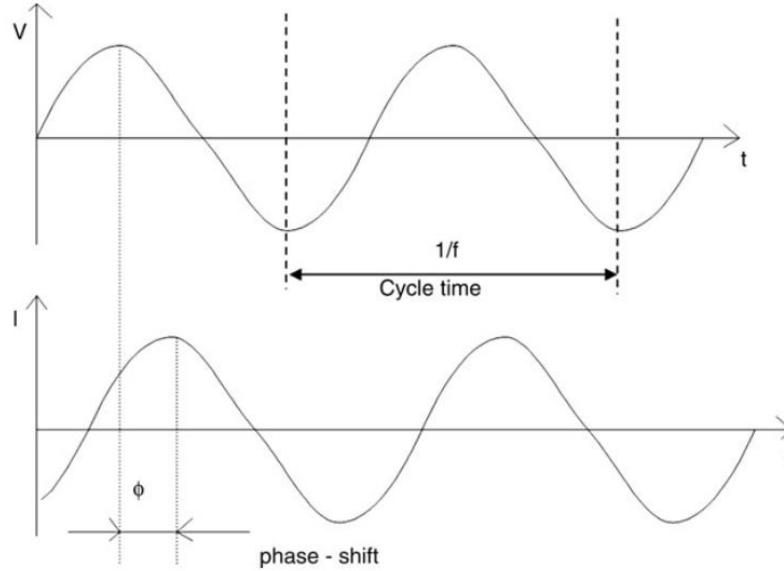


Figure III.1: Principle of EIS, applied voltage (top) and measured current (bottom) [224]

I.1.b. Mathematical considerations

As said in the previous paragraph, the impedance is dependent of the sinusoidal voltage and current. It can be assimilated to the Ohm's law in the time domain according to **Equation III.1:**

$$E(t) = Z(\omega) \times I(t) \quad \text{Equation III.1}$$

Where $Z(\omega)$ is the complex impedance, $E(t)$ is the sinusoidal voltage and $I(t)$ is the sinusoidal current.

The expression of the sinusoidal voltage is equal to **Equation III.2:**

$$E(t) = E_0 \sin(\omega t) \quad \text{Equation III.2}$$

Where E_0 is the amplitude of voltage signal and ω is the angular frequency ($\omega = 2\pi f$).

The expression of the sinusoidal current is expressed in **Equation III.3:**

$$I(t) = I_0 \sin(\omega t + \phi) \quad \text{Equation III.3}$$

Where ϕ represent the phase angle.

By combining those expressions, the impedance can be rewrite in **Equation III.4.**

$$Z(\omega) = \frac{E(t)}{I(t)} = \frac{E_0 \sin(\omega t)}{I_0 \sin(\omega t + \phi)} \quad \text{Equation III.4}$$

By using Euler's formula, Equation III.4 is turned into **Equation III.5.**

$$Z(\omega) = \frac{E_0 e^{i\omega t}}{I_0 e^{i\omega t + \phi}} = Z_0 e^{i\phi} \quad \text{Equation III.5}$$

It is also possible to express the complex impedance by separating the real and the imaginary parts (**Equation III.6**) in order to represent it in a Cartesian plane.

$$Z(\omega) = Z' + iZ'' \quad \text{Equation III.6}$$

Z' , the real part, physically represents the resistance of the system, while Z'' , the imaginary part, is characteristic of the capacitive or inductive behavior of the system.

I.1.c. Representations of the impedance

It exists different ways to represent the impedance of a system. The most usual is the Nyquist plot, in which the imaginary part (charted as $-Z''$) is plotted as a function of the real part. In the fuel cells area, the Nyquist plot generally consists of semi-circles that represent electrochemical phenomena. An example of Nyquist plot is shown in **Figure III.2.a**. In this example, only one electrochemical contribution, i.e., only one semi-circle, is depicted. Since the real part of the impedance represents the resistance, the Nyquist plot allows reading directly on the graph the resistance parameter of the system, here $500 \, \Omega$. However, the frequency, and then the time dependence of the electrochemical phenomena is not easily readable. For this reason, the Bode plot (shown in **Figure III.2.b**) is highly appreciated. It is two plots in one, on one part the impedance Z is reported as a function of the frequency and on the other part, the phase shift (plotted as $-phase$) is reported as a function of the frequency.

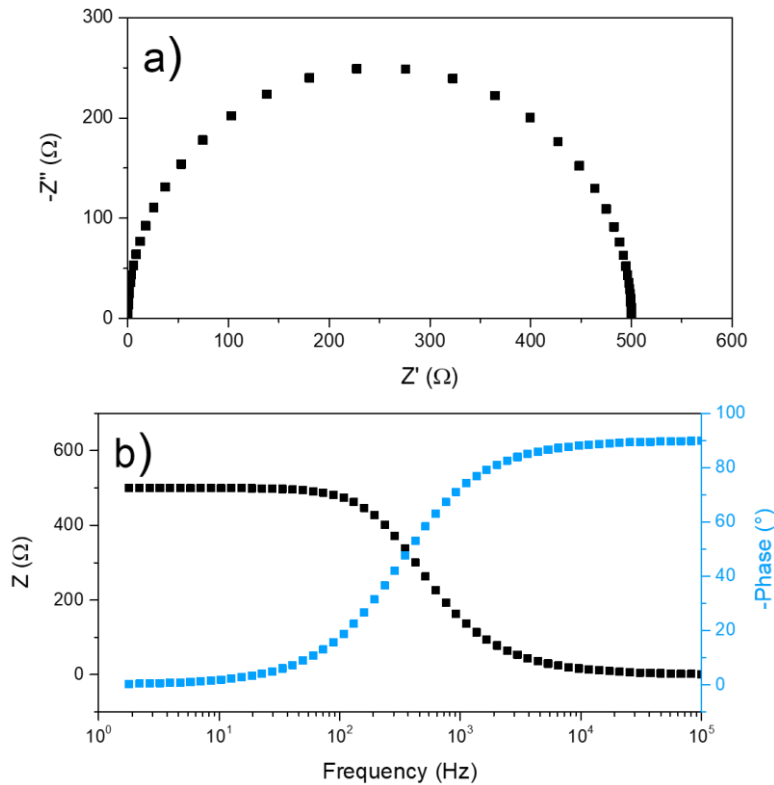


Figure III.2: Impedance representation, a) Nyquist plot ; b) Bode plot.

1.1.d. Exploitation the EIS data

In practice, the different semi-circles representing the electrochemical phenomena can be overlapped. To separate the various contributions, the most common method consists in fitting the spectra with an equivalent circuit using some single elements such as a resistor (R), a capacitor (C), an inductor (L) and a constant phase element (CPE). The CPE describes an imperfect capacitor and is defined by two parameters: Q and n. Q can be assimilated to the capacitance and n to the imperfect behavior. It results in a flatter semi-circle in the Nyquist plot, the degree of flatness is dependent on n value. Experimentally, the imperfect behavior of the CPE is due to the inhomogeneity of the system, for example, the surface roughness [225]. **Table III.1** gives the expression of the impedance of every single element mentioned above and an example of the Nyquist and Bode plot associated with it. A particular case of the CPE is when $n = 0.5$, this case is specific of diffusive processes that can be related to the release of the dissolved species [226]. This parameter describes the blocking ability of the passive layer and is called the Warburg element (W).

Fitting an EIS spectrum usually requires different single elements that can be connected in series or parallel. In the case of a connection in series, the overall impedance is equal to the sum of the impedance of each element (**Equation III.7**). In a parallel connection, the total admittance (the inverse of the impedance (noted Y), **Equation III.8**.) is the sum of each single admittance (**Equation III.9**).

$$Z(\omega) = \sum_{i=1}^n Z_i(\omega) \quad \text{Equation III.7}$$

$$Y(\omega) = \frac{1}{Z(\omega)} \quad \text{Equation III.8}$$

$$Y(\omega) = \sum_{i=1}^n Y_i(\omega) \quad \text{Equation III.9}$$

Then, in parallel, the total impedance is equal to the inverse of the sum of the inverse of the impedance of each element (**Equation III.10**).

$$Z(\omega) = \frac{1}{\sum_{i=1}^n \frac{1}{Z_i(\omega)}} \quad \text{Equation III.10}$$

Each semi-circle is fitted by a R and a C or a R and CPE in parallel if the system does not present an ideal capacitor. In this case a flat semi-circle will be obtained in the Nyquist plot. Then, by combining **Equation III.10** and the impedance of the single elements R, C and CPE depicted in **Table III.1**, the impedance of a contribution fitted by a R and C is given by **Equation III.11** and by fitting with a R and CPE in parallel, **Equation III.12** is obtained:

$$Z(\omega) = \frac{1}{\frac{1}{R} + i\omega C} \quad \text{Equation III.11}$$

$$Z(\omega) = \frac{1}{\frac{1}{R} + (i\omega)^n Q} \quad \text{Equation III.12}$$

The characteristic time of each electrochemical phenomenon is defined by the inverse of the frequency at the maximum of capacitance (i.e. the maximum of $-Z''$) and is calculated according to **Equation III.13** in the case of a R and a C in parallel and to **Equation III.14** in the case of R and CPE in parallel.

$$\tau = R \times C \quad \text{Equation III.13}$$

$$\tau = (R \times Q)^{1/n} \quad \text{Equation III.14}$$

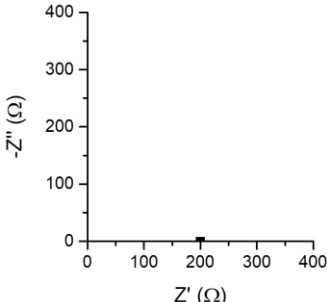
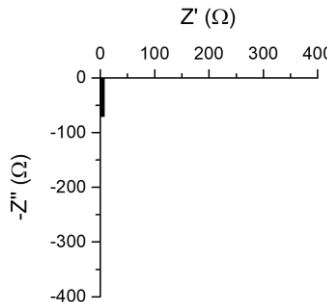
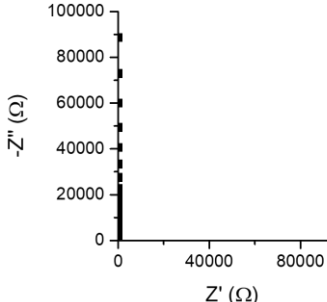
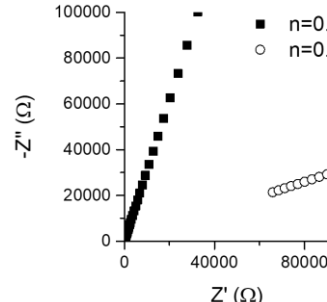
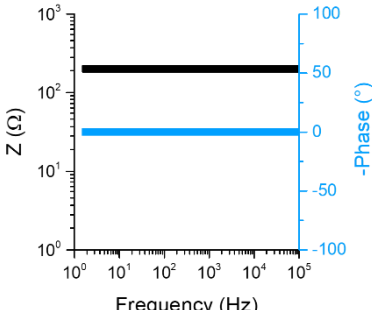
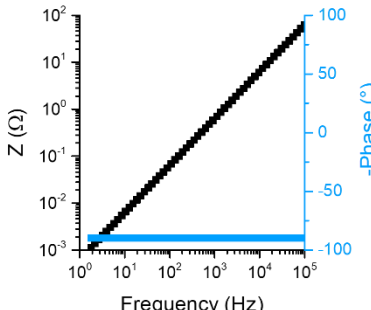
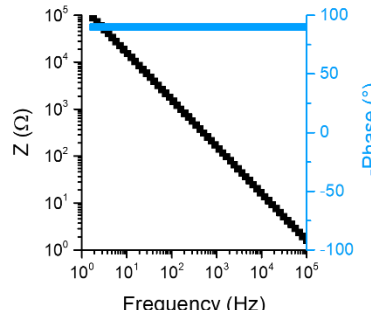
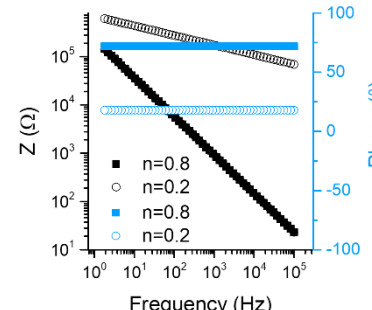
Element	R	C	L	CPE
Definition	$Z_R = R$	$Z_C = \frac{1}{iC\omega}$	$Z_L = i\omega L$	$Z_{CPE} = \frac{1}{Q(i\omega)^n}$ $Q = \frac{1}{ Z }$ at $\omega = 1 \text{ rad.s}^{-1}$ $0 \leq n \leq 1$ ($n = 1$ represent a pure capacitor) $Q = S.s^{-n}$
Value of the example	$R = 200 \Omega$	$C = 1 \mu\text{F}$	$L = 100 \mu\text{H}$	
Nyquist plot				
Bode plot				

Table III.1: Expression and example of R, C, L and CPE element

A complementary approach for analyzing EIS data is the Distribution of Relaxation Time (DRT). This method is a powerful tool to extract the characteristic time of the electrochemical processes involved in the studied system, even for significantly overlapped responses [227]. In DRT, the impedance is considered as an infinite number of (RC) elements (where R and C are in parallel) [228]. The impedance can then be written according to **Equation III.15**:

$$Z(\omega) = R_0 + R_p \int_0^{\infty} \frac{g(\tau)}{1+i\omega\tau} d\tau \quad \text{Equation III.15}$$

Where R_0 is the ohmic resistance of the system, R_p , the overall polarization resistance, $g(\tau)$ is the distribution function and τ is the RC element characteristic time. The mathematical treatment is applied to each EIS point and g is plotted as a function of the frequency as illustrated in **Figure III.3.b**. The relevance of the DRT is well evidenced in this example. Indeed, the four processes at high frequency (in grey) are highly overlapped and then not easily observable in the Nyquist plot raw data (represented by the black points) (**Figure III.3.a**), while in the DRT plot, they are well separated.

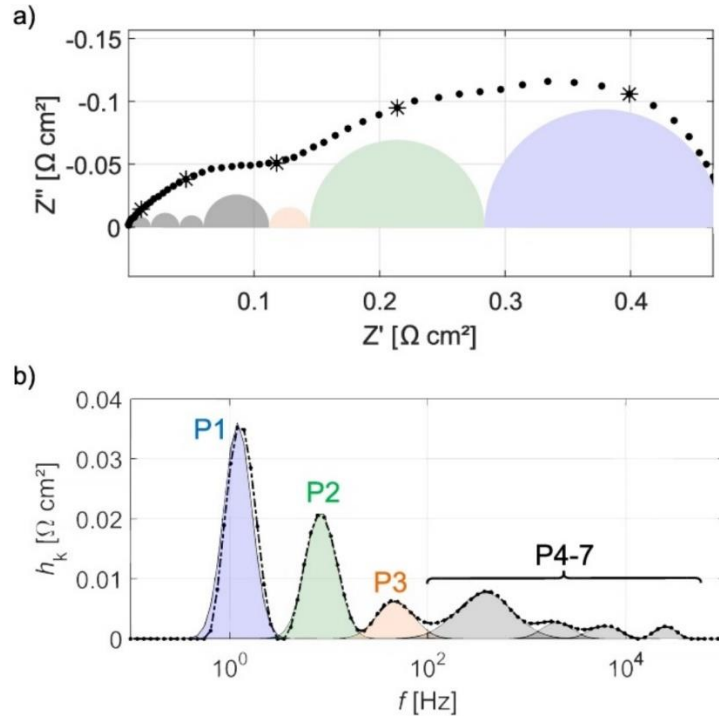


Figure III.3: a) Nyquist plot of PEMFC operating at 160 °C and b) the corresponding DRT plot [228]. (In this plot, g is noted h_k .)

I.2. Application in the PCFC area

To study and understand the behavior of the different constitutive materials of a cell, three kinds of samples are usually analyzed by EIS: the symmetrical cell, the half-cell and the complete cell.

The symmetrical cell consists in a pellet of a material of interest sandwiched between two electrodes (classically made of gold, platinum or silver). This type of experiment allows studying the conductivity (i.e. diffusion of charged species) of the material of interest.

The half-cell consists of three materials: the electrolyte material, one electrode material, and one noble metal (the electrolyte is sandwiched between the two conductive materials). This kind of experiment gives information concerning the electrolyte electrochemical behavior, the one of the electrode and the one of the interface between these two layers.

Lastly, the complete cell is composed of at least an anode, a cathode and an electrolyte. The EIS exploitation gives information about ohmic resistance, polarization, rate-limiting step, diffusion, and space charge layers at the interfaces.

Only the symmetrical and complete cells (presented in the next chapter) were prepared in this thesis work.

I.2.a. Defect chemistry and conduction properties in perovskite

In order to understand the diffusion of the charge carriers, and thus the conductivity, under EIS stimulation in symmetrical cell measurement, it is first necessary to focus on the chemistry of defects in perovskite protonic conductors.

As briefly exposed in the first chapter, depending on the atmosphere, different charge carriers are formed in a protonic conductor ceramic [19], [24]. The following model aims to express the concentration of each charge carrier as a function of the atmosphere, i.e., the partial pressure of O_2 (noted P_{O_2}) and the partial pressure of water vapor (noted P_{H_2O}). It has been developed by Bonanos and Poulsen in 1999 using H_i^\bullet as protonic defect [25]. It was revised by Bonanos in 2001 by replacing H_i^\bullet by OH_O^\bullet . The determined $[OH_O^\bullet]$ as a function of P_{H_2O} and P_{O_2} is the same as $[H_i^\bullet]$ [229]. Only the model describing H_i^\bullet , will be presented. In the following part, an example of the resolution of this model for a substitution rate of 0.1 will be given.

I.2.a.i. Model describing the concentration of defects as a function of the atmosphere

In a perovskite protonic conductor $AB_{1-x}M_xO_{3-x/2}$ (where A and B are cations of valence 2 and 4 respectively, and M is a cation of valence 3), three defect reaction (**Reactions III.1-3**), depending on the atmosphere, and their associated equilibrium have to be considered (**Equations III.16-18**). The generated defects are represented using the Kröger-Vink notation:

Substitutional cation: M_B'

Oxide ion vacancy: $V_O^{\bullet\bullet}$

Proton: H_i^\bullet or OH_O^\bullet

Electron hole: h^\bullet

Electron: e'

Lattice oxygen: O_O^\times

The protons formed by the dissociative adsorption of water vapor.



$$[H_i^{\bullet}]^2 = K_H P_{H_2O} [V_O^{\bullet\bullet}] [O_O^{\times}]^{-1} \quad \text{Equation III.16}$$

The electron holes are generated by the dissolution of oxygen.



$$[h^{\bullet}]^2 = K_h P_{O_2}^{\frac{1}{2}} [V_O^{\bullet\bullet}] [O_O^{\times}]^{-1} \quad \text{Equation III.17}$$

The production of electrons and loss of oxygen occurs at low partial pressure of O_2 .



$$[e']^2 = K_e P_{O_2}^{-\frac{1}{2}} [O_O^{\times}] [V_O^{\bullet\bullet}]^{-1} \quad \text{Equation III.18}$$

The respect of the electroneutrality condition is given in **Equation III.19**.

$$2[V_O^{\bullet\bullet}] + [H_i^{\bullet}] + [h^{\bullet}] - [e'] - [M_B'] = 0 \quad \text{Equation III.19}$$

The anion site conservation condition is described by **Equation III.20**.

$$[V_O^{\bullet\bullet}] + [O_O^{\times}] = 3 \quad \text{Equation III.20}$$

By replacing **Equation III.20** in **Equations III.16-18**, **Equations III.21-25** are obtained.

$$[H_i^{\bullet}] = K_H^{\frac{1}{2}} P_{H_2O}^{\frac{1}{2}} x \quad \text{Equation III.21}$$

$$[h^{\bullet}] = K_h^{\frac{1}{2}} P_{O_2}^{\frac{1}{4}} x \quad \text{Equation III.22}$$

$$[e'] = K_e^{\frac{1}{2}} P_{O_2}^{-\frac{1}{4}} x \quad \text{Equation III.23}$$

$$\text{With } x = \left(\frac{[V_O^{\bullet\bullet}]}{3 - [V_O^{\bullet\bullet}]} \right)^{\frac{1}{2}} \quad \text{Equation III.24}$$

$$\text{i.e. } [V_O^{\bullet\bullet}] = 3x^2 / (x^2 + 1) \quad \text{Equation III.25}$$

Inserting **Equations III.17-19** in the electroneutrality condition (**Equation III.19**) and rearranging gives **Equation III.26**.

$$\beta \cdot x^4 + (6 - [M_B'])x^3 + (\beta - \alpha)x^2 - [M_B']x - \alpha = 0 \quad \text{Equation III.26}$$

$$\text{In which } \alpha = K_e^{\frac{1}{2}} P_{O_2}^{-\frac{1}{4}} \quad \text{Equation III.27}$$

$$\text{And } \beta = K_H^{\frac{1}{2}} P_{H_2O} + K_h^{\frac{1}{2}} P_{O_2}^{\frac{1}{4}} \quad \text{Equation III.28}$$

The concentration of each defect (H_i^{\bullet} , h^{\bullet} , e' and $V_O^{\bullet\bullet}$) is calculating by solving **Equation III.22** and reintroduced x in **Equations III.21-23** and **III.25**.

1.2.a.ii. Example of the $AB_{0.9}M_{0.1}O_{2.95}$ system

The resolution of the concentration of each defect as a function of P_{O_2} and P_{H_2O} in the case of $[M_B'] = 0.1$ as calculated by Bonanos and Poulsen is presented in **Figure III.4** [25]. They used $K_H = 20 \text{ atm}^{-1}$, $K_h = 10^{-5} \text{ atm}^{-1/2}$ and $K_e = 10^{-17} \text{ atm}^{1/2}$ as thermodynamic parameters.

The concentration of oxygen vacancy $[V_O^{\bullet\bullet}]$ is maximum for low P_{H_2O} and low P_{O_2} (**Figure III.4.a**). $[H_i^{\bullet}]$ is maximum for high P_{H_2O} and low P_{O_2} (**Figure III.4.b**). $[h^{\bullet}]$ is maximum for intermediate to low P_{H_2O} (**Figure III.4.c**) and high P_{O_2} and $[e']$ is maximum for intermediate to high P_{H_2O} and low P_{O_2} (**Figure III.4.d**). Then, electrons and protons present a

maximum of concentration in the same atmosphere, $[e']_{max}$ is equal to 0.08 and $[H_i^\bullet]_{max}$ is equal to 0.25, thus, protons remain the dominant charge carrier in these conditions.

It should be noted that $[H_i^\bullet]$ presents a plateau at $\log(P_{H_2O}) > 0$ and for intermediate P_{O_2} corresponding to the intrinsic compensation of the charges ($[H_i^\bullet] = [M_B']$). The same observation can be done concerning the $[V_O^{\bullet\bullet}]$ in the intermediate domain of P_{O_2} and for low P_{H_2O} , in this case, the compensation of the charges is $[V_O^{\bullet\bullet}] = [M_B']/2$.

At very low P_{O_2} , $[V_O^{\bullet\bullet}]$ increases according to **Reaction III.3**, this rise is accompanied by an increase in the concentration of H_i^\bullet due to the dissociative adsorption of water vapor (Reaction III.1) on these new oxygen vacancies.

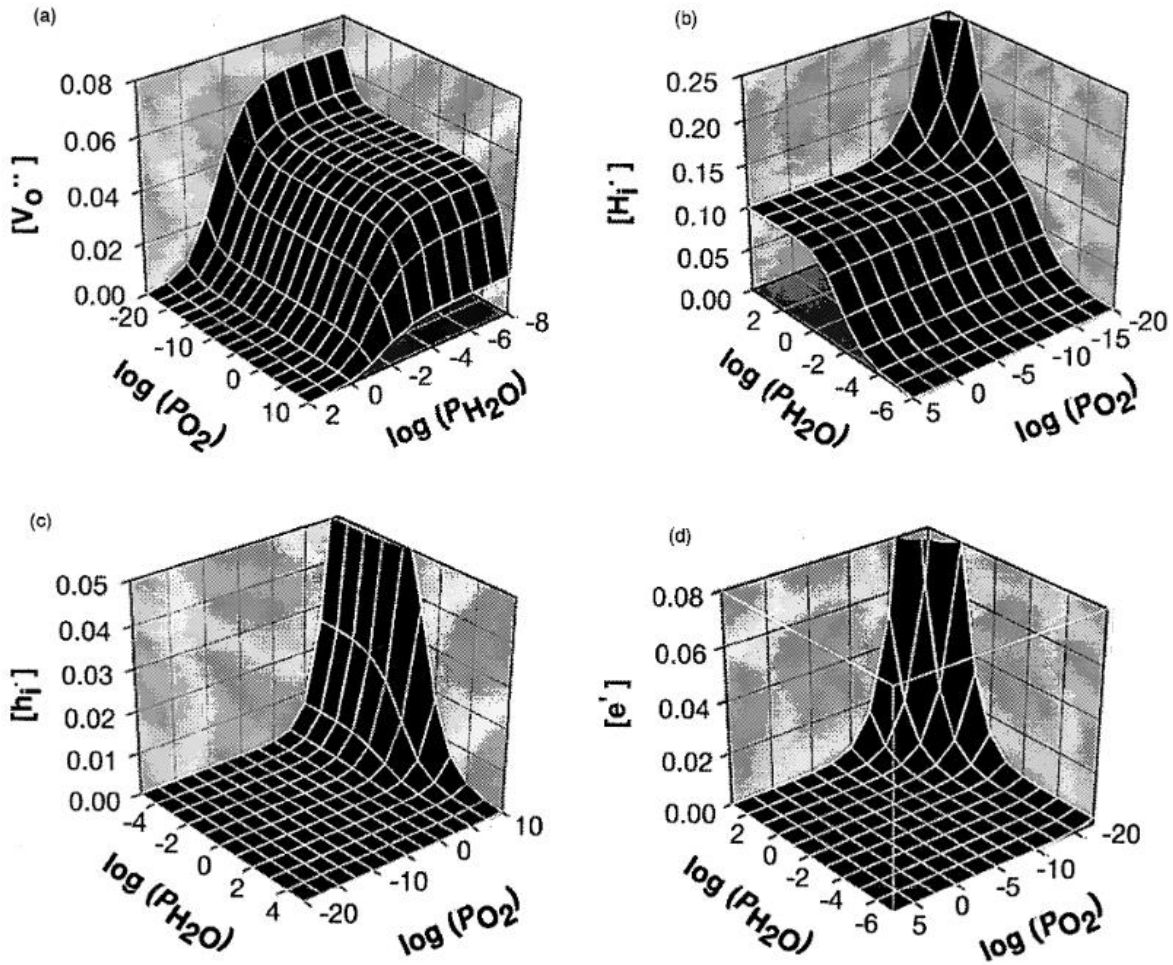


Figure III.4: Defect concentrations as a function of $\log(P_{O_2})$ and $\log(P_{H_2O})$ in the case of $[M_B'] = 0.1$. (a) oxide ion vacancies, (b) protons, (c) holes and (d) electrons. Partial pressures are in atm [25].

Even this example presents the concentration of the charge carriers inputted by a substitution rate of 0.1, it can reasonably be supposed that the general behavior, i.e., the maximum concentration in certain P_{O_2} and P_{H_2O} conditions, is the same for $[M_B'] = 0.2$.

1.2.b. Definition and measurement of the conductivity

Definition

The conductivity (σ), the inverse of the resistivity (ρ), describes the ability of a material to conduct charged species in response to an electric field [230]. It is defined for a considered section (S) and length (L) according to **Equation III.29**.

$$\sigma = \frac{1}{\rho} = \frac{1}{R} \times \frac{L}{S} \quad \text{Equation III.29}$$

Where R is the overall resistance of the material.

Measurement

The conventional method to determine the conductivity is called the four probes measurement. It consists in measuring the potential and the current of a sample of known dimension under an electric field, according to **Equation III.30**. Two wires measure the current and two wires the potential in order to overcome the external resistance and measure only the overall resistance of the material [231]. As presented at the beginning of this chapter, EIS also allows determining the resistance of a sample. Then, by knowing the dimensions, the conductivity is calculated according to **Equation III.29** [231]–[235]. In the case of an EIS measurement, the conductivity is named σ_{AC} (AC = alternative current) and in the case of a four probe measurement, conductivity is noted σ_{DC} (DC = direct current).

$$R = \frac{U}{I} \quad \text{Equation III.30}$$

Conductivity, concentration and mobility of the charged species

The conductivity is also dependent on the mobility of the charge i (μ_i), the effective value of the charge i (q_i) and the number of the charge i (n_i) as shown in **Equation III.31** [236]. Then, the concentration of the defects highlighted in the previous paragraph is a crucial conductivity parameter since it represents the number of species.

$$\sigma = \sum_{i=0}^n \mu_i \times q_i \times n_i \quad \text{Equation III.31}$$

Finally, the conductivity is also equal to the sum of the conductivity of each charged species according to **Equation III.32**.

$$\sigma = \sum_{i=0}^n \sigma_i \quad \text{Equation III.32}$$

In the case of a perovskite protonic conductor, the total conductivity is written as (**Equation III.33**):

$$\sigma = \sigma_i + \sigma_{h\cdot} + \sigma_{e'} \quad \text{Equation III.33}$$

Where σ_i is the ionic conductivity, i.e., the sum of the protonic and the oxygen-ion conductivity.

Conductivity and P_{O_2} dependency

By plotting $\log \sigma$ as a function of $\log P_{O_2}$, a characteristic curve schematically represented in **Figure III.5** is obtained. As it can be seen, the P_{O_2} dependency of the

concentration of defect highlighted in **Equations III.21-23** and **III.25** is also found in the conductivity:

- σ_i does not depend on P_{O_2}
- $\log \sigma_h \propto \log P_{O_2}^{1/4}$
- $\log \sigma_e \propto \log P_{O_2}^{-1/4}$

Equation III.33 can then be rewrite taking into account the partial pressure of oxygen [229], [237]:

$$\sigma = \sigma_i + \sigma_{h^{\circ}} \times P_{O_2}^{1/4} + \sigma_{e^{\circ}} \times P_{O_2}^{-1/4} \quad \text{Equation III.34}$$

Where $\sigma_{h^{\circ}}$ is the conduction of electron holes at $P = 1$ atm and $\sigma_{e^{\circ}}$ is the conductivity of the electrons at $P = 1$ atm.

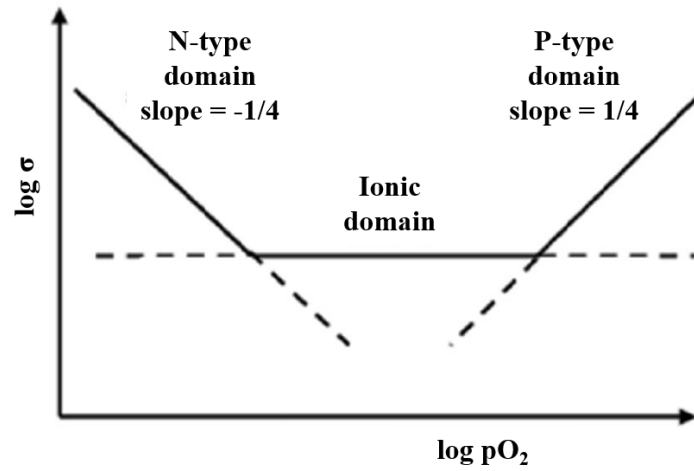


Figure III.5: Schematic representation of $\log \sigma$ as a function of $\log P_{O_2}$ for a protonic conductive ceramic (adapted from [238]).

Competition between protonic and oxygen-ion conductivity

Due to the presence of oxygen vacancies, doped cerate and zirconate perovskite exhibit both protonic and oxygen-ion conduction [19], [237], [239]–[241]. Both protonic and oxygen-ion conductivity follow an Arrhenius behavior, that is to say, they are terminally activated. To be more precise, it is mainly the mobility of the charged species that are affected by this Arrhenius behavior [19], [242, p. 1], [243]. It results in competitiveness between protonic and oxygen-ion conductivity. Due to lower activation energy, protons are much more mobile than oxygen ions at low temperatures. Thus, as exhibited in **Figure III.6**, the protonic conductivity is higher than the oxygen-ion conductivity in the low-intermediate temperature domain. The protonic conductivity presents a maximum before decreasing and the oxygen-ion conductivity becomes predominant. The drop of protonic conductivity is explained by the decrease in proton concentration involved by dehydration [237].

In order to separate the protonic and the oxygen-ion conductivity, the standard method is to calculate the transport number (also called transference number or electromotive force (EMF) method) of a species [235], [244]. It consists in placing a symmetrical cell in an

asymmetric atmosphere chamber for example using a Norecs Probostat set-up illustrated in **Figure III.14**. The atmosphere of one of the electrodes (atmosphere I) is different from the atmosphere of the other electrode (atmosphere II) and the EMF, noted E, is measured and compared to the theoretical EMF, note E_0 , as expressed by **Equation III.31**.

$$t = E/E_0 \quad \text{Equation III.35}$$

For proton, E_0 is given by [235]:

$$E_0 = \frac{RT}{2F} \ln \frac{P_{H_2O(I)}}{P_{H_2O(II)}} \quad \text{Equation III.36}$$

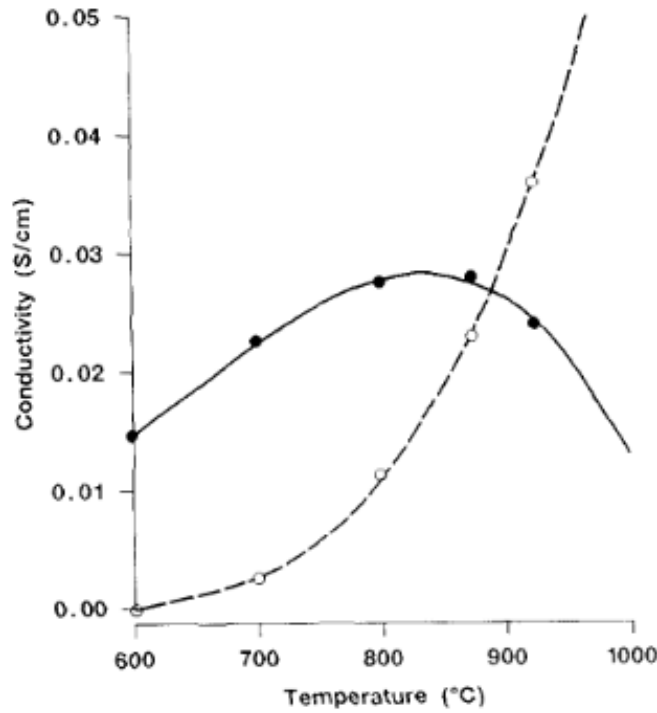


Figure III.6: Ionic conductivity of $BaCe_{0.9}Gd_{0.1}O_{3-\delta}$, protonic is shown by the solid symbol, oxygen-ion by the open symbol [237]. The conductivity of each species was calculated thanks to the transport number of oxygen.

The interest of using EIS to determine the conductivity

It has been presented in the first chapter (paragraph III.3.b) that the total conductivity value shows large discrepancies as it is highly dependent on the microstructure, especially for BZY. Indeed, BZY exhibits a total conductivity value between 10^{-6} to 10^{-2} S.cm⁻¹ at 600°C in wet H₂ [70]. This is explained by the grain boundary being much more resistive than the grain bulk [62], [64], [68], [245]–[247]. Since the diffusion of charge species exhibits different characteristic times in the bulk and in the grain boundary, it is possible to separate these two contributions by EIS and then calculate the conductivity inside the grain and across the grain boundary separately.

I.3. Summary

EIS is a powerful technique that allows to obtain the response of any polarizable layer of a sample. The obtained signal is usually fitted with an equivalent circuit in which each component's resistance can be extracted. By knowing the resistance, σ_{AC} is obtained. EIS permits to determine the conductivity associated with the diffusion of charged species in the bulk of the electrolyte and the conductivity related to the diffusion in the grain boundary.

This conductivity does not represent only the protonic conductivity. Indeed, in $AB_{1-x}M_xO_{3-x/2}$ material, the different charge carriers are the protons, the oxygen ions, the electron-holes and the electrode. The conductivity calculated from the resistance determined by EIS is the sum of conductivity of each charged species. To obtain the conductivity of each charged species, its transport number should be determined.

However, the concentration of each charged carrier is dependent on the atmosphere as highlighted by Bonanos and Poulsen [25]. For example, the concentration of proton is dominant in wet air and wet H_2 at low temperature. Especially in wet H_2 , protons are almost the only charged species, thus the total conductivity determined by EIS can be assimilated to the protonic conductivity of the material.

Finally, the temperature has to be taken into account. Indeed, the protonic conductivity is dominant at low temperatures, while high temperatures favor the formation of oxygen vacancies and the oxygen-ion conduction [19], [237]. Furthermore, the temperature dependence of the conductivity is different for each charge carrier, for example, the activation energy (E_a) for the proton diffusion in doped-perovskite in the range of 0.4 – 0.6 eV [61], [248], [249].

II. Sintering of BZY and preparation of the symmetrical cells

This section presents, in the first part, the study of the densification of the BZY oxide and the strategy used in this work to improve its sinterability. In the second part, the preparation of the symmetrical cell is exposed. Three samples were prepared, one based on BZY-c 1000 °C powder (the initial quantity of the precursor is the stoichiometric ratio), one elaborated from BZY-b 1000 °C and the last one from a commercial BZY powder noted BZY-com. The structure and the microstructure of the electrolyte in the sample are exposed.

II.1. Sinterability

It has been seen in the first chapter that BZY has a highly refractory nature that leads to poor sinterability [38], [43], [58]. To avoid the use of high sintering temperature (1700 °C) and long sintering time that could involve Ba vaporization and Y_2O_3 exsolution, the addition of 1 %wt of ZnO as sintering aid was studied. The densification behavior of the BZY powders was investigated by dilatometry (NETZSCH DIL 402 PC) in air atmosphere from the ambient

temperature to 1550 °C with a ramp of 3 °C.min⁻¹. A dwell time of one hour at 1550 °C was carried out before the cooling at 3 °C.min⁻¹. The data were analyzed by NETZSCH Proteus Thermal Analysis. The expansion/contraction of the alumina sample holder was collected (blank run) and subtracted from the data.

Samples consist of pellets of 8 mm in diameter elaborated by uniaxial pressing under a pressure of 200 MPa. The samples containing 1 wt% of ZnO are prepared by mixing the BZY powder and the ZnO powder in ethanol media in an agate mortar prior to the shaping. The ZnO powder was produced by the continuous hydrothermal synthesis during the thesis work of Romain Piolet [153]. It consists of pure ZnO with spherical grains of 50 nm in diameter.

II.1.a. Dilatometry of BZY-c powder

Three pellets were prepared with the BZY-c powder: only BZY-c, BZY-c mixed with 1 wt% of ZnO and BZY-c annealed at 1000 °C for 1 hour mixed with 1 wt% of ZnO. **Figure III.7.a** exposes the dilatometry profile of these three samples, the shrinkage speed is presented in **Figure III.7.b**. The raw powder starts to shrink at about 1250 °C, the maximum shrinkage speed was not reached at 1550 °C. This result is in perfect agreement with the work of Fabbri *et al.* [250]. The addition of 1 wt% of ZnO allows reducing the temperature of the starting shrinkage of 200 °C for BZY-c and 300 °C for the BZY-c annealed at 1000 °C. It is reported that ZnO enhance the sinterability through the formation of an eutectic that increases ion diffusion in the solid–liquid heterophase system [63], [251].

The two dilatometry curves exhibit the same shape and present a similar temperature of maximum shrinkage speed: 1350 °C for the annealed BZY-c with 1 wt% ZnO and 1320 °C for the BZY-c c with 1 wt% ZnO. The associated maximum shrinkage speeds are -0.0030 and -0.0025 %·K⁻¹ respectively. The reduced shrinkage rate during the dwell time at 1550 °C (1.6 %) of the two samples mixed with ZnO indicates that the maximum of densification was almost reached.

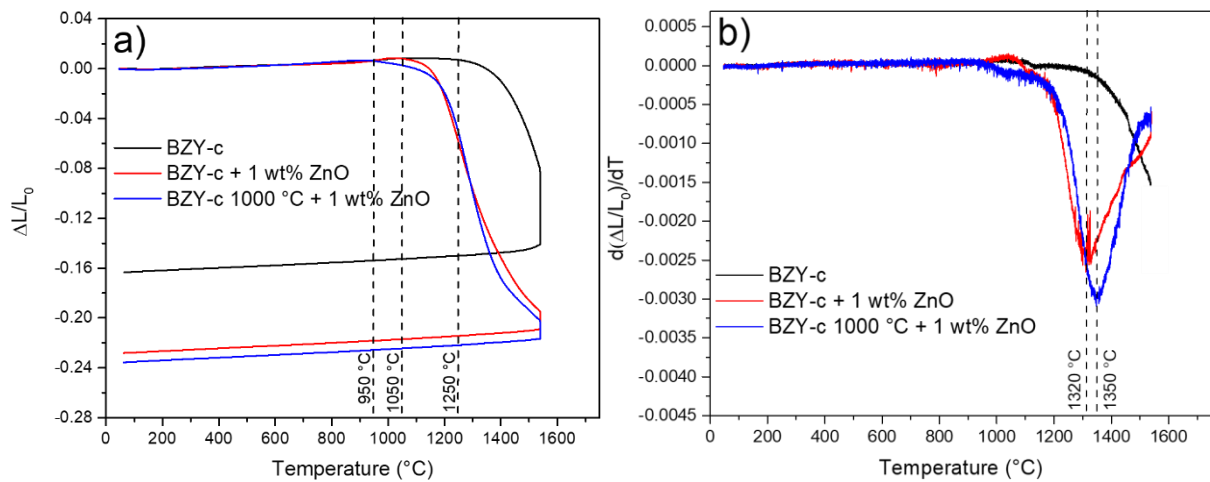


Figure III.7: Dilatometry profile of BZY-c, BZY-c mixed with 1 wt% of ZnO and BZY-c annealed at 1000 °C for 1 hour mixed with 1 wt% of ZnO. a) $\Delta L/L_0$ as a function of the temperature; b) $d(\Delta L/L_0)/dT$ as a function of the temperature

II.1.b. Dilatometry of BZY-b powder

The same procedure was applied to the BZY-b powder. **Figure III.8.a** exhibits the dilatometry profile of the samples and **Figure III.8.b** the associated shrinkage speed. As for BZY-c, the pellet containing raw powder starts to shrink at about 1250 °C and the maximum shrinkage speed is not reached at 1550 °C. The addition of 1 wt % of ZnO decreases the temperature of starting sintering up to 1070 °C for BZY-b annealed at 1000 °C and up to 1100 °C for BZY-b. In parallel, the temperature of maximum shrinkage rate is significantly reduced: 1320 °C for BZY-b and 1360 °C for BZY-b annealed at 1000 °C. Concerning the BZY-b sample with 1 wt% of ZnO, the peak corresponding to maximum shrinkage speed is split into a doublet. The second peak is situated at 1440 °C. As it will be shown in the next section, this behavior indicates the sintering of another phase.

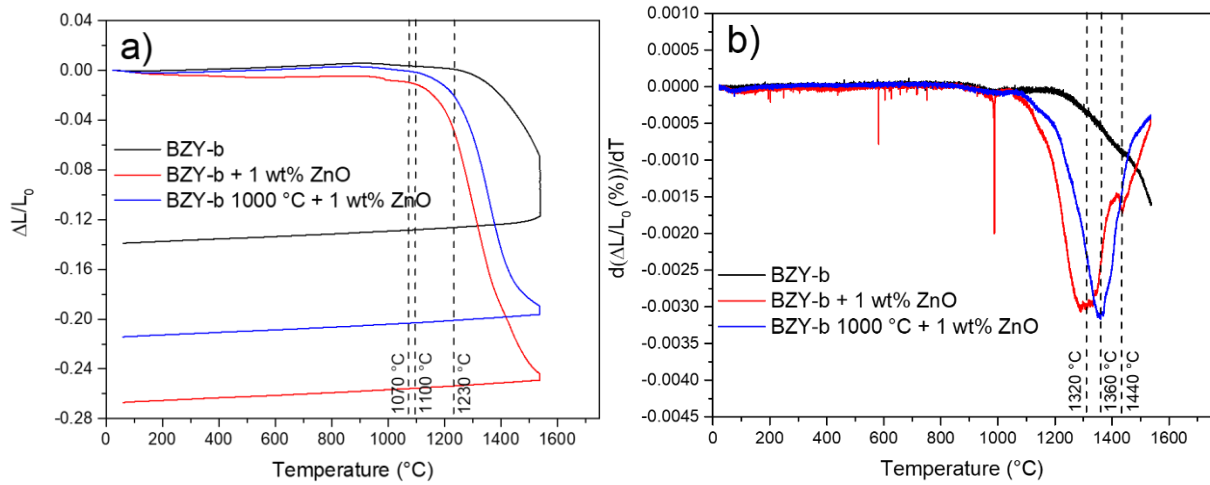


Figure III.8: Dilatometry profile of BZY-b, BZY-b mixed with 1 wt% of ZnO and BZY-b annealed at 1000 °C for 1 hour mixed with 1 wt% of ZnO. a) $\Delta L/L_0$ as a function of the temperature; b) $d(\Delta L/L_0)/dT$ as a function of the temperature

II.2. Determination of the sintering conditions

To determine the sintering conditions, pellets of 8 mm in diameter were shaped by uniaxial pressing at 200 MPa. The influence of the quantity of ZnO was examined by mixing BZY with 1, 2 or 3 wt% of ZnO. The sintering temperature was studied between 1500 °C and 1600 °C. The thermal treatment was applied as follows: a heating ramp of 3 °C.min⁻¹ up to the sintering temperature, a dwell time of 5 hours and a cooling ramp of 3 °C.min⁻¹. **Figure III.9** shows the densification rate as a function of the quantity of ZnO at different sintering temperatures, the study was conducted on the BZY-com powder. The densification rate was calculated by dividing the experimental density by the theoretical density. The experimental density was determined by measuring the weight and the dimensions of the sintered pellet and the theoretical density was calculated according to **Equation III.37** and is 6.11 g.cm⁻³.

$$\rho_{theo} = \frac{Z \times M}{N_A \times a^3} \quad \text{Equation III.37}$$

Where Z is the multiplicity of BZY (equal to 1), M the molecular mass of BZY (equal to 274.49 g.mol⁻¹ for Ba_{1.0}Zr_{0.8}Y_{0.2}O_{2.9}), N_A the Avogadro number and a the lattice parameter (equal to 4.210 Å for sintered BZY).

Densification rates below 60 % were obtained for a sintering temperature of 1500 °C, indicating that this temperature is insufficient. Similar densification rates (approximately 90 %) were achieved at 1550 °C and 1600 °C, however, it is better to prioritize/privilege a temperature of 1550 °C in order to prevent the risk of Ba vaporization [73]. Using 1 or 2 wt% of ZnO leads to a comparable densification rate while 3 wt% of sintering aid decreases densification.

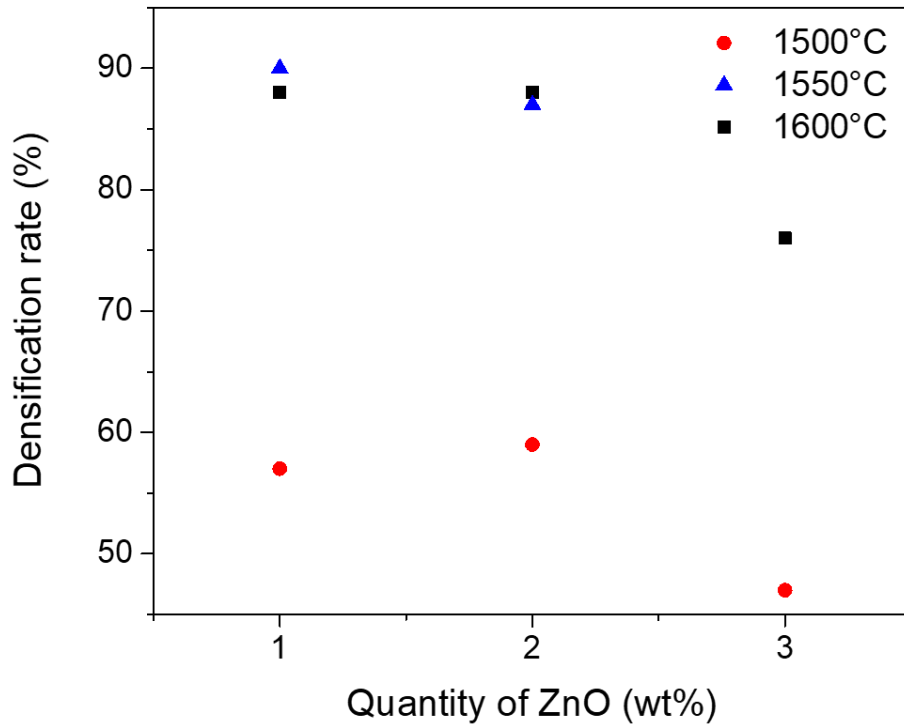


Figure III.9: Densification rate of BZY-com as a function of the quantity of ZnO at different sintering temperature. The sintering time was set to 5 hours.

Similar results were obtained for pellets elaborated with BZY-b and BZY-c powders annealed at 1000 °C. However, the pellets sintered without the annealing treatment present surprisingly low densification rates. For example, BZY-c powder mixed with 1 wt% of ZnO sintered at 1550 °C for 5 hours exhibits a densification rate of only 53 %. As presented in **Figure III.10**, which displays the microstructure of this sintered pellet, a segregation of phases occurred. The SEM (Phenom Pro-X coupled with Bruker EDS detector) used in Back Scattered Electron (BSE) mode highlights the presence of two phases. The white, with spherical morphology, corresponds to BZY, the composition was evaluated by EDS and is Ba_{0.71}Zr_{0.74}Y_{0.26}O_{3-δ}, and the grey, showing a rod morphology, corresponds to Zr-doped yttria presenting the composition Y_{1.82}Zr_{0.18}O_{3+δ}. In agreement with the work of Magrez et al., the

sintering of a Ba-deficient BZY powder promotes the vaporization of this element, giving rise to a segregation of the phases [252].

Then, the double peak highlighted in the shrinkage speed (**Figure III.8.b**) corresponds to the sintering of the BZY phase of one hand and the sintering of Zr-doped Y_2O_3 on the other hand. The melting point of barium zirconate is $2705\text{ }^\circ\text{C}$ [253] and the one of Y_2O_3 is $2410\text{ }^\circ\text{C}$ [254], however, the effect of Zr substitution in Y_2O_3 is unknown. Furthermore, the addition of ZnO decreases the melting point of BZY since it creates an eutectic. Due to these considerations and to the great part of the unknown resulting from it, the assignment of the sintering temperatures to the two phases was not made.

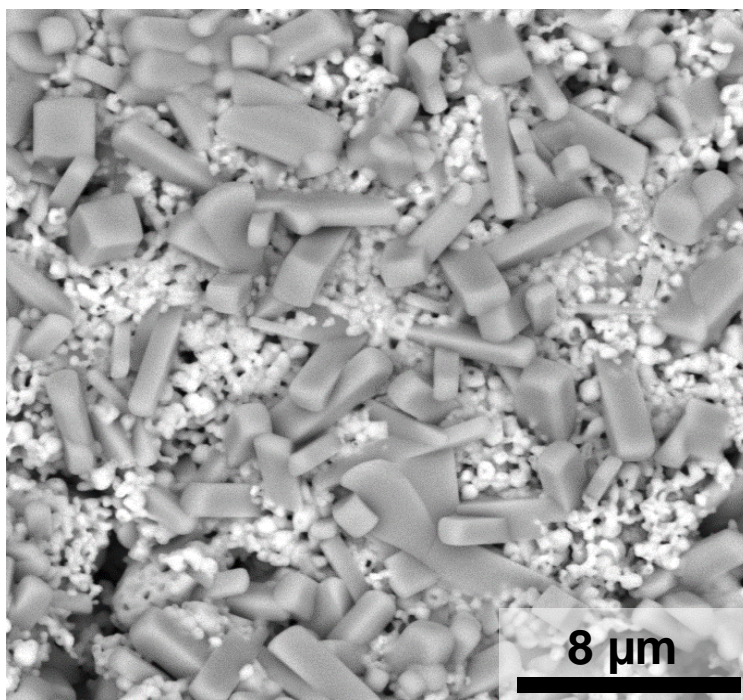


Figure III.10: SEM-micrograph of the BZY-c raw powder mixed with 1 wt% of ZnO sintered at $1550\text{ }^\circ\text{C}$ for 5 hours.

A sintering time of 1, 5 or 24 hours was also examined. As expected, the densification rate increases between 1 and 5 hours and then drops at 24 hours due to the Ba vaporization that leads to the segregation of phases. Thus, the optimal sintering conditions are $1550\text{ }^\circ\text{C}$ for 5 hours and the use of 1 wt% ZnO.

II.3. Preparation of the symmetrical cells

II.3.a. Electrolyte part

Three pellets of 28 mm in diameter were elaborated by uniaxial pressing. The starting powders were BZY-com, BZY-c 1000 °C and BZY-b 1000 °C. They were mixed with 1 wt% ZnO in ethanol media in an agate mortar. After 2 hours of drying, the powders were mixed with Arabic gum as a binder and pressed under a pressure of 200 MPa. The three pellets were then sintered according to the following procedure: a first ramp at 2 °C.min⁻¹ up to 400 °C, a dwell time of 1 hour at 400 °C to eliminate the Arabic gum, a ramp at 3 °C.min⁻¹ up to 1550 °C followed by a dwell time of 5 hours at this temperature and a cooling ramp at 3 °C.min⁻¹.

II.3.a.i. Structural characterization

The as-sintered pellets were analyzed by XRD. **Figure III.11** exposes the obtained diffractograms. Two phases were detected in each pellet, one major cubic perovskite corresponding to BZY and one secondary phase consisting of Zr-doped Y₂O₃. By comparing the intensity of the peaks of the different phases, a small amount of Zr-doped Y₂O₃ is detected in the BZY-com sintered pellet, a little more is present in the BZY-c 1000 °C pellet and the Zr-doped Y₂O₃ peaks are highly intense in the BZY-b 1000 °C pellet.

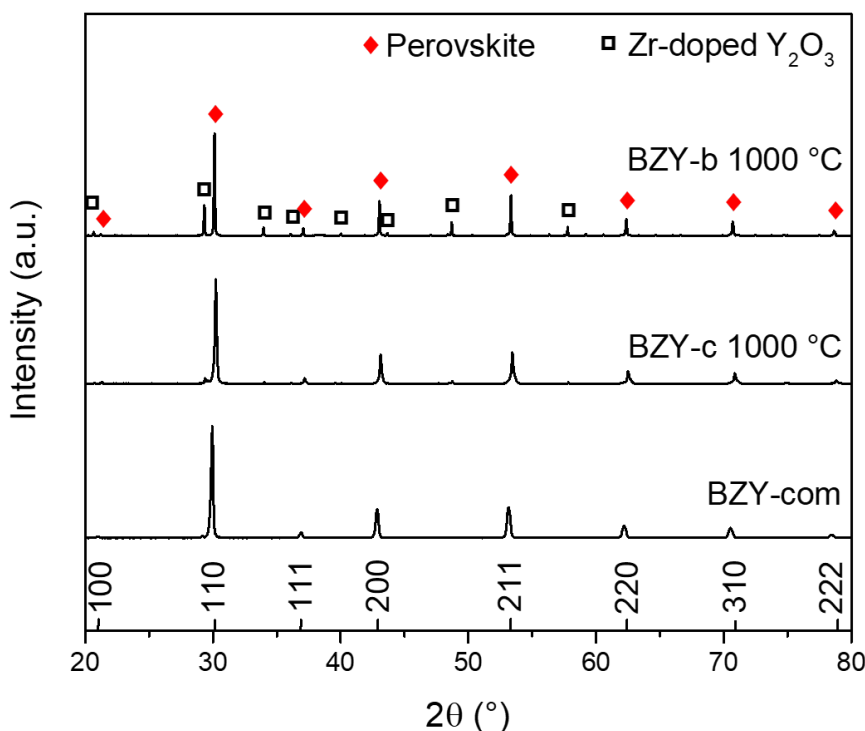


Figure III.11: XRD pattern of the BZY-b 1000 °C, BZY-c 1000 °C and BZY-com after sintering at 1550 °C for 5 hour. Each powder was mixed with 1 %wt of ZnO prior to the shaping.

Each XRD pattern was analyzed by the Rietveld method, the refined lattice parameter and the percentage of each phase are shown in Table III.2. Lattice parameters are close to each other and have increased in comparison with the raw powders. This observation is perfectly in line with the general behavior highlighted in Table II.2 in the second chapter, i.e., the lattice parameter of BZY tends to increase with increasing temperature. As suggested by the intensity of the peaks, a small quantity of Zr-doped Y_2O_3 was found in the BZY-c 1000 °C and BZY-com sintered pellets, indicating very low reactivity (the wt% of Zr-doped Y_2O_3 in BZY-c 1000 °C corresponds to the quantity highlighted after the annealing thermal treatment). In contrast, about one-third of Zr-doped Y_2O_3 was found in the BZY-b 1000 °C pellet, suggesting that the crystal structure of BZY-b is less stable, i.e., more sensitive to Ba-vaporization, than the others.

Sample name	Lattice parameter (Å)	Wt% of BZY	Wt% of Zr-doped Y_2O_3
BZY-c 1000 °C	4.209(4)	96.1	3.0
BZY-b 1000 °C	4.209(8)	68.9	31.1
BZY-com	4.210(0)	99.1	0.9

Table III.2: Refined lattice parameter of the BZY phase and refined phase percentage of the BZY-c, BZY-b and BZY-com pellets.

II.3.a.ii. Microstructural characterization

The density of the three sintered samples was evaluated using the Archimedes' principle buoyant force method in air and water at 20 °C. The results and the calculated densification rate are given in **Table III.3**. The densification rates are perfectly in line with those obtained during the optimization of the sintering conditions.

Sample	ρ_{exp} (g.cm ⁻³)	Densification rate (%)
BZY-c	5.5(0)	90
BZY-b	5.4(7)	90
BZY-com	5.7(6)	94

Table III.3: Densification rate of the BZY-c, BZY-b and BZY-com sintered pellets obtained by Archimedean buoyant force.

The microstructure of each pellet was investigated by SEM. **Figure III.12.a, b and c** expose the microstructure of BZY-com, BZY-c and BZY-b, respectively.

BZY-com exhibits large of 1.91 ± 0.64 μm and shaped grains. In agreement with the densification rate, the grains have highly coalesced and few porosities are highlighted.

As expected thanks to the density measurement, BZY-c exhibits some porosity. The grain size is relatively small (410 ± 130 nm), so the total conductivity may be lower than the one of BZY-com. No chemical reactivity was evidenced.

BZY-b sintered pellet exhibits two kinds of microstructures. The round-shaped grains correspond to BZY, while the faceted grains consist of Zr-doped Y_2O_3 . The composition determined by SEM-EDS is $\text{Y}_{1.72}\text{Zr}_{0.28}\text{O}_{3+\delta}$. The size of the BZY grain is larger than BZY-c and is 960 ± 310 nm, but the presence of disseminated Zr-doped Y_2O_3 grains may disturb the diffusion pathway of the charged species. Indeed, Y_2O_3 is highly dielectric, its total conductivity is 3.2×10^{-6} in wet H_2 at 1100 °C [255], which may hinder the diffusion of charged species and lead to a decrease in total conductivity.

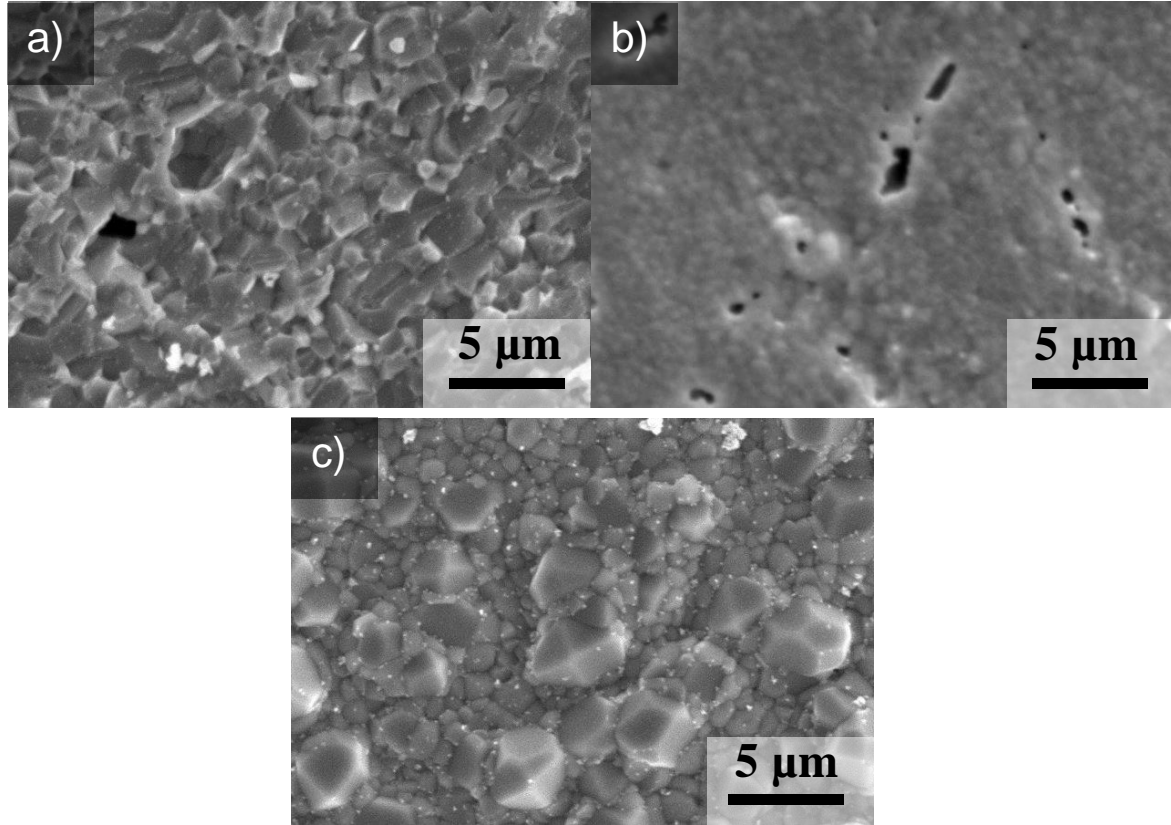


Figure III.12: SEM micrograph of a) BZY-com sintered pellet (cross-section), b) BZY-c 1000 °C sintered pellet (surface) and c) BZY-b 1000 °C sintered pellet (surface).

II.3.a.iii. Bulk chemistry characterization

The composition was evaluated by SEM-EDS on 20 grains for each sample. The A-site/B-site ratio and $\text{Y}/(\text{Zr}+\text{Y})$ ratio are presented respectively in **Figure III.13.a** and **b**. BZY-com A-site/B-site varies from 0.95 to 1.03 with an average value at 1.01 ± 0.2 . The distribution of its $\text{Y}/(\text{Zr}+\text{Y})$ ratio is very narrow (from 0.20 to 0.24 with an average value at 0.21 ± 0.01). BZY-c exhibits value from 0.89 to 1.03 for A-site/B-site ratio and between 0.09 and 0.28 for $\text{Y}/(\text{Zr}+\text{Y})$ ratio. The average values are 0.97 ± 0.04 and 0.14 ± 0.05 respectively. The A-site/B-site ratio of BZY-b is in the range 0.85-1.02 with an average at 0.96 ± 0.05 , its $\text{Y}/(\text{Zr}+\text{Y})$ ratio is in the 0.13-0.31 range with an average at 0.18 ± 0.03 . Then the final compositions can be written as $\text{Ba}_{1.01}\text{Zr}_{0.79}\text{Y}_{0.21}\text{O}_{3-\delta}$ for BZY-com, $\text{Ba}_{0.97}\text{Zr}_{0.86}\text{Y}_{0.14}\text{O}_{3-\delta}$ for BZY-c 1000 °C and $\text{Ba}_{0.96}\text{Zr}_{0.82}\text{Y}_{0.18}\text{O}_{3-\delta}$ for BZY-b 1000 °C.

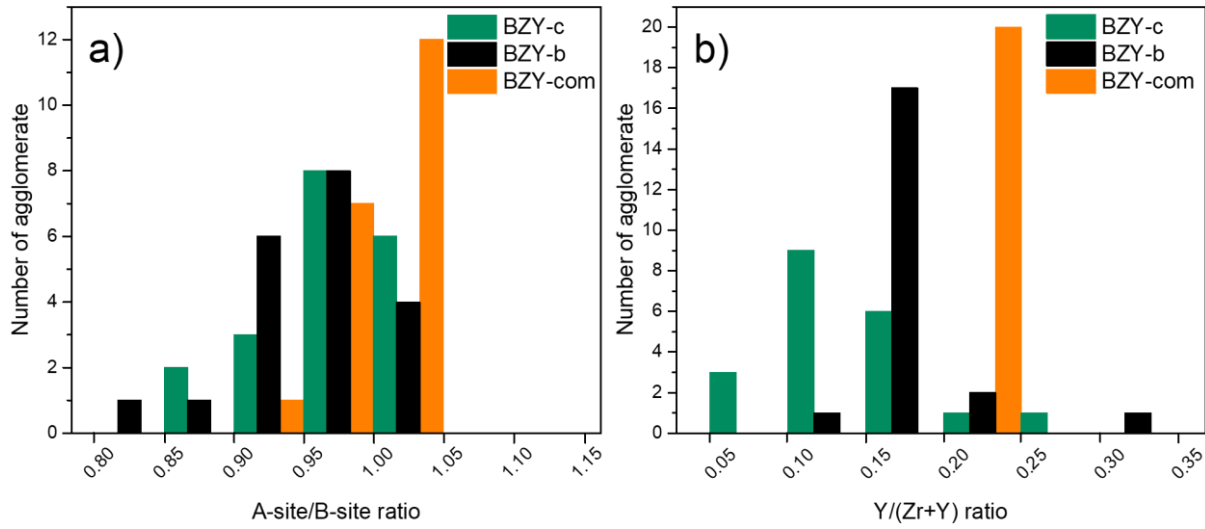


Figure III.13: SEM-EDS measurements of the sintered BZY-b 1000 °C, BZY-c 1000 °C and BZY-com sintered pellets. a) A-site/B-site ratio and b) Y/(Y+Zr) ratio.

II.2.b. Electrode part

To ensure electrical contact and input EIS stimulation to the electrolyte, it is necessary to deposit a conductive material on either side of the pellet. Silver was chosen as the electrode material due to its high electrical conductivity and its non-reactivity with BZY.

Silver paste (L-200N purchased from CDS électronique) was painted through a mask on each side of the BZY pellets and then fired at 800 °C for 2 hours to enhance the adhesion between the electrodes and the pellet. The final diameter of electrodes was 8.0 mm. The thickness of the BZY pellets are 1.8 mm for BZY-com and 1.6 mm for BZY-c 1000 °C and BZY-b 1000°C.

III. Study of the conductivity of BZY

The three symmetrical cells presented in the previous section were studied by electrochemical impedance spectroscopy in a large range of temperature (from 200 to 700 °C) in wet air and wet H₂ in order to study their conductivity. In the first part, the experimental set-up is described, then a selection of EIS spectra is presented for each sample and finally the evolution of the conductivity with the temperature is given and discussed.

III.1. Experimental set-up

Each symmetrical cell was tested in a Norecs Probostat system as depicted in **Figure III.14**. The cell is maintained between an alumina tube and a compression system in alumina loaded by springs. Two Pt meshes on either side of the cell allow to input the potential and to

collect the current. The same atmosphere is sent in the tubes on both sides of the cell. A thermocouple provides the temperature close to the cell.

Impedance measurements were carried out using a Metrohm Autolab PGSTAT302N potentiostat. The investigations were conducted from 200 °C to 700 °C with steps of 25 °C in a symmetrical atmosphere. The purpose was to study the protonic conductivity, then according to the first section of this chapter, the investigations were conducted in wet H₂ and wet air. Moisture was added by bubbling the flow of dry gas at 1 bar through an ebullition water balloon. The refrigerant column was maintained at 25 °C to set the relative humidity percentage at 3 % [256]. The flow of dry gas was maintained to 60 mL.min⁻¹. A stabilization time of at least 30 min was performed at each temperature before performing the measurement. The amplitude of the applied voltage was set to 10 mV. Each spectrum was recorded a second time 15 minutes after to verify the stabilization of the sample and the linearity of the response. The range of frequency was set from 10⁶ Hz to 10⁻² Hz in most of the case, if the signal was too noisy at low frequency, the range of frequency was adapted.

The data were fitted by the equivalent circuit method using Metrohm Nova 2.1 software. The experimental data couldn't be fitted with ideal capacitors but with constant phase elements. Then, the characteristic time constants are calculated with **Equation III.14**, it also corresponds to the inverse of the frequency at the maximum of $-Z''$ for each contribution (noted ω''_{max}).

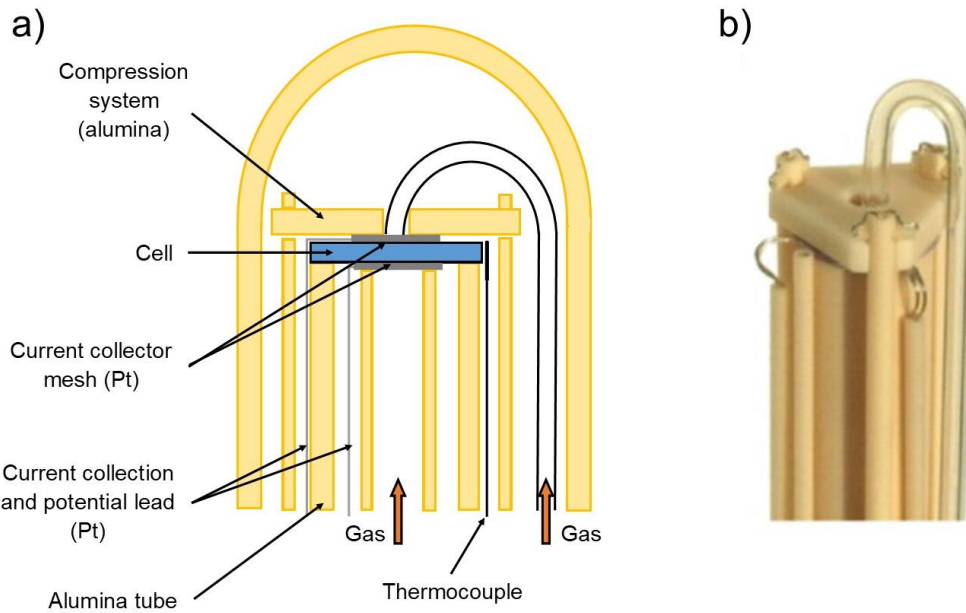


Figure III.14: Norecs Probostat set-up, a) schematical representation and b) photography of the device [257].

III.2. Measured EIS spectra

Among the temperature range depicted above, four temperatures were selected to illustrate the evolution of the response of the sample with the temperature: 250, 400, 550 and 700 °C. The notation of the equivalent circuit is as follow:

- (RQ) represents a resistor and a CPE in parallel
- R(RQ) represents a resistor connected in series to a resistor and a CPE in parallel
- R(RQ)(RQ) represents a resistor connected in series to a resistor and a CPE in parallel, followed by another resistor and CPE in parallel.

The characteristic time of each (RQ) contribution was calculated according to **Equation III.14**.

III.2.a. EIS spectra of BZY-com symmetrical cell

The Nyquist plots at 250 °C, 400 °C, 550 °C and 700 °C of BZY-com symmetrical cell in wet H₂ and wet air are presented in **Figure III.15**. The corresponding Bode plots are shown in **Annex D** (Figures D.1, 2, 3 and 4). To give the time dependence of the electrochemical phenomena, some frequencies are represented on the Nyquist plots.

In wet H₂, from 200 °C to 300 °C, the EIS spectra of BZY-com symmetrical cell are similar. They are composed of four components and were fitted with a $R_0(R_1Q_1)(R_2Q_2)(R_3Q_3)(R_4Q_4)$ equivalent circuit, where R_0 is the intercept of the EIS signal with the real part of the impedance Z' . In most cases, R_0 is equal to zero except if the number of experimental points is insufficient or if the contribution due to the electrical wires becomes preponderant. The Nyquist plot at 250 °C is represented in **Figure III.15.a** and the single fitted elements at 250 °C are presented in **Table III.4**. The points from 10^6 to 4×10^5 Hz are the low-frequency part of the first contribution. From 4×10^5 to 10^3 Hz, it is the second contribution. A small and overlapped semi-circle of $2486 \Omega \cdot \text{cm}^{-2}$ is highlighted from 10^2 to 3.4×10^1 Hz, before the beginning of the fourth arc is shown from 3.4×10^1 to 10 Hz.

All the contributions move toward high frequencies with the increase of the temperature. Then the first contribution (R_1Q_1) gradually disappears while the fourth contribution (R_4Q_4) appears. The first contribution is not visible anymore from 325 °C and the fourth is totally shown from 400 °C as highlighted in **Figure III.15.b**. At this temperature, the data were fitted with an $R_0(R_2Q_2)(R_3Q_3)(R_4Q_4)$ equivalent circuit and the single fitted elements at 400 °C are presented in **Table III.4**. It should also be noticed that the third contribution (R_3Q_3) becomes more and more evident from 350 °C to 450 °C before this trend is reversed from 475 °C to 575 °C due to the decrease of the resistance. At 400 °C, the low-frequency part of the second contribution (R_2Q_2) goes from 10^6 to 3.2×10^4 Hz. From 3.2×10^4 to 3×10^2 Hz, it is the third contribution and from 3×10^2 to 10^{-2} Hz, it is the fourth contribution.

At 550 °C (**Figure III.15.c**), the data were fitted with an $R_0(R_2Q_2)(R_3Q_3)(R_4Q_4)$ equivalent circuit, results are shown in **Table III.4**. The second contribution occurs from 10^6 to 8.2×10^4 Hz, the third from 8.2×10^4 to 6.8×10^3 Hz and the fourth from 6.8×10^3 to 10^{-2} Hz.

From 600 °C, the third contribution disappears. Then, as illustrated in **Figure III.15.d** only the second contribution (from 10^6 to 1.1×10^5 Hz) and the fourth contribution remains (from 1.1×10^5 to 10^{-2} Hz). The single fitted elements values are presented in **Table III.4**.

In wet air, the 200 °C to 325 °C, the EIS spectra can be fitted with a four components ($R_0(R_1Q_1)(R_2Q_2)(R_3Q_3)(R_4Q_4)$ equivalent circuit). The Nyquist plot at 250 °C is shown in **Figure III.15.a** and the fitted elements are presented in **Table III.5**. In contrast with the spectra at 250 °C in wet H_2 , the first contribution is totally shown (from 10^6 to 9.2×10^3 Hz). The second contribution occurs from 9.2×10^3 to 4.6×10^1 Hz), the third from 4.6×10^1 to 1.5 Hz and the high-frequency part of the fourth is situated from 1.5 Hz to 10^{-2} Hz.

The first contribution is too shifted toward high frequencies from 350 °C. The third disappears from 375 °C. Then, as illustrated in **Figure III.15.b** which presents the spectra at 400 °C, only the second contribution (R_2Q_2) from 10^6 to 4.1×10^2 Hz and the fourth contribution (R_4Q_4) from 4.1×10^2 to 10^{-2} Hz remains. The single fitted elements of the $R_0(R_2Q_2)(R_4Q_4)$ equivalent circuit are presented in **Table III.5**.

From 450 °C, a new contribution (noted $R_3'Q_3'$) is visible between the second and the fourth. Then, as illustrated on **Figure III.15.c**, at 550 °C, three contributions are highlighted. The second (R_2Q_2) goes from 10^6 to 2.7×10^3 Hz, the new third ($R_3'Q_3'$) from 2.7×10^3 to 2.0 Hz and the fourth from 2.0 to 10^{-2} Hz. The results of the $R_0(R_2Q_2)(R_3'Q_3')(R_4Q_4)$ equivalent circuit are exhibited in **Table III.5**. The values of the ($R_3'Q_3'$) contribution are written in italic.

The spectrum at 700 °C (**Figure III.15.d**) has the same shape as the one at 550 °C. The (R_2Q_2) contribution is visible from 10^6 to 6.8×10^3 Hz, the ($R_3'Q_3'$) from 6.8×10^3 to 1.8×10^1 Hz and the (R_4Q_4) from 1.8×10^1 to 10^{-2} Hz. Results of the fitting are shown in **Table III.5**.

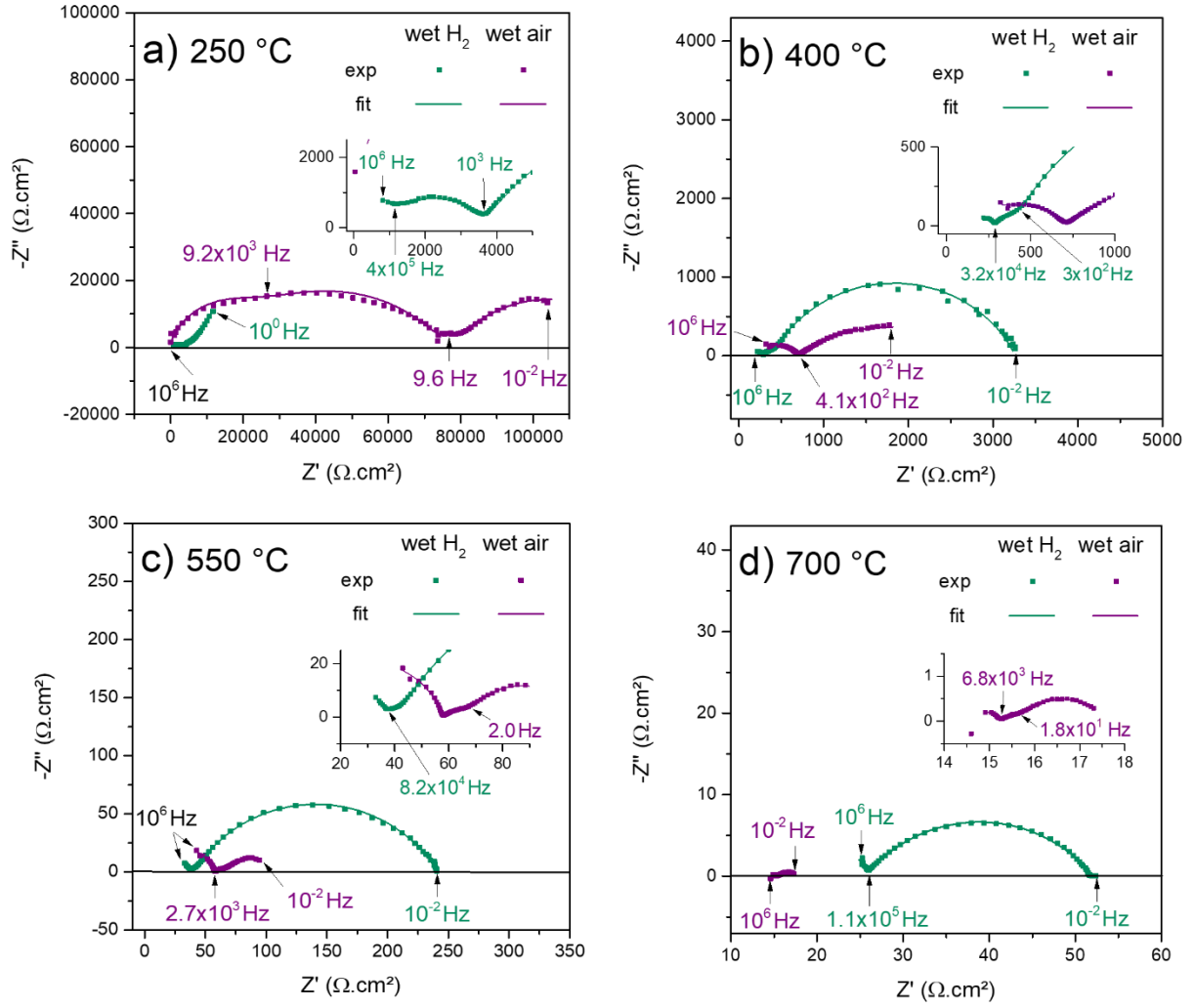


Figure III.15: Nyquist plots of the BZY-com symmetrical cell at a) 250 °C, b) 400 °C, c) 550 °C, and d) 700 °C in wet H_2 and wet air atmospheres. The frequencies delimiting the different contributions are written on the graph, those in black are for the two spectra.

Tempe- rature	R ₀ (Ω.cm ²)	R ₁ (Ω.cm ²)	CPE ₁ (F) (n ₁)	τ ₁ (s)	R ₂ (Ω.cm ²)	CPE ₂ (F) (n ₂)	τ ₂ (s)	R ₃ (Ω.cm ²)	CPE ₃ (F) (n ₃)	τ ₃ (s)	R ₄ (Ω.cm ²)	CPE ₄ (F) (n ₄)	τ ₄ (s)
250 °C	0	1118	7.6×10 ⁻¹¹ (0.98)	1.2×10 ⁻⁷	2486	2.3×10 ⁻⁸ (0.73)	3.9×10 ⁻⁶	2471	4.4×10 ⁻⁶ (0.74)	5.5×10 ⁻³	5.5×10 ⁵	1.1×10 ⁻⁵ (0.70)	37
400 °C	0				300	1.4×10 ⁻⁷ (0.55)	3.7×10 ⁻⁸	97	3.4×10 ⁻⁶ (0.86)	1.9×10 ⁻⁴	2867	3.3×10 ⁻⁵ (0.73)	9.9×10 ⁻²
550 °C	0				37	1.8×10 ⁻⁸ (0.78)	2.6×10 ⁻⁸	3.5	4.6 ×10 ⁻⁶ (0.85)	5.6×10 ⁻⁶	200	9.0×10 ⁻⁵ (0.67)	7.1×10 ⁻³
700 °C	14				12	2.4×10 ⁻⁸ (0.82)	2.4×10 ⁻⁸				26	2.9 ×10 ⁻⁴ (0.89)	8.9×10 ⁻³

Table III.4: Evolution of the elementary component of the equivalent circuits of the BZY-com symmetrical cell as a function of the temperature in wet H₂.

Tempe- rature	R ₀ (Ω.cm ²)	R ₁ (Ω.cm ²)	CPE ₁ (F) (n ₁)	τ ₁ (s)	R ₂ (Ω.cm ²)	CPE ₂ (F) (n ₂)	τ ₂ (s)	R ₃ (Ω.cm ²)	CPE ₃ (F) (n ₃)	τ ₃ (s)	R ₄ (Ω.cm ²)	CPE ₄ (F) (n ₄)	τ ₄ (s)
250 °C	0	18432	8.2 ×10 ⁻¹¹ (0.98)	2.3×10 ⁻⁶	53518	8.2×10 ⁻⁹ (0.73)	6.9×10 ⁻⁵	4923	1.9×10 ⁻⁶ (0.93)	1.3×10 ⁻²	56991	3.7×10 ⁻⁵ (0.56)	12.7
400 °C	0				718	5.1×10 ⁻⁷ (0.47)	2.5×10 ⁻⁷				1915	7.0×10 ⁻⁴ (0.46)	8.7
550 °C	0				58	1.5×10 ⁻⁸ (0.80)	6.8×10 ⁻⁸	<i>13</i>	<i>8.7×10⁻³</i> <i>(0.45)</i>	<i>3.6×10⁻²</i>	36	5.9×10 ⁻² (0.71)	7.7
700 °C	29				1.1	2.9 ×10 ⁻⁷ (0.82)	1.2×10 ⁻⁸	<i>0.46</i>	<i>5.6×10⁻²</i> <i>(0.48)</i>	<i>2.0×10⁻³</i>	1.9	3.1×10 ⁻¹ (0.58)	1.3

Table III.5: Evolution of the elementary component of the equivalent circuits of the BZY-com symmetrical cell as a function of the temperature in wet air. The values in italic corresponds to the values of the (R₃'Q₃') contribution.

The semi-circles are classically assigned to the electrochemical phenomena using the magnitude of Area Specific Capacitance (ASC) [24], [250], [258]–[260]. The possible interpretations are given in **Table III.6**. The charge transfer is usually included the electrochemical reactions, but when it is a rate-limiting step, it can give rise to a separated (RQ) component with an ASC of the order of $10^{-4} \text{ F.cm}^{-2}$ [259].

ASC (F.cm^{-2})	Phenomenon Responsible
$10^{-12} - 10^{-11}$	Bulk diffusion
10^{-11}	Minor, second phase
$10^{-11} - 10^{-7}$	Grain boundary diffusion
$10^{-10} - 10^{-9}$	Bulk ferroelectric
$10^{-9} - 10^{-7}$	Surface layer
$10^{-7} - 10^{-4}$	Electrolyte-electrode interface
$10^{-7} - 10^{-5}$	Double layer capacitance at the electrolyte-electrode interface
$10^{-5} - 10^{-4}$	Charge transfer electrolyte-electrode
$10^{-4} - 10^{-3}$	Electrochemical reactions
$10^{-4} - 10^0$	Chemical capacitance (usually as oxygen vacancies)
$10^{-2} - 10^{-1}$	Gas dissociation/adsorption
10^{-1}	Adsorbed species surface diffusion

Table III.6: ASC values and their possible interpretation, based of the work from Irvine *et al.* [258] and adapted from various authors [24], [67], [84], [250], [259], [261]–[268].

The ASC is calculated by multiplying the capacitance C by the electrode surface area. However, since the EIS spectra were fitted using a non-ideal capacitor, i.e., using CPE, it is first necessary to calculate the equivalent capacitance C_{eq} . Different methods are proposed in the literature to evaluated C_{eq} and are listed below.

- van Westing *et al.* propose **Equation III.38** [269]:

$$C_{eq} = \frac{Q\omega_{max}''^{n-1}}{\sin(\frac{n\pi}{2})} \quad \text{Equation III.38}$$

- Hirschorn *et al.* give **Equation III.39** [270]:

$$C_{eq} = Q^{1/n} R^{(1-n)/n} \quad \text{Equation III.39}$$

- Hsu and Mansfeld propose **Equation III.40** [271]:

$$C_{eq} = Q\omega_{max}''^{n-1} \quad \text{Equation III.40}$$

- Chang *et al.* proposes **Equation III.41** [272]:

$$C_{eq} = \frac{(QR)^{1/n}}{R} \sin(\frac{n\pi}{2}) \quad \text{Equation III.41}$$

The different equations were applied to the (R1Q1) and the (R2Q2) components of the BZY-com at 250 °C in wet H_2 , and the results are shown in **Table III.7**. As evidenced, the equivalent capacitances are very close with the equations from Hirschorn *et al.* and Hsu and Mansfeld. The equation from Van Westing *et al.* seems to overestimate the equivalent

capacitance while the one from Chang *et al.* appears to underestimate the equivalent capacitance.

	Van Westing <i>et al.</i>	Hirschorn <i>et al.</i>	Hsu and Mansfeld	Chang <i>et al.</i>
C_{eq} of (R_1Q_1)	5.55×10^{-11}	5.55×10^{-11}	5.55×10^{-11}	5.54×10^{-11}
C_{eq} of (R_2Q_2)	8.75×10^{-10}	7.98×10^{-10}	7.98×10^{-10}	7.28×10^{-10}

Table III.7: Calculated equivalent capacitance of the (R_1Q_1) and (R_2Q_2) components from Equations III.34-37. R (in Ω) and not ASR (Area Specific Resistance – in $\Omega.cm^2$) was used for the calculation.

Then, for following results, **Equation II.39** from Hirschorn *et al.* was used to calculate the equivalent capacitance. The ASC of the components in wet H_2 at 250, 400, 550 and 700 °C are presented in **Table III.8**. According to **Table III.6**, the (R_1Q_1) contribution could be attributed to the diffusion of charged species in the bulk of BZY or to secondary phases. Since very few (only 0.9 wt%) minor phase was evidenced by XRD, this contribution is attributed to the diffusion into the bulk. The (R_2Q_2) contribution corresponds to the diffusion in the grain boundary of BZY. As expected, the resistance of the electrolyte bulk is lower than the one of the grain boundaries, of about 2 times less (values are highlighted in **Table III.4**).

The interpretation of (R_3Q_3) and (R_4Q_4) is more complex. The (R_3Q_3) contribution is related to a phenomenon at the interface electrode-electrolyte. The phenomena usually linked to the interface are the double layer capacitance and the charge transfer limiting step. According to the value of ASC, it is supposed to be a double layer capacitance. To verify this assumption, measurements by varying P_{O_2} and P_{H_2O} could have been made. Indeed, the capacity of a double layer is greatly dependent on the concentration of charged species [261], here $V_O^{\bullet\bullet}$, OH_O^\bullet , h^\bullet and e' , and it has been seen in **Figure III.4** that the concentration of these species evolves with P_{O_2} and P_{H_2O} . The (R_4Q_4) contribution could be assigned to the interface electrode-electrolyte (charge transfer rate-limiting step) and/or to the electrode electrochemical reactions. According to the high values of R_4 in comparison with the other R_1 , R_2 and R_3 values, this contribution with attributed to the electrochemical reactions.

Temperature	ASC (F.cm ²) of (R_1Q_1)	ASC (F.cm ²) of (R_2Q_2)	ASC (F.cm ²) of (R_3Q_3)	ASC (F.cm ²) of (R_4Q_4)
250 °C	2.8×10^{-11}	4.0×10^{-10}	5.6×10^{-7}	1.7×10^{-5}
400 °C		3.2×10^{-11}		8.7×10^{-6}
550 °C		1.8×10^{-10}	7.3×10^{-4}	8.9×10^{-6}
700 °C		5.1×10^{-10}	1.1×10^{-3}	8.7×10^{-5}

Table III.8: Calculated ASC of the (RC) components of the BZY-com symmetrical cell depicted in Table III.4 in wet H_2 .

The ASC of the components in wet air at 250, 400, 550 and 700 °C are presented in **Table III.9**. As in wet H₂ condition, (R₁Q₁) corresponds to the diffusion of charged species in the bulk and (R₂Q₂) to the diffusion in the grains boundaries. The diffusion into the grain boundaries is 2.9 times more resistive than the diffusion in the bulk, it is the same order as in wet H₂. At 250 °C, the (R₃Q₃) contribution is assigned to a double layer capacitance. But at 550 °C and 700 °C, regarding the shape of points related to the third and fourth contribution, another explanation can be given. The geometry of the pores of the electrodes can be at the origin of this “half pear” shape [225]. This phenomenon is known as the porous electrode theory de Levie. The shape of the spectrum changes with the temperature: at a temperature below around 500 °C, the spectrum is in the form of a semi-circle, and at a higher temperature, the spectrum has this characteristic skewed shape [268]. This is in line with the spectrum of the BZY-com symmetrical cell in wet air but not in wet H₂. Since the geometry of the pores in the electrode is not supposed to change with the atmosphere, this explanation is rejected. Another phenomenon can give rise to a skewed semi-circle, it occurs when the surface diffusion of gas and adsorption/dissociation of the gas at the surface of the electrode are co-limiting steps [273]. This phenomenon is known as the Gerischer impedance and is the retained explanation.

Temperature	ASC (F.cm ²) of (R ₁ Q ₁)	ASC (F.cm ²) of (R ₂ Q ₂)	ASC (F.cm ²) of (R ₃ Q ₃)	ASC (F.cm ²) of (R ₄ Q ₄)
250 °C	3.1×10 ⁻¹¹	3.3×10 ⁻¹⁰	6.7×10 ⁻⁷	4.3×10 ⁻⁵
400 °C		8.6×10 ⁻¹¹		1.2×10 ⁻³
550 °C		3.0×10 ⁻¹⁰	7.1×10 ⁻⁴	5.4×10 ⁻²
700 °C		5.5×10 ⁻⁹	1.1×10 ⁻³	1.7×10 ⁻¹

Table III.9: Calculated ASC of the (RC) components of the BZY-com symmetrical cell depicted in Table III.5 in wet air.

III.2.b. EIS spectra of BZY-c 1000 °C symmetrical cell

The Nyquist plots at 250 °C, 400 °C, 550 °C and 700 °C of BZY-c 1000 °C symmetrical cell in wet H₂ and wet air are presented in **Figure III.16** and the corresponding Bode plots are shown in **Annex D** (Figures D.5, 6, 7 and 8).

In wet H₂, at 250 °C, (**Figure III.16.a**), the spectrum was fitted with an equivalent circuit denoted R₀(R₁Q₁)(R₂Q₂)(R₃'Q₃')(R₃Q₃). The results are shown in **Table III.10**. The (R₁Q₁) contribution at very high frequencies exhibits an ASC value of 7.2×10⁻¹² F.cm² as presented in **Table III.12**. Thus, it corresponds to the diffusion of charged species in the bulk of BZY. The second contribution, from 10⁶ to 10³ Hz, presents a ASC of 3.4×10⁻¹⁰ F.cm² and corresponds to the diffusion in the grain boundaries. With the increasing temperature, this contribution is situated from 10⁶ to ~10⁴ Hz and exhibits values between 5.2×10⁻¹¹ and 1.0×10⁻¹⁰ F.cm². These values support the assignation of the (R₂Q₂) contribution to the diffusion in the grain boundaries. The characteristic time constants of this contribution are lower than 10⁻⁶ seconds,

except at 250 °C, indicating a fast diffusion process. The ($R_3'Q_3'$) contribution is shown from 10^3 to 6.2×10^1 Hz at 250 °C. It exhibits an ASC value of 1.9×10^{-6} F.cm² (**Table III.12**) and a resistance (ASR) of 368 Ω .cm² (**Table III.10**), very small in comparison to the resistance of the third contribution. This behavior indicates a double layer capacitance at the interface electrode-electrolyte. With the increase of the temperature, the resistance of this contribution decreases and becomes negligible from 375 °C. The (R_3Q_3) contribution (from 6.2×10^1 to 10^{-2} Hz) is in the shape of a half semi-circle and presents an ASC value of 2.2×10^{-5} (**Table III.12**) that could fit to a charge transfer limiting step at the interface electrode-electrolyte.

With the increase of the temperature, all the phenomena become faster and are shifted toward higher frequencies. From 325 °C, a fourth contribution appears at low frequencies. In the Nyquist plot at 400 °C (**Figure III.16.b**), this (R_4Q_4) contribution is situated from 1.7×10^{-1} to 10^{-2} Hz. At this temperature, the EIS spectrum presents three contributions and was fitted by an $R_0(R_2Q_2)(R_3Q_3)(R_4Q_4)$ equivalent circuit. The single fitted elements values are displayed in **Table III.10**. Their ASC are shown in **Table III.12**. As a reminder, (R_2Q_2) belongs to the diffusion in the grain boundary. The (R_3Q_3) contribution exhibits a value of 3.1×10^{-5} F.cm², supporting the assignation of this contribution to a charge transfer limiting step. The contribution (R_4Q_4) has an ASC of 1.9×10^{-4} F.cm² and be assigned to the electrochemical reactions at the electrode.

At 550 °C, the shape of the EIS spectra (**Figure III.16.c**) and the equivalent circuit used to fit it is the same as at 400 °C. According to the ASC values presented in **Table III.12**, (R_2Q_2) corresponds to diffusion in the grain boundary, (R_3Q_3) to the charge transfer between electrode and electrolyte and (R_4Q_4) to the electrochemical reactions. It should be noticed that the resistance associated with the charge transfer is higher than the resistance of the electrochemical reaction, indicating that the charge transfer is the most limiting step. This behavior probably comes from a bad contact between the BZY-c pellet and the Ag electrodes, but unfortunately, this was not verified due to the sample breaking during the post-mortem analyzes.

At 700 °C, the spectrum (**Figure III.16.d**) is globally the same as at 400 °C and 550 °C and the assignation of the (R_2Q_2), (R_3Q_3) and (R_4Q_4) contribution thanks to their ASC values highlighted in **Table III.12** remains the same. The differences in the shape of the Nyquist plots between 700 °C and 550 °C, is due to the resistance of the (R_3Q_3) similar to the (R_4Q_4) at 700 °C.

In wet air, a total of three contributions (R_1Q_1), (R_2Q_2) and (R_3Q_3) is evidenced. From 200 to 250 °C, all three are seen. The values of the fitted elementary component of the $R_0(R_1Q_1)(R_2Q_2)(R_3Q_3)$ equivalent circuit are presented in **Table III.11**. On the spectrum at 250 °C (**Figure III.16.a**), only the very low-frequency part of the (R_1Q_1) contribution is visible from 10^6 to 7.3×10^5 Hz. Its ASC (shown in **Table III.13**) is 8.9×10^{-12} F.cm², corresponding to the diffusion of charged species in the bulk of BZY. The second contribution starts at 7.3×10^5 Hz and ends at 1.2×10^2 Hz. The (R_2Q_2) contribution exhibits an ASC of 3.8×10^{-10} F.cm² and then is attributed to the diffusion in the grain boundaries. The diffusion in the bulk presents an ASR of 1635 Ω .cm² while the diffusion in the grain boundary has an ASR of 3098 Ω .cm². The grain boundaries are then about two times more resistive than the bulk, according to the

microstructure of the sintered BZY-c 1000 °C which presents small grains and thus a large concentration of grain boundaries, this observation is surprising. The third contribution presents a too few number of points and they are too aligned to be accurately fitted, however according to the low value of its ASC, it can reasonably be assumed that it is related to a phenomenon linked to the electrodes.

From 275 °C, the contribution of the bulk of BZY is too shifted toward high frequencies to be seeable. Then, at 400 °C (**Figure III.16.b**), the EIS spectrum was fitted with the $R_0(R_2Q_2)(R_3Q_3)$ equivalent circuit. As highlighted in **Table III.13**, the (R_2Q_2) from 10^6 to 2.4×10^4 Hz has an ASC of $4.6 \times 10^{-10} \text{ F.cm}^2$, this is consistent with the assignation to the grain boundaries diffusion. As previously, the (R_3Q_3) contribution from 2.4×10^4 to 10^{-2} Hz cannot be fitted precisely but is attributed to an electrode-related phenomenon.

The spectra at 550 °C (**Figure III.16.c**) and the results of the fitting by the $R_0(R_2Q_2)(R_3Q_3)$ equivalent circuit are consistent with observations given at 250 °C and 400 °C. The (R_2Q_2) contribution presents an ASC characteristic of diffusion in the grain boundary and the (R_3Q_3) contribution has an of 1.0 F.cm^2 . This high value is also uncertain due to the highly skewed semi-circle shape that be imputed to the Gerischer behavior.

At 700 °C (**Figure III.16.d**), the contribution of the grain boundary is hidden by the inductive behavior of the electrical wires, thus, the spectrum was fitted by a $L_0R_0(R_3Q_3)$, where L_0 is the inductance of the wires (from 10^6 to 2.4×10^4 Hz on the Nyquist plot). In this case, the resistance of the electrolyte can be considered as the intercept of the experimental points with the real part of the impedance and then correspond to R_0 . The skewed semi-circle from 2.4×10^4 to 10^{-2} Hz corresponds the electrode-related processes.

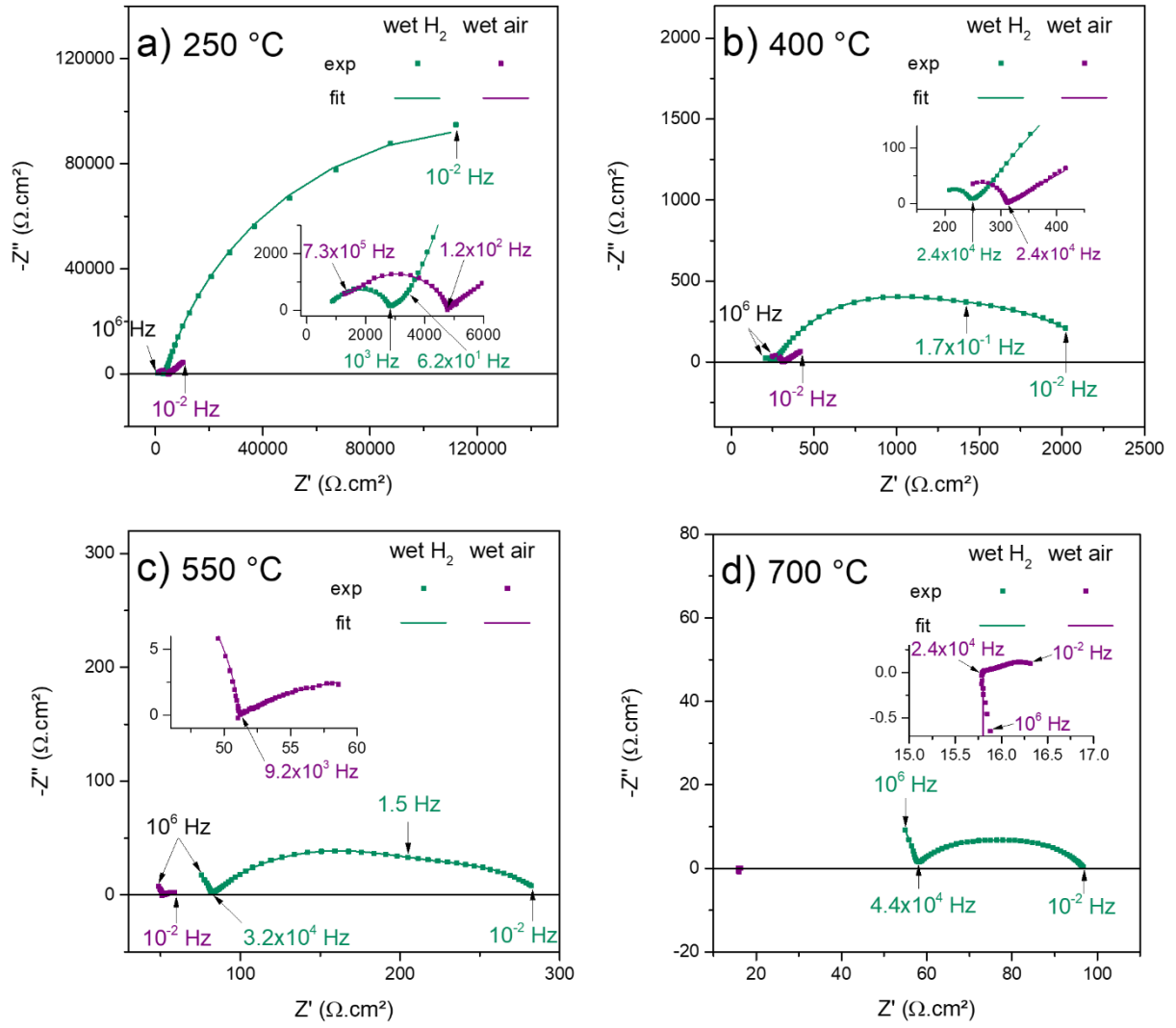


Figure III.16: Nyquist plots of the BZY-c 1000 °C symmetrical cell at a) 250 °C, b) 400 °C, c) 550 °C, and d) 700 °C in wet H_2 and wet air atmosphere. The frequencies delimiting the different contributions are written on the graph, those in black are for the two spectra.

Temperature	R_0 ($\Omega \cdot \text{cm}^2$)	R_1 ($\Omega \cdot \text{cm}^2$)	CPE_1 (F) (n_1)	τ_1 (s)	R_2 ($\Omega \cdot \text{cm}^2$)	CPE_2 (F) (n_2)	τ_2 (s)	R_3 ($\Omega \cdot \text{cm}^2$)	CPE_3 (F) (n_3)	τ_3 (s)	R_4 ($\Omega \cdot \text{cm}^2$)	CPE_4 (F) (n_3)	τ_4 (s)
250 °C	0	782	5.0×10^{-11} (0.93)	2.2×10^{-8}	2157	1.4×10^{-8} (0.76)	2.9×10^{-6}	2.6×10^5	2.4×10^{-5} (0.81)	23	368	4.7×10^{-6} (0.97)	2.8×10^{-2}
400 °C	171				77	1.1×10^{-8} (0.74)	1.6×10^{-8}	538	1.1×10^{-4} (0.79)	6.7×10^{-2}	1538	3.5×10^{-4} (0.48)	1.1
550 °C	0				82	1.5×10^{-9} (0.88)	3.1×10^{-8}	134	1.9×10^{-4} (0.60)	7.1×10^{-3}	73	4.7×10^{-3} (0.52)	0.52
700 °C	0				57	6.5×10^{-10} (0.93)	2.3×10^{-8}	17	3.2×10^{-4} (0.57)	3.8×10^{-3}	22	2.5×10^{-3} (0.53)	1.6×10^{-2}

Table III.10: Evolution of the elementary component of the equivalent circuit of the BZY-c 1000 °C symmetrical cell as a function of the temperature in wet H_2 . The values in italic corresponds to the values of the (R_3 ' Q_3 ') contribution.

Temperature	L_0 (H)	R_0 ($\Omega \cdot \text{cm}^2$)	R_1 ($\Omega \cdot \text{cm}^2$)	CPE_1 (F) (n_1)	τ_1 (s)	R_2 ($\Omega \cdot \text{cm}^2$)	CPE_2 (F) (n_2)	τ_2 (s)	R_3 ($\Omega \cdot \text{cm}^2$)	CPE_3 (F) (n_3)	τ_3 (s)
250 °C		0	1635	3.7×10^{-9} (0.68)	5.8×10^{-8}	3098	5.5×10^{-9} (0.84)	4.6×10^{-6}	5.0×10^4	2.2×10^{-4} (0.45)	866
400 °C		212				99	1.1×10^{-8} (0.84)	1.8×10^{-7}	1.0×10^5	6.8×10^{-4} (0.48)	8.0×10^3
550 °C		11				41	1.1×10^{-9} (0.94)	3.2×10^{-8}	21	1.0×10^{-1} (0.32)	88
700 °C	2.6×10^{-7}	16							9.6	1.1 (0.29)	3.5×10^4

Table III.11: Evolution of the elementary component of the equivalent circuit of the BZY-c 1000 °C symmetrical cell as a function of the temperature in wet air.

Temperature	ASC (F.cm ²) of (R ₁ Q ₁)	ASC (F.cm ²) of (R ₂ Q ₂)	ASC (F.cm ²) of (R ₃ Q ₃)	ASC (F.cm ²) of (R ₄ Q ₄)
250 °C	7.2×10 ⁻¹²	3.4×10 ⁻¹⁰	2.2×10 ⁻⁵	<i>1.9×10⁻⁶</i>
400 °C		5.2×10 ⁻¹¹	3.1×10 ⁻⁵	1.9×10 ⁻⁴
550 °C		9.6×10 ⁻¹¹	1.3×10 ⁻⁵	1.8×10 ⁻³
700 °C		1.0×10 ⁻¹⁰	5.5×10 ⁻⁶	1.8×10 ⁻⁴

Table III.12: Calculated ASC of the (RC) components of the BZY-c 1000 °C symmetrical cell depicted in Table III.10 in wet H₂. The values in italic corresponds to the values of the (R₃'Q₃') contribution.

Temperature	ASC (F.cm ²) of (R ₁ Q ₁)	ASC (F.cm ²) of (R ₂ Q ₂)	ASC (F.cm ²) of (R ₃ Q ₃)
250 °C	8.9×10 ⁻¹²	3.8×10 ⁻¹⁰	4.3×10 ⁻³
400 °C		4.6×10 ⁻¹⁰	3.7×10 ⁻²
550 °C		1.1×10 ⁻¹⁰	1.1
700 °C			9.4×10 ²

Table III.13: Calculated ASC of the (RC) components of the BZY-c 1000 °C symmetrical cell depicted in Table III.11 in wet air.

III.2.c. EIS spectra of BZY-b 1000 °C symmetrical cell

The Nyquist plots at 250 °C, 400 °C, 550 °C and 700 °C of BZY-b 1000 °C symmetrical cell in wet H₂ and wet air are presented in **Figure III.17** and the corresponding Bode plots are shown in **Annex D** (Figures D.9, 10, 11 and 12).

At 250°C, in wet H₂ (**Figure III.17.a**), the spectrum can be fitted with four contributions. The results of the R₀(R₁Q₁)(R₂Q₂)(R₃Q₃)(R₄Q₄) equivalent circuit are shown in **Table III.14**. According to the calculation of ASC presented in **Table III.16**, the (R₁Q₁) contribution, from 10⁶ to 1.5×10⁵ Hz, corresponds to the diffusion of charged species in the bulk of BZY-b. The (R₂Q₂) contribution, from 1.5×10⁵ to 6.8×10³ Hz, presents an ASC of 1.5×10⁻¹⁰ F.cm² and can then be attributed to the diffusion in the grain boundaries or to a secondary phase. According to the sample microstructure and composition and to the ASC value of the third contribution, the (R₂Q₂) is assigned to the secondary phase Zr-doped Y₂O₃. The (R₃Q₃) contribution, from 6.8×10³ to 5.8×10⁻¹ Hz, with an ASC of 4.4×10⁻⁸ F.cm², corresponds to the diffusion of charged species in the grain boundaries of the electrolyte while the (R₄Q₄) contribution, from 5.8×10⁻¹ to 10⁻² Hz, is associated with the electrode processes, probably to the charge transfers limiting step. The diffusion in the bulk presents an ASR of 2556 Ω.cm² and the one associated with the diffusion in grain boundaries is 6.4×10⁴ Ω.cm².

Then, in the BZY-b 1000 °C sample, the grain boundaries are much more resistive than the bulk, about 25 times more. Furthermore, the resistance due to the secondary phase increases even more the electrolyte's total resistance and then decreases the total conductivity of BZY-b 1000 °C.

At 400 °C (**Figure III.17.b**), the first contribution is too shifted toward high frequency to be visible anymore and the spectrum was fitted with an $R_0(R_2Q_2)(R_3Q_3)(R_4Q_4)$ equivalent circuit. The values of the single fitted elements of the equivalent circuit are shown in **Table III.14**. According to the values of ASC displayed in **Table III.16**, the attribution of the contributions remains the same as at 250 °C.

From 475 °C, the contribution due to Zr-doped Y_2O_3 is hidden by the electrical wires inductance response. Then, at 550 °C (**Figure III.17.c**), the spectrum was fitted by an $L_0R_0(R_3Q_3)(R_4Q_4)$ equivalent circuit and the single fitted elements values are shown in **Table III.14**. Where (R_3Q_3) , from 7.3×10^5 to 9.2×10^3 Hz, still correspond to the diffusion in the grain boundary and (R_4Q_4) , from 9.2×10^3 to 10^{-2} Hz, to the electrode processes, according to their values of ASC (**Table III.16**).

At 700 °C (**Figure III.17.d**), the spectrum is similar to the one at 550 °C. The third contribution from 2.3×10^5 to 6.8×10^3 Hz is the contribution of the diffusion of charged species in the grain boundaries. The (R_4Q_4) contribution, from 6.8×10^3 to 10^{-2} Hz, is the electrode response.

In wet air, at 200 and 225 °C, the EIS spectra were not sufficiently resolved to be fitted. At 250 °C (**Figure III.17.a**), the spectrum is fitted with an $R_0(R_1Q_1)(R_2Q_2)(R_3Q_3)$ equivalent circuit. The first contribution (R_1Q_1) , from 10^6 to 4.9×10^4 Hz, corresponds to the diffusion in the bulk according to its ASC value exposed in **Table III.17**. The (R_2Q_2) contribution, from 4.9×10^4 to 4.2×10^3 Hz, exhibits an ASC of 5.9×10^{-10} F.cm² and then is attributed to the Zr- Y_2O_3 secondary phase. The (R_3Q_3) contribution, from 4.2×10^3 to 10 Hz, corresponds to the diffusion in the grain boundary according to its ASC value of the order of 10^{-8} F.cm². The ASR related to the diffusion of charged species in the bulk (**Table III.15**) is 9893 Ω .cm² and the ASR associated with the diffusion in the grain boundary is 1.8×10^5 Ω .cm². Then, the diffusion of charge species is 18 times more resistant than is the bulk. This ratio is surprisingly lower than in wet H₂.

At 400 °C (**Figure III.17.b**), as in wet H₂, the first contribution disappears due to its shift toward high frequency and a new contribution note (R_4Q_4) appear at low frequency (from 6.5×10^4 to 10^{-1} Hz). The spectrum was fitted with a $R_0(R_2Q_2)(R_3Q_3)(R_4Q_4)$ equivalent circuit and the values of the single elements are shown in **Table III.15**. According to the ASC value in **Table III.17** of each contribution, (R_2Q_2) is due to the secondary phase and (R_3Q_3) to the diffusion in grain boundary. The (R_4Q_4) contribution exhibits a higher than expected ASC value because the points are too aligned to be accurately fitted with an (RQ) component, but is attributed to the electrode processes.

As in wet H₂, at 550 °C (**Figure III.17.c**), the second contribution is hidden by the inductance of the electrical wires. Then, the spectrum was fitted by an $L_0R_0(R_3Q_3)(R_4Q_4)$

equivalent circuit. According to the ASC values exhibited in **Table III.17**, (R_3Q_3) corresponds to the diffusion in the grain boundaries. (R_4Q_4) can still not be fitted accurately and is associated with the electrode process.

At 700 °C (**Figure III.17.d**), the inductance of the electrical is not seen and the spectrum was fitted with an $R_0(R_3Q_3)(R_4Q_4)$ equivalent circuit. (R_3Q_3) has an ASC of the order of 10^{-9} F.cm² and is associated with the diffusion in the grain boundary and (R_4Q_4) has an ASC of 4.0×10^{-2} F.cm² which indicates gas dissociation/adsorption limiting step.

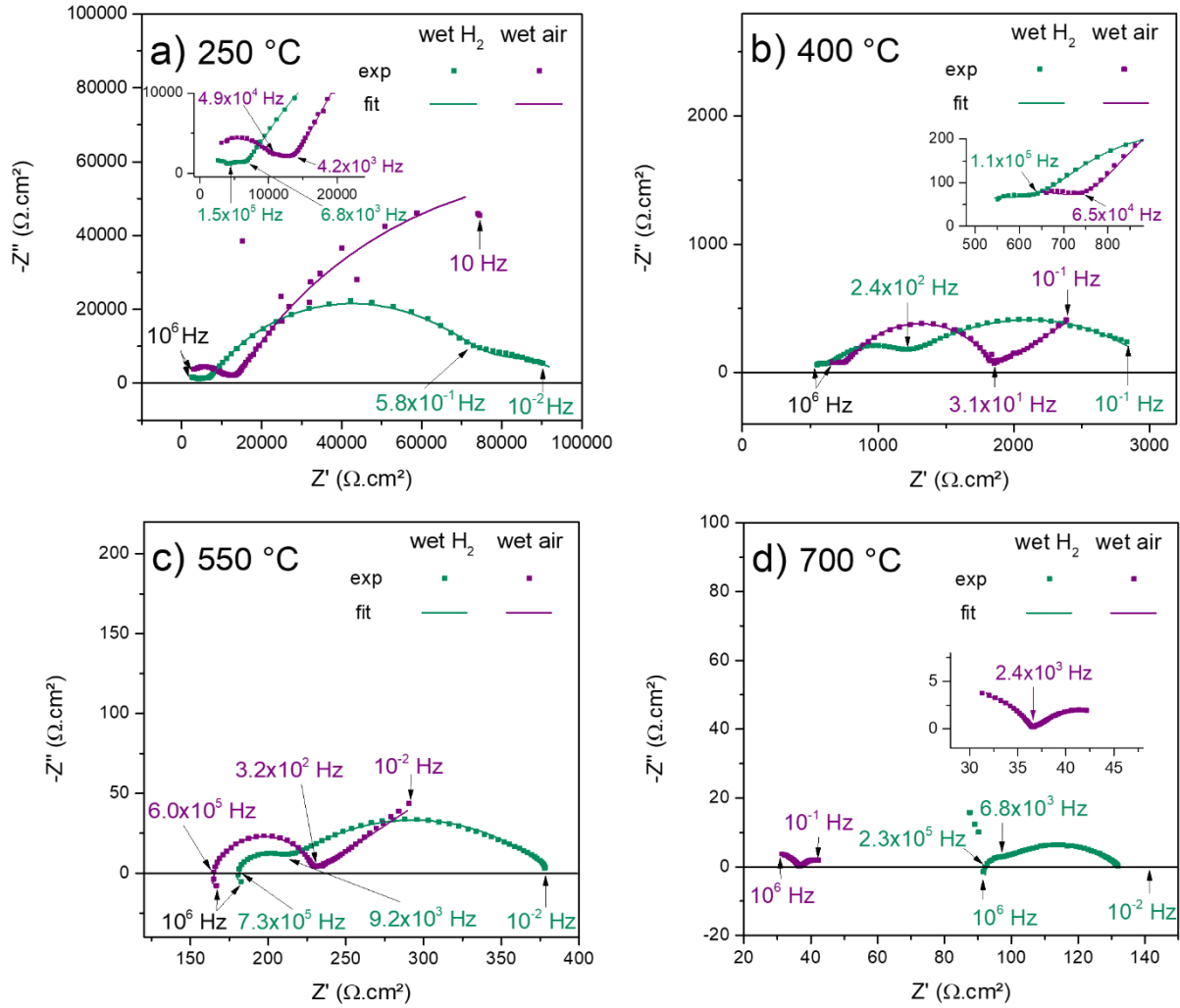


Figure III.17: Nyquist plots of the BZY-b 1000 °C symmetrical cell at a) 250 °C, b) 400 °C, c) 550 °C, and d) 700 °C in wet H₂ and wet air atmosphere. The frequencies delimiting the different contributions are written on the graph, those in black are for the two spectra.

Temperature	L_0 (H)	R_0 ($\Omega \cdot \text{cm}^2$)	R_1 ($\Omega \cdot \text{cm}^2$)	CPE_1 (F) (n_1)	τ_1 (s)	R_2 ($\Omega \cdot \text{cm}^2$)	CPE_2 (F) (n_2)	τ_2 (s)	R_3 ($\Omega \cdot \text{cm}^2$)	CPE_3 (F) (n_3)	τ_3 (s)	R_4 ($\Omega \cdot \text{cm}^2$)	CPE_4 (F) (n_4)	τ_4 (s)
250 °C		0	2556	7.4×10^{-11} (0.92)	1.0×10^{-7}	4652	2.3×10^{-7} (0.48)	2.4×10^{-6}	6.8×10^4	3.4×10^{-7} (0.70)	1.2×10^{-2}	2.3×10^4	4.2×10^{-5} (0.53)	3.4
400 °C		507				87	2.1×10^{-9} (0.98)	2.6×10^{-7}	606	1.4×10^{-6} (0.64)	5.1×10^{-5}	1863	6.3×10^{-5} (0.53)	6.4×10^{-2}
550 °C	2.5×10^{-6}	177							27	8.4×10^{-7} (0.77)	1.9×10^{-6}	178	2.8×10^{-4} (0.45)	5.9×10^{-3}
700 °C	1.0×10^{-6}	91							4.6	5.7×10^{-6} (0.78)	3.3×10^{-6}	36	8.7×10^{-4} (0.44)	2.5×10^{-5}

Table III.14: Evolution of the elementary component of the fitted equivalent circuit of the BZY-b 1000 °C symmetrical cell as a function of the temperature in wet H_2 .

Temperature	L_0 (H)	R_0 ($\Omega \cdot \text{cm}^2$)	R_1 ($\Omega \cdot \text{cm}^2$)	CPE_1 (F) (n_1)	τ_1 (s)	R_2 ($\Omega \cdot \text{cm}^2$)	CPE_2 (F) (n_2)	τ_2 (s)	R_3 ($\Omega \cdot \text{cm}^2$)	CPE_3 (F) (n_3)	τ_3 (s)	R_4 ($\Omega \cdot \text{cm}^2$)	CPE_4 (F) (n_4)	τ_4 (s)
250 °C		0	9893	1.3×10^{-10} (0.86)	3.1×10^{-7}	3746	3.3×10^{-8} (0.71)	8.8×10^{-6}	1.8×10^5	2.6×10^{-7} (0.71)	3.5×10^{-2}			
400 °C		614				138	8.5×10^{-9} (0.89)	4.3×10^{-7}	1056	3.8×10^{-7} (0.78)	1.0×10^{-4}	1.1×10^5	8.5×10^{-4} (0.38)	1.6×10^{-5}
550 °C	3.4×10^{-6}	162							67	6.5×10^{-7} (0.76)	4.3×10^{-6}	1.1×10^5	8.0×10^{-3} (0.38)	4.7×10^7
700 °C		22							15	1.1×10^{-6} (0.63)	7.3×10^{-8}	11	5.8×10^{-2} (0.44)	1.8

Table III.15: Evolution of the elementary component of the fitted equivalent circuit of the BZY-b 1000 °C symmetrical cell as a function of the temperature in wet air.

Temperature	ASC (F.cm ²) of (R ₁ Q ₁)	ASC (F.cm ²) of (R ₂ Q ₂)	ASC (F.cm ²) of (R ₃ Q ₃)	ASC (F.cm ²) of (R ₄ Q ₄)
250 °C	1.0×10 ⁻¹¹	1.5×10 ⁻¹⁰	4.4×10 ⁻⁸	3.7×10 ⁻⁵
400 °C		7.7×10 ⁻¹⁰	2.1×10 ⁻⁸	8.7×10 ⁻⁶
550 °C			1.8×10 ⁻⁸	8.4×10 ⁻⁶
700 °C			1.8×10 ⁻⁷	1.3×10 ⁻⁵

Table III.16: Calculated ASC of the (RC) components of the BZY-b 1000 °C symmetrical cell depicted in Table III.14 in wet H₂.

Temperature	ASC (F.cm ²) of (R ₁ Q ₁)	ASC (F.cm ²) of (R ₂ Q ₂)	ASC (F.cm ²) of (R ₃ Q ₃)	ASC (F.cm ²) of (R ₄ Q ₄)
250 °C	7.9×10 ⁻¹²	5.9×10 ⁻¹⁰	4.9×10 ⁻⁸	
400 °C		7.9×10 ⁻¹⁰	2.4×10 ⁻⁸	8.1×10 ⁻¹
550 °C			1.6×10 ⁻⁸	2.4×10 ²
700 °C			1.2×10 ⁻⁹	4.0×10 ⁻²

Table III.17: Calculated ASC of the (RC) components of the BZY-b 1000 °C symmetrical cell depicted in Table III.15 in wet air.

III.2.d. Summary

Each symmetrical cell presents a characteristic EIS spectrum in the 200 – 300 °C range, where the contribution due to the diffusion of charged species into the bulk is situated at high frequency, the contribution from the diffusion in the grain boundary is located at medium frequency and the phenomena related to the electrode or to the electrode-electrolyte interface are seen at low frequency. A characteristic Nyquist plot of the symmetrical cell at low temperature is given in **Figure.III.18**. The spectrum was simulated using the equivalent circuit inserted in the figure. Values were chosen arbitrarily. The blue semi-circle noted 1 corresponds to the diffusion in the bulk, the green semi-circle noted 2 to the diffusion in the grain boundary. The third contribution is associated with the electrode processes. In an ideal spectrum, R₀ is equal to zero and then the resistance of the diffusion in the bulk is R₁ and the resistance of the diffusion in the grain boundary is R₂. The total resistance of the electrolyte is R₁ + R₂. However, in practice, the semi-circle associated to the diffusion in the bulk is partially out of the range of frequency leading to a lack of points and a shift of the R₀ value. In this case, the resistance due to the diffusion in the bulk (noted R_B) is equal to R₀ + R₁ while the resistance associated with the boundary (note dR_{GB}) is still equal to R₂. Finally, the total resistance of the electrolyte (noted R_{TOT}) is equal to R₀ + R₁ + R₂.

These are the definitions of R_B , R_{GB} and R_{TOT} which will be used in the following paragraph dealing with the evolution of the resistances with the temperature and the verification of the Arrhenius law.

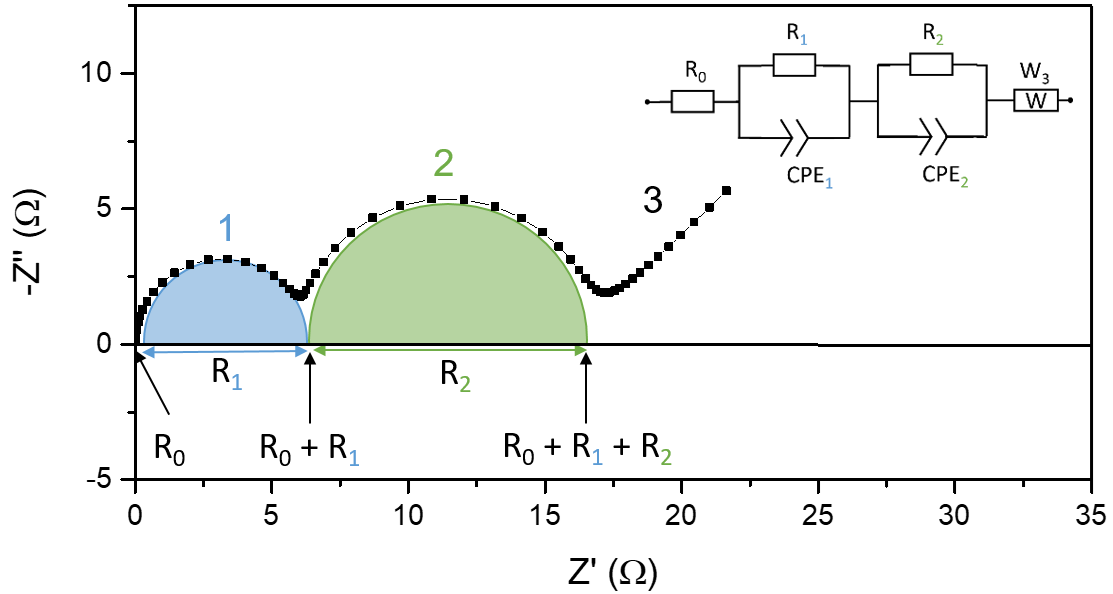


Figure III.18: Typical Nyquist plot of a symmetrical cell at low temperature. The spectrum was simulated by Nova 2.1 software according to the inserted equivalent circuit.

III.3. Evolution with the temperature

III.3.a. Conductivity in the bulk and in the grain boundaries

III.3.a.i. Arrhenius plot of BZY-com, BZY-c 1000 °C and BZY-b 1000 °C

The conductivity σ_{AC} of charged species in the bulk was calculated according to **Equation III.29**, where R is the resistance obtained from the fitting of the EIS spectra. The specific grain boundary conductivity, independent of the sample microstructure, was calculated using **Equation III.42**.

$$\sigma_{GB} = \frac{L}{S} \left(\frac{C_B}{C_{GB}} \right) \frac{1}{R_{GB}} \quad \text{Equation III.42}$$

In which, L is the thickness, S is the active area, C_B and C_{GB} are the equivalent capacitance calculated from the EIS spectra and R_{GB} is the resistance of the grain boundaries extracted from the EIS spectra.

The diffusion of charged species in the bulk and in the grain boundary of the electrolyte is thermally activated and follows an Arrhenius behavior as expressed in **Equation III.43**.

$$\sigma = A e^{-E_a/k_b T} \quad \text{Equation III.43}$$

The evolution of σ_{AC} is reported in a Arrhenius $\log \sigma = f(\frac{1000}{T})$ plot in **Figure III.19**. For each sample (BZY-com, BZY-c 1000 °C and BZY-b 1000 °C), the points are aligned, indicating an Arrhenius behavior.

Figure III.19.a exhibits the Arrhenius plot of BZY-com. In both wet H₂ and wet air, the conductivity is higher in the bulk than in the grain boundaries, as indicated by the resistance values. The σ_{AC} in the bulk (noted $\sigma_{AC,B}$) in wet H₂ as in wet air is approximatively 30 times higher than in the grain boundaries (noted $\sigma_{AC,GB}$). Furthermore, the conductivity in wet H₂ is more important than in wet air. For example, $\sigma_{AC,B}$ in wet H₂ at 300 °C is 5.5 times higher than $\sigma_{AC,B}$ in wet air at 300 °C.

The Arrhenius plot of BZY-c 1000 °C is exposed in **Figure III.19.b**. As for the BZY-com sample, the conductivity in the bulk in wet H₂ and in wet air is higher than in the grain boundary, of about 113 times. Furthermore, the conductivity is slightly higher in wet H₂ than in wet air, by a factor of about 1.4.

Figure III.19.c presents the σ_{AC} in the bulk and the grain boundary of BZY-b 1000 °C, the resistance due to the secondary phase was not taken into account. Due to the noise in the EIS spectrum at 200 °C in wet air, only the points from 225 °C to 300 °C are reported. The conductivity in both atmospheres is much higher in the bulk than in the grain boundaries, on average 1.1×10^5 times higher. The conductivity is higher in wet H₂ than in wet air. At 300 °C, $\sigma_{AC,B}$ in wet H₂ is 3.8 times higher than $\sigma_{AC,B}$ in wet air.

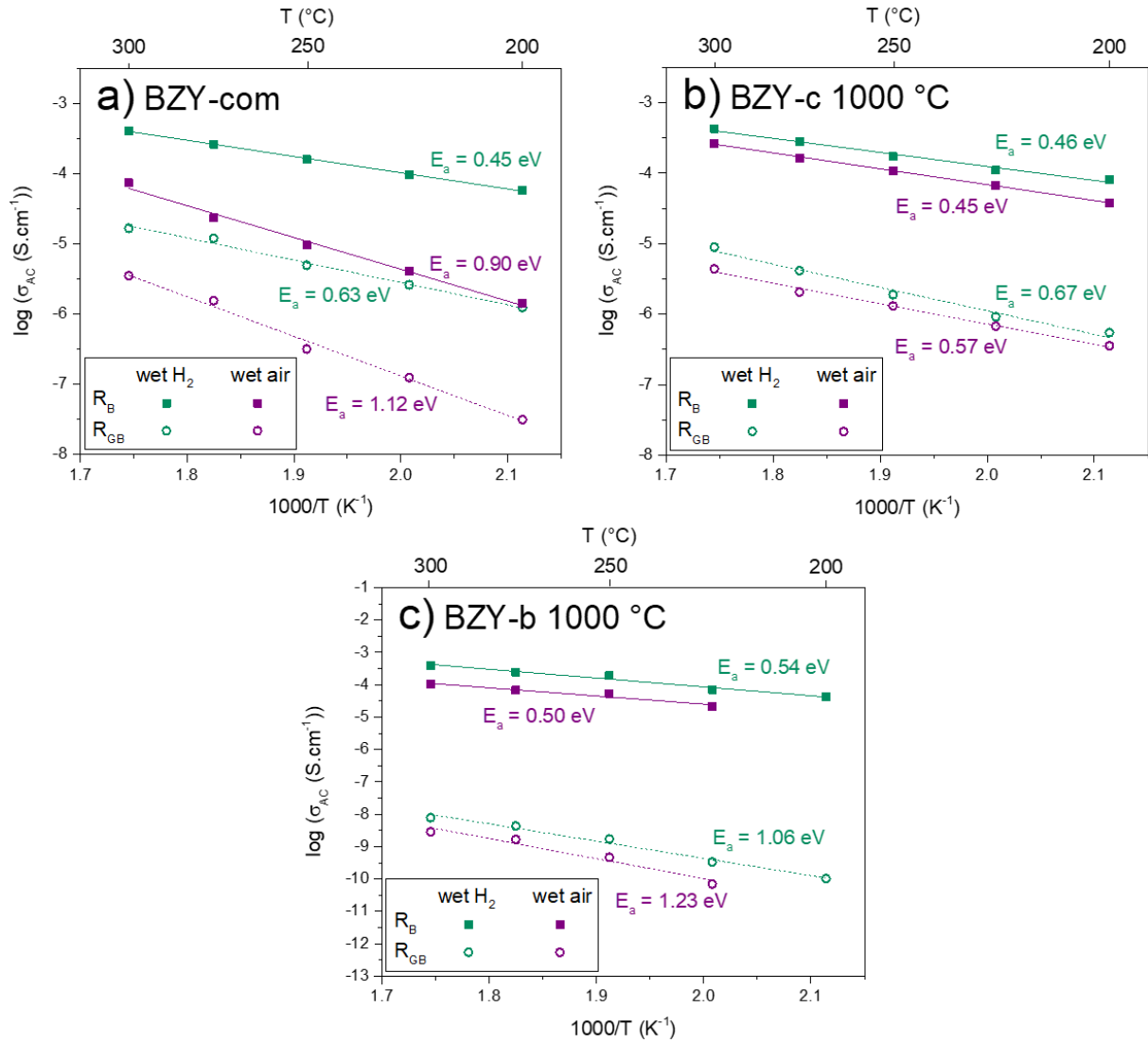


Figure III.19: Arrhenius diagram of σ_{AC} calculated from R_B or R_{GB} in wet air and wet H_2 . a) BZY-com symmetrical cell, b) BZY-c 1000 °C symmetrical cell and c) BZY-b 1000 °C symmetrical cell

The activation energy of charged species transport in the bulk and in the grain boundary in wet air and in wet H_2 was calculated for each sample according to **Equation III.43**.

$$E_a = -1000k_b \times \frac{d \ln\left(\frac{1}{R_{e \cdot s}}\right)}{d\left(\frac{1000}{T}\right)} \quad \text{Equation III.43}$$

The results are written in the Arrhenius plot and reported in **Table III.18**, as a comparison, activation energy reported by Sun et al. [274], Babilo et al. [70] and Yamazaki et al. [68] are also presented. In agreement with the literature, each sample shows a lower activation energy in the bulk than in the grain boundary. The behavior indicates a facilitated transport of charged species in the bulk than in the grain boundary [275]. The BZY-com sample exhibits surprisingly high activation energy of 0.90-1.12 eV in wet air. The BZY-c 1000 °C sample has activation energy values in agreement with the literature but BZY-b 1000 °C shows an activation energy in the grain boundary higher than expected. This observation is consistent with the microstructure of the BZY-b 1000 °C sample. Indeed, the Zr-doped Y_2O_3 grains disturb

the diffusion pathway of charged species: the charged species have to bypass the impurity grains and therefore cross more grain boundaries than in the other samples, leading to a higher activation energy of the grain boundary.

Sample	E _a in wet H ₂ (eV)		E _a in wet air (eV)	
	Bulk	Grain boundary	Bulk	Grain boundary
BZY-com	0.45	0.63	0.90	1.12
BZY-c 1000 °C	0.46	0.67	0.45	0.57
BZY-b 1000 °C	0.54	1.06	0.50	1.23
BZY20 Sun 2010	0.45	0.58	0.41	0.58
BZY20 Babilo 2007			0.45	0.71
BZY20 Yamazaki 2009			0.47	0.67

Table III.18: Calculated activation energy of charge carrier transport in the bulk and in the grain boundary in wet air and wet H₂ for BZY-com, BZY-c 1000 °C and BZY-b 1000 °C and reported activation energy from Sun et. al [274], Babilo et al. [70] and Yamazaki et al. [68].

III.3.a.ii. Discussion

Two general behaviors are highlighted from the Arrhenius of plots $\sigma_{AC,B}$ and $\sigma_{AC,GB}$ of the three samples in wet air and wet H₂.

First, the conductivity in wet H₂ is higher than the conductivity in wet air at low temperature (from 200 °C to 550-575 °C as shown in the next paragraph). This observation can be explained by the definition of the conductivity given in **Equation III.31** which correlates the conductivity, the mobility and the concentration of charged species. For the same sample, the mobility of defects at one given temperature is constant regardless of the atmosphere, then the conductivity only depends on the concentration of the charged species. It has been shown in **Figure III.6** that the conductivity is mainly protonic in wet atmosphere at low temperature, then charged species are supposed to be protons in these conditions. Regarding the concentration of defects as a function of the atmosphere exposed in **Figure III.4**, the concentration of OH_O^\bullet is more important in wet H₂ than in wet air, leading to the higher σ_{AC} in wet H₂ than in wet air.

Secondly, the conductivity in the bulk is higher than in the grain boundaries. The most plausible cause of the high resistivity of the grain boundary is that the grain boundary acts as a space charge layer, as represented in **Figure III.20**. The core of the grain boundary is positively charged and, to respect the electroneutrality, the concentration of M_B' increases at both sides of the grain boundary resulting in a decrease of the concentration of $V_O^{\bullet\bullet}$ and OH_O^\bullet and a decrease in the conductivity [240], [276].

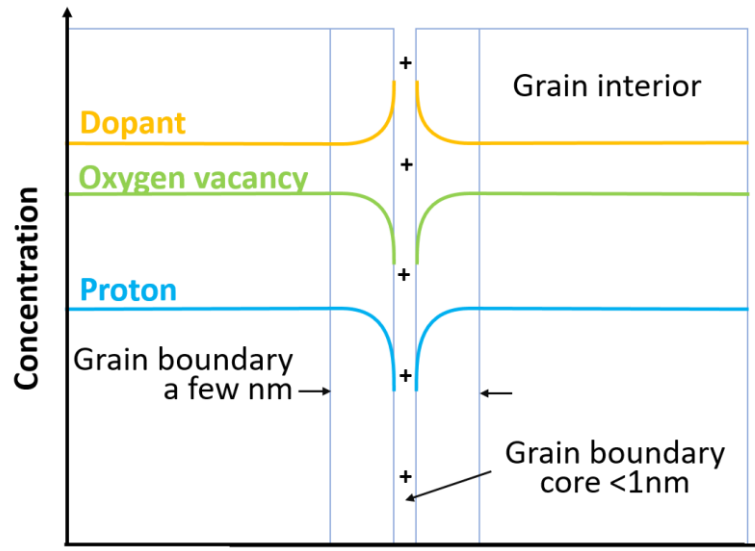


Figure III.20: Schematic illustration of the space charge layer at the grain boundary, adapted from [240]

III.3.b. Total resistance

III.3.b.i. Arrhenius plot of BZY-com, BZY-c 1000 °C and BZY-b 1000 °C

The Arrhenius plot of the $\sigma_{AC,TOT}$ calculated from R_{TOT} of each sample in wet air and wet H_2 of each sample is shown in **Figure III.21**. For each sample, from 200 to 575 °C (550 °C for BZY-c 1000 °C), the total conductivity in wet H_2 is higher than in wet air. This is explained by the higher concentration of protons in wet H_2 .

BZY-com sample (**Figure III.21.a**) exhibits two distinct behaviors in both atmospheres depending on the temperature. From 200 to 575 °C, the conductivity follows an Arrhenius behavior with an activation energy of 0.50 eV in wet H_2 and 0.89 eV in wet air. From 275 to 700 °C, the curves bend resulting in a decrease in the activation energies.

BZY-c 1000 °C (**Figure III.21.b**) exposes three different domains in wet H_2 : from 200 to 400 °C, from 400 to 575 °C and from 600 to 700 °C. At each step, with the increase of the temperature, the activation energy decrease. In wet air, the total conductivity follows an Arrhenius behavior in the whole range of temperature with an activation energy of 0.56 eV.

BZY-b 1000 °C (**Figure III.21.c**) presents three different behaviors in each atmosphere. In wet H_2 , from 200 to 350 °C, the activation energy is 1.02 eV. It decreases at 0.58 eV from 350 °C to 550 °C and at 0.35 eV from 575 to 700 °C. In wet air, the domains are separated as follows: from 200 to 450 °C with an activation energy of 0.89 eV, from 450 °C to 475 °C the activation energy is 0.67 eV before increasing at 0.89 eV from 575 to 700 °C.

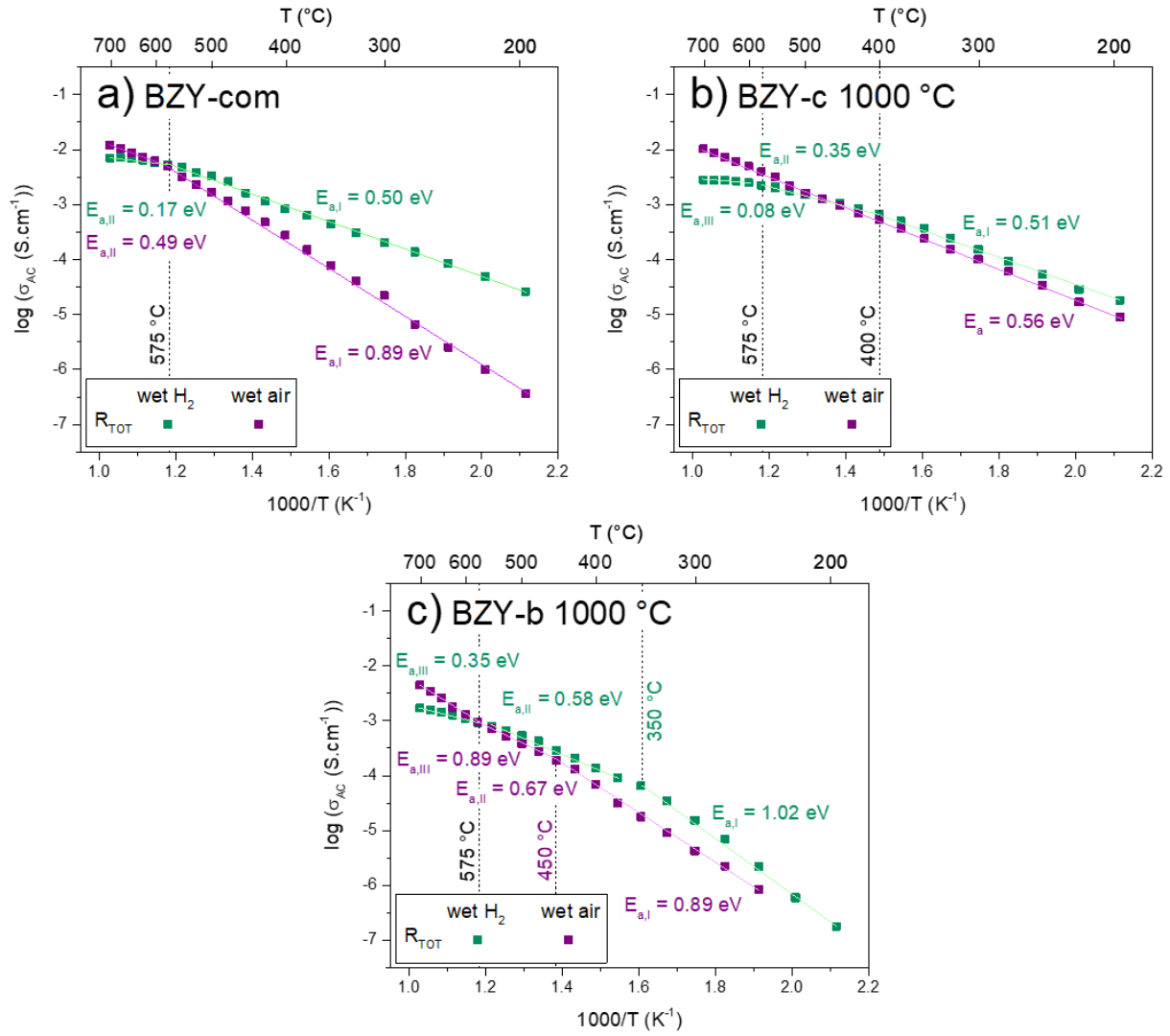


Figure III.21: Arrhenius diagram of σ_{AC} calculated from R_{TOT} in wet air and wet H_2 . a) BZY-com symmetrical cell, b) BZY-c 1000 °C symmetrical cell and c) BZY-b 1000 °C symmetrical cell

III.3.b.ii. Discussion

The general behavior of the $\sigma_{AC,TOT}$ in wet H_2 is the same for each sample. An activation energy of 0.50-0.58 eV is obtained at low-intermediate temperatures. This value is typical of protonic conductivity, indicating that protons are the dominant charge carrier in BZY at a temperature lower than 575 °C [24], [61], [177], [243], [248], [250], [277]. The high activation energy of the BZY-b 1000 °C sample between 200 °C and 350 °C is due to the presence of Zr-doped Y_2O_3 . The bend of the curves in the intermediate temperature domain (from 400 to 575 °C for BZY-c 1000 °C and from 350 °C to 575 °C for BZY-b 1000 °C) is explained by the dehydration of the sample resulting in a decrease in protons concentration [278], [279]. Since BZY-com does present this behavior, it is assumed that the dehydration is more abrupt and occurs at 575 °C. The high-temperature behavior of $\sigma_{AC,TOT}$ in wet H_2 can be explained by two phenomena. First, the decrease in proton concentration is compensated by the higher proton mobility at high temperature and thus the total conductivity in wet H_2 reaches a plateau from

575 °C [280]. Secondly, the high temperatures promotes the formation of electron-holes defects in low P_{O_2} atmosphere resulting in the decrease of the activation energy [67], [236].

In wet air, in the low-temperature domains, protons are the dominant charge carrier. As in wet H_2 , the dehydration of the sample results in a decrease of the proton concentration at intermediate temperature. However, high temperature promotes the emergence of the oxygen-ion conductivity [19], [23]. According to **Equation III.33** which indicates that the total conductivity is the sum of the conductivity of each charged species, the decrease of the proton conductivity is compensated by the increase of the oxygen-ion conductivity, resulting in a constant rise in the total conductivity. It also explains the higher total conductivity in wet air than in wet H_2 from 575 °C in all samples.

Finally, the values of $\log \sigma_{AC,TOT}$ in the 200 – 300 °C range in either atmosphere are similar to the values $\log \sigma_{AC,GB}$ suggesting that BZY total conductivity is dominated by the grain boundary. Thus, elaborating an electrolyte with large grains or columnar grains in order to minimize the space charge layer effect at the grain boundary would greatly improve the protonic conductivity and thus the performances of the cell.

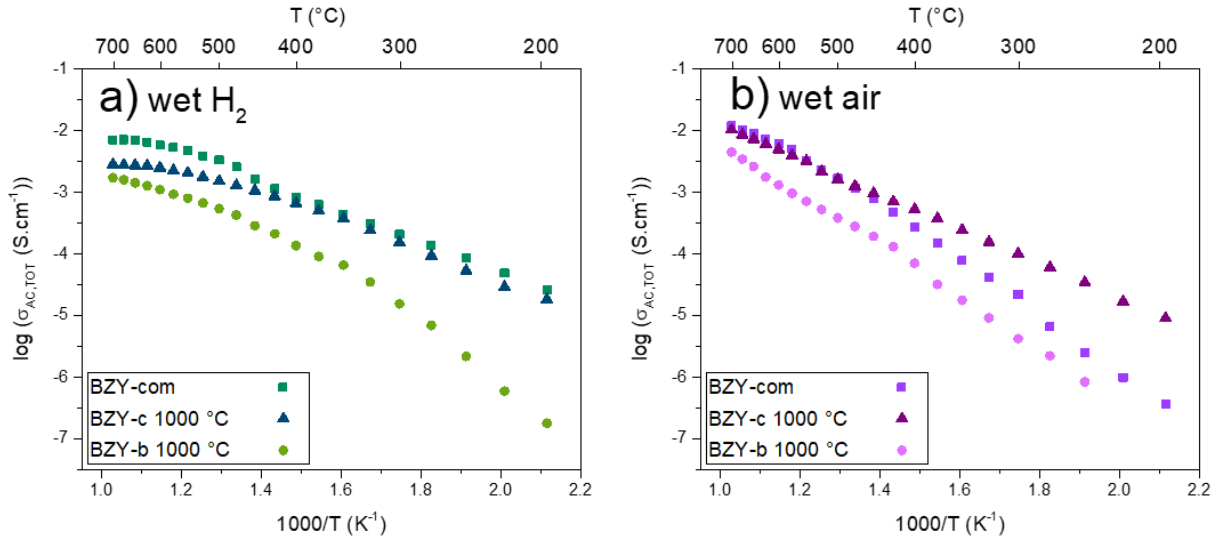
II.4. Comparison of conductivity of BZY-com, BZY-c 1000 °C and BZY-b 1000 °C samples

To be more comparable, the Arrhenius plot of each sample in wet H_2 and in wet air is presented in **Figure III.22.a and b** respectively. In addition, the $\sigma_{AC,TOT}$ in wet H_2 and wet air at 300 °C and 600 °C are presented in **Table III.19**.

As represented in the Arrhenius plot in wet H_2 presented in **Figure III.22.a**, the conductivity of the BZY-com sample and the BZY-c 1000 °C sample are comparable in wet H_2 at low temperature. The conductivity in wet H_2 at 300 °C is about $2 \times 10^{-4} \text{ S.cm}^{-1}$, similar values were reported by Sun *et al.* for BZY20 [275]. BZY-b 1000 °C exhibits a value of one order of magnitude lower due to the presence of Zr-doped Y_2O_3 . At 600 °C, in wet H_2 , the $\sigma_{AC,TOT}$ is higher for BZY-com than BZY-c 1000 °C and, of course, than BZY-b 1000 °C. The values are 5.8×10^{-3} and $2.5 \times 10^{-3} \text{ S.cm}^{-1}$ for BZY-com and BZY-c 1000 °C respectively. This difference could be explained by the lower dopant concentration in BZY-c 1000 °C than in the BZY-com. Moreover, as a reminder, the reported total conductivity values of BZY differ from 10^{-6} to $10^{-2} \text{ S.cm}^{-1}$ at 600°C in wet H_2 [70]. Then, the conductivity of BZY-com and BZY-c 1000 °C is situated in the upper part of the range.

In wet air, at low temperature, BZY-c 1000 °C has the highest conductivity. At 300 °C, the $\sigma_{AC,TOT}$ is $1.0 \times 10^{-4} \text{ S.cm}^{-1}$, slightly lower than the value in wet H_2 . It suggests that the proton incorporation and the proton mobility is similar in wet air and wet H_2 for BZY-c 1000 °C, while it is favored in wet H_2 for BZY-com and BZY-b 1000 °C. At high temperatures, the conductivity of BZY-com and BZY-c 1000 °C becomes similar and reached a value about $5 \times 10^{-3} \text{ S.cm}^{-1}$ while BZY-b 1000 °C still exhibits lower values due to the presence Zr-doped Y_2O_3 .

Sample	BZY-com	BZY-c 1000 °C	BZY-b 1000 °C
$\sigma_{AC,TOT}$, wet H_2 , 300 °C ($S.cm^{-1}$)	2.0×10^{-4}	1.5×10^{-4}	1.5×10^{-5}
$\sigma_{AC,TOT}$, wet H_2 , 600 °C ($S.cm^{-1}$)	5.8×10^{-3}	2.5×10^{-3}	1.1×10^{-3}
$\sigma_{AC,TOT}$, wet air, 300 °C ($S.cm^{-1}$)	2.2×10^{-5}	1.0×10^{-4}	4.2×10^{-6}
$\sigma_{AC,TOT}$, wet air, 600 °C ($S.cm^{-1}$)	6.2×10^{-3}	5.0×10^{-3}	1.3×10^{-3}

 Table III.19: Total conductivity of each sample in wet H_2 and wet at 300 and 600 °C

 Figure III.22: Arrhenius diagram of σ_{AC} calculated from R_{TOT} of BZY-com, BZY-c 1000 °C and BZY-b 1000 °C symmetrical cell. a) in wet H_2 and b) in wet air.

IV. Conclusion

The AC total conductivity was evaluated in BZY-com, BZY-c 1000 °C and BZY-b 1000 °C in wet air and wet H_2 by electrochemical impedance spectroscopy. The symmetrical cells, consisting of BZY as electrolyte, were prepared by uniaxial pressing and sintering at 1550 °C for 5 hours. 1 wt% of ZnO was added as sintering aid to reach a densification rate of the order of 90 %. Ag-electrodes were painted on both sides of the BZY pellet and fired at 800 °C for two hours.

The AC total conductivity of BZY-b 1000 °C in both atmospheres is one order of magnitude lower than the other sample due to the presence of Zr-doped Y_2O_3 . Then, it is crucial to avoid the formation of (Y,Zr)O(OH) species that lead to the formation of Zr-doped Y_2O_3 during annealing at 1000 °C and sintering by controlling the synthesis parameters.

The EIS measurement on the BZY-c 1000 °C evidenced that the resistance of grain boundary is lower than the one of the other samples, this is a result of a lower space charge effect in the BZY-c 1000 °C sample. This could be due to the lower dopant concentration in the initial powder evidenced in chapter II. However, at a higher temperature, a lower dopant concentration is detrimental for the conductivity since it decreases the proton incorporation. As

a reminder, proton incorporation occurs via the oxygen vacancies introduced by the substitution of a trivalent element.

BZY-com sample presents the highest total conductivity values: $5.8 \times 10^{-3} \text{ S.cm}^{-1}$ in wet H_2 and $6.1 \times 10^{-3} \text{ S.cm}^{-1}$ in wet air. BZY-c 1000 °C exhibits slightly lower values of $2.5 \times 10^{-3} \text{ S.cm}^{-1}$ in wet H_2 and $5.0 \times 10^{-3} \text{ S.cm}^{-1}$ in wet air. These values are acceptable for utilization in PCFC. Moreover, it is supposed a higher total conductivity could be obtained from an electrolyte with large or columnar grains.

To finish, the conductivity determined in this study takes into account all the charged carriers species. Even if it can reasonably be supposed that protons are the dominant charge carriers at a temperature lower than 575 °C in both atmosphere, it would be interesting to determine the nature of the charge carrier depending on the temperature by performing electromotive force measurement and calculate the transport number of each species.

CHAPTER IV: ELABORATION AND CHARACTERIZATION OF PCFC

The present chapter describes in the first part the elaboration specification of a PCFC and the elaboration routes used in this work.

The second section presents the fabrication and the characterization of PCFC half-cells elaborated by a co-tape casting and co-sintering process.

The third part exposes the fabrication of PCFC by a process consisting of co-tape casting, co-sintering and reactive pulsed direct current sputtering and spray-coating. The characterizations at each step are presented.

In the last section, the electrochemical performances measured by electrochemical impedance spectroscopy are shown and the reduction step prior to the cell operation is described.

I. Presentation of the complete cell and elaboration procedures

Despite their highly promising performances and various advantages, the PCFCs attract skepticism about their applicability. It mainly stems from the difficulty to scale up the fabrication procedure of such cells due to the highly refractive nature of conventional electrolyte materials [115], [124]. Then, the fabrication of large area, stable and exhibiting reasonable performances PCFCs still remains a challenge [281]. This section aims to provide an overview of the specification of PCFCs and the different elaboration routes. Finally, the two routes used in this work, one aiming the large at low-cost production and the other one targeting a high-performances goal, will be presented.

I.1. Specifications

The choice of materials has been discussed in the first chapter, but specifications concerning the elaboration will be presented in this paragraph. The complete cell is an anode-supported fuel cell as illustrated by the schematic in **Figure IV.1**. The cell is composed of four layers.

- The anode, place of the Hydrogen Oxidation Reaction (HOR) and composed of a Ni-BZY cermet, ensures the mechanical strength of the cell and, for this reason, needs to be sufficiently thick. The target thickness is in the range of 350 – 400 μm . Furthermore, the anode must be porous to assure the gas diffusion.

- The anode functional layer (noted AFL) is made of the same materials as the anode but is denser. The purpose is to improve the contact between the porous anode and the

electrolyte. From the electrochemical point of view, it results in an increase of the number of Triple Phase Boundary (TPB) and gain of the performances on the HOR side [282], [283]. From the elaboration point of view, it avoids the risk of crack and delamination, as shown by the pictures of half-cells in **Annex E**. Its thickness should be between 20 and 60 μm .

- The BZY electrolyte is the key component of the cell. It has to be dense, covering and homogeneous over the entire surface of the cell. Furthermore, it should be as thin as possible to decrease the ohmic loss [284]. Typically, the thickness should be less than 10 μm . BZY-com exhibited $5 \times 10^{-3} \text{ S.cm}^{-1}$ at 600 $^{\circ}\text{C}$, indicating that, for the same microstructure, a thickness of the electrolyte should be maximum 10 μm to have an ASR of $0.2 \Omega.\text{cm}^2$ for the ohmic resistance at 600 $^{\circ}\text{C}$ [285].

- The cathode, place of the Oxygen Reduction Reaction (ORR), is a composite of BZY and BSCF and should be sufficiently porous to allow the steam diffusion. The thickness should be in the 20 – 60 μm to ensure effective charge transfer [102].

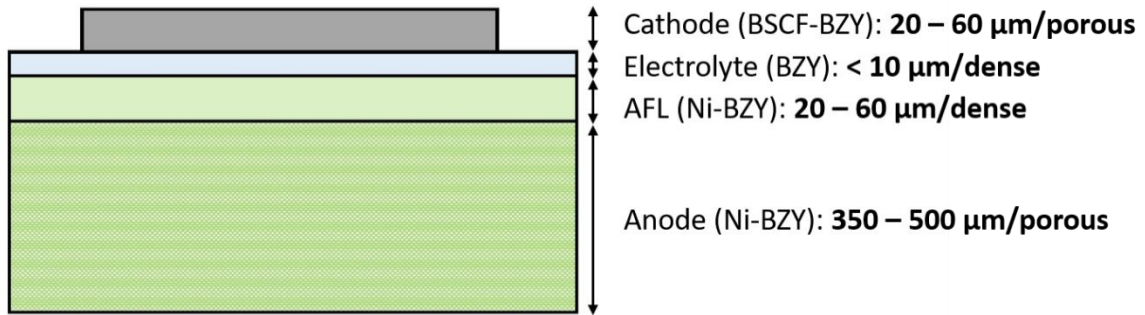


Figure IV.1: Schematical representation of the target PCFC cell

I.2. Fabrication procedures of the cells

The conventional method of elaboration of complete PCFC cell consists in the elaboration of the anode and the AFL together, followed by the deposition of the electrolyte and the co-sintering of the half cell. The following steps are the cathode deposition on the top of the electrolyte and its sintering at a reduced temperature to achieve the final complete cell [286]. A comparison of the classical elaboration method is given in **Table IV.1**. A highly conventional elaboration process is not exposed in this Table: the uniaxial pressing. This method is widely used for the anode or anode-AFL elaboration [287]–[291]. It is a cost-effective process that allows the fabrication of robust anode support, however, the thickness and the geometry are not easily controllable and thin layers are difficult to obtain.

To achieve the goal of low cost, high efficiency, and mass fabrication, the more efficient methods are the screen printing and the tape casting. In this thesis work, the tape-casting was chosen. The fabrication by tape-casting of SOFC based on the $\text{Ce}_{0.8}\text{Gd}_{0.2}\text{O}_{2-\delta}$ electrolyte was developed in the ICB-laboratory as part of Visweshwar Sivasankaran thesis [15]. A patent on complete cell fabrication by co-tape casting followed by a single step sintering was deposited

[292]. However, the highly refractory nature of BZY involves high sintering temperature that makes the co-sintering of BZY and BSCF impracticable due to a strong mismatch between their TEC (TEC of BSCF is $\sim 20 \times 10^{-6} \text{ K}^{-1}$ [293] and TEC of BZY is $\sim 8 \times 10^{-6} \text{ K}^{-1}$ [121]). Then, the procedure was adapted to the fabrication of PCFC as shown in **Figure IV.2**. It consists in the co-tape casting of the anode-AFL-electrolyte assembly followed by a sintering at high temperature. NiO powder was used in the elaboration process and is reduced in Ni during cell operation. The cathode was then deposited by spray using an airbrush and the complete cell was fired at intermediate temperature to sinter the cathode layer. The heating and cooling ramp for the two sintering procedures is $3 \text{ }^{\circ}\text{C}.\text{min}^{-1}$. A dwell time at $400 \text{ }^{\circ}\text{C}$ for 2 hours was applied to eliminate the organic component of the slurries used for tape casting and spray deposition before heat up to $1500 \text{ }^{\circ}\text{C}$ for 5 hours in the case of the half cell and $800 \text{ }^{\circ}\text{C}$ for 2 hours in the case of the complete cell.

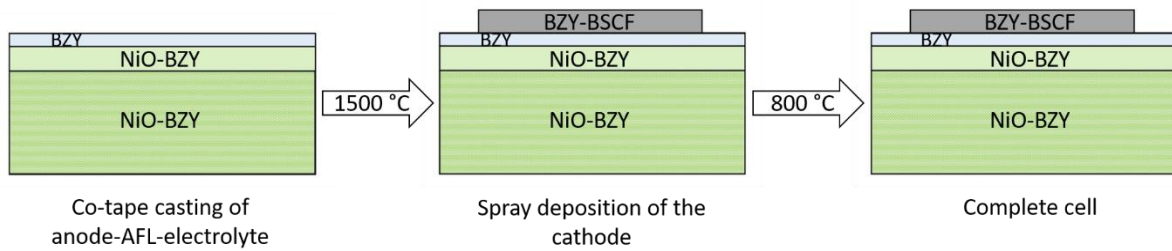
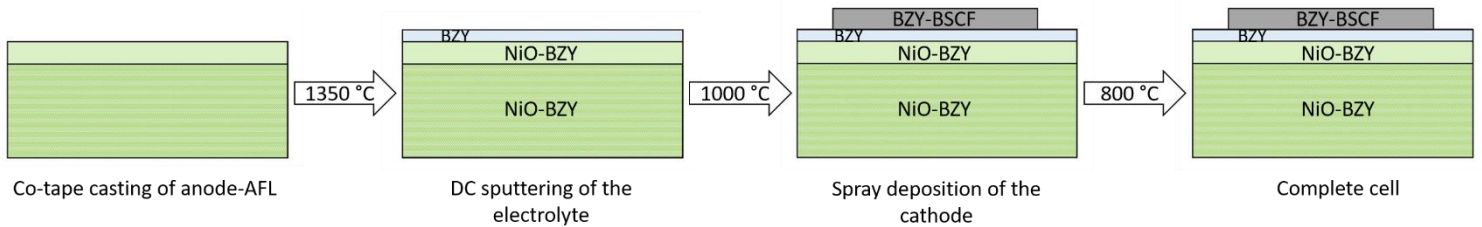


Figure IV.2: Schematic representation of the fabrication of PCFC by co-tape casting and spray deposition

Furthermore, a second approach was also carried out in order to improve the performance of the cell to the detriment to the cost efficiency. In this elaboration route, the BZY electrolyte was deposited by reactive pulsed DC sputtering on the top of the anode-AFL assembly prepared by co-tape casting and co-sintered at $1350 \text{ }^{\circ}\text{C}$ for 5 hours. Finally, the cathode was spray-deposited prior to the sintering at $800 \text{ }^{\circ}\text{C}$ for 2 hours to obtain the final complete cell. This procedure route is schematically represented in **Figure IV.3**.

Figure IV.3: Schematic representation of the fabrication of PCFC by co-tape casting, reactive pulsed DC sputtering and spray deposition



Method	Advantages	Disadvantages	Deposition rate or thickness of film	Cost
Screen printing	Minimization of the cracks problem during sintering process and easy scaling-up	Formulation of the ink	1.5 – 30 μm	Economical
Tape casting	Large thickness range, multilayer production, large-area, flat and fabrication of green material	Slow drying process, possibility of crack, formulation of the ink	25 – 2000 μm	Economical
Sol-gel	Control of the stoichiometry	Require many steps	0.5 – 1 μm for each coating	Expensive
Chemical vapor deposition	High quality of thin film	Require high operating temperature	1 – 10 $\mu\text{m/h}$	Expensive
Electrochemical vapor deposition	Easy deposition of dense material on a porous substrate, highly homogeneous film production	High-cost production, possible corrosion by gases	3 – 50 $\mu\text{m/h}$	Expensive
Physical vapor deposition	Simple and accessible target material, control of the stoichiometry	High-cost production	0.25 – 2.5 $\mu\text{m/h}$	Expensive
Pulsed laser deposition	High quality of coating, control of the stoichiometry, nanostructuration	Sensitive to pollution and high-cost production	60 – 150 $\mu\text{m/h}$	Expensive
Dip and spin coating	High performance coating	Formulation of the ink, long-time process	25 – 200 μm	Economical

Table IV.1: Comparison of some classical elaboration method of SOFC, adapted from [294], [295]

II. Fabrication of PCFC half-cells by co-tape casting

In this section, half-cells were elaborated by a co-tape casting and co-sintering cost-effective process. When the parameters are adjusted and optimized, this route allows the production of half-cells exhibiting perfectly adherent layers at a large scale. A highly covering 10 μm thick electrolyte is obtainable with high reproducibility. However, the need for a high sintering temperature to achieve sufficient densification of the electrolyte involves slight reactivity that could lead to a decrease in cell performances.

II.1. Formulation of the slurries and preparation of the green half-cells

The shaping of ceramic layer by tape-casting involves the use of slurry containing the ceramic powder, solvent, binder, plasticizer and eventually additive such as pore-former, dispersant or surfactant [296], [297]. The slurry has to be formulated in order to obtain a tape with a good flexibility and manageability [296]. The quantity used for the first slurries preparation, based on the thesis from Visweshwar Sivasankaran, is presented in **Table IV.2** [15]. In a first step, ceramic powders (BZY and NiO) and eventually additive such as carbon as pore-former or ZnO as sintering aid, were mixed with the solvents (ethanol (EtOH) and methyl ethyl ketone (MEK)) and the triethanolamine (TEA) as dispersant. This preparation was ball milled in a Turbula-T2F device (Willy A. Bachofen AG Group) for 16 h. In the second step, polyvinyl butyral (PVB) as the binder and polyethylene glycol (PEG) and benzylbutyl phthalate (BBP) as plasticizers were added to the preparation and ball milled for 24 h. The NiO/BZY weight ratio was set to 60/40 to reach a 50/50 volumic ratio and ensure the percolation of the two sub-lattice [298].

	BZY (g)	NiO (g)	ZnO (g)	C (g)	EtOH (g)	MEK (g)	TEA (g)	PVB (g)	PEG (g)	BBP (g)
Anode	20	30	0	5	10.3	10.3	1.6	3.5	1.6	1.6
AFL	8	12	0	0	3.6	3.6	0.6	1.2	0.6	0.6
Electrolyte	5	0	0.05	0	3.1	3.1	0.35	0.9	0.35	0.35

Table IV.2: Quantity used for the first anode, AFL and electrolyte slurry preparation, based on the thesis from Visweshwar Sivasankaran [15].

The electrolyte slurry was firstly tape cast on a glass plate using an automatic tape caster Elcometer 4340 (Elcometer) at a casting rate of $1 \text{ cm} \cdot \text{s}^{-1}$. The blade gap thickness was fixed 60 μm . The electrolyte layer was air-dried at room temperature for 30 min before the AFL was tape cast above, the doctor blade height was set to 120 μm . After a new drying period of 30 min, the anode was tape cast on the top of the AFL at a thickness of 1 mm. Due to the thickness of the anode layer, the drying time was 16 hours. **Figure IV.4.a** exhibits a picture of the anode-AFL-electrolyte green tape after the night of drying. As it can be seen, the anode layer is

fractured. The main reason is the inhomogeneous drying due to the large thickness of the layer: the surface dries faster than the bulk, when the volatile species of the bulk evaporate, it cracks the surface. The green half-cells were cut with a punch of 28 mm in diameter in the clean areas. **Figure IV.4.a** exhibits a picture of two green cells. As it can be seen, a binding effect resulting from too significant surface tension is apparent. Furthermore, the electrolyte layer, highlighted on the bottom cell, presents many defects such as delamination, pin-holes and cracks, indicating the non-suitability of the slurry formulation.

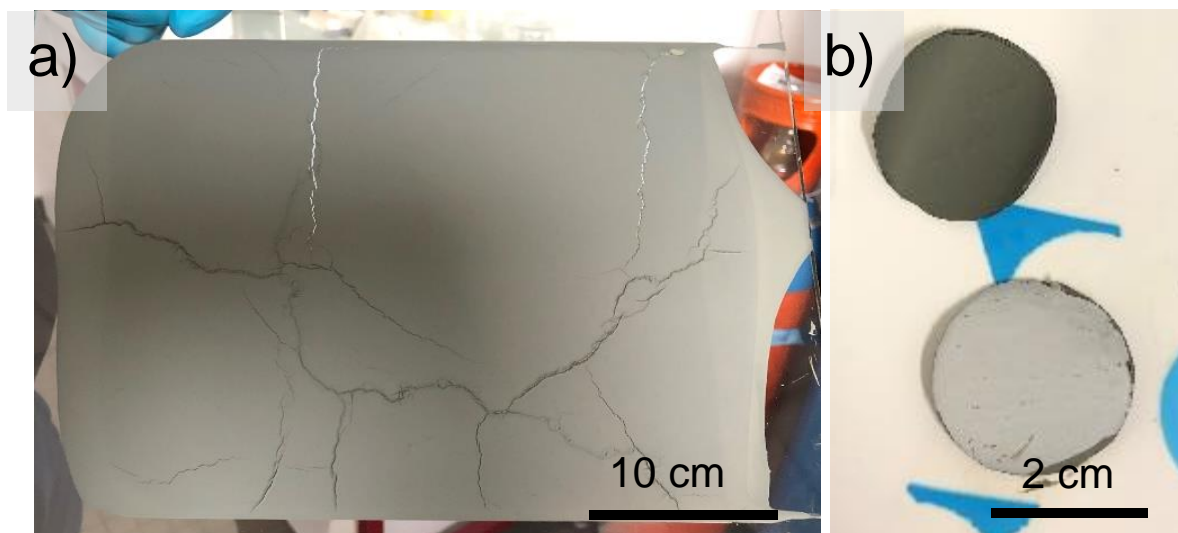


Figure IV.4: Pictures of a) anode-AFL-electrolyte green tape after the night of drying, view from the anode side and b) two green cells after cutting, anode side on the top and electrolyte side on bottom

Several trials were attempted before reaching a good flexibility and plasticity of the green tapes. The optimized quantity used in each slurry is presented in **Table IV.3**. In the anode and AFL slurries, the quantity of solvent, dispersant and plasticizer was increased by 33 % and the amount of binder by 50 %. In the electrolyte slurry, the amount of solvent and dispersant was increased by 6 % and the quantity of binder and plasticizer by 10 %.

	BZY (g)	ZnO (g)	NiO (g)	C (g)	EtOH (g)	MEK (g)	TEA (g)	PVB (g)	PEG (g)	BBP (g)
Anode	20	0	30	5	13.7	13.7	2.1	5.25	2.1	2.1
AFL	8	0	12	0	4.8	4.8	0.8	1.8	0.8	0.8
Electrolyte	5	0.05	0	0	3.3	3.3	0.37	1	0.38	0.38

Table IV.3: Optimized quantity of anode, AFL and electrolyte slurries.

The shaping procedure was the same as before. The drying time of the electrolyte was decreased down to 10 min to enhance its adherence with the AFL tape. As shown in **Figure IV.5.a** and **b**, no cracks appear in the green tape. The half-cells are easy to cut and peel off from the glass plate, each layer is adherent to the others and the assembled tape is very flexible and malleable.

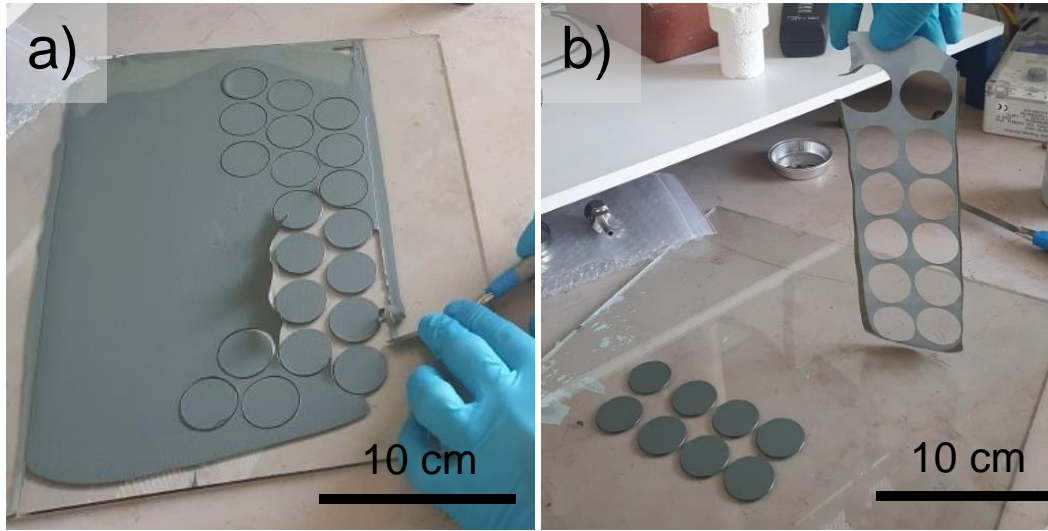


Figure IV.5: Pictures of the anode-AFL-electrolyte green tape, a) during the punching of the half-cells, b) after cutting

II.2. Co-sintering of the green half-cells

A pellet of 8 mm in diameter consisting of 60 %wt of NiO and 40 %wt of BZY-c 1000 °C, the same ratio as in the slurries, was prepared by uniaxial pressing under a pressure of 200 MPa. **Figure IV.6** presents the dilatometry profile up to 1500 °C using rates of 3 °C.min⁻¹ of the composite pellet. As shown in **Figure IV.6.a** which represents the $\Delta L/L_0$ as a function of the temperature, the shrinkage of the pellet starts at 875 °C and is globally homogeneous. On the derivative signal shown in **Figure IV.6.b** two peaks of maximum shrinkage speed are highlighted. The one at 1350 °C is attributed to the shrinkage of BZY according to the dilatometry profiles of BZY exhibited in Chapter III while the peak at 1200 °C corresponds to the shrinkage of NiO. It should be noticed that the signal of BZY in this sample is very similar to the one of BZY mixed with 1 wt% of ZnO since NiO also acts as a sintering aid [64], [299].

The homogeneity of the shrinkage and the acceptable temperature difference between the two maximum shrinkage speeds indicates the feasibility of the co-sintering of NiO and BZY.

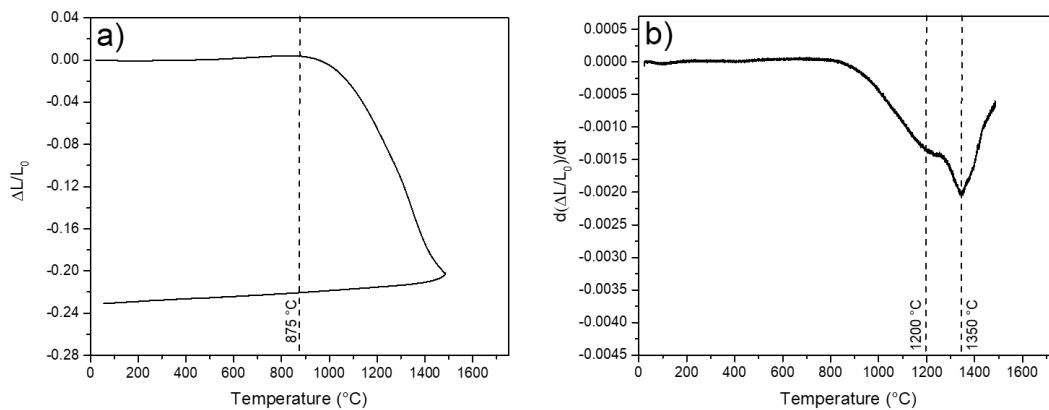


Figure IV.6: Dilatometry profile of the BZY-c 1000 °C-NiO pellet. 60%wt NiO/40%wt BZY. a) $\Delta L/L_0$ as a function of the temperature; b) $d(\Delta L/L_0)/dt$ as a function of the temperature

In the previous chapter, the sintering temperature of BZY-1 wt% ZnO was 1550 °C to ensure a densification rate of at least 90 %. The same procedure was attempted for the co-sintering of half-cells. To maintain the half-cells' flatness, they were sintered between a Pt plate on the electrolyte side and a cordierite plate on the anode side. The thermal treatment was carried out at 3 °C.min⁻¹ and a dwell time at 400 °C was added to decompose the organic component of the slurry before the plateau at 1550 °C for 5 hours.

The XRD pattern of a half-cell sintered at 1550 °C is exposed in **Figure IV.7.a** for the electrolyte face and **Figure IV.7.a** for the anode face. Two phases are highlighted in the electrolyte layer: one major BZY phase (69 wt% determined by Rietveld refinement) and one Zr-doped Y₂O₃ (31 wt%). On the anode side, three phases were detected: BZY, NiO and Zr-doped Y₂O₃ with respective relative percentages determined by Rietveld refinement of 36, 49 and 15 wt%.

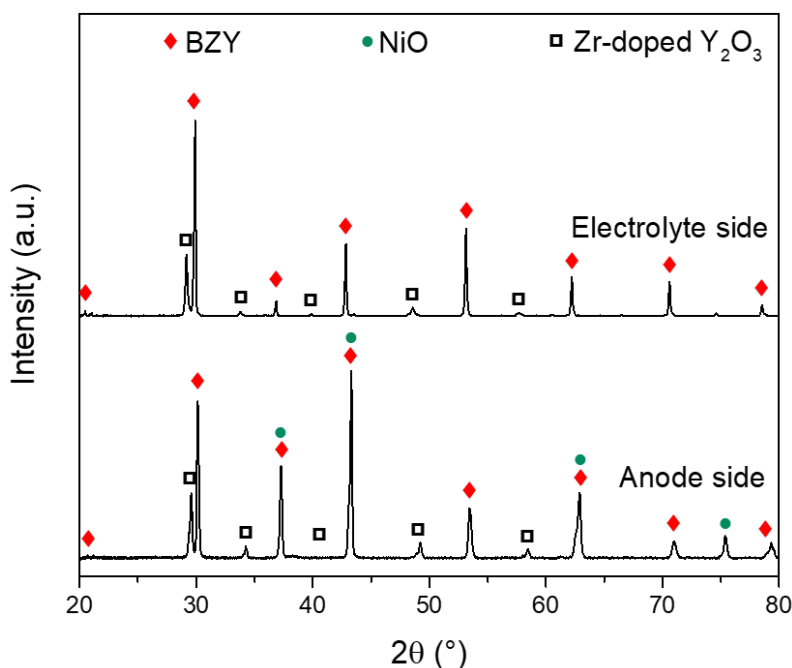


Figure IV.7: X-ray diffractograms of the half-cell sintered at 1550 °C for 5 hours, top: electrolyte side and bottom: anode side

To limit the proportion of Zr-doped yttria highly detrimental to the electrolyte performances, the sintering temperature was decreased at 1500 °C. The microstructure of the half-cell is exposed in **Figure IV.8**. In the BSE-SEM micrograph (**Figure IV.8.a**), BZY is the lightest color while NiO is in dark grey. As shown in **Figure IV.8.a** and **b**, the thickness of the anode layer is 480 µm, the AFL is 50 µm thick and the electrolyte is 9 µm, corresponding perfectly to the specifications. Furthermore, the anode is porous while both AFL and electrolyte are quite dense. Some porosity is present in the electrolyte as shown by the surface view in **Figure IV.8.c** but they are not detrimental for the cell performance since they are not crossing the electrolyte layer. Each layer presents a homogeneous thickness, is highly covering and perfectly adherent to each other. Finally, the BZY sub-lattice and the NiO sub-lattice are well

distributed. The main defect is the coarsening of NiO particles that could lead to the cell disruption during the reduction [89].

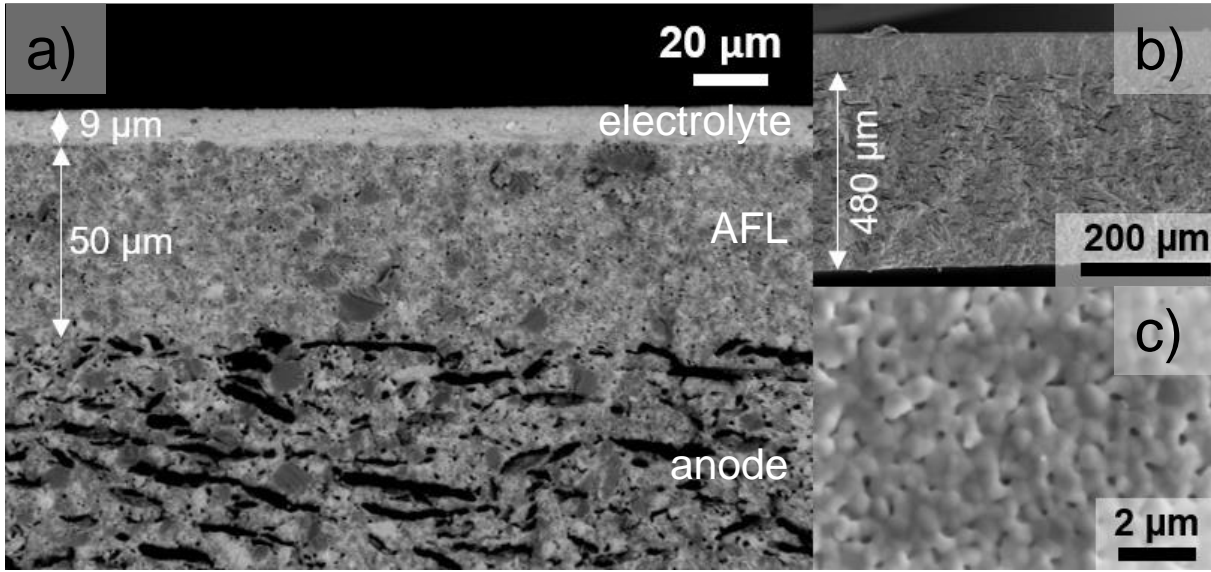


Figure IV.8: SEM micrographs of the anode-AFL-electrolyte assembly elaborated by co-tape casting and co-sintering at 1500 °C. a) cross-section, b) cross-section (global view) and c) surface of the electrolyte

Furthermore, the composition of BZY is not preserved during the sintering. The starting powder was BZY-com, showing a composition of $\text{Ba}_{1.01 \pm 0.02} \text{Zr}_{0.81} \text{Y}_{0.19 \pm 0.01} \text{O}_{3-\delta}$ determined by EDS. After sintering, the chemical composition of BZY in the electrolyte layer was $\text{Ba}_{0.96 \pm 0.04} \text{Zr}_{0.89} \text{Y}_{0.11 \pm 0.02} \text{O}_{3-\delta}$. As exhibited by the X-ray diffractogram presented in **Figure IV.9**, segregation of phase due to Ba vaporization still occurs during sintering at 1500 °C leading to the formation of Zr-doped Y_2O_3 secondary phase. In contrast, no reactivity was highlighted on the anode side.

To decrease the amount of Zr-doped Y_2O_3 again, the sintering was carried out at 1450 °C for five hours. However, as exhibited in **Figure IV.10**, it leads to insufficient densification of the electrolyte layer, leading to a drop in the cell performances. Then, the second elaboration procedure, i.e., depositing the electrolyte layer by pulsed reactive DC sputtering on anode-AFL substrates prepared by co-tape casting was attempted.

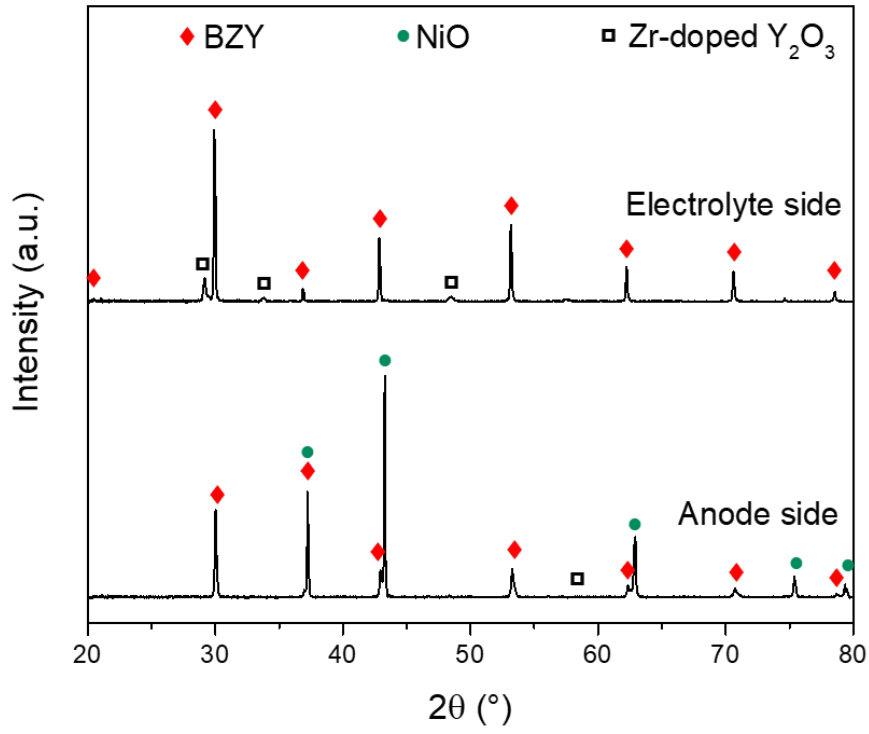


Figure IV.9: X-ray diffractograms of the half-cell sintered at 1500 °C for 5 hours, top: electrolyte side and bottom: anode side

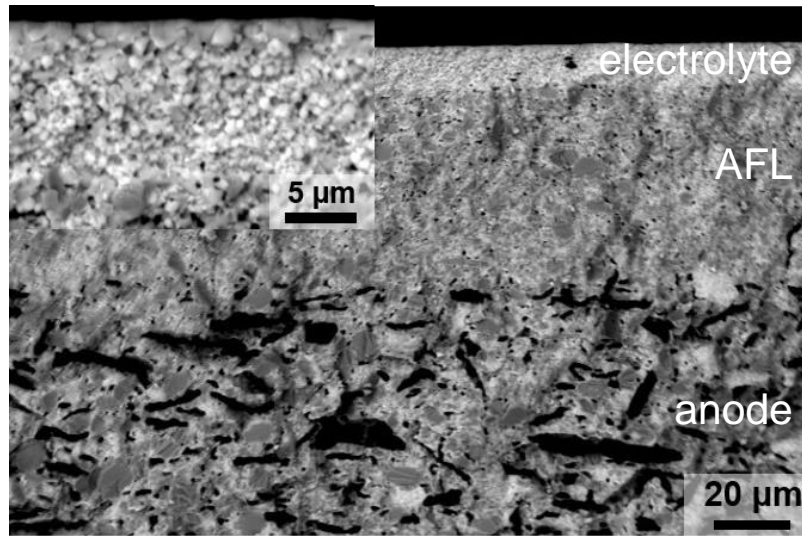


Figure IV.10: SEM micrographs of the anode-AFL-electrolyte assembly elaborated by co-tape casting and co-sintering at 1450 °C.

III. Fabrication of PCFC complete cells

Physical preparation method such as pulsed laser deposition and reactive Direct Current (DC) sputtering allows the elaboration of thin, dense and highly texturized coating [294], [295]. The efficiency of such techniques has already been demonstrated in the PCFC area. For example, Pergolesi *et al.* have reported an extremely high total conductivity of 0.11 S.cm^{-1} at 500°C in wet H_2 for epitaxial BZY20 of 60 nm thick elaborated on MgO single-crystal substrate by pulsed laser deposition [69]. More recently, Bae *et al.* have reported a maximum power density of 740 mW.cm^{-2} at 600°C for a $2 \mu\text{m}$ thick BZY15 electrolyte deposited by pulsed laser deposition [300]. No studies were found in the literature concerning the deposition of BZY by reactive DC sputtering in the preparation of complete cells. However, Arab Pour Yazdi *et al.* have demonstrated the possibility of depositing BZY on polycrystalline alumina support by this technique [301]. This section presents the feasibility of elaborating complete PCFC cells by co-tape casting, reactive DC sputtering and spray deposition. The physical deposition of BZY was carried out in collaboration with Mohammad Arab Pour Yazdi and Pascal Briois from the FEMTO-ST laboratory from Université de Technologie de Belfort Montbéliard (UTBM).

III.1. Elaboration of anode-AFL by co-tape casting

The slurries of anode and AFL were prepared according to the procedure described previously and using the quantity shown in **Table IV.3**. The carbon graphic pore-former was replaced by black carbon pore-former to avoid the formation of needle-shaped porosity that could act as pre-crack and lead to the disruption of the cell [302]. Different sintering temperatures were attempted: 1450°C , 1400°C and 1350°C using the same heating and cooling rates and the debinding step as in the previous section. As shown in **Figure IV.11**, where pictures of anode-AFL substrates sintered at different temperatures are displayed, the reject rate representing the number of unusable substrates increases with the sintering temperature. For sintering at 1450°C , the reject rate is 100 % while it approaches 0 % for the substrates sintered at 1350°C .

The microstructure of the substrates sintered at 1350°C for 5 hours is highlighted in **Figure IV.12**. As shown in **Figure IV.12.a**, the AFL layer of $20 \mu\text{m}$ looks dense while the $460 \mu\text{m}$ thick anode is porous. The small and light gray grains in **Figure IV.12.b** corresponds to BZY, they are homogeneously distributed around the larger and darker grains of NiO.

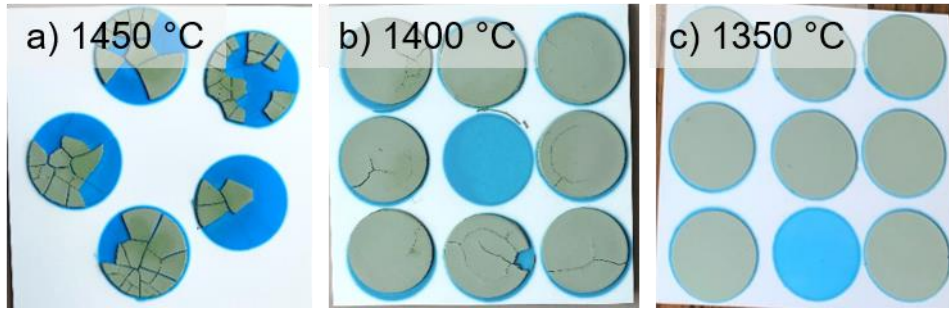


Figure IV.11: Pictures of sintered anode-AFL assembly elaborated by co-tape casting, a) 1450 °C, b) 1400 °C and c) 1350 °C

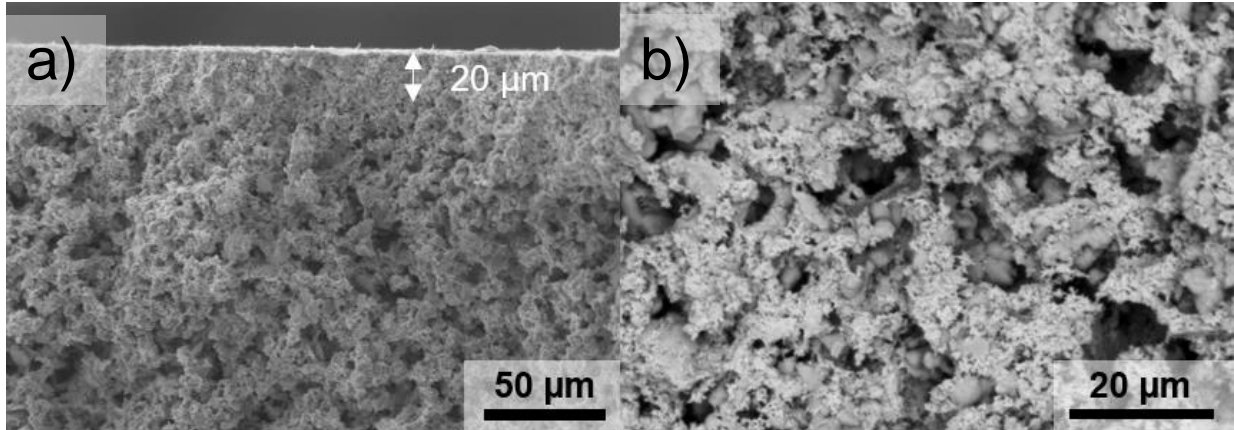


Figure IV.12: SEM micrographs of the anode-AFL substrate elaborated by co-tape casting and co-sintering at 1350 °C. a) cross-section (global view) and b) zoom in the anode layer

III.2. Deposition of the electrolyte by reactive pulsed DC sputtering

III.2.a. Presentation of the device and depositions conditions

The electrolyte layer was deposited in a 90 L Alcatel 604 SCM sputtering chamber pumped down via a system combining XDS35i dry pump and a 5401CP turbo-molecular pump pumping down to 10^{-4} Pa. A photograph of the device is exposed in **Figure IV.13.a**. The BZY layer was elaborated by co-sputtering of Ba (purity 99.9 %, Ø 50 mm × 3 mm) and $Zr_{0.8}Y_{0.2}$ (purity 99.9 %, Ø 50 mm × 6 mm) targets. The two targets are highlighted in **Figure IV.13.b**. They were supplied with a pulsed DC (Direct Current) Advanced Energy dual generator authorizing the control of the discharge power.

The rotating sample holder, supporting the anode-AFL substrates, is heated by radiative effect at 400 °C and placed opposite to the targets, at a distance of 60 mm. During the deposition stage, a radiofrequency bias (15V to 30V) is applied to the sample holder to favor the stability of the magnetron discharge. The gas flow rates for reactive conditions are set at 5 mL.min⁻¹ for oxygen and 50 mL.min⁻¹ for argon. The final pressure is around 1 Pa. The parameters of each target are presented in **Table IV.4**. The deposition time was set to 1 hour to obtain a layer of 2.5 µm and 2 hours for a layer of 5 µm.

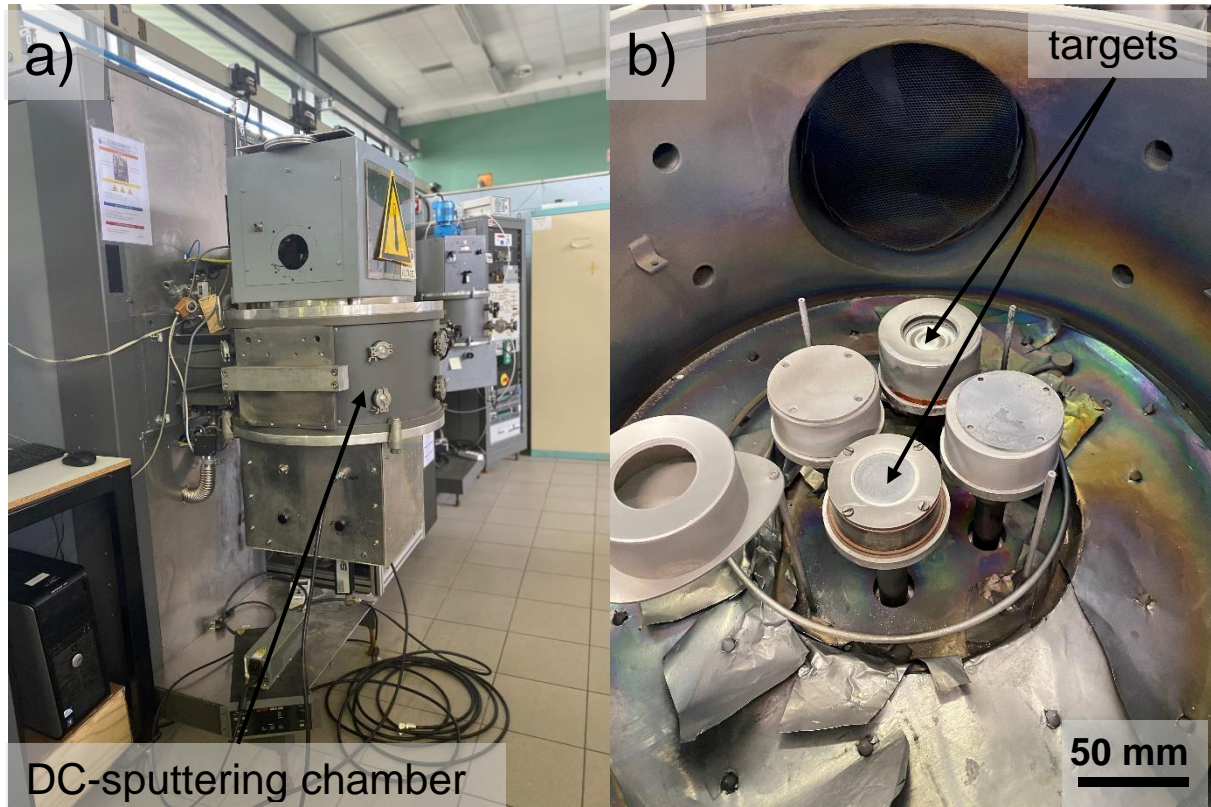


Figure IV.13: Photographs of the DC sputtering device. a) general view, b) inner chamber

Target	Power (W)	Tension (V)	Intensity (A)	Time off (μ s)	Frequency (kHz)
Ba	85	161	0.56	2	150
Zr _{0.8} Y _{0.2}	80	242	0.33	4	50

Table IV.4: Sputtering deposition parameters of Ba and Zr_{0.8}Y_{0.2} targets

III.2.b. Characterization of the BZY electrolyte

The microstructure of the BZY layer elaborated by DC sputtering was investigated by SEM Hitachi SU8230 coupled with a Thermo-Scientific UltraDry EDS detector. The micrograph is shown in **Figure IV.14.a**. The thickness is 2.5 μ m, the layer is highly covering, dense and no delamination between AFL and electrolyte was found. Furthermore, grains are highly epitaxial, presenting the characteristic columnar shape of thin film deposited by physical vapor methods. The columns are tilted due to the vapor flux angle [303], [304]. Indeed, the Ba and Zr_{0.8}Y_{0.2} targets were tilted by 15 ° to the normal to the surface of the support.

To improve the crystal quality, an annealing treatment at 1000 °C was carried out [305], [306]. The micrograph post-annealing is exposed in **Figure IV.14.b**. The same dense columnar microstructure is observed and the AFL-electrolyte interface is not altered by the thermal treatment. Furthermore, a straightening of the columns occurred. This straightening is attributed to the stress relaxation [307], [308].

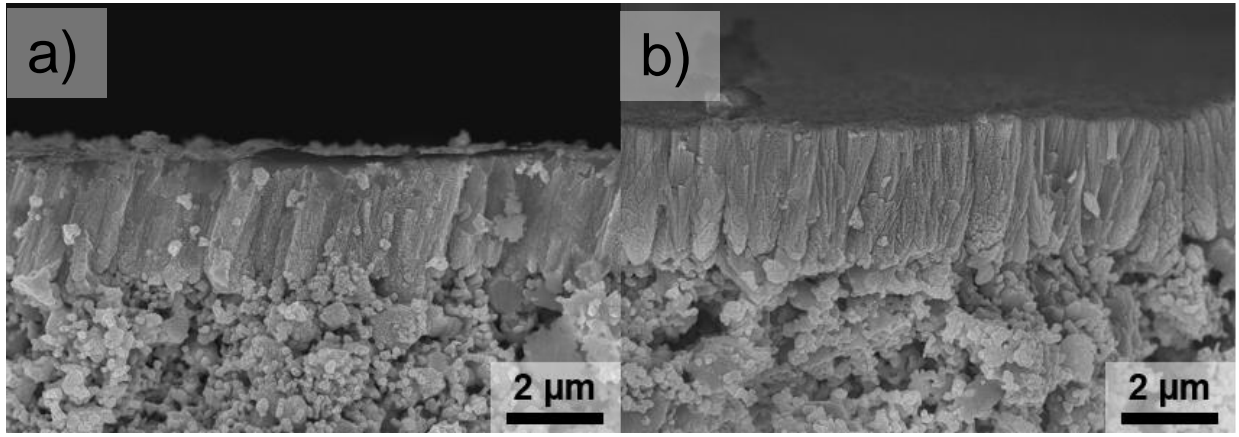


Figure IV.14: SEM micrographs of the BZY electrolyte elaborated by reactive pulsed DC sputtering. a) as-deposited, b) after annealing at 1000 °C for 2 hours

The X-ray diffraction patterns of the BZY electrolyte deposited by reactive pulsed DC sputtering before and after annealing treatment at 1000 °C for 2 hours are shown in **Figure IV.15**. Two phases corresponding to BZY are highlighted on the raw sample, and the diffraction peaks from NiO are also collected. The two phases of BZY were attributed to BZY from the substrate (BZY-substrate) and BZY deposited by pulsed reactive DC sputtering (BZY-PVD). The parameters were calculated from the position of each peak and are exposed in **Table IV.5**. Rietveld refinement was not conducted on the diffractograms due to their highly textured feature. The lattice parameter of BZY-PVD is 4.23(6) Å, much higher than the usual values due to lattice strain [309], while BZY-substrate exhibits a lattice parameter of 4.20(5) Å, in perfect agreement with the previous result in Chapters II and III. Furthermore, by comparing the intensity of the peaks with the intensity calculated using CaRine software for a sample exhibiting no preferential orientation (presented at the bottom of Figure IV.15), the BZY-PVD phase shows a highly textured structure along the [100] and [211] direction.

After the annealing treatment at 1000 °C, the position of the peaks of the two BZY phases (from the substrate and from the PVD layer) is the same. The calculated lattice parameter is 4.20(6) Å suggesting a stress relaxation. The preferred orientation along the [100] direction is still present and is attributed to BZY-PVD. The preferred orientation along the [211] is more visible anymore, agreeing well with the straightening of the columns highlighted by SEM.

The NiO lattice parameter is not impacted by the annealing treatment.

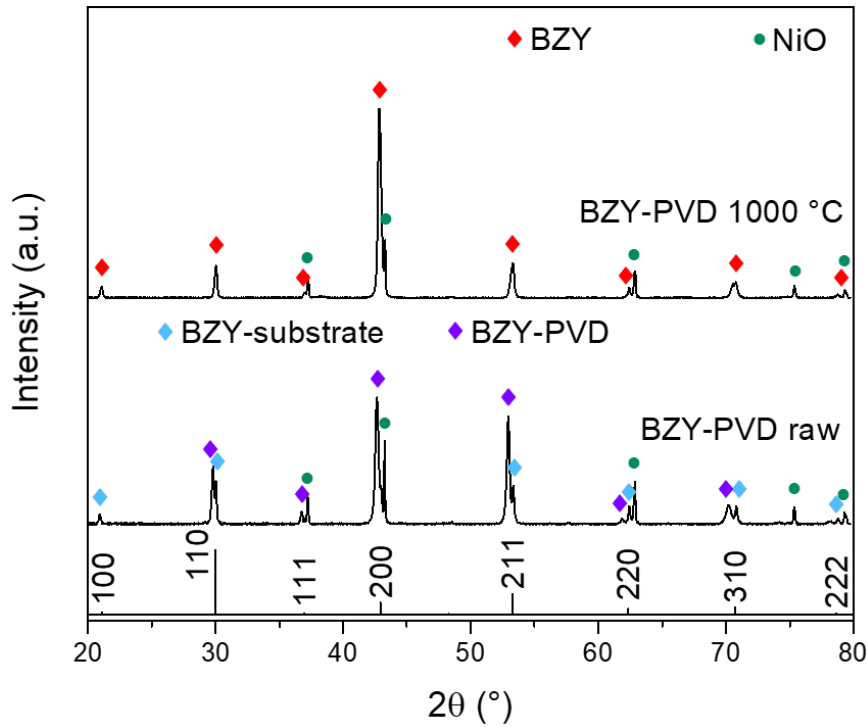


Figure IV.15: X-ray diffractograms of the BZY electrolyte elaborated by reactive pulsed DC sputtering. a) as-deposited, b) after annealing at 1000 °C for 2 hours. The relative intensity of a non-textured BZY phase calculated using CaRine software is presented at the bottom of the figure.

Sample	Lattice parameter of BZY (Å)		Lattice parameter of NiO (Å)
	BZY-PVD	BZY-substrate	
BZY-PVD raw	4.23(6)	4.20(5)	4.18(0)
BZY-PVD 1000 °C		4.20(6)	4.18(0)

Table IV.5: Lattice parameter of BZY and NiO phases before and after annealing at 1000 °C

III.3. Deposition of the cathode by spray

The cathode layer was deposited on the top of the electrolyte by spray using an airbrush (Revell). The slurry for the spray has to be more liquid than for tape casting. The composition is given in **Table IV.6**. The procedure of mixing is the same as for tape casting. The cathode was sprayed through a mask of 18 mm in diameter. The nozzle-to-substrate distance was maintained to 20 cm. The time of deposition to achieve a thickness of 80 μm was 4 times 10 seconds. A thermal treatment à 800 °C for 5 hours (heating and cooling of 3 °C.min⁻¹ and a debinding step at 800 °C) was carried out to sinter the cathode.

BZY (g)	BSCF (g)	C (g)	EtOH (g)	TEA (g)	PVB (g)	PEG (g)	BBP (g)
10	10	0.4	50	0.2	1.8	1.8	0.1

Table IV.6: Quantity used for the cathode ink

Figure IV.16 shows the cathode microstructure after thermal treatment at 800 °C for two hours. This micrograph was obtained on a sample without electrolyte. The cathode layer is 80 μm thick and porous.

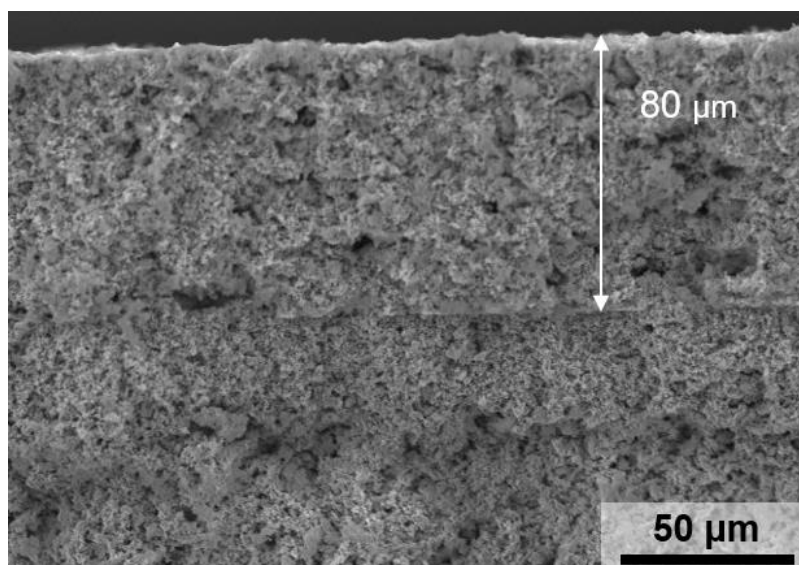


Figure IV.16: SEM micrographs of the cathode layer deposited by spray

IV. Electrochemical test of the cells

Before the cell operation, the NiO from the anode has to be reduced to metallic Ni. As shown in the first part of this section, this step is crucial and delicate because a too sudden reduction can generate mechanical stresses that can lead to the fracture of the cell. The second part will present the electrochemical performances of a cell elaborated by the co-tape casting, pulsed reactive DC sputtering, and spray deposition.

IV.1. Study of the reduction of NiO

The study of NiO reduction was carried out in collaboration with Maria-Paola Carpanese and Davide Clematis from the DICCA laboratory (University of Genova, Italy). The reduction was carried out at 540 °C. The anode side was fed by gas at 45.4 mL.min⁻¹ using a pressure of 1.2 bar. Pure N₂ was send during the increase of temperature at 1.5 °C.min⁻¹. The cathode side was fed by dry air at 100 mL.min⁻¹ (1.5 bar) during the heating and the reduction. **Figure III.17** shows a typical reduction profile of a complete cell. The OCV was recorded all along the reduction using Nova 2.1 software while of the amount of H₂ in a N₂-H₂ gas mixture was increased step by step when the OCV was stable. The OCV started to rise when the percent of H₂ was 33 %. It increased up to a value of 0.73 V before dropping suddenly to 0.05 V when the anode was supplied by a 50-50 H₂-N₂ gas mixture.

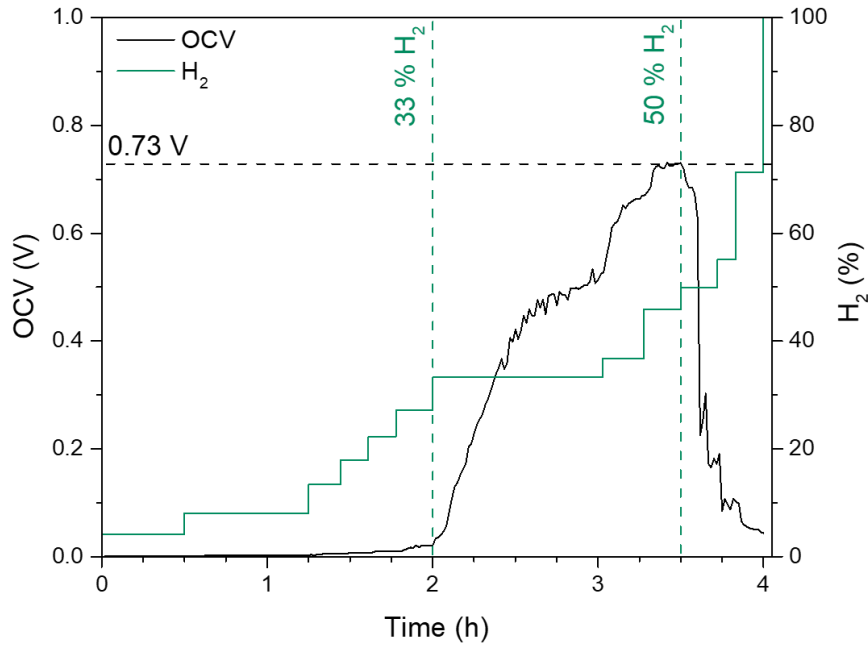


Figure IV.17: Recorded OCV and H₂% in the N₂-H₂ gas mixture during the reduction as a function of the time

The microstructure of the cell after reduction is exposed in **Figure IV.18**. The electrolyte layer presents severe cracks all along the studied cross-section leading to the drop of OCV. To analyze the origin of the cracks formation, an anode-AFL-electrolyte assembly elaborated by co-tape casting and pulsed reactive DC sputtering was half reduced (2 hours under hydrogen flow at 550 °C) and studied by X-ray microtomography (RX-solution Easytom-XL Ultra). The tomography is based on the Beer-Lambert law of attenuation (**Equation IV.1**). Since not only the nature of the material but also its density affect the attenuation coefficient, the tomography allows an image in contrast of density. Then in tomography micrographs presented in **Figure III.19**, the porosity is in dark grey. BZY appears in white and Ni in light grey. The median grey corresponds to a mix of BZY and NiO, these two phases are not properly separated because the resolution of the tomograph (350 nm) is lower than the grain size of BZY.

$$I = I_0 e^{-\mu s} \quad \text{Equation IV.1}$$

Where I is the measured intensity of the X-ray, I_0 the initial intensity of the X-ray, μ the X-ray attenuation coefficient and s the length of sample crossed by the X-ray.

As clearly exhibited by the circle surrounding a Ni grain in **Figure III.19.a** and **b**, the reduction of NiO into Ni leads to the formation of a porosity around the grain due to the contraction of the lattice (the lattice parameter of Ni is 3.54 Å while it is 4.17 Å for NiO). This phenomenon results in the contraction of the anode volume as schematically exhibited in **Figure III.20**. To compensate for the compressive force exerted in the anode and the AFL, a tensile force results in the electrolyte layer leading to the electrolyte rupture. Then, the reduction procedure has to be as smooth as possible in order minimize the stress in the cell.

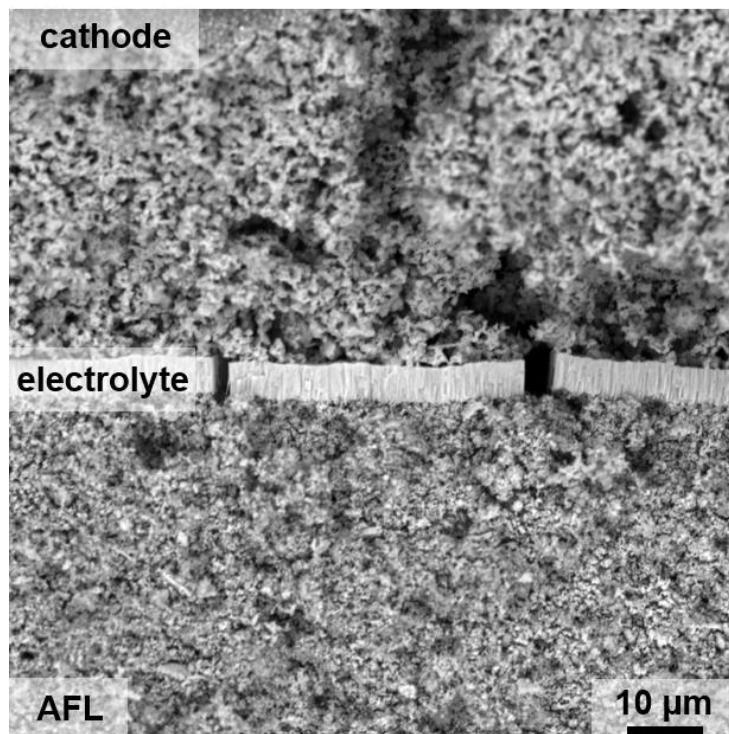


Figure IV.18: SEM micrograph of the complete cell after reduction

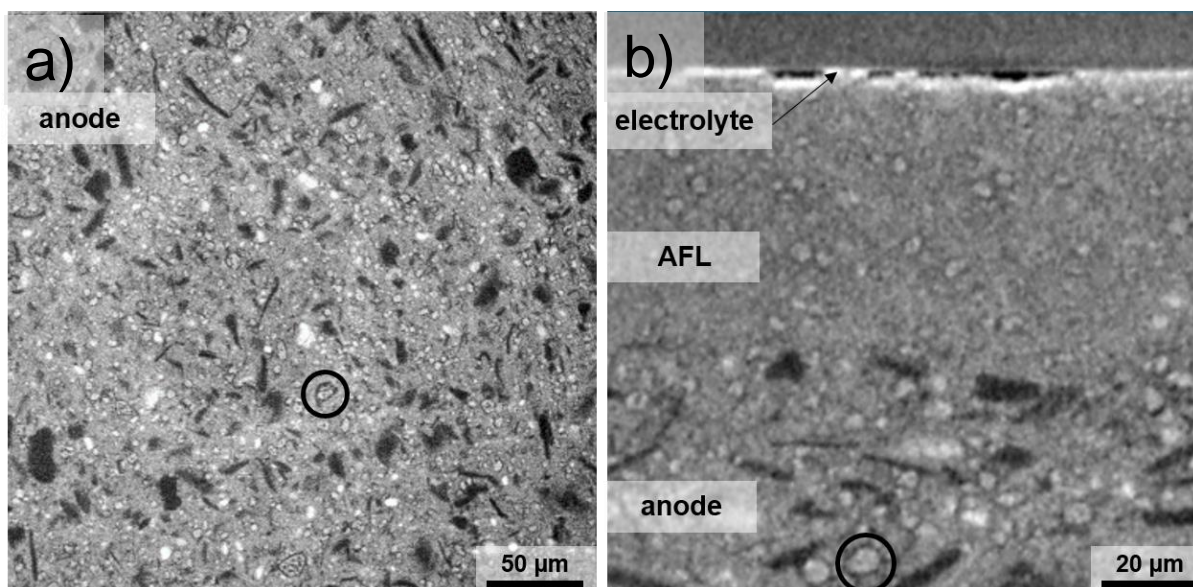


Figure IV.19: Tomography micrographs of the complete cell after half-reduction. a) view from the bulk of the anode, b) cross-sectional view of the anode-AFL-electrolyte assembly

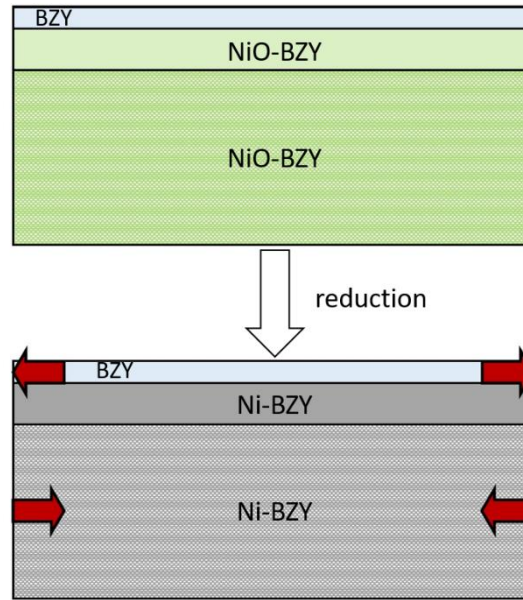


Figure IV.20: Schematic representation of the reduction of NiO into Ni. The red arrows represent the compressive and tensile forces

IV.2. Electrochemical impedance spectroscopy of complete PCFC

IV.2.a. Theoretical EIS spectra of a complete PCFC

In an operating fuel cell, the HOR (**Reaction IV.1**) takes place on the anode side while the ORR (**Reaction IV.2**) occurs at the cathode side. In fact, these reactions are divided into several elementary steps, including diffusion, adsorption, dissociation and charger transfer, as depicted in **Table IV.7** [265], [310], [311]. The HOR is divided into four elementary steps. Usually, the adsorption and dissociation of H_2 are the rate-limiting steps that give to the semi-circle related to the anode in an EIS Nyquist spectrum. The ORR is composed of six elementary steps, here again, the adsorption and dissociation of O_2 are the rate-limiting steps that lead to the semi-circle related to the cathode in EIS. The proton transfer between the protonic conductor and the mixed ionic-electronic conductor is also a rate-limiting step, usually its response in EIS is overlapped with the one related to the adsorption and dissociation of O_2 . These limiting steps on the cathode side make the ORR the most critical reaction in PCFC, leading to a high polarization resistance of the cathode [125], [312].



Place of the phenomena	Name of the elementary process	Chemical notation of the elementary process
Anode/TPB	Adsorption	$H_{2(g)} \rightarrow H_{2(ads,A)}$
	Dissociation	$H_{2(ads,A)} \rightarrow 2H_{(ads,A)}$
	Diffusion	

	Charge Transfert	$H_{(ads,A)} \rightarrow H_{(ads,TPB)}$ $H_{(ads,TPB)} \rightarrow H_{(E)}^+ + e_{(A)}^-$
Electrolyte/TPB	Diffusion (bulk)	$H_{(E,A \text{ side})}^+ \rightarrow H_{(E,C \text{ side})}^+$
	Diffusion (GB)	$H_{(E,A \text{ side})}^+ \rightarrow H_{(E,C \text{ side})}^+$
Cathode/TPB	Adsorption and dissociation	$O_{2(g)} \rightarrow 2O_{(ads,C)}$
	Oxygen reduction I	$O_{(ads,C)} + e_{(C)}^- \rightarrow O_{(ads,C)}^-$
	Diffusion	$O_{(ads,C)}^- \rightarrow O_{(TPB)}^-$
	Oxygen reduction II	$O_{(TPB)}^- + e_{(C)}^- \rightarrow O_{(TPB)}^{2-}$
	Proton transfer	$H_{(E,C \text{ side})}^+ \rightarrow H_{(TPB)}^+$
	Hydroxide formation	$H_{(TPB)}^+ + O_{(TPB)}^{2-} \rightarrow OH_{(TPB)}^-$
	Water formation	$H_{(TPB)}^+ + OH_{(TPB)}^- \rightarrow H_2O_{(TPB)}$
	Water evaporation	$H_2O_{(TPB)} \rightarrow H_2O_{(g)}$
Current collector	Mass transport	$e_{(A)}' \rightarrow e_{(C)}'$

Table IV.7: Elementary steps involved in PCFC operation. The sense of reaction is given in the fuel cell mode, in electrolyze mode, all the elementary steps occur in the non-spontaneous way. Anode is noted A, cathode, C and electrolyte, E. TPB refers to the triple-phase boundary, ads refers to adsorbed. Adapted from [84], [265], [310], [311].

The typical EIS spectra of a complete cell are given in **Figure III.21.a** (Nyquist plot) and **b** (Bode plot). It consists of an inductive tail and two semi-circles. The inductive tail is due to the inductive behavior of the electrical wires and is fitted by an inductor. The intercept with the real part of the impedance at high frequencies represents the ohmic resistance mainly related to the electrolyte resistance (noted R_Ω). The characteristic time associated (τ_Ω) is read when the phase is equal to zero. At intermediate frequency, a semi-circle fitted by a resistor and a capacitor (or CPE) in parallel is highlighted. As exposed before, it is characteristic of the response of the anode. Finally, the ORR at the cathode gives to the last semi-circle modeled by a R and a C in parallel at low frequencies. Both HOR and ORR characteristic times (noted τ_A and τ_C) are highlighted on the Bode plot. As explained before, the polarization resistance of the cathode (noted $R_{p,C}$) is usually higher than the polarization of the anode ($R_{p,A}$).

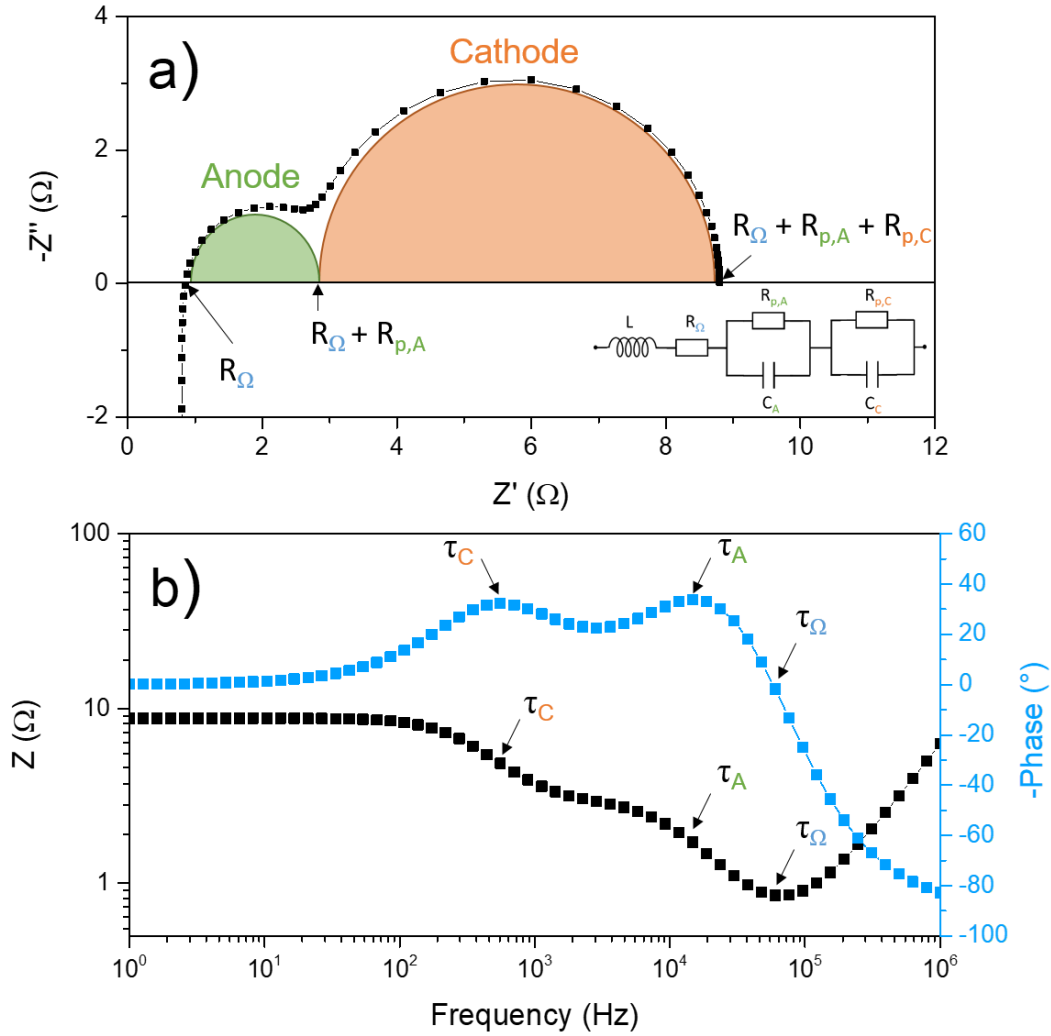


Figure IV.21: Classical a) Nyquist and b) Bode plot of a complete cell

IV.2.b. Experimental EIS spectra of a complete PCFC

The complete cell elaborated by co-tape casting, reactive pulsed DC sputtering and spray deposition was tested by EIS using an Autolab PGSTAT302N. The pulverization time was set to 2 hours to obtain a 5 μm electrolyte layer. The microstructure of a complete cell after cell operation is presented in **Figure IV.22**. The AFL is highly porous after reduction and the dense electrolyte of 5 μm thick deposited by reactive pulsed DC sputtering presents the characteristic columnar microstructure. The cathode shows well distributed BZY (in white) and BSCF (in grey) sub-lattices. No delamination is observed between the layers

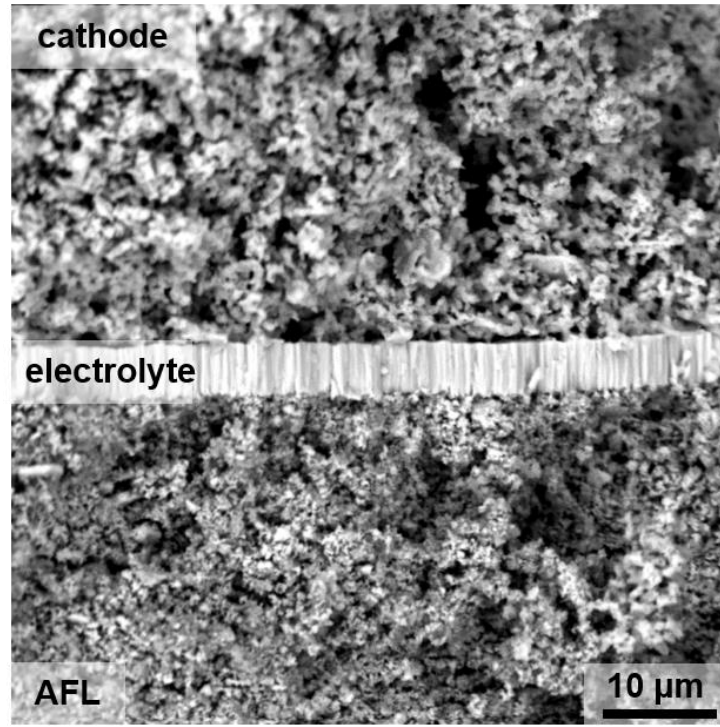


Figure IV.22: SEM micrographs of the complete cell after cell operation

The cell was placed in a Norecs ProboStat for the analysis. The reduction was carried out at 525 °C to decrease the kinetics of the chemical reaction. The quantity of H_2 was increased step by step according to the procedure described previously. The final OCV was 0.78 V for 100 % of wet H_2 at a pressure of 1.4 bar using a flow of 50 mL.min⁻¹. The air flow was maintained at 100 mL.min⁻¹ at a pressure of 1.7 bar. This value is lower than expected due to gas leakages but was stable for some hours before dropping at 0 V due to the breaking of the sample during the increase of temperature from 525 to 550 °C. EIS measurements were carried out from 10⁵ Hz to 10⁻¹ Hz with an amplitude of 10 mV at 525 °C.

The EIS spectra are presented in **Figure IV.23.a** (Nyquist plot) and **b** (Bode plot). The Nyquist plot consists of an inductive tail attributed to the electrical wires followed by a skewed semi-circle. The ohmic resistance (R_Ω) taken at the intercept with the real part of the impedance at high frequencies is 7.02 Ω .cm² and was stable for the duration of the measurements carried out at 525 °C (4 hours). This value is significantly higher than other reported values for similar samples. For example, Duan *et al.* obtained a R_Ω of 1.85 Ω .cm² for a Ni-BZY//BZY deposited by PLD (4 μ m thick)//La_{0.6}Sr_{0.4}Co_{0.2}Fe_{0.8}O_{3- δ} -BaCe_{0.9}Yb_{0.1}O_{3- δ} cell at 600 °C and Bae *et al.* reported a R_Ω of 0.15 Ω .cm² for a Ni-BZY//BZY deposited by PLD (2 μ m thick)//La_{0.6}Sr_{0.4}CoO_{3- δ} cell at 600 °C [124], [300]. However, the temperature has to be taken into account, since the diffusion is thermally activated, it is reasonable to suppose that the ohmic resistance of the BZY electrolyte deposited by reactive pulsed DC sputtering would have shown a lower resistance value at a higher temperature.

Concerning the electrodes, in contrast with the theoretical spectrum presented in **Figure IV.21**, the anode and cathode contribution cannot be separated due to too close a characteristic time constant. This is well evidenced in the Bode plot in **Figure IV.23.b**. Then the spectra cannot be fitted with the classical equivalent circuit of a complete cell depicted in **Figure**

IV.21.a and the values of resistance polarization of anode and cathode associated with the HOR and the ORR cannot be discussed. However, according to the shape of the Nyquist plot, the cathode process is not dominant, suggesting that the use of a composite material that presents a protonic-electronic-oxygen ion conduction is beneficial for the performance of the cell regarding the ORR.

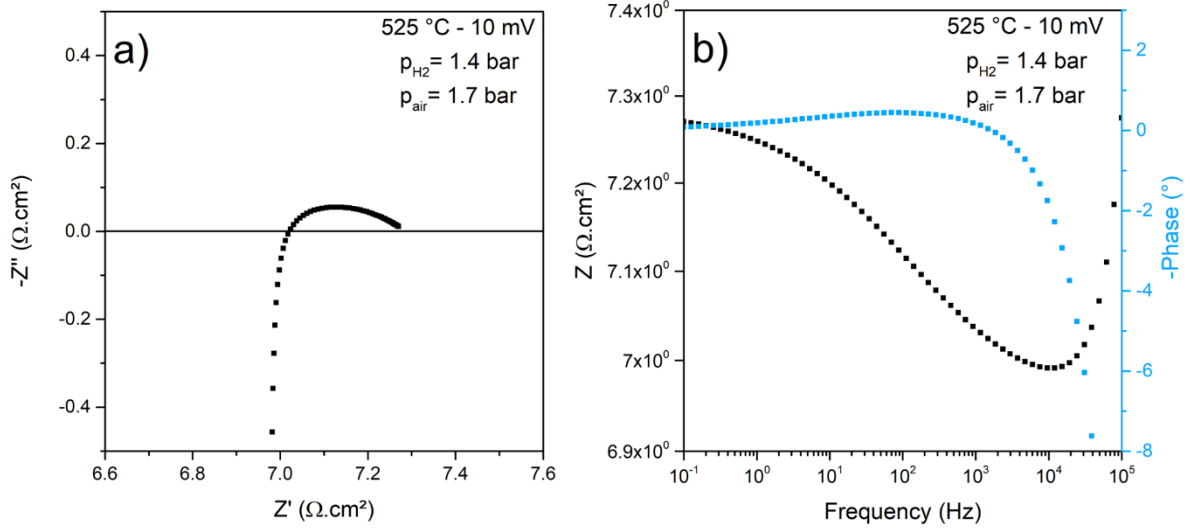


Figure IV.23: EIS spectra at OCV of a complete cell with 5 μm thick electrolyte deposited by reactive DC sputtering. a) Nyquist plot and b) Bode plot

V. Conclusion

Two elaboration processes were evaluated in this study, the first consisting of co-tape casting and co-sintering in order to promote cost-efficiency and the second one by co-tape casting, reactive pulsed DC sputtering and spray deposition in order to improve the performances of the cells.

Using the first route, only half-cells were fabricated. The half-cells exhibit a great microstructure consisting of well adherent layer with controlled thickness and a sufficient densification rate for the electrolyte after a co-sintering at 1500 °C for 5 hours. However, chemical reactivity in the electrolyte layer was highlighted. Indeed, such high sintering temperature promotes the Ba-vaporization and lead to the formation of Zr-doped Y_2O_3 secondary phase. As shown in the previous chapter, this secondary phase is highly detrimental for the conductivity. Thus, the sintering temperature was decreased in order to avoid reactivity. This leads to a drop in the densification rate of the electrolyte layer, also highly detrimental for the cell performance, then, this route was put aside.

The second elaboration process consists of the fabrication anode-AFL substrate by co-tape casting and co-sintering at 1350 °C. The electrolyte layer is then deposited by reactive pulsed DC sputtering with controlled thickness. The microstructural investigations highlighted the formation of skewed column grains. This observation was also confirmed by XRD analysis. A thermal treatment at 1000 °C for 2 hours allows to straighten the column. The cathode is then

deposited on the top of the electrolyte by spray using a aerograph and fired at 800 °C to enhance its adherence with the electrolyte.

The reduction is a crucial and delicate step that can easily lead to the sample failure and then has to be carried out very slowed at intermediate temperature. A complete cell with a 5 μm electrolyte was studied by electrochemical impedance spectroscopy. The cell showed an OCV 0.78 V at 525 °C, lower than expected due to gas leakages. The ohmic resistance is about 7 $\Omega\cdot\text{cm}^2$. As a comparison, the area specific resistance at 525 °C in wet H_2 is 47 and 92 for BZY-com and BZY-c 1000 °C. Then the use of textured BZY-electrolyte is highly beneficial for the cell performance. However, the ohmic resistance is still higher than expected. As a reminder, the targeted resistance presented in chapter I is 0.2 $\Omega\cdot\text{cm}^2$. The measurement was performed at 525 °C and the ohmic resistance is supposed to decrease with increasing the temperature, then, it can reasonably be supposed that an acceptable ohmic resistance value could be obtained at 600 °C. Unfortunately, the cell broke during the increase of temperature and then the Arrhenius behavior has not been verified.

To finish, EIS measurement also highlighted that the cathode process is not dominant, meaning that the ORR is not as limiting step as usual, in the elaborated complete cell. It was attributed to the use of a mixed protonic-electronic-oxygen ion conduction as cathode material resulting in the increase of the number of points where the ORR can occur.

GENERAL CONCLUSION

The main objectives of this thesis work were to synthesize a possible electrolyte material for PCFC, to evaluate the electrochemical properties of the synthesized oxides and to elaborate PCFC elementary cells.

Among the selected materials in the Y-doped BaCeO₃–BaZrO₃ solid solution, only the synthesis of BaZrO₃ and Y-doped BaZrO₃ were achieved. Indeed, the fast nucleation of CeO₂ in supercritical water conditions hinders the integration of cerium into the perovskite structure, then BZY was chosen as electrolyte material. BZY was synthesized by two different hydrothermal devices (batch and continuous) at a temperature as low as 400 °C under a pressure of 300 bar in basic conditions (pH of 13). The as-synthesized materials exhibit a strong Ba-deficiency, the determined compositions are Ba_{0.88}Zr_{0.73}Y_{0.27}O_{3-δ} and Ba_{0.93}Zr_{0.86}Y_{0.14}O_{3-δ} for BZY-b and BZY-c respectively. However, a thermal treatment at 1000 °C compensates the Ba-vacancy by the incorporation of BaO from the decomposition of BaCO₃. Furthermore, the annealing treatment is also beneficial of the chemical stability of BZY during sintering. The composition of the perovskite phase after the annealing treatment is Ba_{0.96}Zr_{0.76}Y_{0.24}O_{3-δ} for BZY-b and Ba_{1.01}Zr_{0.85}Y_{0.15}O_{3-δ} for BZY-c. Then the batch synthesis promotes better integration of Y while the continuous synthesis is better to avoid Ba-deficiency.

BaCO₃ and (Y,Zr)O(OH) are also formed during the synthesis. BaCO₃ is not detrimental since it decomposes at high temperatures, but (Y,Zr)O(OH) is problematic. Indeed, (Y,Zr)O(OH) changes into oxide from 240 to 610 °C and (Y,Zr)₂O₃ is highly insulating, resulting in a dramatic drop of the conductivity value. For example, a sample containing about 30 wt% of (Y,Zr)₂O₃ after sintering at 1550 °C exhibits one order of magnitude lower total conductivity than the samples containing 3 or less wt% of (Y,Zr)₂O₃. The tremendous increase of the (Y,Zr)₂O₃ content during sintering occurs due to the segregation of phases involved by the instability of Ba-deficient BZY. Then, the continuous process should be preferred to the batch process for the synthesis of BZY.

Furthermore, the synthesis in the continuous devices was optimized by increasing the initial quantity of Ba precursor, and, for a ratio $[Ba^{2+}]/([Zr^{4+}]+[Y^{3+}])$ of 2, the formation of oxyhydroxide phase is avoided.

The total conductivity of sintered BZY was evaluated by EIS in wet atmosphere. BZY-b and BZY-c annealed at 1000 °C were compared to a commercial BZY powder. The BZY pellet was sintered at 1550 °C for 5 hours to reach a densification of 90 %. BZY-b exhibited strong reactivity after sintering (30 wt% of (Y,Zr)₂O₃), leading to a dramatic decrease of its conductivity. Thus, BZY elaborated by the batch process does not present an interest for the PCFC application.

BZY-com has a conductivity value of $2.1 \times 10^{-3} \text{ S.cm}^{-1}$ in wet air and wet H_2 at 600 °C. BZY-c 1000 °C exhibits slightly lower values, $8.1 \times 10^{-4} \text{ S.cm}^{-1}$ in wet H_2 and $1.6 \times 10^{-3} \text{ S.cm}^{-1}$ in wet air at 600 °C. This order of magnitude is acceptable for an application in PCFC even if a higher value is preferable. Moreover, the dominant charge carrier is assumed to be mainly proton at a temperature lower than 575 °C in wet H_2 . This assumption is based on the determination of activation energy since transport number measurements were not performed.

In addition, BZY-c shows interestingly low grain boundary resistance at low temperature in comparison with the other samples resulting in higher total conductivity value. In contrast, BZY-com has a higher total conductivity value at high temperature (higher than 500 °C). It is because the grain boundary resistance is mainly dominant at low temperature. Then BZY-com should be preferred for a PCFC operating temperature higher than 500 °C while BZY-c could be interesting as protonic conductor in the 400 – 500 °C range.

PCFC half-cells and cells were elaborated by two different routes: one based on co-tape casting to decrease the manufacturing cost and the other one based on co-tape casting, reactive pulsed DC sputtering and spray deposition to improve the performances of the cells. However, the co-tape casting route was put aside due to the impossibility to obtain a good electrolyte layer, i.e., sufficient densification and the absence of reactivity.

PCFC cells were successfully elaborated by the second method. The electrolyte of controlled thickness shows a columnar microstructure. Since the grain boundaries of BZY are more resistive than the grain bulk, this microstructure is highly beneficial for the cell performance. Indeed, the ohmic resistance is about $7 \text{ } \Omega.\text{cm}^2$ at 525 °C. However, the mechanical strength of the cells was insufficient. Thus, many cells broke during the reduction of NiO into Ni step and long-term measurements were not carried out due to the systematic break of the cells during operation.

In terms of prospects, the first aim is to improve the mechanical resistance of the cell, and in particular, the anode-AFL substrate. Two options are under consideration:

- the optimization of the co-sintering of anode-AFL assembly. It is necessary to improve the densification of the BZY sub-lattice in order to increase the mechanical resistance of the cell after NiO reduction. The considered solution is to employ sintering aid in the slurry formulation.

- adding another material with lower sintering temperature than BZY in the anode slurry to increase the mechanical resistance of the cell, for example, yttria-stabilized zirconia.

Secondly, to increase the power delivered by fuel cells, it is a matter of scaling up. Thus, the diameter of the PCFC has to be increased. The target is fixed to at least 5 cm in diameter. In a second time, the stack of two or more PCFC has to be also considered.

Then, in order to study the hydrogen cycle over a wider range, the behavior of the cells in electrolysis mode has to be analyzed. This aim requires to study the chemical stability of the materials in a high $P_{\text{H}_2\text{O}}$ atmosphere.

Finally, the long-term stability of the system, in both fuel cell and electrolysis mode has to be studied in order to demonstrate the feasibility of using protonic ceramic electrochemical cells on a large scale.

ANNEX CHAPTER: STUDY OF INTERMEDIATE TEMPERATURE SOFC

A study carried out in parallel of this thesis on PCFC is presented in this annex chapter. In this study, the material of interest is Sm-doped ceria, an oxygen ion conductor that operate in the 400-600 °C range. This chapter will be divided in three parts.

The first one will introduce the Sm-doped ceria material.

The second one will focus on symmetrical cells with a focus on the interaction between the electrolyte material and the electrode material.

The last one will present the preparation of complete cells based on SDC, the performance obtain and the study of the degradation mechanism occurred leading to the drop of performances. The major part of the results presented in this third part have been published in *Energies* journal in 2021 [313].

I. Presentation of Sm-doped Ceria

Up to now, the strategy that has been presented to reduce the working temperature of classical SOFC is the use of PCFC. However, another alternative solution is to employ oxygen-ion conductor electrolyte that present interesting conductivity properties in the 400-600 °C range. Among the oxygen-ion conductors, many researchers have focused on the use of ceria-based compounds as the electrolyte material.

As YSZ, ceria (CeO_2) crystallizes in a fluorite structure, this structure is presented in **Figure V.1.a**. In such oxides, the oxygen-ion transport occurs via a vacancy mechanism, where the oxygen-ion jumps to a neighboring vacancy, as illustrated in **Figure V.1.b** [314]–[316]. Then, to obtain an oxygen-ion conductivity, it is necessary to have oxygen-vacancies in the fluorite crystal structure. By substituting cerium with a trivalent element, oxygen vacancies are introduced, resulting in a high mobility of oxygen ions and, thus, high ionic conductivity, even at 600 °C [317], [318]. However, the insertion of oxygen-vacancies also results in local structure defects that involve instability of the structure [319]. It is thus a matter of finding the compromise between oxygen-vacancies concentration and stability of the system. As illustrated on **Figure V.2**, where the activation energy and the conductivity at 400 °C are reported as function of the Sm concentration in the Sm-doped ceria system, the optimum dopant concentration appears to be 20 % as it corresponds to the maximum of conductivity [320]. This observation has also been supported by Jung et al., Acharya et al. and Yahiro et al. [321]–[323].

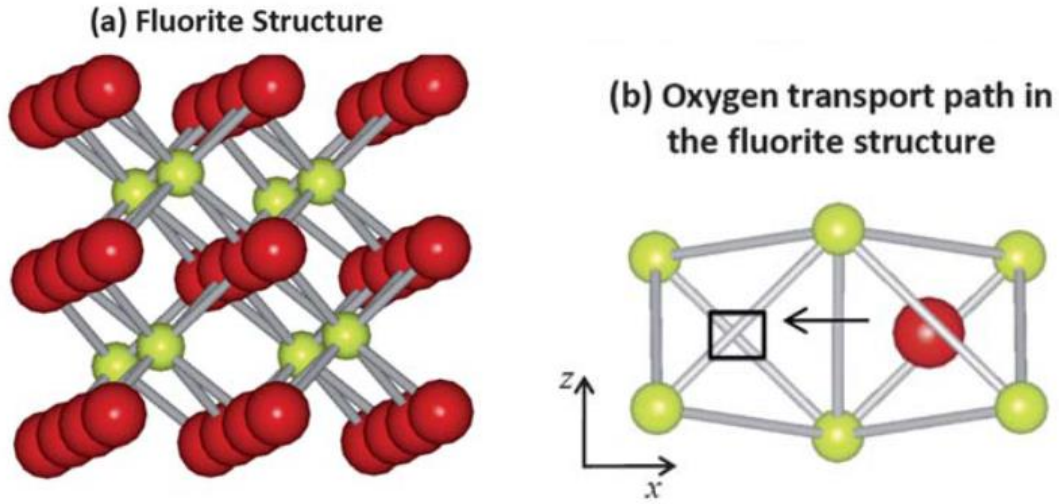


Figure 1: a) Fluorite crystal structure and b) oxygen migration path the fluorite structure. The red spheres represent the oxygen ions, the yellow-green the cations and the square the oxygen vacancy [314].

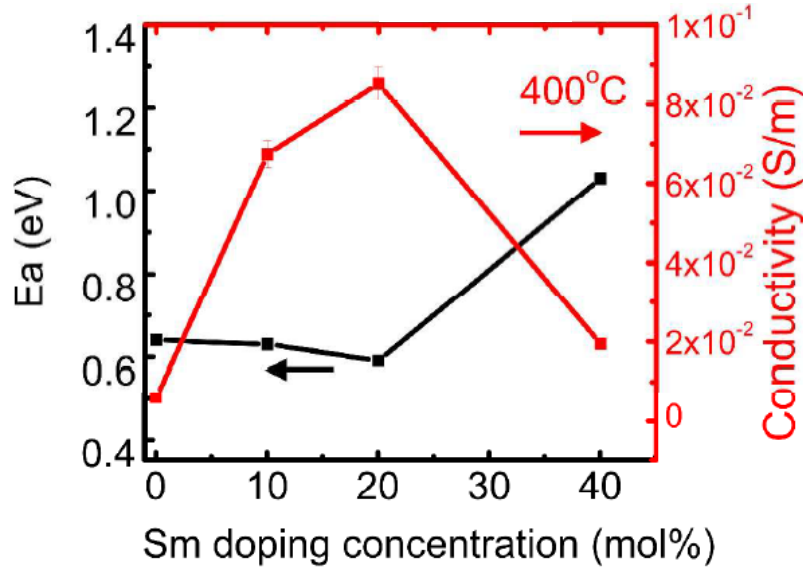


Figure 2: Activation energy and total conductivity in air at 400 °C as a function of Sm dopant concentration [320]. The samples consist of an epitaxial thin film of Sm-doped CeO_2 sandwiched between two Pt electrodes deposited by photolithography. This preparation explains the unusually high conductivity values.

Among the different doped ceria, $\text{Ce}_{0.8}\text{Gd}_{0.2}\text{O}_{2-\delta}$ and $\text{Ce}_{0.8}\text{Sm}_{0.2}\text{O}_{2-\delta}$ have attracted much attention [324]–[326]. However, Sm^{3+} , which has an ionic radius very close to Ce^{4+} , promotes less structural distortion, and thus more phase stability [327]. Furthermore, Sm-doped ceria ($\text{Ce}_{0.8}\text{Sm}_{0.2}\text{O}_{2-\delta}$ noted SDC) exhibits an ionic conductivity higher than $10^{-2} \text{ S}\cdot\text{cm}^{-1}$ at 600 °C [234], [320]–[323], [328]–[331]. For these reasons, SDC is one of the most promising electrolytes for intermediate temperature solid oxide fuel cell (IT-SOFC) and is the chosen electrolyte material of this study.

II. Symmetrical cell

The purpose of the study of the symmetric cell is twofold. It is, first, to examine the interactions between the SDC electrolyte material and the complete cell cathode material. And, second, it is to study the conduction properties of SDC. As the cathode material operates in an oxidizing atmosphere in fuel cell mode, the study was conducted in air.

In IT-SOFC, reducing the operating temperature leads to an inevitable drop in cell performance, mainly due to the less efficient ORR [332], [333]. As explained in the first chapter, the use of MIEC allows to increase the number of TPB and thus the ORR efficiency. Among the MIEC operating in the 400-600°C range, $\text{La}_{0.6}\text{Sr}_{0.4}\text{Co}_{0.2}\text{Fe}_{0.8}\text{O}_{3-\delta}$ (LSCF) and $\text{Sm}_{0.5}\text{Sr}_{0.5}\text{CoO}_{3-\delta}$ are widely used because of their high catalytic activity towards ORR and good oxygen-ion and electron conduction properties [117], [334]. However, the strong thermal expansion coefficient mismatch between SDC and SSC ($\sim 12 \times 10^{-6} \text{ K}^{-1}$ for SDC and $\sim 24 \times 10^{-6} \text{ K}^{-1}$ for SSC) limits the practical utilization of SSC [110]. In contrast, LSCF exhibits a thermal expansion coefficient of $15.4 \times 10^{-6} \text{ K}^{-1}$, which allows it to be used with SDC [335].

Two symmetrical cells were prepared: one with LSCF as electrode material to study the interface cathode-electrolyte and one with Pt electrode as reference.

II.1. Preparation of the symmetrical cell

II.1.a. Electrolyte part

The SDC powder was purchased from Fuel Cell Materials – FCM, Ohio (Ref: SDC20-N, Lot #9C007, Item #111202, surf. area $201.3 \text{ m}^2\text{.g}^{-1}$). The electrolyte powder was pressed into pellets of 28 mm under uniaxial pressure of 200 MPa. A thermal treatment at 1215 °C for 3 hours is applied to sinter the pellet, final pellet is 24 mm large in diameter and 1.8 mm thick with a densification rate of 92 % measured by the Archimedean buoyant force method.

The X-ray diffractogram of the sintered pellet is presented in **Figure V.3**. It consists of a pure SDC phase (ICCD 04-013-0036 corresponding to $\text{Ce}_{0.8}\text{Sm}_{0.2}\text{O}_{2-\delta}$) with a lattice parameter obtained by Rietveld refinement of $5.429(0) \text{ \AA}$.

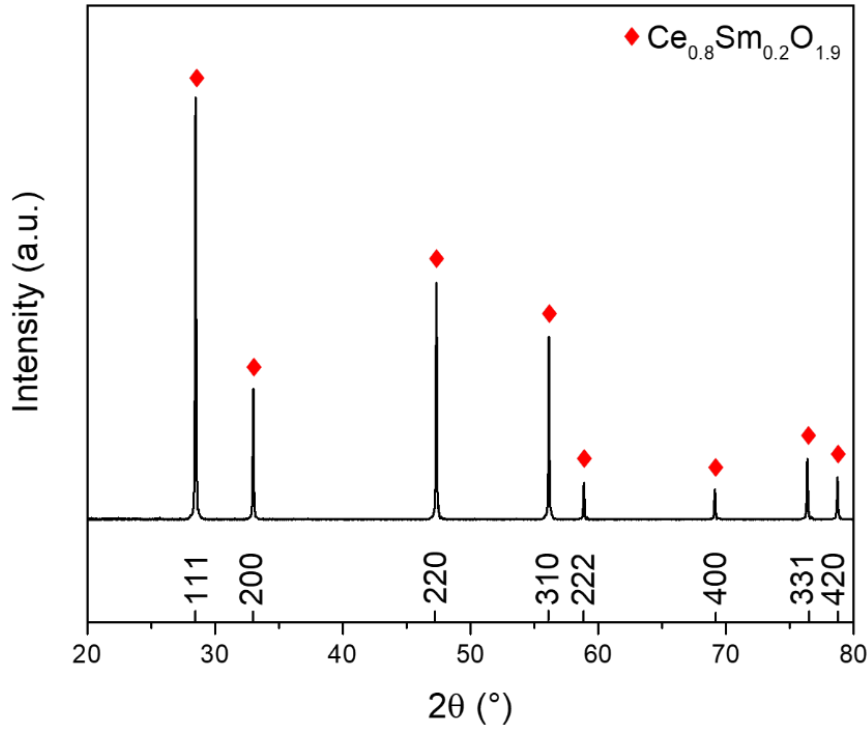


Figure 3: XRD pattern of the SDC pellet sintered at 1215 °C for 3 hours.

The microstructure examined by SEM is presented in **Figure V.4**. The pellet is highly densified as suggested by the Archimedes' buoyant force measurement. The polyhedral shaped grains are widely coalesced and exhibits a mean value of $0.52 \pm 0.32 \mu\text{m}$. The same microstructure was observed for the two pellets.

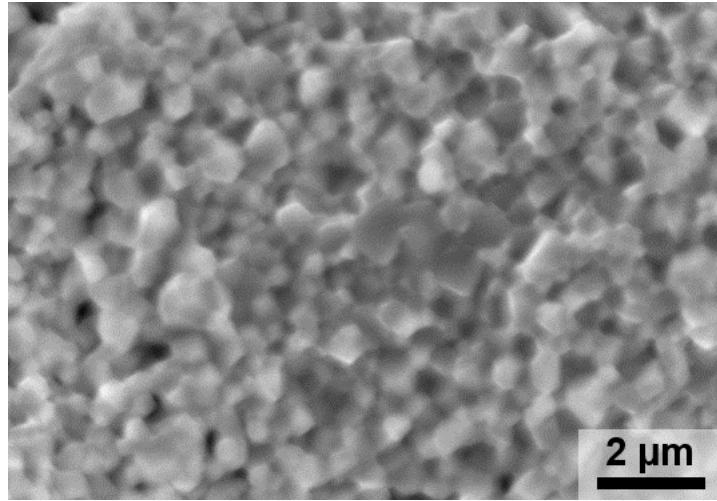


Figure 4: SEM micrograph of the SDC pellet sintered at 1215 °C for 3 hours.

II.1.a. Electrode part

A slurry of LSCF was used as ink for screen-printing. The slurry was prepared as follow: LSCF powder was mixed with graphite as pore former, ethanol and methyl ethyl ketone (MEK) as solvents and triethanolamine (TEA) as dispersant. This preparation was mixed in a Turbula-T2F device for 16 hours. In a second step, polyvinyl butyral (PVB) as binder, polyethylene

glycol (PEG) and benzylbutyl phthalate (BBP) as plasticizers were added to preparation and mixed for 24 hours. The quantity of each component is presented in **Table V.1**. This ink was then screen-printed on both side of the SDC-pellet by using a mask. A thermal treatment at 800 °C was carried out to enhance adhesion between the electrodes and the pellet. The final diameter of the electrodes is 8 mm.

Component	LSCF	Graphite	Ethanol	MEK	TEA	PVB	PEG	BBP
Quantity (g)	25	1.9	5.9	5.6	1.2	2	0.8	0.8

Table 1: Quantity of each component of the LSCF slurry

The second symmetrical cell was prepared by depositing Pt by DC magnetron sputtering on both side of the other SDC pellet for a final diameter of 9 mm.

II.2. Impedance measurements

Both LSCF//SDC//LSCF and Pt//SDC//Pt symmetrical cells were tested by EIS from 200 °C to 700 °C with steps of 25 °C in laboratory air under atmospheric pressure. As for the BZY symmetrical cells, each was studied a Norecs Probostat system in symmetrical atmosphere. Sinusoidal voltage was applied with an amplitude of 10 mV in the frequency range from 10^6 to 10^{-2} Hz.

Figure V.5 shows the Nyquist plots of the two symmetrical cells at various temperatures. Three different behaviors are observed depending on the temperature. From 200 °C to 325 °C (**Figure V.5.a and b**), the semi-circle corresponding to the grain bulk of the electrolyte response (from 10^6 Hz to 10^4 Hz) is much larger than the semi-circle corresponding to the grain boundaries of the electrolyte response (from 10^4 Hz to 10 Hz). From 250 °C, the beginning of a third semi-circle corresponding to the electrode response appears at low frequencies. The second behavior happens from 350 °C to 525 °C (**Figure V.5.c and d**), the electrolyte-related arches (from 10^6 to 10^3 Hz on Fig. 1.c. and from 10^6 to 10^5 Hz on Fig. 1.d.) overlap and gradually disappear while the temperature increases, until electrode-related arch is totally shown at 525 °C. From 550 °C (**Figure V.5.e and f**), only one single semi-circle can be observed, corresponding to the response of the electrodes. As expected, both real and imaginary part of the impedance decrease when the temperature increases.

At a temperature lower than 350 °C, the electrolyte bulk grain semi-circle is larger than the electrolyte grain boundary related arch due to the highly coalesced microstructure. As expected, the total electrolyte resistance is comparable for both LSCF and Pt electrodes. Platinum is a pure electronic conductor while LSCF is a MIEC, thus, the resistance related to the electrode is higher for Pt electrode.

By comparing the shape of the electrode related arch, it appears that the response starts by a straight line for LSCF electrode, which is characteristic of diffusion mechanism [331]. A small semi-circle can be observed on **Figure V.5.b**. at the beginning of the Pt semi-circle, corresponding to the presence of a double layer capacitance at the interface Pt//SDC [220].

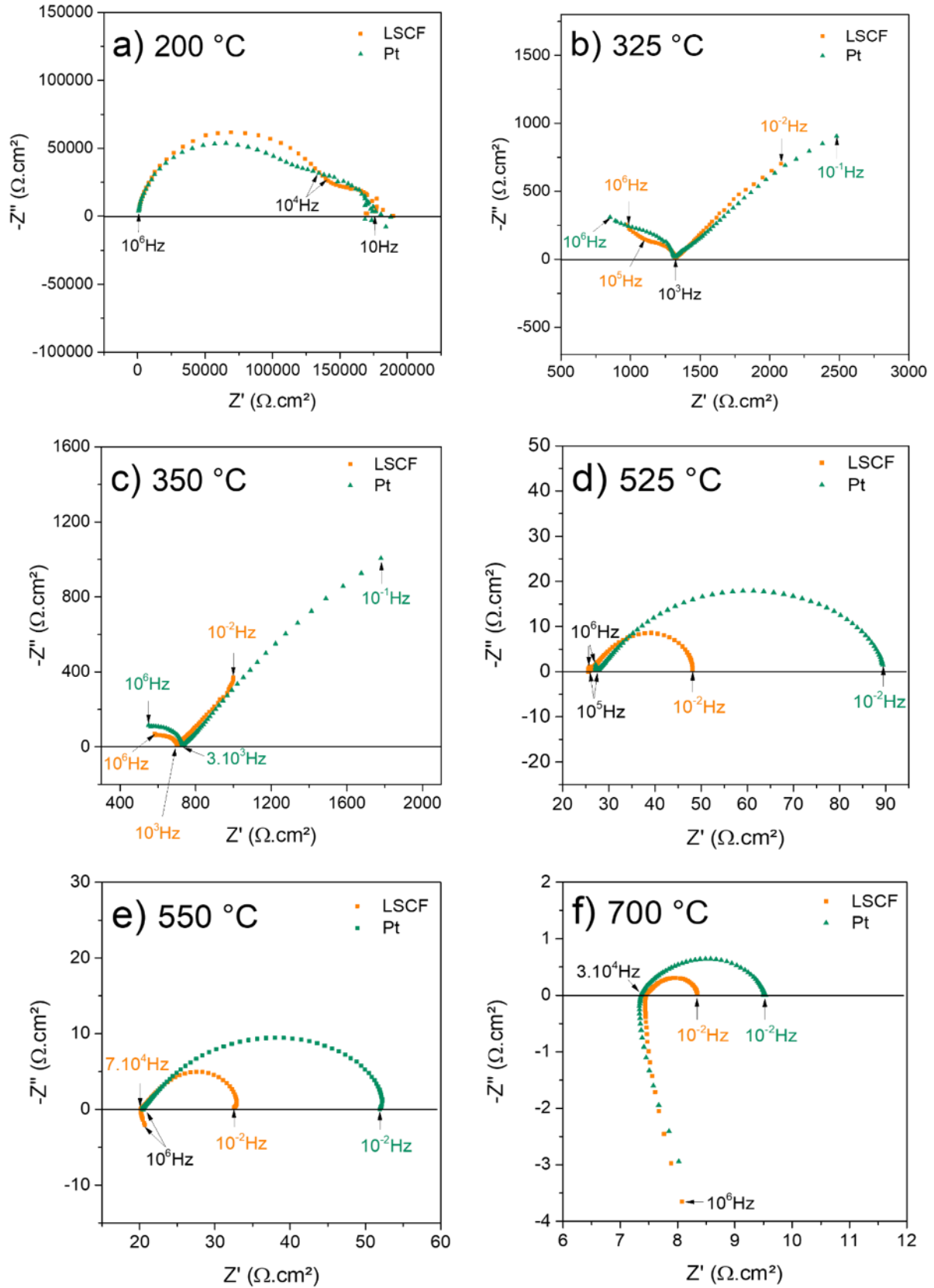


Figure 5: Nyquist plots of LSCF//SDC//LSCF and Pt//SDC//Pt symmetrical cells at a) 200 °C, b) 325 °C, c) 350 °C, d) 525 °C, e) 550 °C and f) 700 °C in air atmosphere. Some frequencies are written on the graph, the one in black correspond to the two spectra.

Electrolyte total resistance values are extracted at the high frequency intercept of the impedance arch with the real-axis on Nyquist plots. **Figure V.6** shows the inverse of the total resistance of the electrolyte (grain bulk + grain boundary) obtained from the two symmetrical cells. The values reported map the conductivity of the electrolyte, according to **Equation III.25**:

$$\sigma = \frac{1}{\rho} = \frac{1}{R} \times \frac{L}{S} \quad \text{Equation III.25}$$

Three Arrhenius-like behaviors are highlighted in three different domains: from 200 °C to 350 °C (A), from 350 °C to 550 °C (B) and from 550 °C to 700 °C (C), corresponding well to the three behaviors in the impedance spectra.

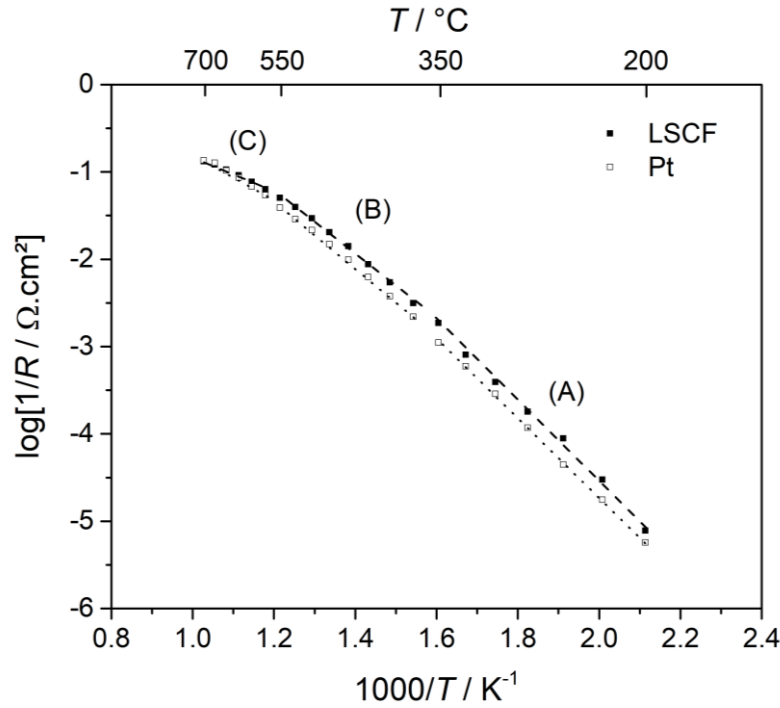


Figure 6: Arrhenius diagram of the two symmetrical cells in the temperature range 200 – 700 °C. The values reported correspond to the high frequency intercept of the impedance spectra with the x-axis.

The calculated activation energies for each domain are given in **Table V.2**. The values of activation energies decrease when the temperature increases and are very similar for the two samples from 200 °C to 550 °C. A higher temperature promotes an easier diffusion of oxygen ions in both bulk and grain boundary regions of the electrolyte and, thus, a lower activation energy.

Domain	$E_{a,LSCF}$ (eV)	$E_{a,Pt}$ (eV)
(A) Low temperature (200 – 350 °C)	0.89	0.90
(B) Intermediate temperature (350 – 550 °C)	0.74	0.76
(C) High temperature (550 – 700 °C)	0.45	0.58

Table 2: Obtained activation energies of SDC conduction on both LSCF//SDC//LSCF and Pt//SDC//Pt sample.

As a comparison, Ramesh et al. obtained 0.91 eV in the 150 – 300 °C range of temperature and 0.83 eV in the 500 – 700 °C range of temperature for a Ag//SDC//Ag sample [336]. Even if the obtained values correspond to the literature at low temperature, those obtained at higher temperature remain lower, especially in the 550 – 700°C range of temperature. The drop of activation energies from 350 °C is explained by the diffusion of oxygen and/or cation highlighted in the Nyquist plots. The decrease becomes more important as, from 550 °C to 700 °C, it is assumed that an electronic conductivity appears to compensate oxygen vacancies created by the cationic diffusion.

III. Complete cell

In this study, a NiO-SDC//SDC//LSCF cell was fabricated by co-tape casting and co-sintering procedures. The evolution of the SDC–LSCF interface after cell manufacturing and 40 h of operation was investigated. The novel methodology presented in this study consists of a microstructural and bulk chemistry analysis prior to a selective dissolution of the cathode layer in order to study the cathode–electrolyte interface by surface chemistry characterization.

III.1. Preparation of the complete cell

The starting NiO-SDC powder used in the anode was provide by fuel cell materials (Ref: NISDC-P Lot #BD105, Item #121205, surf. area 5.8 m².g⁻¹). The other powders are the same than those used for the symmetrical cells.

Complete cells are composed of five layers: NiO-SDC with pore former (graphite) as the anode, NiO-SDC without pore former as the anode functional layer (denoted AFL), SDC as the electrolyte, LSCF-SDC without pore former as the cathode functional layer (denoted CFL) and LSCF with pore former (graphite) as the cathode. Slurries were prepared according to the procedure described in chapter IV. Quantities used for each slurry are given in **Table V.3**.

Slurries	Powder (g)	Graphite (g)	Ethanol (g)	MEK (g)	TEA (g)	PVB (g)	PEG (g)	BBP (g)
Cathode (LSCF)	25	1.9	5.9	5.6	1.2	2	0.8	0.8
Cathode Functional layer (LSCF-SDC)	LSCF-SDC 12-12	1.9	5.9	5.6	0.8	2	0.8	0.8
Electrolyte (SDC)	22	0	6.8	6.8	0.8	2	0.8	0.8
AFL (NiO-SDC)	22	0	4.5	4.5	1	1.75	0.7	0.7
Anode (NiO-SDC)	63	5	13	13	2	5	2	2

Table 3: Quantities used for slurries preparation.

The cathode slurry is firstly tape casted on a glass at a casting rate of $1 \text{ cm} \cdot \text{s}^{-1}$. The blade gap thickness is fixed by taking into account the sintering shrinkage. The cathode layer is air-dried at room temperature for half an hour before the cathode functional layer is tape casted above. After a drying period of 1 h, the tape is punch-cut to the desired dimensions, 18 mm in diameter, before the electrolyte layer is directly tape casted onto. After a new period of drying, the anode functional layer is deposited, always by the same method. The last step consists of the anode, which is tape casted after a final period of drying. The complete cell is co-sintered at $1380 \text{ }^{\circ}\text{C}$ for 5 h at a heating and cooling rate of $1 \text{ }^{\circ}\text{C}$ per minute; two hours isothermal at $300 \text{ }^{\circ}\text{C}$ is applied to eliminate binder and plasticizers. The final size of the cell is 22 mm in diameter with a cathode of 16 mm in diameter.

III.2. Impedance measurement

The complete cell sintered was tested by EIS (Autolab PGSTAT302N) in a Norecs ProboStat from 10^5 Hz to 10^{-1} Hz with an amplitude of 50 mV at $550 \text{ }^{\circ}\text{C}$. The cell was fed by air at a pressure of 1.6 bar ($100 \text{ mL} \cdot \text{min}^{-1}$) to the cathode side and by H_2 at a pressure of 1.25 bar ($50 \text{ mL} \cdot \text{min}^{-1}$) at the anode side for the entire duration of testing (40 h). **Figure V.7.a** shows the evolution of the Nyquist plots at $550 \text{ }^{\circ}\text{C}$ over time. All spectra exhibited a similar shape, i.e., a short inductive tail, characteristic of electrical wires and cables, followed by two overlapped semi-circles at high and medium frequencies (hf and mf) and a partial semicircle at low frequencies (lf). Experimental data were fitted using the equivalent circuit presented in **Figure V.7.a** and the fitted elements are listed in **Table V.5**. The time constants (denoted as τ_{hf} , τ_{mf} and τ_{lf}) were calculated using the frequency at the maximum value of the impedance's imaginary part, and are highlighted in the Bode plot in **Figure V.7.b**. The intercept at high frequency with the real axis corresponds to the ohmic resistance (noted R_{Ω}), mainly related to the electrolyte. The evolution of the resistances over the time are presented in **Figure V.7.c**.

According to the ASC values presented in **Table V.4**, the first contribution at high frequency (ASC of about $10^{-5} \text{ F} \cdot \text{cm}^{-2}$) can be attributed to charge transfer, probably at the cathode/electrolyte [182]. The second contribution at medium frequency exhibiting an ASC value of the order of $10^{-3} \text{ F} \cdot \text{cm}^{-2}$ corresponds the HOR at the anode while the third contribution (ASC of about $10^{-2} \text{ F} \cdot \text{cm}^{-2}$) is associated with the ORR at the cathode side [258], [264].

The values of the resistances presented in **Table V.5** are relatively high in comparison with the results from Liu et al. at $550 \text{ }^{\circ}\text{C}$ [337]. Looking at the trends of the complex plots (**Figure V.8.a**) and of the Bode plots (**Figure V.8.b**), it is apparent that all resistances increased over time. The greatest contribution to the global polarization resistance R_p derived from the low frequency process (R_{lf}), while the one that underwent the greatest increment (450%) is the resistance at high frequencies (R_{hf}), which is associated with charge transfer at the cathode/electrolyte interface.

According to these considerations, the microstructural investigation contributes to shed light on the degradation mechanism both at the cathode–electrolyte interface and in the bulk cathode itself, as detailed in the following paragraphs.

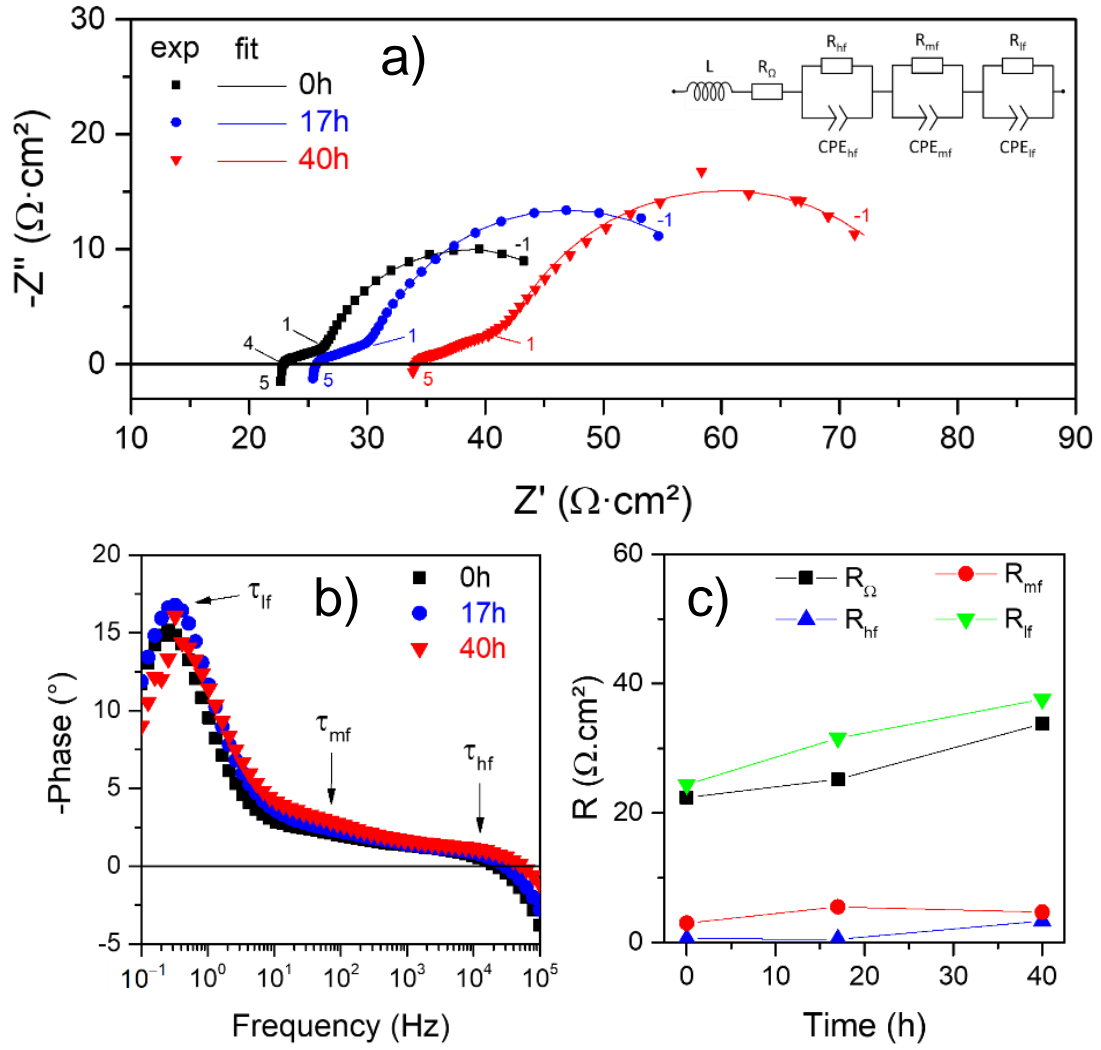


Figure 7: Electrochemical measurement at 550 °C of the cell sintered at 1380 °C at $t = 0$, 17 and 40 h. a) Nyquist plots, the numbers reported in the figure indicate the log of the frequency; b) Bode plots and c) evolution of the electrolyte resistance over the time.

Aging Time	Equivalent Capacitance, C_{eq} [F cm^{-2}]		
	hf	Mf	Lf
0 h	3.06×10^{-5}	3.87×10^{-3}	8.33×10^{-2}
17 h	1.94×10^{-5}	3.57×10^{-3}	5.56×10^{-2}
40 h	4.14×10^{-5}	2.23×10^{-3}	3.41×10^{-2}

Table 4: Equivalent capacitances for the three contributions, calculated from Hirschorn [270].

Time	L (H)	R_{Ω} ($\Omega\cdot\text{cm}^2$)	R_{hf} ($\Omega\cdot\text{cm}^2$)	Q_{hf} (F) (n_{hf})	τ_{hf} (s)	R_{mf} ($\Omega\cdot\text{cm}^2$)	Q_{mf} (F) (n_{mf})	τ_{mf} (s)	R_{lf} ($\Omega\cdot\text{cm}^2$)	Q_{lf} (F) (n_{lf})	τ_{lf} (s)
0 h	1.3×10^{-6}	22.4	0.6	2.4×10^{-3} (0.60)	3.4×10^{-4}	3.0	2.3×10^{-2} (0.60)	2.3×10^{-2}	24.4	7.6×10^{-2} (0.87)	5.5
17 h	1.2×10^{-6}	25.2	0.5	3.5×10^{-4} (0.75)	2.1×10^{-4}	5.5	3.1×10^{-2} (0.45)	1.8×10^{-2}	31.6	5.2×10^{-2} (0.88)	4.9
40 h	6.6×10^{-7}	33.8	3.3	1.9×10^{-3} (0.57)	1.7×10^{-4}	4.7	7.3×10^{-3} (0.74)	1.8×10^{-2}	37.6	3.3×10^{-2} (0.86)	4.4

Table 5: Fitted elements and mean time constants of the three semicircles

III.3. Post-mortem characterizations

III.3.a. Microstructural Investigations and Bulk Chemistry Analysis

The interface between the cathode (dark grey) and the electrolyte (light grey) after co-sintering at 1380 °C (**Figure V.9.a**) and after co-sintering at 1380 °C and testing 40 h at 550 °C (**Figure V.9.b**) was examined by SEM micrograph in Back Scattered Electrons (BSE) mode. The EDX mappings are also reported in order to show the distribution of the elements. The studied area is the cathode on which the electrolyte layer was deposited, viewed from above. The surface of the tested cell appears highly densified whereas the cell without electrical testing exhibits a porous microstructure. It is assumed that the tested cell underwent dramatic grain growth in this part of the sample. As shown in the micrograph at the top of **Figure V.10.b**, the rest of the tested sample is not as well densified.

As presented on the EDX mappings, for both samples, Ce and Sm are uniformly distributed in the electrolyte layer. The cathode–electrolyte interface is very sharp for Ce whereas it is more diffused for Sm. La and Fe are also well dispersed within the cathode layer with a sharp cathode–electrolyte separation for Fe. Little Co appears in the cathode layer. Additionally, some Sr-rich or Sr-depleted areas are observed in both samples.

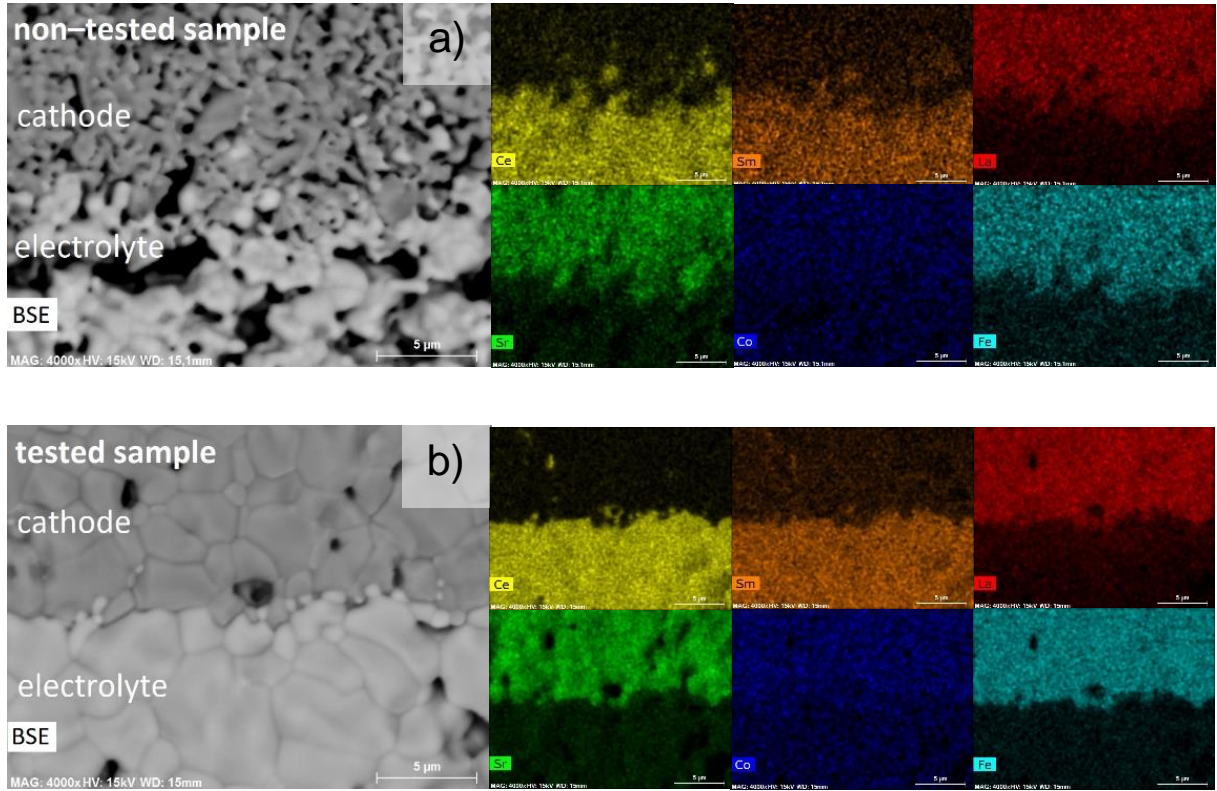


Figure 8: BSE-SEM surface micrograph and EDX mappings of the cathode–electrolyte interface, a) before and b) after cell testing.

The elemental content evolution as a function of the distance from the cathode–electrolyte interface on either side of the cathode–electrolyte interface is exhibited in **Figure V.10.a** for the non-tested sample and on **Figure V.10.b** for the tested sample. Only cation-related signals recorded are reported. EDS measurements were acquired at each cross on the SEM-BSE micrograph inserted at the top of the figures. Content variations of La, Sr and Fe are observed in the cathode layer. For the following interpretation, La and Sr are assumed to occupy to the A-site of the perovskite whereas Fe and Co to belong to the B-site. The A-site/B-site ratio ranges from 0.95 to 1.16, which is higher than the theoretical value of 0.95. The La/A-site ratio is also higher than the expected value of 0.60, varying from 0.67 to 0.78 with an average value of 0.72, while the Co/B-site ratio is much lower than the theoretical value of 0.20, ranging from 0.01 to 0.05. In the electrolyte layer, Ce and Sm contents are stable, reaching a $\text{Sm}/(\text{Ce}+\text{Sm})$ ratio of 0.19 ± 0.01 , close to the 0.20 theoretical value. Lanthanum is also detected in the electrolyte layer up to a distance of 8 μm , while significant amounts of Sm and Ce are observed in the cathode layer up to a distance of 7 μm .

Considering the size of the cations, 0.97 Å for Ce^{4+} and 1.079 Å Sm^{3+} in cubic site, La^{3+} (ionic radius of 1.16 Å in cubic site) could not easily occupy the cationic site of the ceria structure [338]. However, the substitution of Ce^{4+} with Sm^{3+} creates oxygen vacancies and therefore enhances the reduction of Ce^{4+} into Ce^{3+} , which has an ionic radius of 1.143 Å [339], [340]. In that configuration, depending on the reduction of cerium, La^{3+} could substitute for

Ce^{3+} in the structure. Several authors have studied the incorporation of La into SDC, for example, Giannici et al. highlighted a diffusion up to 30% at 1150 °C while Chang et al. noticed a diffusion of La into SDC up to 15% at 1000 °C [341], [342].

The A-site of the perovskite (12-coordinate site), occupied by La^{3+} and Sr^{2+} with ionic radii of 1.36 Å and 1.44 Å, can also host Sm^{3+} and Ce^{4+} ions, which have ionic radii of 1.24 Å and 1.14 Å respectively in the 12-coordinate environment [338]. Moreover, Sm presents a good chemical affinity with Sr and Fe, as evidenced by the $\text{Sm}_{0.5}\text{Sr}_{0.5}\text{FeO}_{3-\delta}$ compounds [343], and Ce can also be incorporated into the LSCF structure as highlighted in the $\text{La}_{0.54}\text{Ce}_{0.06}\text{Sr}_{0.4}\text{Co}_{0.2}\text{Fe}_{0.8}\text{O}_{3-\delta}$ compound [344].

In order to investigate the origin of the cationic diffusion, i.e., during co-sintering or during cell operation, another cell, elaborated by the same procedure and co-sintered at 1380 °C without any electrochemical testing, was studied by SEM-EDX. In the cathode layer, La, Fe and Co contents are more stable than in the tested sample, the Sr amount shows important variation, and Ce and Sm are detected up to a distance of 5 µm. The A-site/B-site ratio is 1.04 ± 0.05 . La/A-site ratio is 0.62 ± 0.03 , not far from the theoretical value and the Co/B-site is a little larger than the tested sample and is equal to 0.07 ± 0.02 . In the electrolyte, Ce and Sm have the same profile as the tested sample, the $\text{Sm}/(\text{Ce} + \text{Sm})$ is 0.18 ± 0.01 and lanthanum is detected in a significant amount up to a distance of 7 µm.

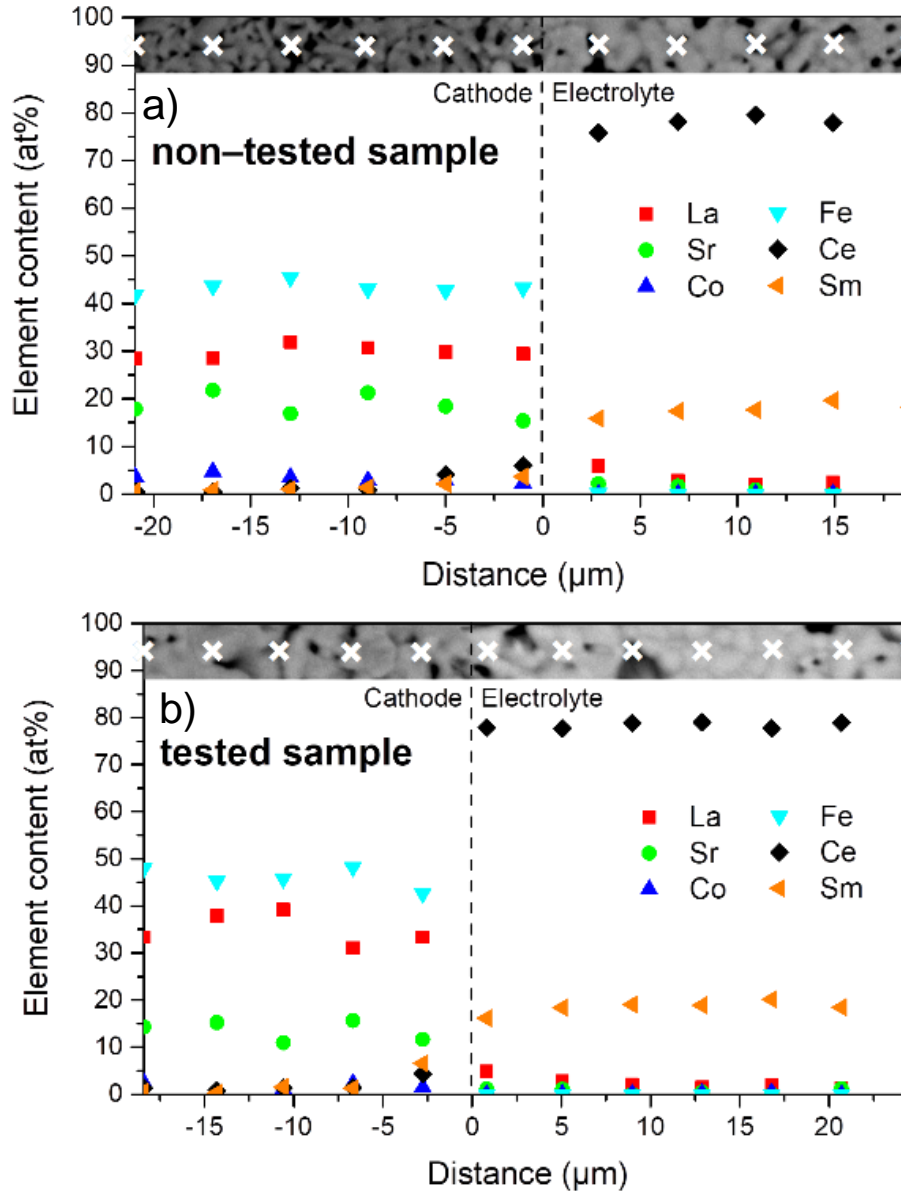


Figure 9: Elemental content evolution in the cathode and the electrolyte layers as a function of the distance from the interface, represented as a dashed line, for a) the non-tested sample and b) the tested sample. EDX point measurements were acquired at each cross on the SEM-BSE micrograph inserted at the top of the figures.

III.3.b. Structural and Surface Chemistry Analysis

In order to study the SDC–LSCF interface, the cathode layer was selectively dissolved in HCl 6M for 20 min at room temperature after cell testing. **Figure V.10** exhibits the SEM-BSE micrograph of the cathode–electrolyte microstructure interface after the selective dissolution of the cathode. The light area represents SDC grains while the dark clusters correspond to LSCF grains that were not totally dissolved.

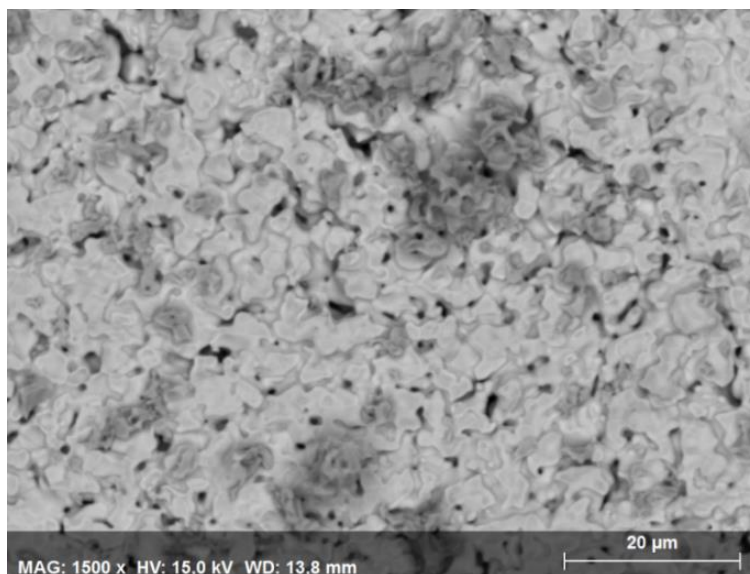


Figure 10: BSE-SEM micrograph of the cathode–electrolyte interface after selective dissolution of LSCF.

The low incidence angle X-ray diffractogram of the cathode-electrolyte interface after the selective dissolution of LSCF is reported in **Figure V.11**. The major phase obtained is a cubic fluorite structure with a Fm-3m space group corresponding to the doped ceria phase. Since LSCF was not totally dissolved, traces of perovskite are also detected. Rietveld refinement was performed on the diffractogram. The refined lattice parameter of the doped ceria phase is 5.465(0) Å. As a comparison, X-ray diffraction was also carried out on the same sample on the electrolyte area 2 mm far from the cathode layer. The refined lattice parameter is 5.426(2) Å, similar to the 5.432 Å obtained by Mandal *et al.* for $\text{Ce}_{0.8}\text{Sm}_{0.2}\text{O}_{1.9}$ (ICDD 04-013-0036) [345]. The increase in the lattice parameter of the ceria structure at the cathode–electrolyte interface cannot be imputed to defects generated by the sintering step and evidences the co-doping of cerium by lanthanum and samarium doped $\text{Ce}_{1-x}(\text{Sm},\text{La})_x\text{O}_{2-\delta}$, denoted LSDC. The LSCF phase can either be cubic perovskite (space group Pm-3m) or rhombohedral perovskite (space group R-3c) [346], [347]. However, the rhombohedral structure presents a clear separation of the peak. In the diffractogram presented in **Figure V.11**, no separation is visible. Therefore, the LSCF after co-sintering and cell testing is assumed to be cubic perovskite. The refined lattice parameter of the cubic LSCF phase is 3.889(6) Å, as a comparison, Hardy *et al.* obtained a cubic lattice parameter of 3.9250 Å [348]. The lower value of the lattice parameter obtained is consistent with the ex-solution of Sr and the diffusion of La. The low amount of Sm and Ce diffusion into the LSCF structure resulted in a decrease in the lattice parameter.

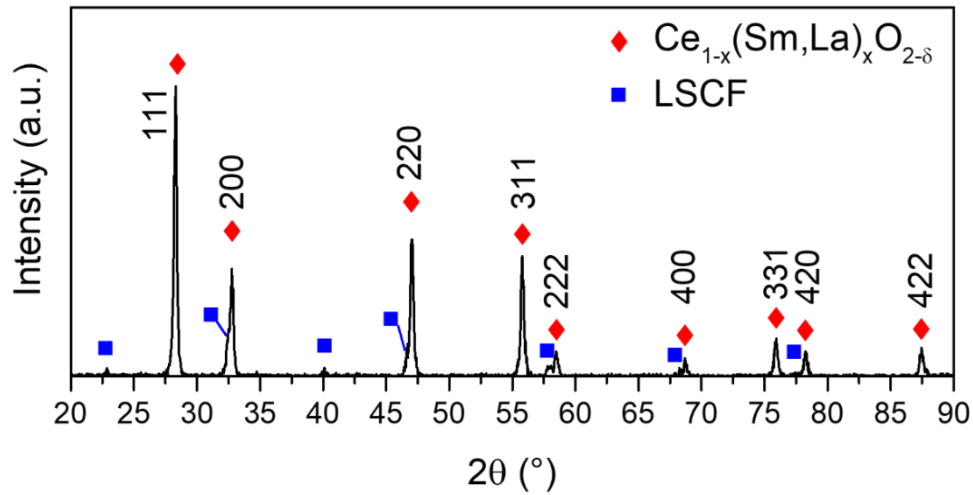


Figure 11: Low incidence angle (2°) X-ray diffractogram of the cathode–electrolyte interface after the selective dissolution of LSCF.

Two areas were selected for XPS surface chemistry analyses, one corresponding to the cathode-electrolyte interface (denoted tested interface) and one corresponding to the electrolyte area which is not in contact with LSCF material (denoted reference SDC). Furthermore, another cell sintered at 1380°C without any electrochemical testing was analyzed to give a reference for the LSCF layer. The elemental content of each area obtained is presented in **Table V.6**. Compared to the theoretical composition, oxygen is more present than expected, due to adventitious oxygen such as OH, C-O and O-C=O bonding. The obtained Sm/(Ce+Sm) ratios for the tested interface and for the reference SDC are both 0.18, not far from the theoretical value of 0.20. In the reference LSCF, the ratio La/A-site is 0.23, almost three times lower than the expected 0.6, suggesting a Sr-rich phase at the extreme surface of the cathode. Due to interference with iron characteristic peaks, cobalt was excluded from the analysis.

Area	C	Ce	Sm	La	Sr	Fe	O
Tested interface	ND	10.2	2.2	4.6	4.1	11.3	67.7
Reference SDC	ND	19.4	4.4	ND	ND	ND	76.2
Reference LSCF	8.5	ND	ND	4.7	15.4	5.7	65.7

Table 6: Elemental composition (atomic%) of the tested interface, reference SDC and reference LSCF obtained by XPS. Adventitious carbon, cobalt and residual chlorine were removed from the elemental composition. ND (Non Determined).

Figure V.12 shows the Ce 3d (**Figure V.12.a**) and Sm $3d_{5/2}$ (**Figure V.12.b**) core-level spectra of the tested interface and reference SDC and the La 3d (**Figure V.12.c**), Sr 3d (**Figure**

V.12.d) and Fe 2p (**Figure V.12.e**) core-level spectra of both the tested interface and reference LSCF. Furthermore, the C 1s spectrum (**Figure V.12.f**) of the reference LSCF is also presented in **Figure V.12**.

The Ce 3d spectra, typical of a ceria environment, can be decomposed into four spin-orbit components. The peaks labeled v and u refer to 3d_{5/2} and 3d_{3/2} spin-orbit components respectively. The peaks denoted v, v'', v''', u, u'' and u''' are characteristic of Ce ions in the +IV oxidation state, while the v' and u' peaks correspond to cerium ions in the +III oxidation state [322], [349], [350]. Both samples exhibit Ce⁴⁺ and Ce³⁺ characteristic peaks. The percentage of reduced cerium ion can be obtained by summing the relative area of the v' and u' peaks. The obtained %Ce³⁺ are 7.8% and 12.9% for the reference SDC and the tested area, respectively. Several studies showed that lanthanum incorporation into the ceria structure promotes the reduction of Ce⁴⁺ into Ce³⁺ [351], [352]. Thus, the higher concentration of Ce³⁺ in the tested area can be attributed to lanthanum incorporation into the ceria structure.

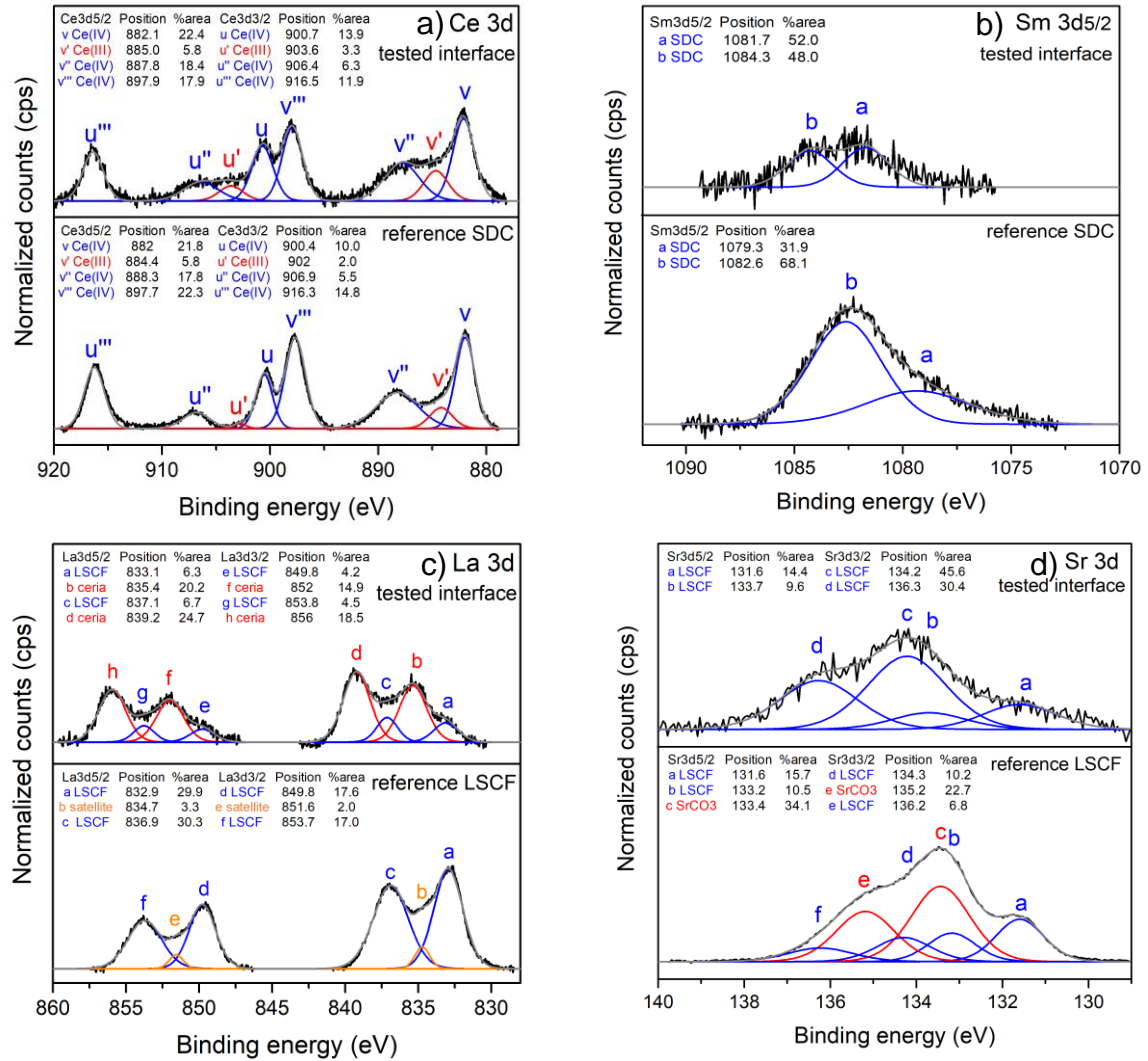
The Sm 3d_{5/2} core level spectra exhibit two peaks at 1079.3 eV and 1082.6 eV for the reference SDC and 1081.7 eV and 1084.3 eV for the tested interface. The contribution at high binding energy for the two samples corresponds to Sm in the +III oxidation state while the one at 1079.1 eV corresponds to charge transfer of the unpaired 4f electron [52,57,58]. The coordination number induces a chemical shift of the binding energy [353]–[356], however, the Sm 3d_{5/2} spectrum of the tested interface was too noisy to separate the contributions of Sm³⁺ from SDC and Sm³⁺ from LSCF.

The La 3d spectra present well separated spin-orbit components and each spin-orbit component is split into doublets. The degree of splitting and the position of the doublet allow the determination of the element's chemical environment [357], [358]. In the case of the reference LSCF, the doublet at 832.9 eV shows a split of 3.9 eV corresponding to LSCF [359], [360]. A satellite component was added to fit the asymmetric shape of the doublet [361]. The tested interface presented two doublets, suggesting two different chemical environments. The doublet at the lower binding energy (833.1 eV) with a split of 4.0 eV is attributed to LSCF that was not totally dissolved. The second doublet at 835.4 eV has a split of 3.9 eV. By taking into account the previous deduction concerning La diffusion, the second doublet is assigned to lanthanum in the ceria environment.

The classical figure of Sr 3d spectra in LSCF exhibits two contributions, the one at low binding energy corresponding to the bulk and the one at high binding energy corresponding to the surface [362]–[364]. Thus, for the tested interface, the doublet at 131.6 eV is attributed to the bulk component and the doublet at 134.2 eV to the surface component. However, the reference LSCF could not be fitted by only two spin-orbit components. A third contribution at 133.4 eV was added to fit the spectra. According to the literature, this contribution is assigned to strontium carbonate [365], [366]. This assignment is supported by the C 1s core-level spectra of reference LSCF, which exhibited a peak at 289.1 eV, well corresponding to strontium carbonate. Thus, the strontium-rich areas highlighted by EDX mappings correspond to SrCO₃.

During the selective dissolution of the cathode, SrCO_3 was also dissolved, resulting in only two contributions of Sr in LSCF in the Sr 3d window of the tested interface.

The Fe 2p present well separated spin-orbit components and a satellite. The two samples present the classical figure of iron from LSCF, where each spin-orbit component can be fitted by two contributions, the one at low binding energy corresponding to iron +III oxidation state while the one at higher binding energy belongs to iron +IV oxidation state [50,73,74].



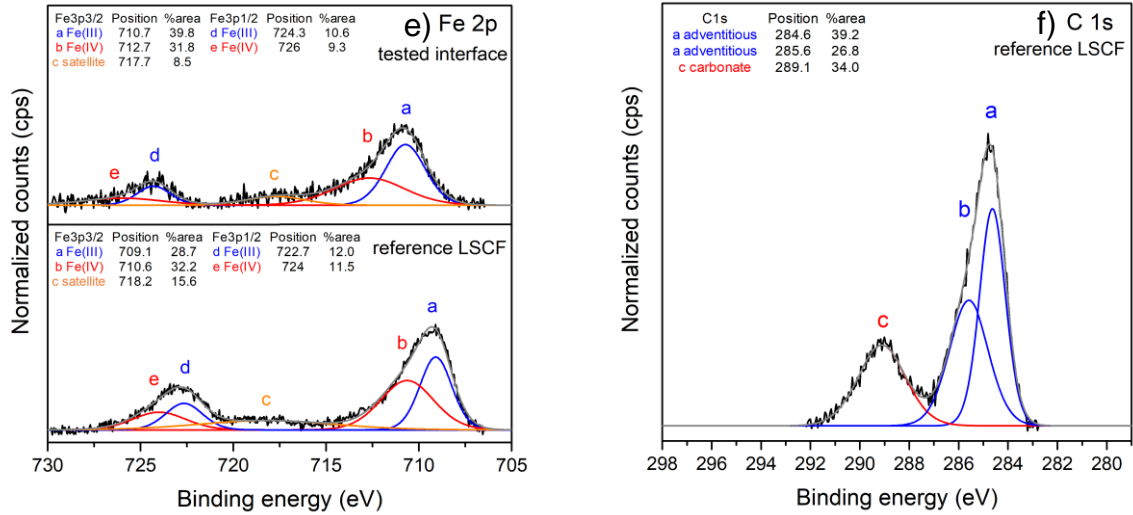


Figure 12: XPS windows spectra of the tested interface and the reference sample, a) Ce 3d core-level spectra, b) Sm 3d_{5/2} core-level spectra, c) La 3d core-level spectra, d) Sr 3d core-level spectra, e) Fe 2p core-level spectra and f) C 1s core-level spectra.

III.3. Discussion

The two chemical behaviors, the strontium segregation and the lanthanum diffusion towards SDC, highlighted in this study are depicted in **Figure V.13**. As investigated by several authors, Sr segregation generally occurs during cell operation and long-term testing. For example, Simner et al. pointed out a significant performance degradation at 750 °C/0.7 V after 500 h due to Sr segregation [367]. Wang et al. highlighted a tremendous increase in Sr-rich areas after cell testing at 800 °C/OCV for 800 h [368]. In this work, a massive increase in the cathodic polarization resistance was found after only 40 h of cell operation. As suggested by Kubicek et al. and Dai et al., this rapid degradation is caused by the high temperature sintering [369], [370]. According to the XPS results, the strontium segregated into SrCO₃, consisting of SrO formation at high temperature followed by carbonation after returning to room temperature. The degradation of the cathode surface by SrCO₃ resulted in a decrease in the ORR sites. This led to mass transfer process deterioration, i.e., oxygen surface adsorption and desorption and surface diffusion of the species, thus inducing an increase in the cathodic polarization resistance (R_{lf}) [371], [372].

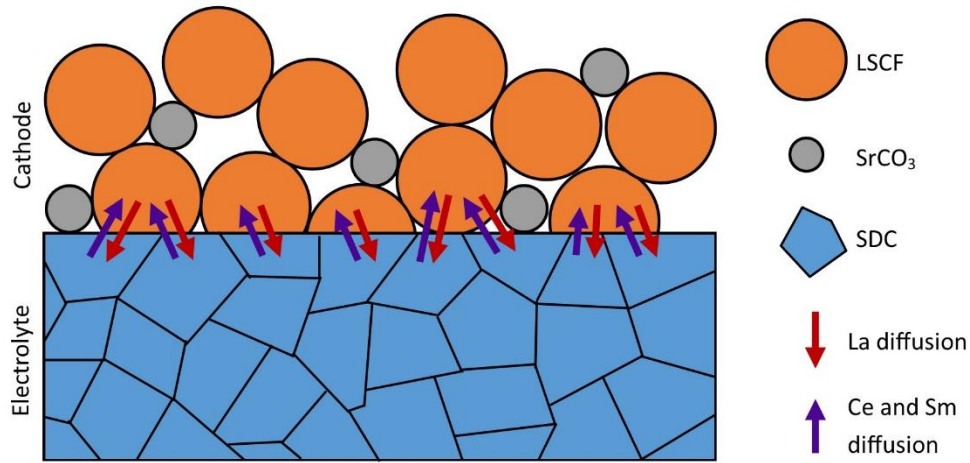


Figure 13: Schematic of the strontium segregation and lanthanum, cerium and samarium diffusion.

The La 3d XPS spectrum of the tested interface clearly indicated that lanthanum is present both in LSCF and in ceria. The La/(Ce + Sm + La) ratio in the electrolyte layer at 2.5 μm from the interface with LSCF obtained by EDX quantification is 0.04 after cell testing. Lanthanum is also detected in significant quantities in the electrolyte layer near the interface in the non-tested sample, indicating that lanthanum diffusion occurs mainly during sintering. Moreover, this diffusion is assumed to be mainly surface diffusion. The grain boundaries have more crystallographic defects than the bulk, implementing a facilitated pathway for cation diffusion [373]. Thus, cations diffuse preferentially through the grain boundaries; however, bulk diffusion is also possible, creating a concentration gradient from the grain boundaries to the bulk of the grain [374], [375].

The high sintering temperature led to an increase in the mobility of cations, causing the interdiffusion of Ce and Sm from the electrolyte and La from the cathode. The La diffusion into the electrolyte led to the high R_{Ω} resistance value highlighted in Table 2 due to the decrease in oxygen vacancies mobility and/or defect clustering as well as lattice strains [321], [376]. Moreover, the increase in R_{Ω} during cell testing suggests that the cation interdiffusion continued under operating conditions. This assumption is supported by the highlight of the diffusion mechanism in LSCF//SDC//LSCF cell measurements. On the other side, diffusion of both Sm and Ce into the cathode layer caused the slight increase in R_{hf} .

As highlighted before, Sr-segregation is widely reported, which is not the case for the diffusion of lanthanum. In the classical YSZ-based SOFC, an SDC or GDC layer is added as a diffusion barrier layer between YSZ and LSCF [377], [378]. The results presented in this work suggest that GDC is more effective than SDC to hinder lanthanum ion diffusion.

IV. Conclusions

Impedance measurement of a Ni-SDC//SDC//LSCF cell fabricated by a cost-effective process consisting of co-tape casting and co-sintering showed a strong degradation in performance after the first 40 h of operation. By studying the electrochemical properties of LSCF//SDC//LSCF and Pt//SDC//Pt symmetrical cells, a diffusion mechanism appears for the LSCF symmetrical cell while this is not the case for Pt symmetrical cell. This diffusion may induce a chemical degradation between LSCF and SDC. EDX and XPS observations evidence that lanthanum diffuses into the $\text{Ce}_{0.8}\text{Sm}_{0.2}\text{O}_{2-\delta}$ electrolyte layer, the preferred diffusion paths appear to be the grain boundaries. It occurs during sintering and cell operation and leads to the formation of a La- and Sm-doped ceria, resulting in a slight increase of the ohmic resistance. On the other hand, a strontium segregation into SrCO_3 clusters at the interface and at the surface of LSCF grains is also highlighted. This mechanism occurs during sintering and possibly pursues during cell operation and leads to a tremendous increase of the cathode polarization resistance. This severe drop in the performances is enhancing by the destabilization of the perovskite structure during thermal treatment due to the segregation of the strontium ions out of the LSCF phase. Finally, strontium segregation is very detrimental for the cell performance while lanthanum diffusion into Sm-doped ceria only results in a small increase of the degree of reduction of cerium

ANNEX A: RIETVELD REFINEMENT DATA

This annex presents the Rietveld refinement data as imputed in FullProf software. The occupation rate (noted occupation*), as given in FullProf manual, was calculated according to **Equation A.1**.

$$\text{Occupation}^* = \text{Occupation} \times \frac{\text{site multiplicity}}{\text{general multiplicity}} \quad \text{Equation A.1}$$

Phase BaZrO₃

CIF number: 1538369

System: cubic

Space group: *Pm-3m* (221)

General multiplicity: 48

Lattice parameter: 4.1815 Å ($\alpha = \beta = \gamma = 90^\circ$)

Atom	Oxidation state	x	y	z	Occupation	Site	Occupation*
Ba	+2	0	0	0	1	1b	0.02083
Zr	+4	0.5	0.5	0.5	0.8	1a	0.02083
O	-2	0	0.5	0.5	1	3d	0.0625

Table A.1: Structural parameters of the cubic BZ.

Phase BaCO₃

CIF number: 1000033

System: orthorhombic

Space group: *Pnma* (62)

General multiplicity: 8

Lattice parameter: a = 5.3126 Å, b = 8.8958 Å and c = 6.4284 Å ($\alpha = \beta = \gamma = 90^\circ$)

Atom	Oxidation state	x	y	z	Occupation	Site	Occupation*
Ba	0	0.25	0.41631	0.7549	1	4c	0.5
C	0	0.25	0.757	-0.081	1	4c	0.5
O	0	0.25	0.9011	-0.0878	1	4c	0.5
O	0	0.25	0.6839	-0.079	1	8d	1

Table A.2: Structure parameter of the orthorhombic BaCO_3 .Phase CeO_2

CIF number: 9009008

System: cubic

Space group: $Fm\bar{3}m$ (225)

General multiplicity: 192

Lattice parameter: 4.4110 Å ($\alpha = \beta = \gamma = 90^\circ$)

Atom	Oxidation state	x	y	z	Occupation	Site	Occupation*
Ce	+4	0	0	0	1	4a	0.02083
O	-2	0.25	0.25	0.25	1	8c	0.04167

Table A.3: Structural parameters of the cubic CeO_2 .Phase $\text{BaZr}_{0.8}\text{Y}_{0.2}\text{O}_{2.9}$

Adapted from CIF number: 7202179

System: cubic

Space group: $Pm\bar{3}m$ (221)

General multiplicity: 48

Lattice parameter: 4.2088 Å ($\alpha = \beta = \gamma = 90^\circ$)

Atom	Oxidation state	x	y	z	Occupation	Site	Occupation*
Ba	+2	0	0	0	1	1b	0.02083

Annex A: Rietveld refinement data

Zr	+4	0.5	0.5	0.5	0.8	1a	0.01667
Y	+3	0.5	0.5	0.5	0.2	1a	0.00417
O	-2	0	0.5	0.5	0.9667	3d	0.06042

Table A.4: Structural parameters of the cubic BZY20.

Phase YO(OH)

Adapted from Klevtsova and Klevtosov [379]

System: monoclinic

Space group: $P2_1/m$ (11)

General multiplicity: 4

Lattice parameter: $a = 4.28 \text{ \AA}$, $b = 3.63 \text{ \AA}$, $c = 6.05 \text{ \AA}$, $\alpha = \beta = 90^\circ$ and $\gamma = 112.5^\circ$.

Atom	Oxidation state	x	y	z	Occupation	Site	Occupation*
Y	+3	0.643	0.25	0.312	1	2e	0.5
O1	-2	0.781	0.75	0.552	1	2e	0.5
O2*	-1	0.310	0.75	0.058	1	2e	0.5

*Table A.5: Structural parameters of the monoclinic YO(OH).. *O2 is the oxygen supporting the hydrogen.*

Phase $Y_{0.8}Zr_{0.2}O(OH)$

Adapter from Klevtsova and Klevtosov [379]

System: monoclinic

Space group: $P2_1/m$ (11)

General multiplicity: 4

Lattice parameter: $a = 4.28 \text{ \AA}$, $b = 3.63 \text{ \AA}$, $c = 6.05 \text{ \AA}$, $\alpha = \beta = 90^\circ$ and $\gamma = 112.5^\circ$.

Atom	Oxidation state	x	y	z	Occupation	Site	Occupation*
Y	+3	0.643	0.25	0.312	0.8	2e	0.4
Zr	+4	0.643	0.25	0.312	0.2	2e	0.1
O1	-2	0.781	0.75	0.552	1	2e	0.5

O2**	-1	0.310	0.75	0.058	1	2e	0.5
------	----	-------	------	-------	---	----	-----

*Table A.6: Structural parameters of the c monoclinic $Y_{0.8}Zr_{0.2}O(OH)$. ** O2 is the oxygen supporting the hydrogen.*

Phase $Y_{1.6}Zr_{0.4}O_{3.2}$

Adapted from CIF number: 1009013

System: cubic

Space group: $Ia-3$ (206)

General multiplicity: 48

Lattice parameter: 10.3935 Å ($\alpha = \beta = \gamma = 90^\circ$)

Atom	Oxidation state	x	y	z	Occupation	Site	Occupation*
Y	+3	0.96742	0	0.25	0.8	24d	0.4
Y	+3	0.25	0.25	0.25	0.8	8b	0.13333
Zr	+4	0.96742	0	0.25	0.2	24d	0.1
Zr	+4	0.25	0.25	0.25	0.2	8b	0.03333
O	-2	0.39072	0.1519	0.38016	1.0667	48e	1.06667

Table A.7: Structural parameters of the cubic $Y_{1.6}Zr_{0.4}O_{3.2}$.

ANNEX B: DIFFRACTOGRAM OF THE BAF₂ SAMPLE

This annex presents the diffractogram of the BaF₂ single-cristal used to determine the broadening due to the instrument. The experimental diffractogram is presented in **Figure B.1**.

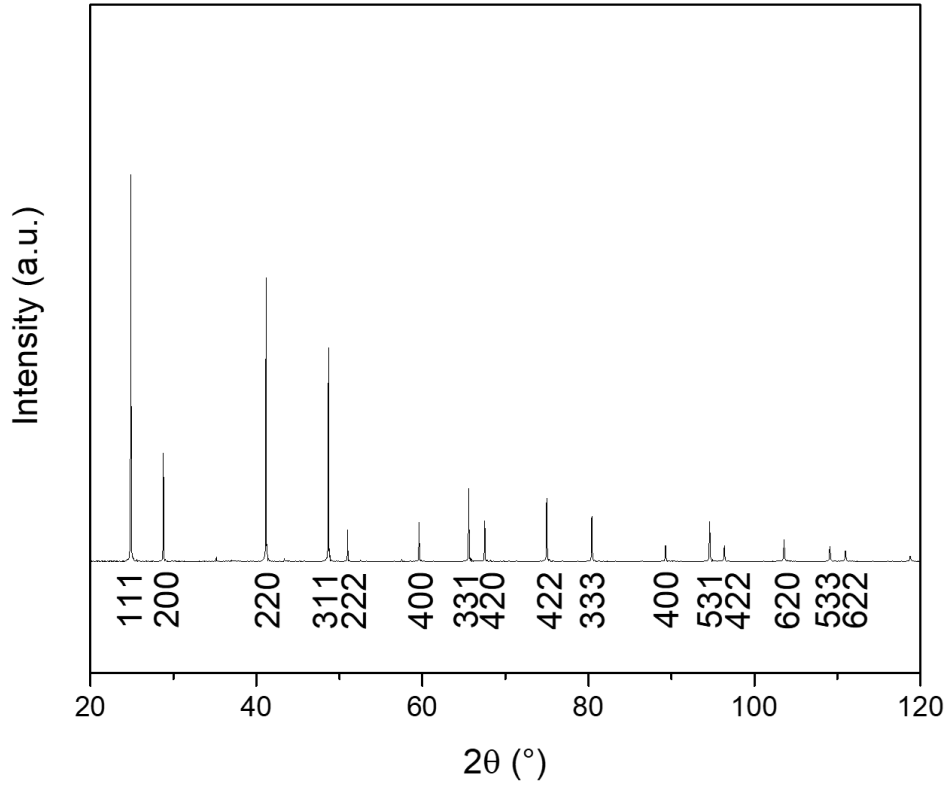


Figure B.1: XRD pattern of the BaF₂ single-cristal

The plot representing the integral breadth β (that can be assimilated to $\beta_{\text{instrumental}}$) as a function of 2θ is presented in **Figure B.2**. The experimental integral breadths were determined using Eva software. The curve can be fitted with a second degree polynomial function expressed as **Equation B.1**:

$$\beta = 1.3574 \times 10^{-5} \times (2\theta)^2 - 9.8955 \times 10^{-4} \times (2\theta) + 1.0403 \times 10^{-1} \quad \text{Equation B.1}$$

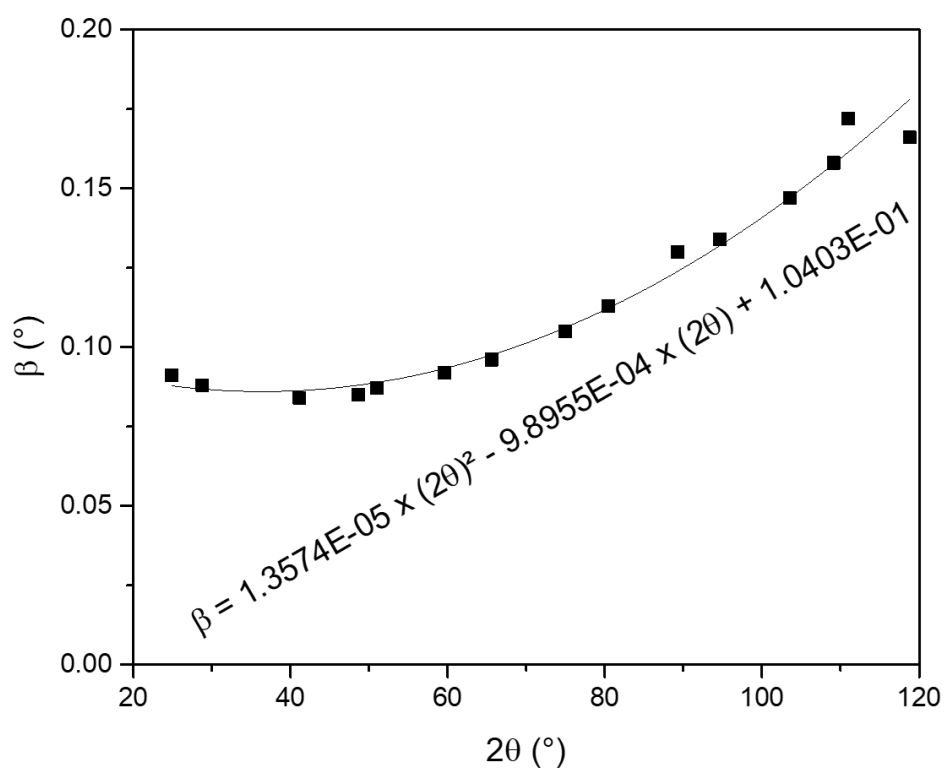
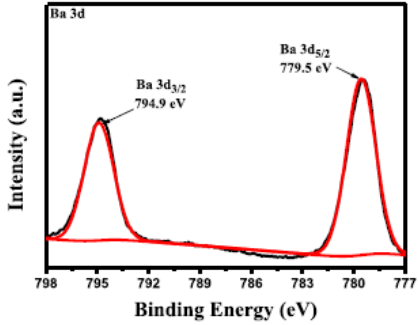
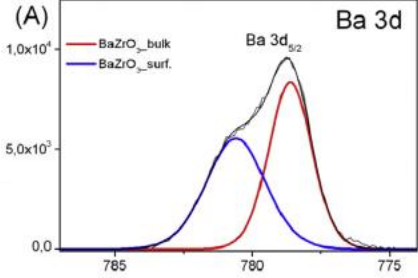
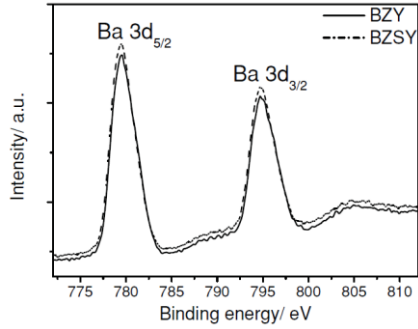


Figure B.2: β as a function of 2θ plot of the BaF₂ single-cristal

ANNEX C: XPS LITERATURE SURVEY

This annex presents the literature data used for the plot in **Figure II.26** and the interpretation of XPS spectra in Chapter II.

Ba 3d

Compound (elaboration method)	Binding energy (eV)	Figure caption	Ref
BZ (solvothermal using ethylene- diamine)	Ba 3d _{5/2} (BZ) = 779.5		Chen 2019
BZ (hydrothermal synthesis)	Ba 3d _{5/2} (BZ, bulk) = 778.7 Ba 3d _{5/2} (BZ, surface) = 780.6	(A) 	Miodynska 2017
BZY20 (combustion)	Ba 3d _{5/2} (BZY) = 779.7		Sun 2013
BaCO ₃	Ba 3d _{5/2} (BaCO ₃) = 779.5 – 780.3	No figure	Handbook of XPS 1993
BaCO ₃ (purchased from Hopkins and Williams)	Ba 3d _{5/2} (BaCO ₃) = 779.4	No figure	Christie 1983

BaCO_3
(purchased
from CERAC)

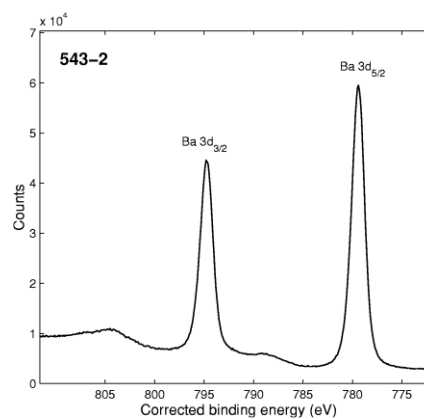
$\text{Ba } 3d_{5/2} (\text{BaCO}_3) =$
779.8

No figure

Gauzzi
1990

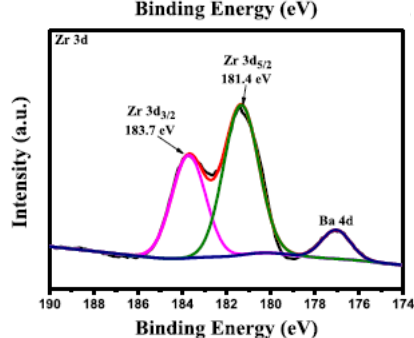
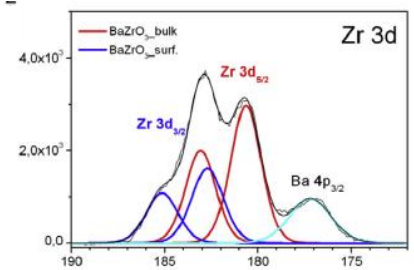
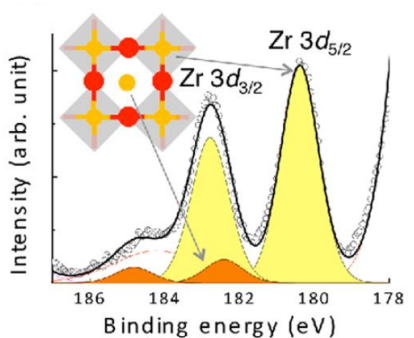
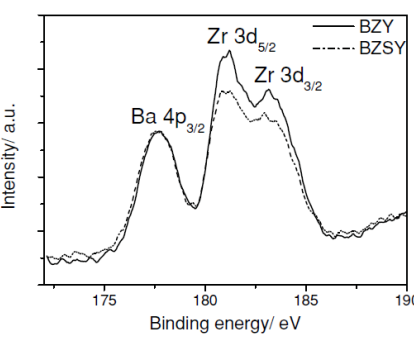
BaCO_3
(purchased
from from
Alfa/AESARS)

$\text{Ba } 3d_{5/2} (\text{BaCO}_3) =$
779.4



Schmitz
2001

Table C.1: Ba 3d literature review

Zr 3d			
Compound (elaboration method)	Binding energy (eV)	Figure caption	Ref
BZ (solvothermal using ethylenediamine)	Zr 3d _{5/2} (BZ) = 181.4 Zr 3d _{3/2} (BZ) = 183.7		Chen 2019
BZ (hydrothermal synthesis)	Zr 3d _{5/2} (BZ, bulk) = 180.6 Zr 3d _{3/2} (BZ, bulk) = 183.0 Zr 3d _{5/2} (BZ, surface) = 182.7 Zr 3d _{3/2} (BZ, surface) = 185.1		Miodynska 2017
BZY20 (pulsed laser deposition)	Zr 3d _{5/2} (Zr _{Zr}) = 180.3 Zr 3d _{3/2} (Zr _{Zr}) = 182.8 Zr 3d _{5/2} (Zr _{Ba} ^{••}) = 182.2 Zr 3d _{3/2} (Zr _{Ba} ^{••}) = 184.9		Aruta 2016 [202]
		Partial substitution of Ba by Zr and Y	
BZY20 (combustion)	Zr 3d _{5/2} (BZY) = 181.0 Zr 3d _{3/2} (BZY) = 183.3		Sun 2013
ZrO ₂	Zr 3d _{5/2} (ZrO ₂) = 182.0 – 182.5	No figure	Handbook of XPS 1993

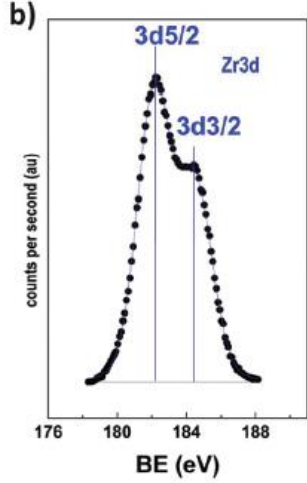
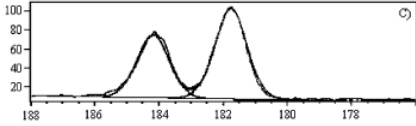
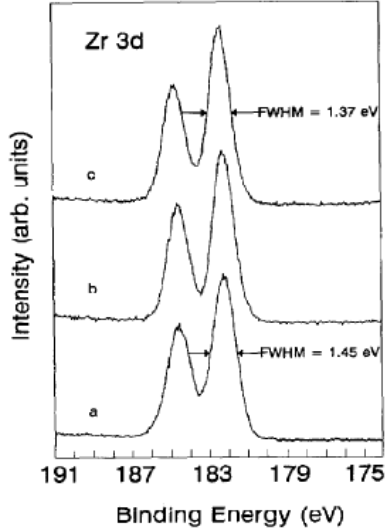
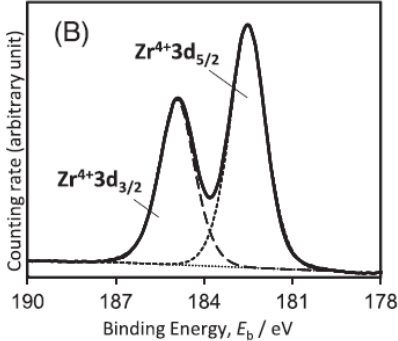
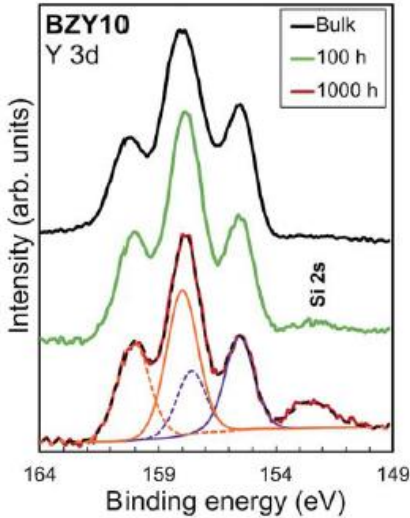
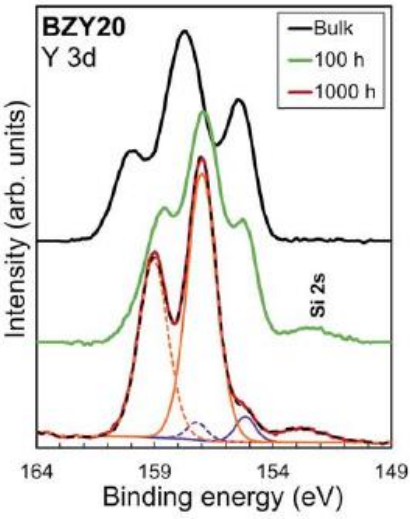
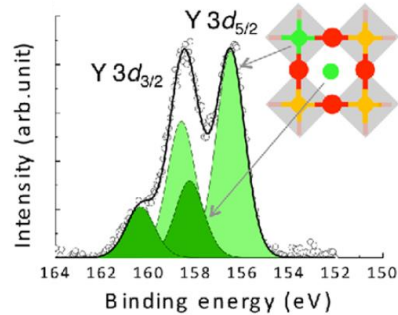
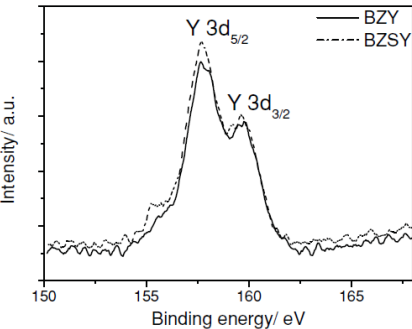
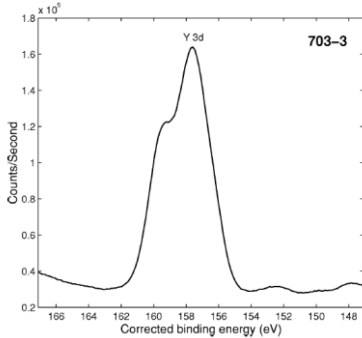
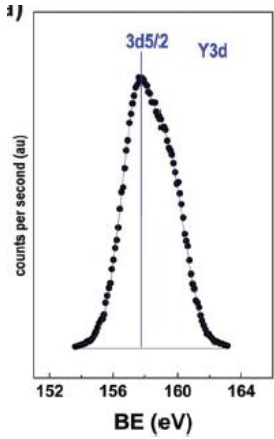
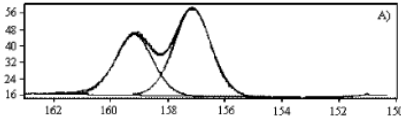
8YSZ (hydrothermal synthesis)	Zr 3d _{5/2} (YSZ) = 182.2 Zr 3d _{3/2} (YSZ) = 184.4		Gonzalo- Juan 2014
8YSZ (purchased from Aldrich Chemical Co.)	Zr 3d _{5/2} (YSZ) = 181.8 Zr 3d _{3/2} (YSZ) = 184.2		Pomfret 2005
12YSZ (purchased from CERES)	Zr 3d _{5/2} (YSZ) = 182.2 Zr 3d _{3/2} (YSZ) = 184.6		Parmigiani 1993
13YSZ (purchased from Dalian Keri Optoelectronic Technology Co.)	Zr 3d _{5/2} (YSZ) = 182.5 Zr 3d _{3/2} (YSZ) = 184.9		Oishi 2017sa
ZrO(OH) ₂ (precipitation between ZrOCl ₂ and NH ₄ OH)	Zr 3d _{5/2} (ZrO(OH) ₂) = 182.2	No figure	Wyrwalski 2005

Table C.2: Zr 3d literature review

Y 3d

Compound (elaboration method)	Binding energy (eV)	Figure caption	Ref
BZY10 (spray pyrolysis)	$Y3d_{5/2} (BZY, Y_{Zr'}) = 155.5$ $Y3d_{3/2} (BZY, Y_{Zr'}) = 157.5$ $Y3d_{5/2} (BZY, Y_{Ba'}) = 158.0$ $Y3d_{3/2} (BZY, Y_{Ba'}) = 160.2$	 <p>Partial substitution of Ba by Y</p>	Sažinas 2019
BZY20 (spray pyrolysis)	$Y3d_{5/2} (BZY, Y_{Zr'}) = 155.3$ $Y3d_{3/2} (BZY, Y_{Zr'}) = 157.3$ $Y3d_{5/2} (BZY, Y_{Ba'}) = 157.5$ $Y3d_{3/2} (BZY, Y_{Ba'}) = 159.8$	 <p>Partial substitution of Ba by Y</p>	Sažinas 2019
BZY20 (PLD)	$Y3d_{5/2} (BZY, Y_{Zr'}) = 156.5$ $Y3d_{3/2} (BZY, Y_{Zr'}) = 158.6$ $Y3d_{5/2} (BZY, Y_{Ba'}) = 158.2$ $Y3d_{3/2} (BZY, Y_{Ba'}) = 160.4$		Aruta 2016 [202]

BZY20 (combustion)	Y3d _{5/2} (BZY) = 157.8 Y3d _{3/2} (BZY) = 159.8	<p>Partial substitution of Ba by Zr and Y</p> 	Sun 2013
Y ₂ O ₃	Y3d _{5/2} (Y ₂ O ₃) = 156.4 - 157	No figure	Handbook of XPS 1993
Y ₂ O ₃	Y3d _{5/2} (Y ₂ O ₃) = 157.4 Y3d _{3/2} (Y ₂ O ₃) = 159.3		Barreca 2001
8YSZ (hydrothermal synthesis)	Y 3d _{5/2} (YSZ) = 157.7		Gonzalo- Juan 2014
8YSZ (purchased from Aldrich Chemical Co.)	Y 3d _{5/2} (YSZ) = 157.1 Y 3d _{3/2} (YSZ) = 159.2		Promfret 2005

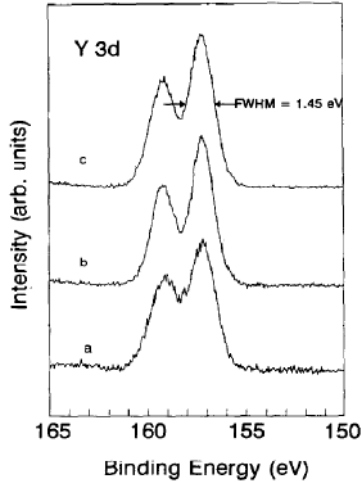
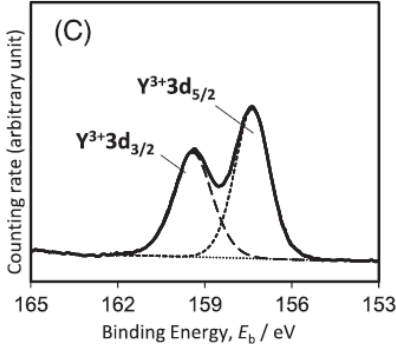
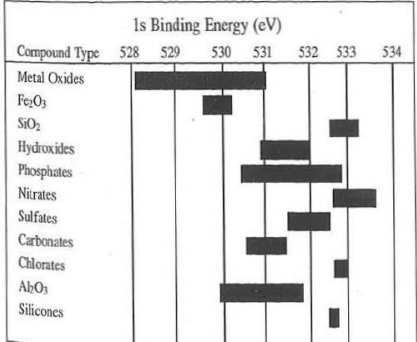
12YSZ (purchased from CERES)	Y 3d _{5/2} (YSZ) = 157.2 Y 3d _{3/2} (YSZ) = 159.2		Parmigiani 1993
13YSZ (purchased from Dalian Keri Optoelectronic Technology)	Y 3d _{5/2} (YSZ) = 157.5 Y 3d _{3/2} (YSZ) = 159.5		Oishi 2017
YO(OH)	Y3d _{5/2} (YOOH) = 158.5	No figure	Barr 1978

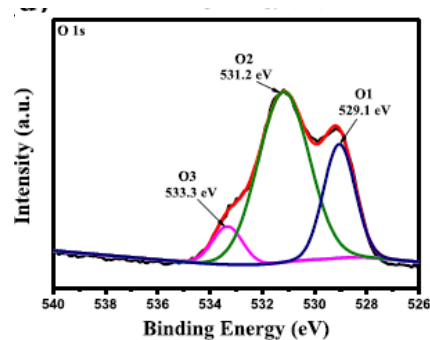
Table C.3: Y 3d literature review

O 1s

Compound (elaboration method)	Binding energy (eV)	Figure caption	Ref
O 1s (metal oxides) = 528.1 – 531.1			Handbook of XPS 1993
O 1s (hydroxides) = 529.9 – 532.0			
O 1s (carbonates) = 530.5 – 531.5			

BZ
(solvothelmal
using ethylene-
diamine)

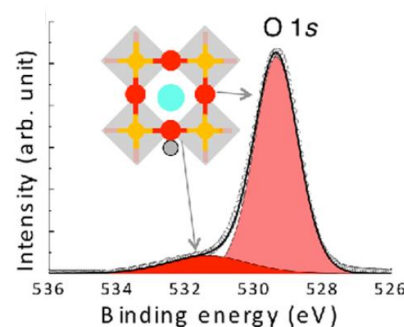
O1: inner perovskite
O2: oxygen vacancy
O3: OH-/surface adsorb
oxygen



Chen 2019

BZY20
(PLD)

O 1s (BZY) = 529.3
O 1s (OH) = 531.5



Aruta 2016
[202]

BaCO₃
(purchased
from Hopkins
and Williams)

O 1s (BaCO₃) = 530.8

No figure

Christie
1983

BaCO₃
(purchased
from CERAC)

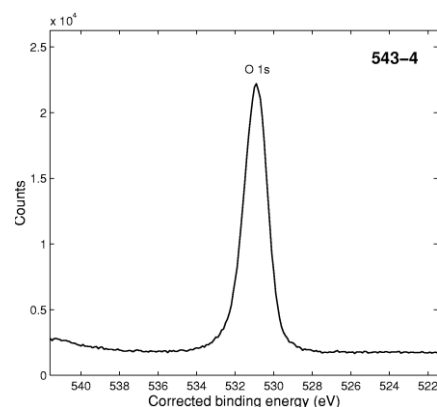
O 1s (BaCO₃) = 531.1

No figure

Gauzzi
1990

BaCO₃
(purchased
from from
Alfa/AESARS)

O 1s (BaCO₃) = 531.0



Schmitz
2001

BaCO₃
(Exposition of
BaO to CO₂)

O 1s (BaCO₃) = 531.7

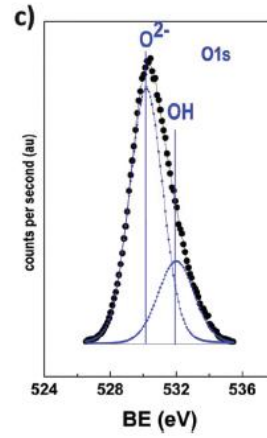
No figure

Karslioglu
2018

8YSZ
(hydrothermal
synthesis)

O1s (YSZ) = 530.1
O1s (OH ads) = 532.0

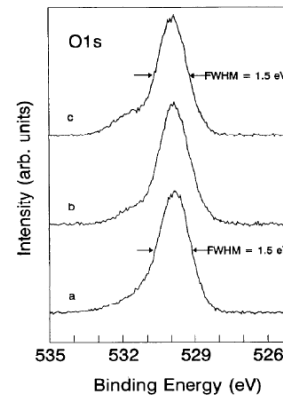
Gonzalo-
Juan 2014



12YSZ
(purchased
from CERES)

O 1s (YSZ) = 529.8

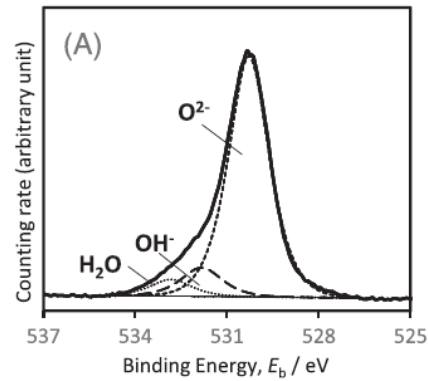
Parmigiani
1993



13YSZ
(purchased
from Dalian
Keri
Optoelectronic
Technology
Co.)

O1s (YSZ) = 530.2
O1s (OH ads) = 531.8
O1s (H₂O ads) = 532.7

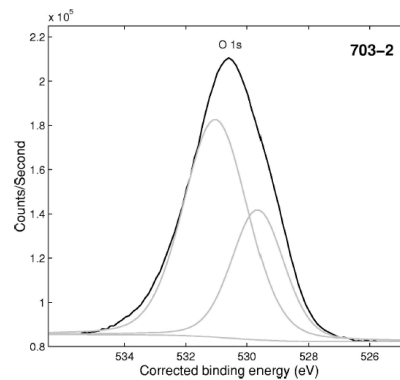
Oishi 2017



Y₂O₃

O 1s (Y₂O₃) = 529.7

Barreca
2001



YO(OH)

O 1s (YOOH, hydroxide) =
530.5

No figure

Barr 1978

Table C.4: O 1s literature review

C 1s

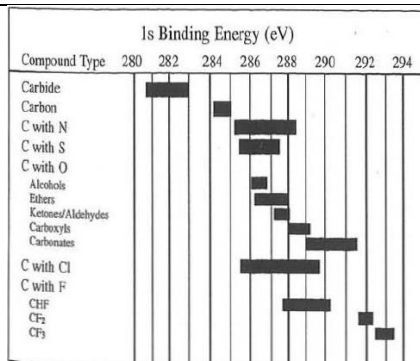
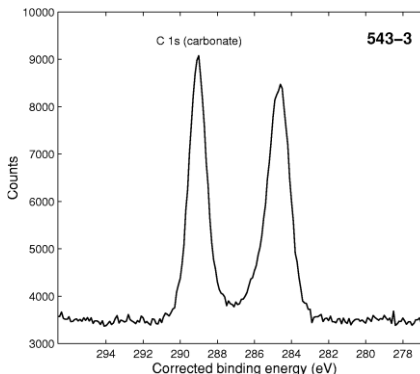
Compound (elaboration method)	Binding energy (e28V)	Figure caption	Ref
	C 1s (carbonates) = 288.5 – 290.8		Handbook of XPS 1993
BaCO ₃ (purchased from Hopkins and Williams)	C 1s (BaCO ₃) = 289.9	No figure	Christie 1983
BaCO ₃ (purchased from CERAC)	C 1s (BaCO ₃) = 284.8	No figure	Gauzzi 1990
BaCO ₃ (purchased from from Alfa/AESARS)	C 1s (BaCO ₃) = 289.1		Schmitz 2001
BaCO ₃ (Exposition of BaO to CO ₂)	C 1s (BaCO ₃) = 289.9	No figure	Karslioglu 2018

Table C.5: C 1s literature review

ANNEX D: BODE PLOTS

This annex presents the Bode plots associated with the Nyquist plots of BZY-com, BZY-c 1000 °C and BZY-b 1000 °C presented in Chapter III.

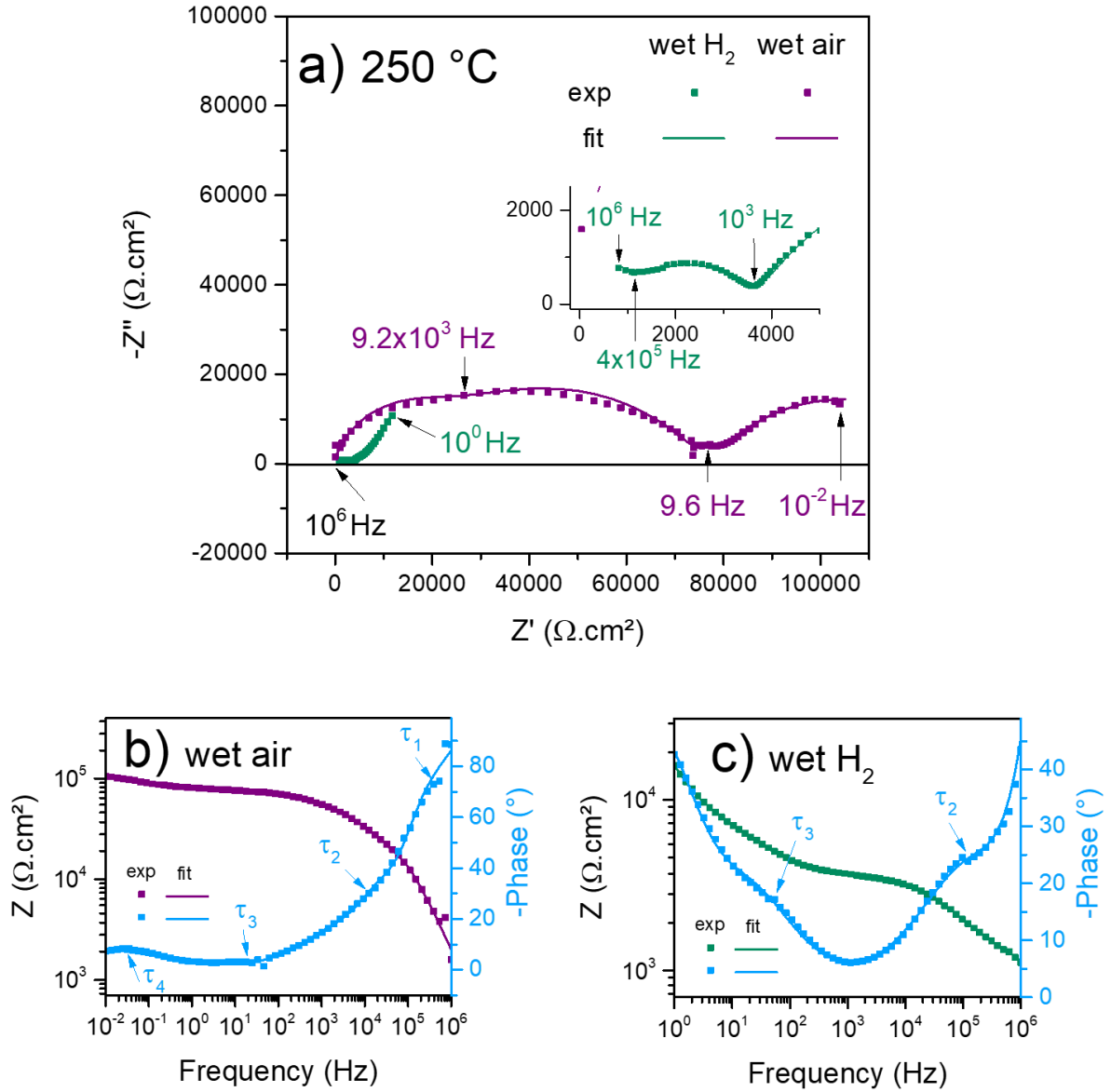


Figure D.1: EIS spectra of BZY-com symmetrical cell at 250 °C. a) Nyquist plot; b) Bode plot in wet air and c) Bode plot in wet H₂. The insert in the Nyquist plot exposes a zoom of the high frequencies points.

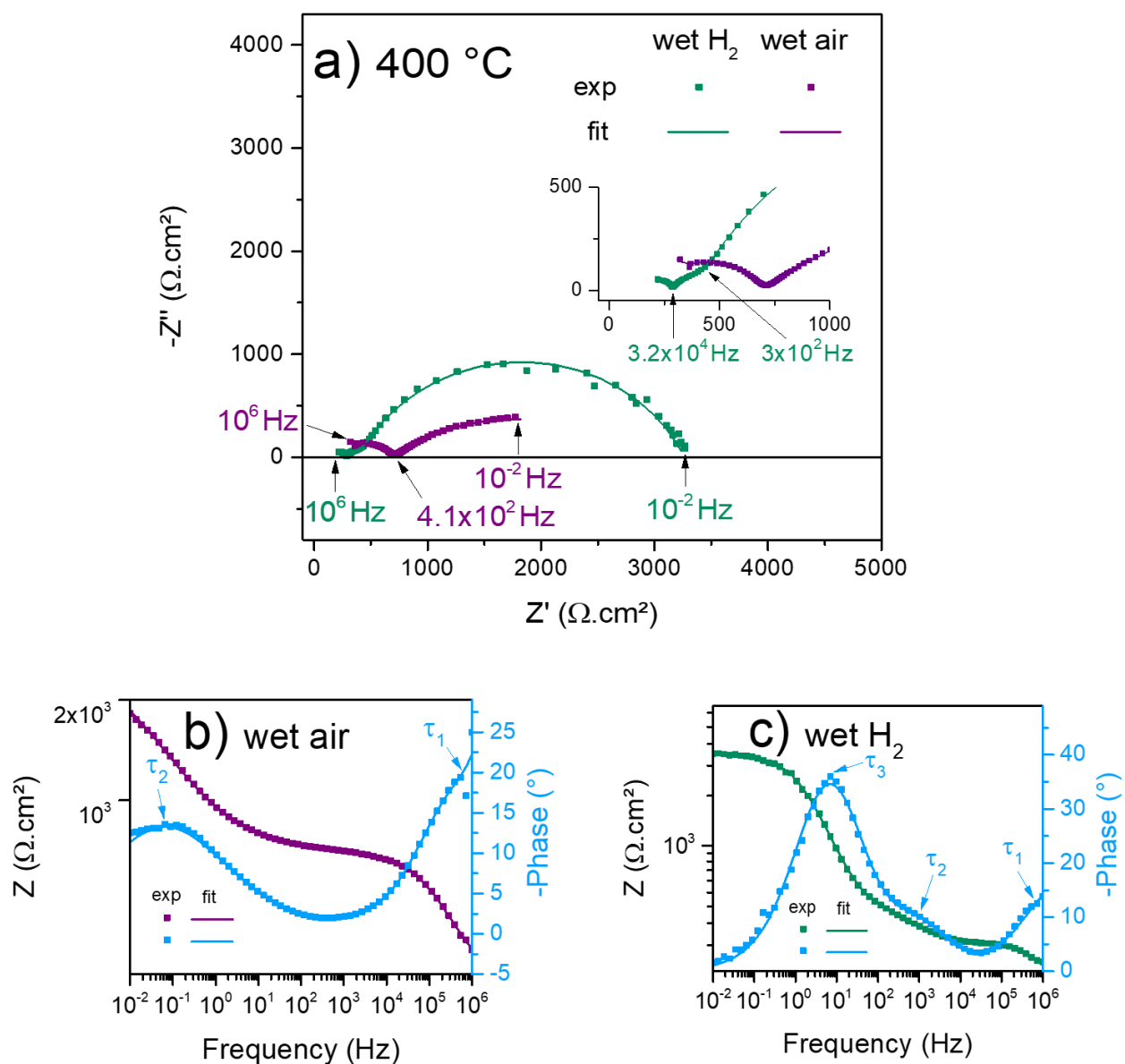


Figure D.2: EIS spectra of BZY-com symmetrical cell at 400 °C. a) Nyquist plot; b) Bode plot in wet air and c) Bode plot in wet H_2 . The insert in the Nyquist plot exposes a zoom of the high frequencies points.

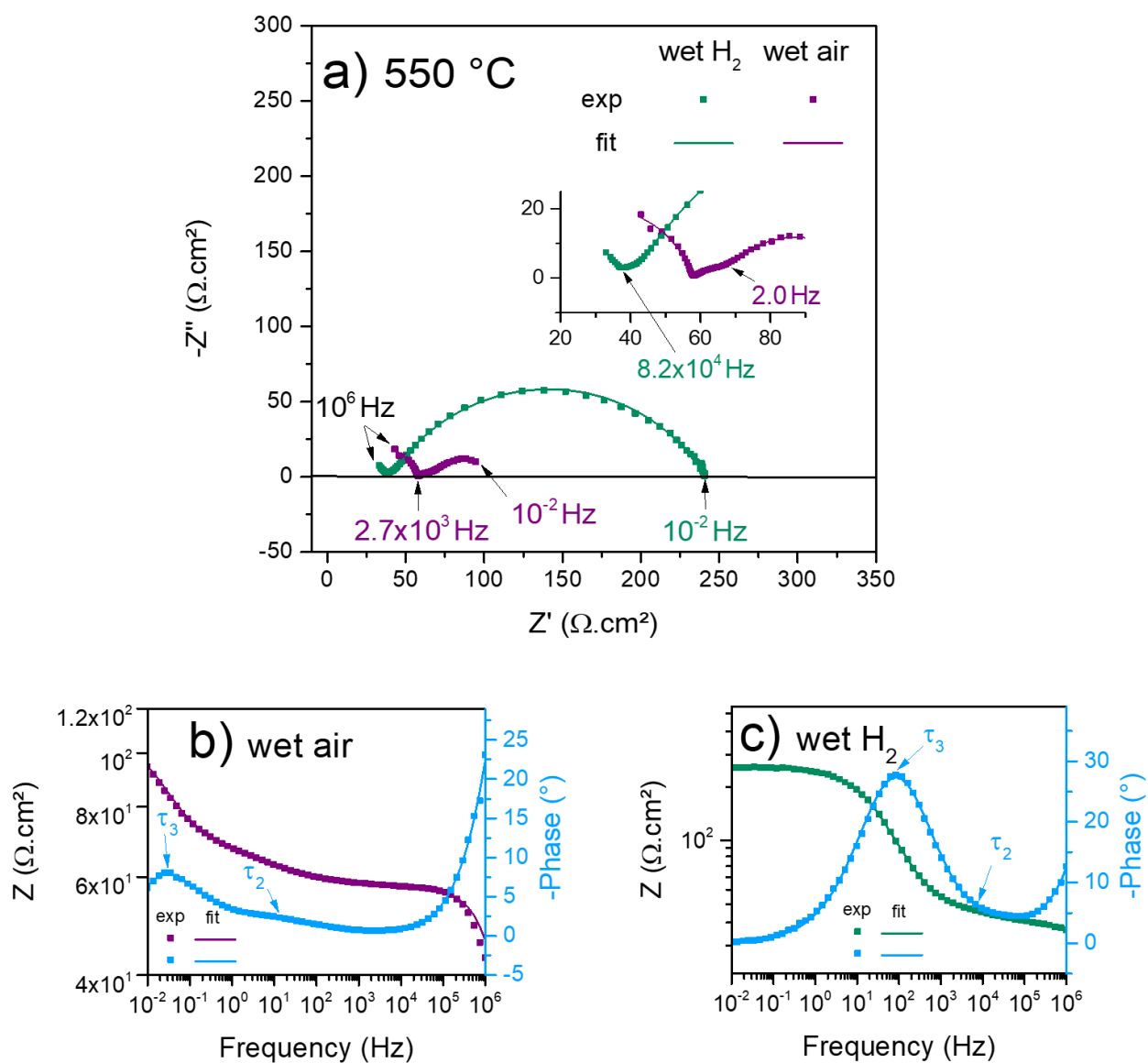


Figure D.3: EIS spectra of BZY-com symmetrical cell at 550 °C. a) Nyquist plot; b) Bode plot in wet air and c) Bode plot in wet H₂. The insert in the Nyquist plot exposes a zoom of the high frequencies points.

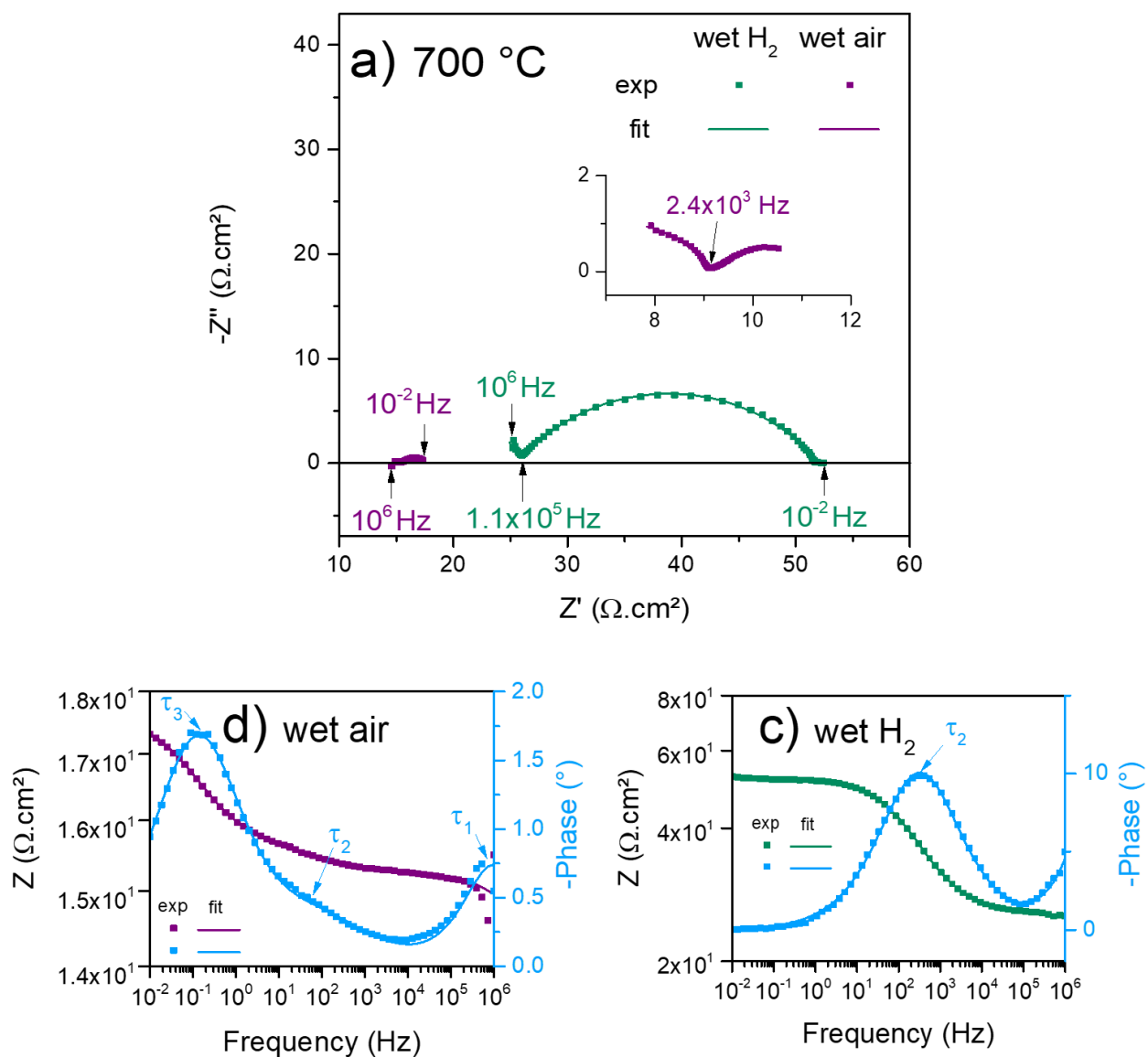


Figure D.4: EIS spectra of BZY-com symmetrical cell at 700 °C. a) Nyquist plot; b) Bode plot in wet air and c) Bode plot in wet H_2 . The insert in the Nyquist plot exposes a zoom of the high frequencies points.

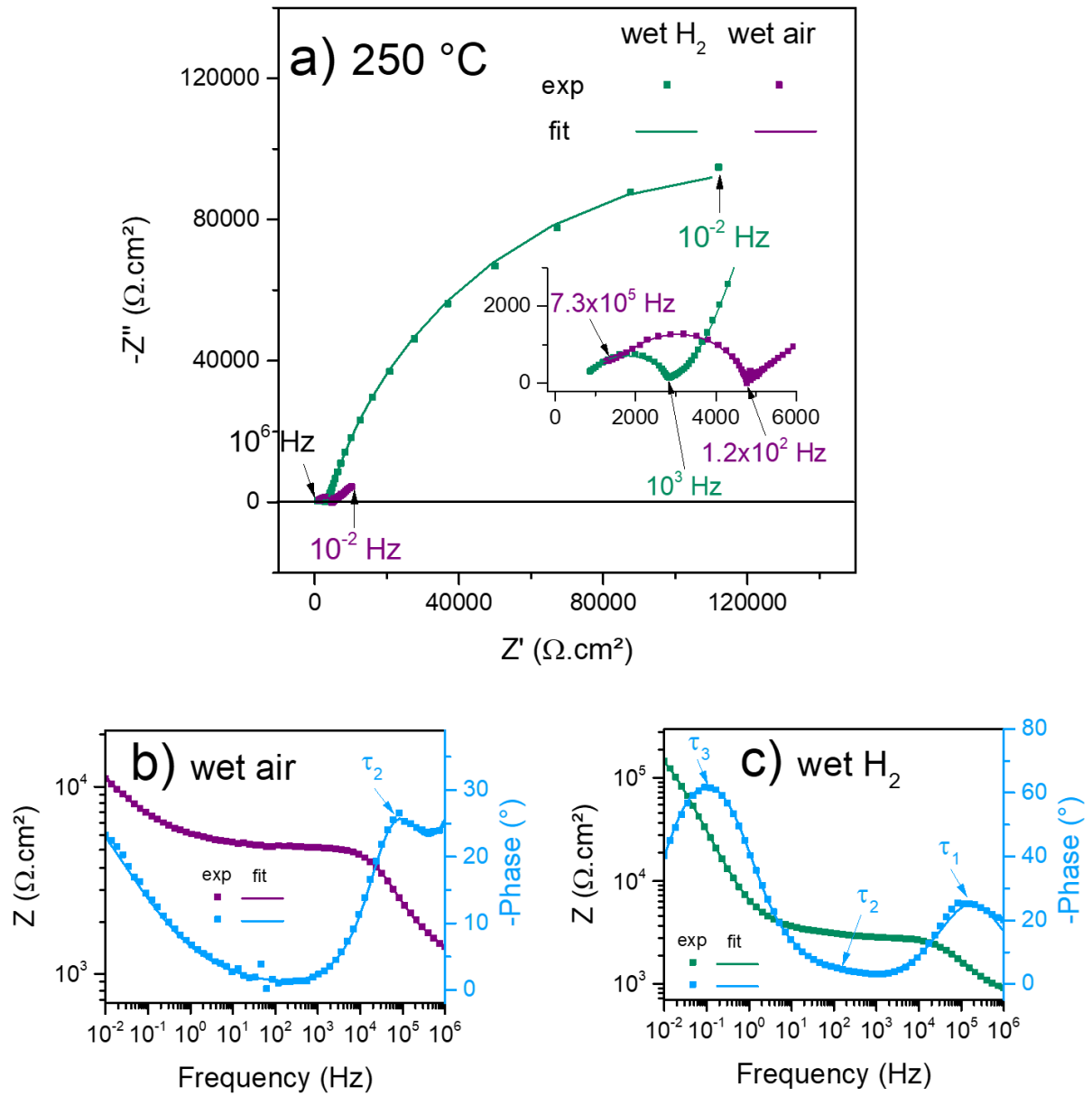


Figure D.5: EIS spectra of BZY-c symmetrical cell at 700 °C. a) Nyquist plot; b) Bode plot in wet air and c) Bode plot in wet H_2 . The insert in the Nyquist plot exposes a zoom of the high frequencies points.

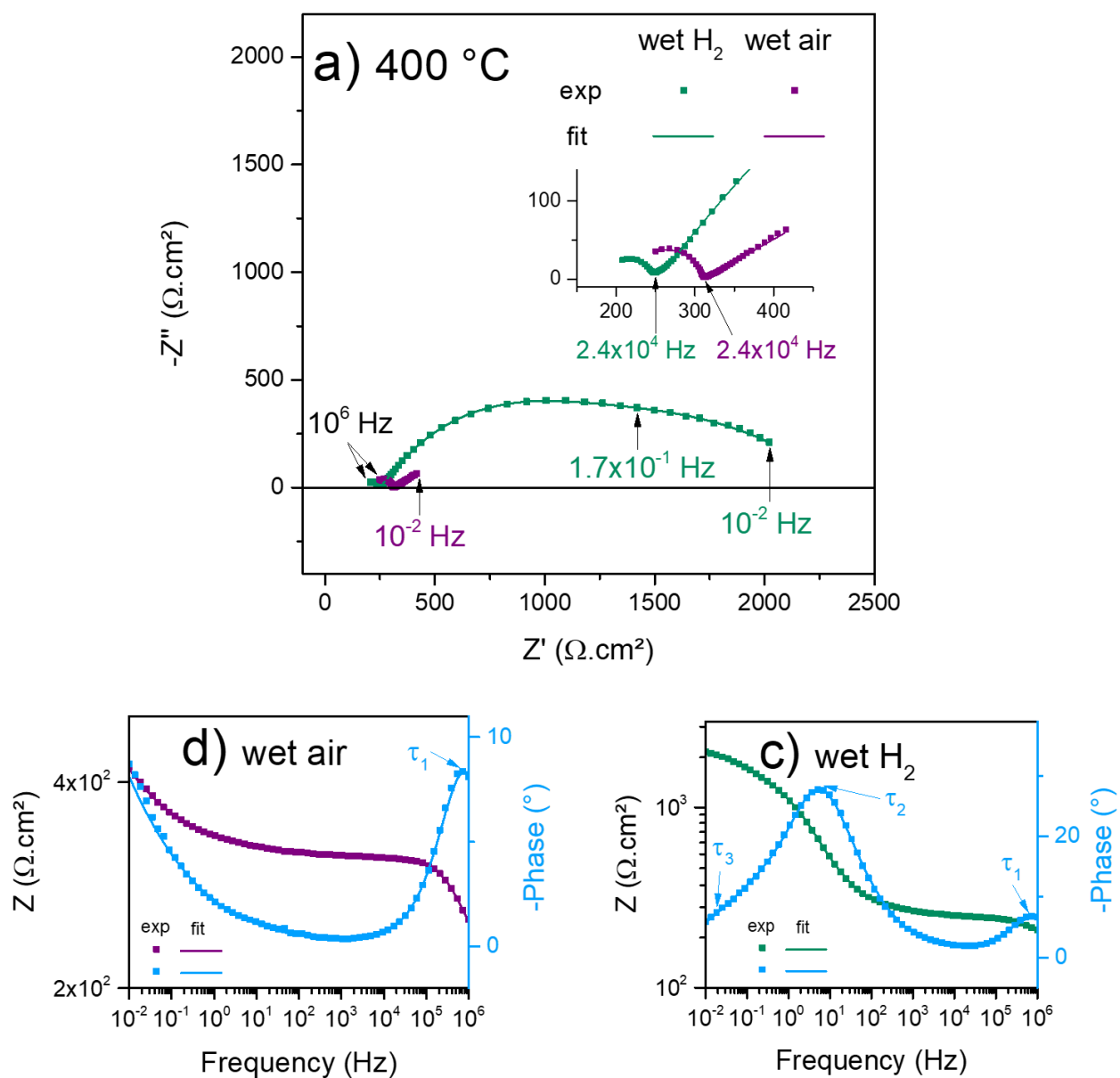


Figure D.6: EIS spectra of BZY-c symmetrical cell at 400 °C. a) Nyquist plot; b) Bode plot in wet air and c) Bode plot in wet H_2 . The insert in the Nyquist plot exposes a zoom of the high frequencies points.

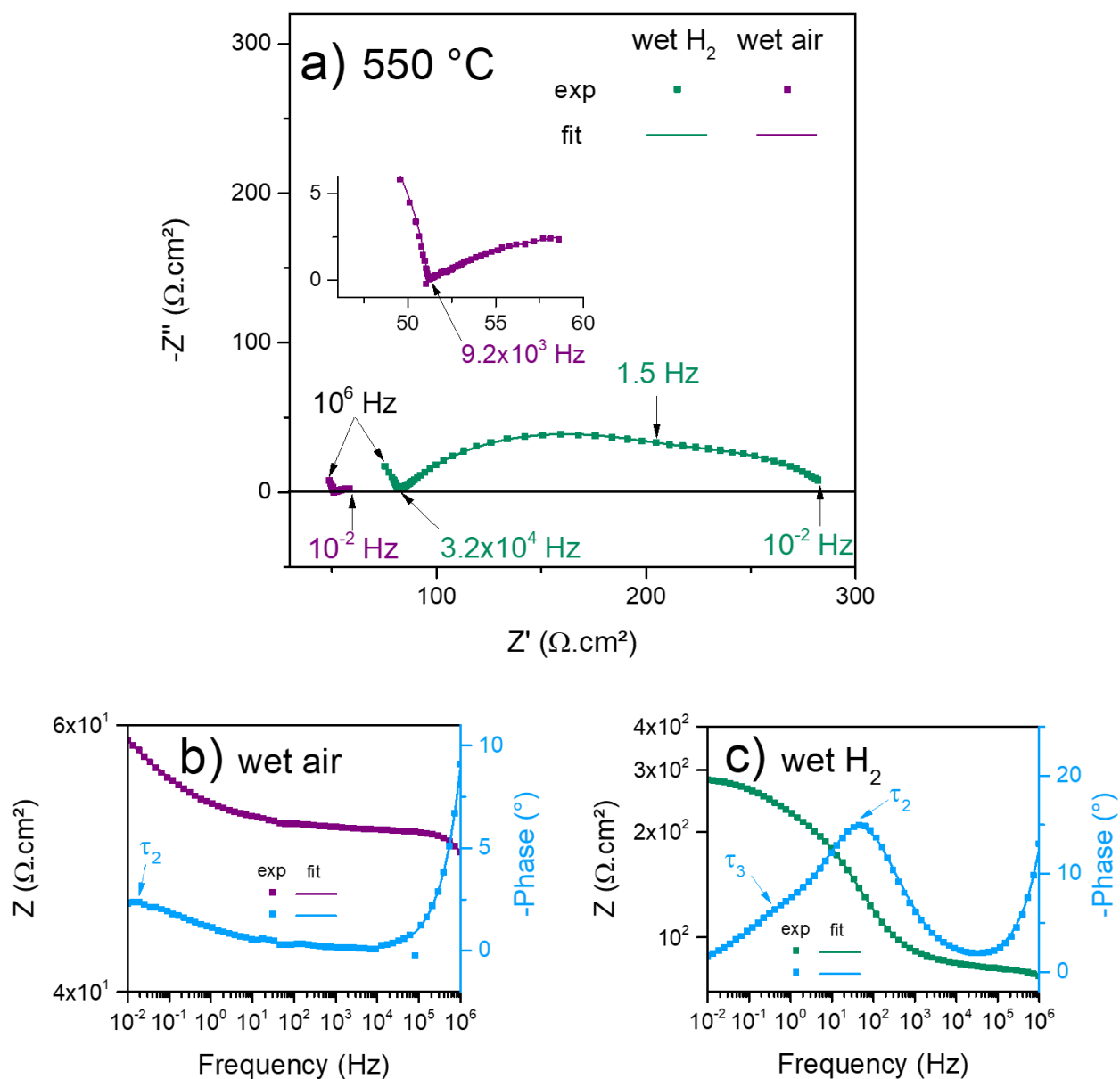


Figure D.7: EIS spectra of BZY-c symmetrical cell at 550 °C. a) Nyquist plot; b) Bode plot in wet air and c) Bode plot in wet H_2 . The insert in the Nyquist plot exposes a zoom of the high frequencies points.

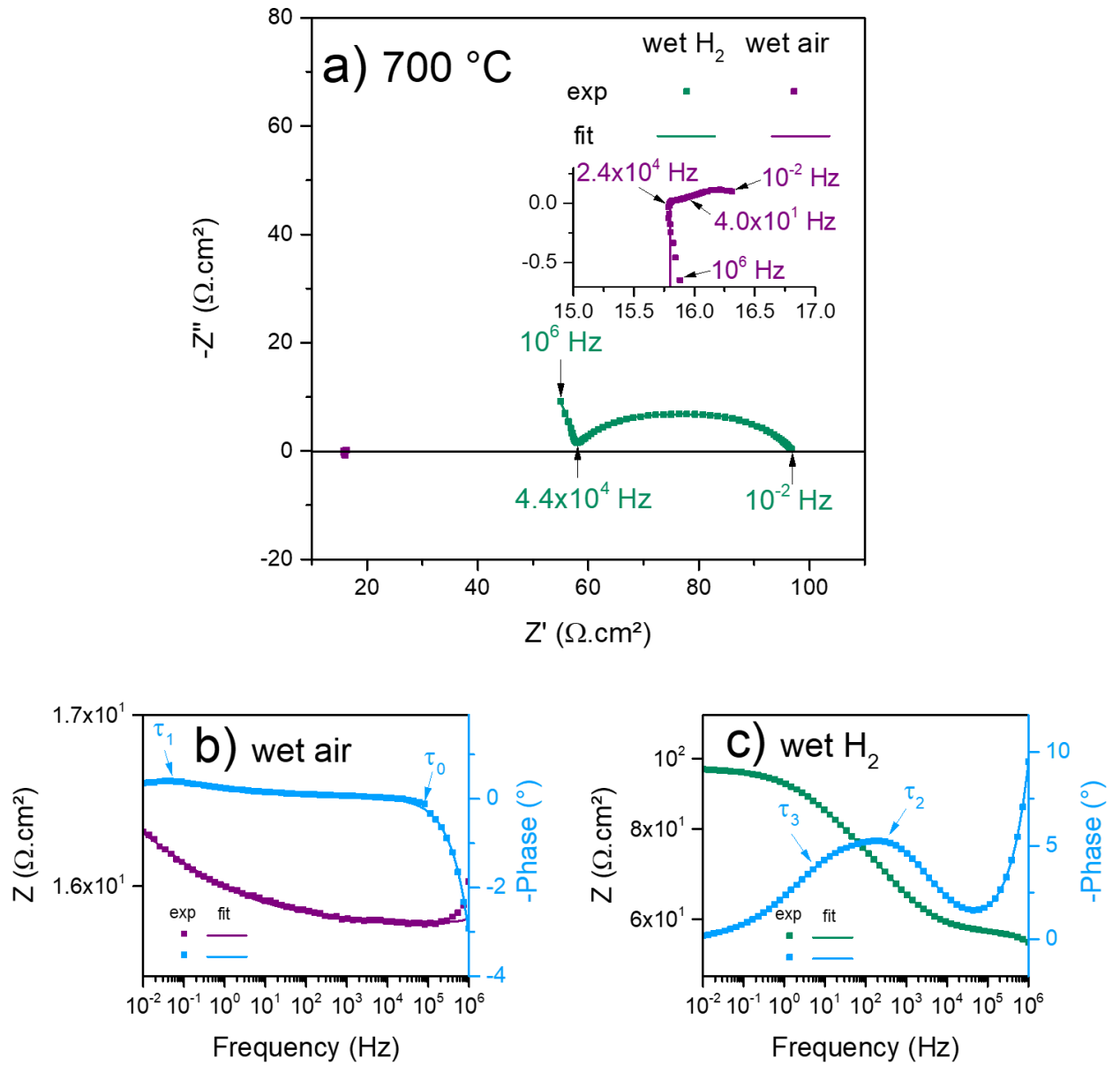


Figure D.8: EIS spectra of BZY-c symmetrical cell at 700 °C. a) Nyquist plot; b) Bode plot in wet air and c) Bode plot in wet H₂. The insert in the Nyquist plot exposes a zoom of the high frequencies points.

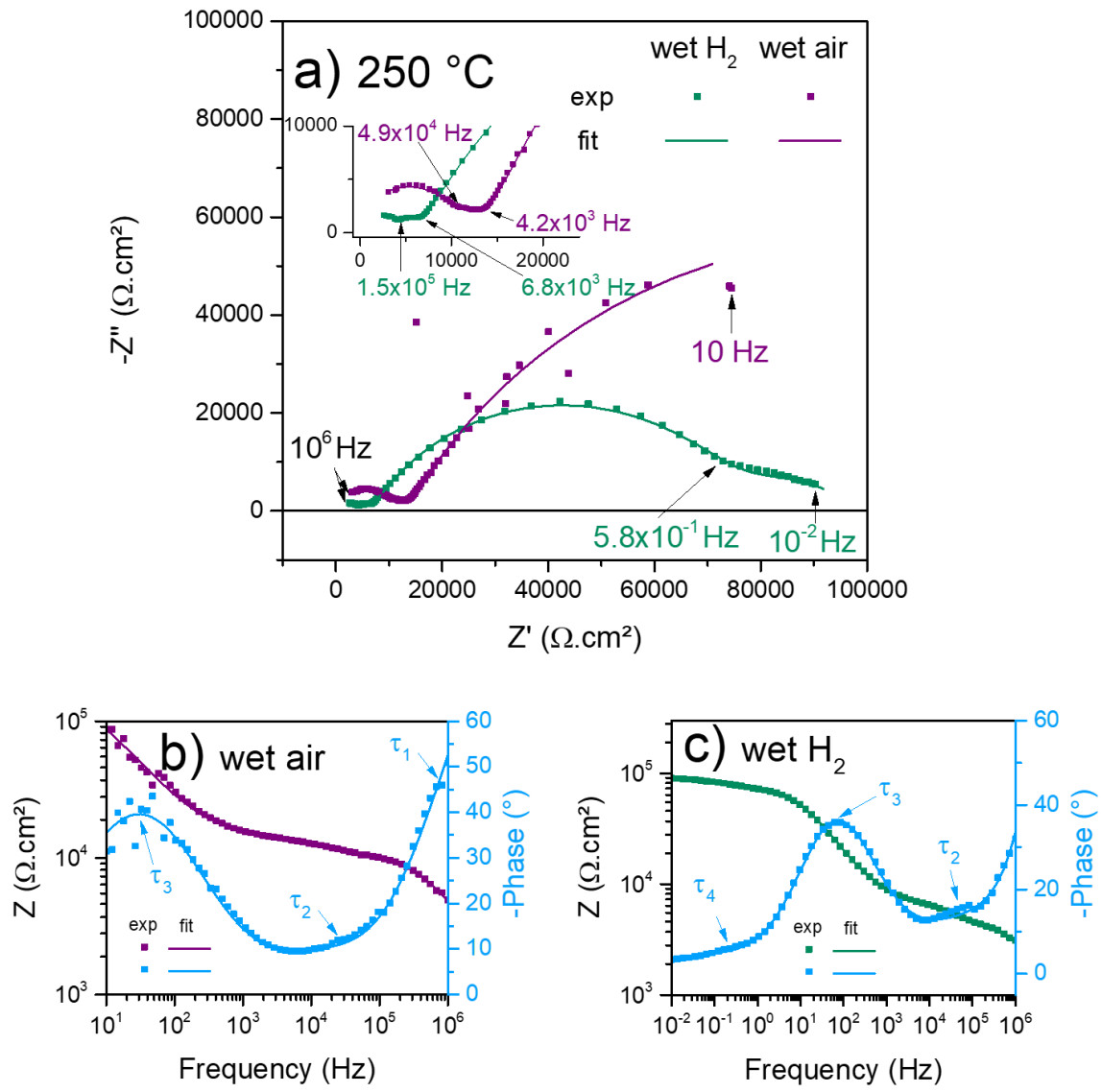


Figure D.9: EIS spectra of BZY-b symmetrical cell at 250 °C. a) Nyquist plot; b) Bode plot in wet air and c) Bode plot in wet H₂. The insert in the Nyquist plot exposes a zoom of the high frequencies points.

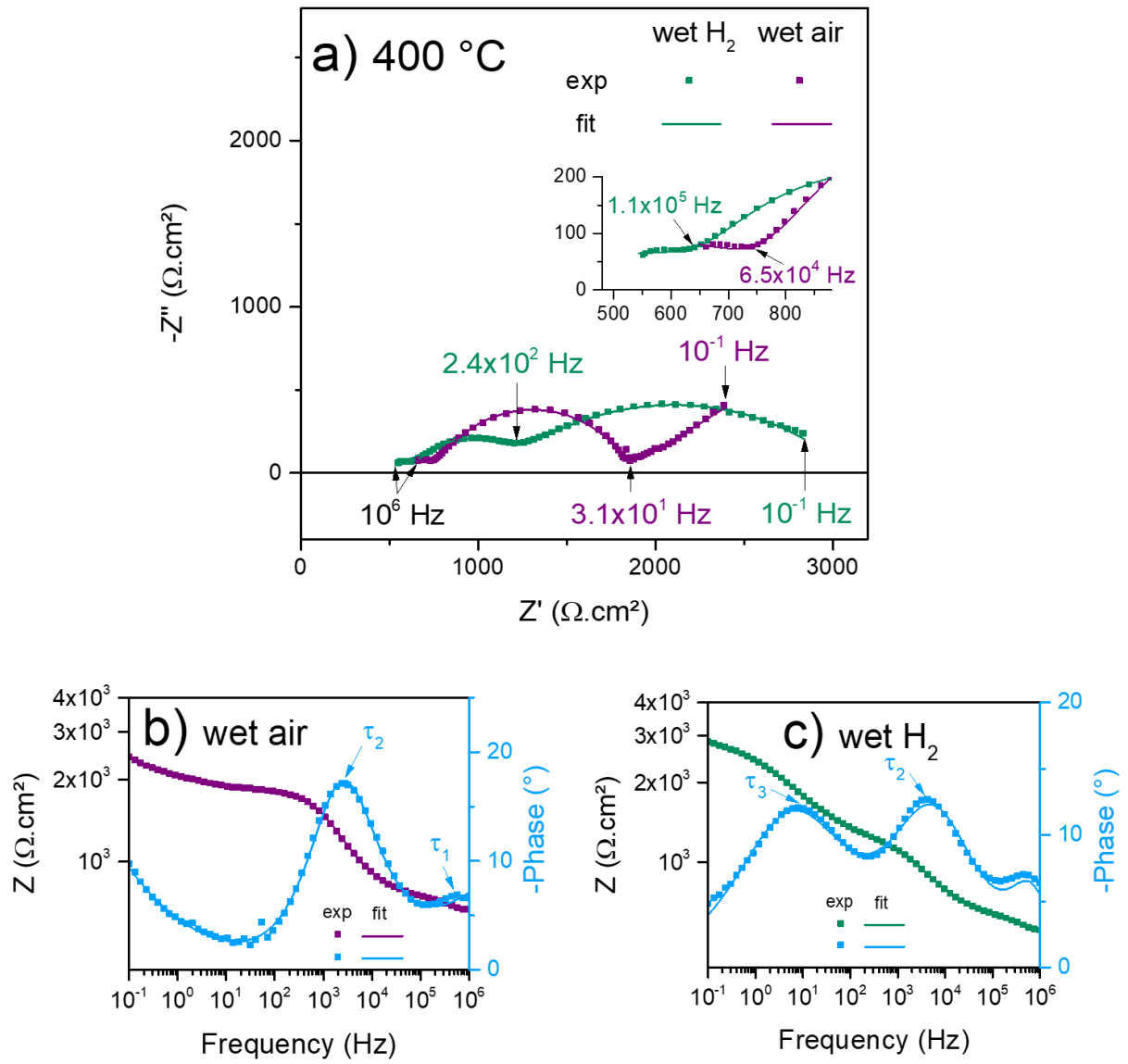


Figure D.10: EIS spectra of BZY-b symmetrical cell at 400 °C. a) Nyquist plot; b) Bode plot in wet air and c) Bode plot in wet H_2 . The insert in the Nyquist plot exposes a zoom of the high frequencies points.

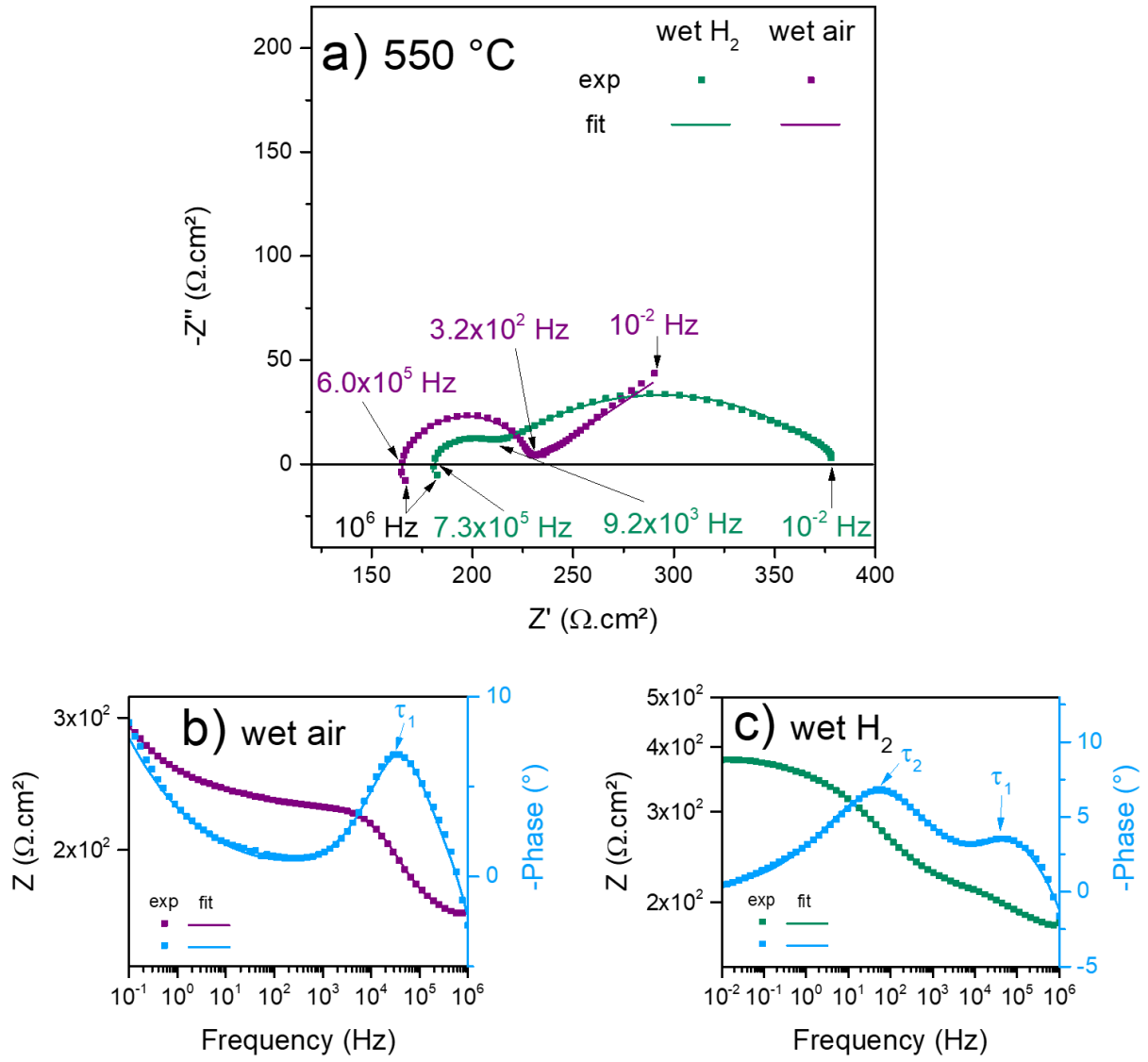


Figure D.11: EIS spectra of BZY-b symmetrical cell at 550 °C. a) Nyquist plot; b) Bode plot in wet air and c) Bode plot in wet H₂. The insert in the Nyquist plot exposes a zoom of the high frequencies points.

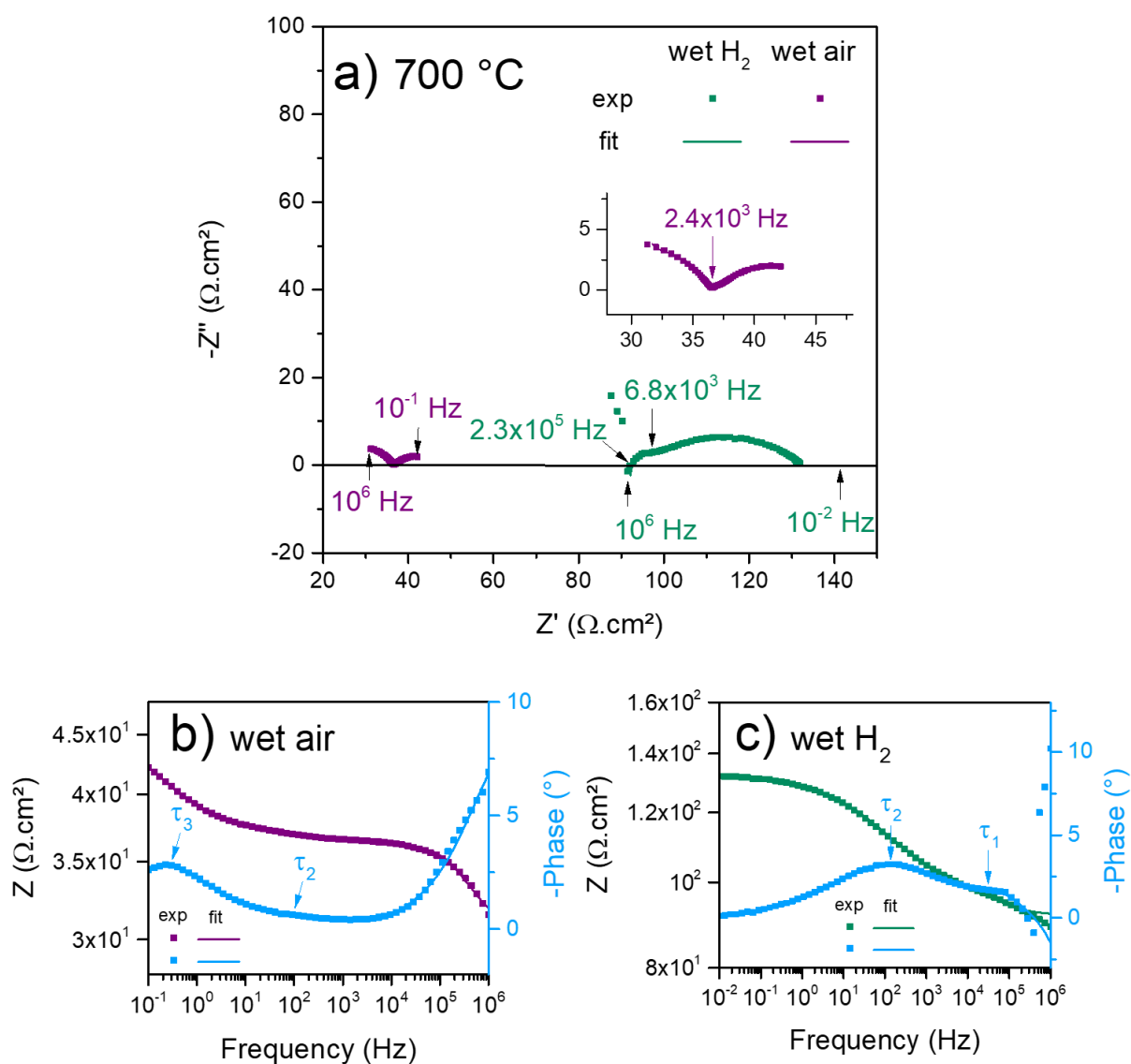


Figure D.12: EIS spectra of BZY-b symmetrical cell at 700 °C. a) Nyquist plot; b) Bode plot in wet air and c) Bode plot in wet H_2 . The insert in the Nyquist plot exposes a zoom of the high frequencies points.

ANNEX E: IMPACT OF THE AFL ON THE ELABORATION PROCESS

This annex exhibits pictures of co-sintered half-cell made NiO and BZY, with and without AFL.

Without AFL – co-sintering
at 1200 °C for 5 hours



With AFL – co-sintering
at 1400 °C for 5 hours



Figure E.1: Pictures of half-cell after co-sintering, the electrolyte layer is on the top side

BIBLIOGRAPHY

- [1] S. Ricote, "Elaboration et caractérisation du matériau d'électrolyte pour pile à combustible à conduction protonique : $\text{BaCe}_{(0,9-x)}\text{Zr}_x\text{Y}_{0,1}\text{O}_{3-\delta}$," Université de Bourgogne, Dijon, 2008.
- [2] "BP Statistical Review of World Energy," *ENGIE*, 2019.
- [3] Enerdata, "Global energy trend - 2021 Edition," 2021. [Online]. Available: <https://www.enerdata.net/publications/reports-presentations/world-energy-trends.html>
- [4] Intergovernmental Panel on Climate Change, "Global Warming of 1.5°C," 15, 2018.
- [5] "Key World Energy Statistics 2019," p. 81.
- [6] Engie, "Un monde d'Energie," Engie, 2017. Accessed: Oct. 16, 2018. [Online]. Available: <https://library.engie.com/media/fd3d5ef7-3158-4f6d-b5aa-81f899ed54f1/#v=Version1&l=fr&p=42>
- [7] "www.h2data.de." www.h2data.de (accessed May 03, 2020).
- [8] R. Pinsky, P. Sabharwall, J. Hartvigsen, and J. O'Brien, "Comparative review of hydrogen production technologies for nuclear hybrid energy systems," *Prog. Nucl. Energy*, vol. 123, p. 103317, May 2020, doi: 10.1016/j.pnucene.2020.103317.
- [9] "EOLBUS project." <https://www.vehiculedefutur.com/2018-05-24-Eolbus-pour-des-bus-a-hydrogene.html> (accessed May 03, 2020).
- [10] "Energy Observer." <https://www.energy-observer.org/actu/en/> (accessed May 03, 2020).
- [11] W. R. Grove, "On voltaic series and the combination of gases by platinum," *Philos. Mag.*, vol. 14, no. 86, pp. 126–131, 1839.
- [12] P. Stevens, F. Novel-Cattin, A. Hammou, C. Lamy, and M. Cassir, "Piles à combustible," *Tech. Ing.*, no. Ref D3340, pp. 2–28, 2000.
- [13] F. S. da Silva and T. M. de Souza, "Novel materials for solid oxide fuel cell technologies: A literature review," *Int. J. Hydrog. Energy*, vol. 42, no. 41, pp. 26020–26036, Oct. 2017, doi: 10.1016/j.ijhydene.2017.08.105.
- [14] H. Iwahara, T. Esaka, H. Uchida, and N. Maeda, "Proton conduction in sintered oxides and its application to steam electrolysis for hydrogen production," *Solid State Ion.*, vol. 3–4, pp. 359–363, Aug. 1981, doi: 10.1016/0167-2738(81)90113-2.
- [15] V. Sivasankaran, "Manufacturing and characterization of single cell intermediate-temperature solid oxide fuel cells for APU in transportation application," Université de Bourgogne, 2014.
- [16] A. B. Stambouli and E. Traversa, "Solid oxide fuel cells (SOFCs): a review of an environmentally clean and efficient source of energy," *Renew. Sustain. Energy Rev.*, vol. 6, no. 5, pp. 433–455, Oct. 2002, doi: 10.1016/S1364-0321(02)00014-X.
- [17] S. Hossain, A. M. Abdalla, S. N. B. Jamain, J. H. Zaini, and A. K. Azad, "A review on proton conducting electrolytes for clean energy and intermediate temperature-solid oxide fuel cells," *Renew. Sustain. Energy Rev.*, vol. 79, pp. 750–764, Nov. 2017, doi: 10.1016/j.rser.2017.05.147.
- [18] R. E. Rosli *et al.*, "A review of high-temperature proton exchange membrane fuel cell (HT-PEMFC) system," *Int. J. Hydrog. Energy*, vol. 42, no. 14, pp. 9293–9314, Apr. 2017, doi: 10.1016/j.ijhydene.2016.06.211.
- [19] H. Iwahara, "Technological challenges in the application of proton conducting ceramics," *Solid State Ion.*, vol. 77, pp. 289–298, Apr. 1995, doi: 10.1016/0167-2738(95)00051-7.

-
- [20] H. Iwahara, "Oxide-ionic and protonic conductors based on perovskite-type oxides and their possible applications," *Solid State Ion.*, vol. 52, no. 1–3, pp. 99–104, May 1992, doi: 10.1016/0167-2738(92)90095-7.
- [21] A. Satapathy and E. Sinha, "A comparative proton conductivity study on Yb-doped BaZrO₃ perovskite at intermediate temperatures under wet N₂ environment," *J. Alloys Compd.*, vol. 772, pp. 675–682, Jan. 2019, doi: 10.1016/j.jallcom.2018.08.329.
- [22] N. Bonanos, A. Huijser, and F. W. Poulsen, "H/D isotope effects in high temperature proton conductors," *Solid State Ion.*, vol. 275, pp. 9–13, Jul. 2015, doi: 10.1016/j.ssi.2015.03.028.
- [23] T. Ishihara, Ed., *Perovskite Oxide for Solid Oxide Fuel Cells*. Boston, MA: Springer US, 2009. doi: 10.1007/978-0-387-77708-5.
- [24] K. Nomura and H. Kageyama, "Transport properties of Ba(Zr_{0.8}Y_{0.2})O_{3-δ} perovskite," *Solid State Ion.*, vol. 178, pp. 661–665, 2007.
- [25] N. Bonanos and F. W. Poulsen, "Considerations of defect equilibria in high temperature proton-conducting cerates," *J. Mater. Chem.*, vol. 9, no. 2, pp. 431–434, 1999, doi: 10.1039/a805150j.
- [26] D. W. Keogh, "Actinides: Inorganic & Coordination Chemistry," pp. 2104–2122.
- [27] K. D. Kreuer, "Proton-Conducting Oxides," *Annu. Rev. Mater. Res.*, vol. 33, no. 1, pp. 333–359, Aug. 2003, doi: 10.1146/annurev.matsci.33.022802.091825.
- [28] W. Münch, G. Seifert, K. D. Kreuer, and J. Maier, "A quantum molecular dynamics study of proton conduction phenomena in BaCeO₃," *Solid State Ion.*, vol. 86–88, pp. 647–652, Jul. 1996, doi: 10.1016/0167-2738(96)00229-9.
- [29] C. Zhang, H. Zhao, and S. Zhai, "Electrical conduction behavior of proton conductor BaCe_{1-x}Sm_xO_{3-δ} in the intermediate temperature range," *Int. J. Hydrog. Energy*, vol. 36, no. 5, pp. 3649–3657, Mar. 2011, doi: 10.1016/j.ijhydene.2010.12.087.
- [30] A. S. Nowick and A. V. Vaysleyb, "Isotope effect and proton hopping in high-temperature protonic conductors," *Solid State Ion.*, vol. 97, no. 1–4, pp. 17–26, May 1997, doi: 10.1016/S0167-2738(97)00081-7.
- [31] A. Dubois, S. Ricote, and R. J. Braun, "Benchmarking the expected stack manufacturing cost of next generation, intermediate-temperature protonic ceramic fuel cells with solid oxide fuel cell technology," *J. Power Sources*, vol. 369, pp. 65–77, Nov. 2017, doi: 10.1016/j.jpowsour.2017.09.024.
- [32] *Fuel Cell Handbook (Seventh Edition)*.
- [33] M. Marrony, *Proton-Conducting Ceramics: From Fundamentals to Applied Research*, 0 ed. Jenny Stanford Publishing, 2015. doi: 10.1201/b18921.
- [34] R. Zohourian, R. Merkle, and J. Maier, "Proton uptake into the protonic cathode material BaCo_{0.4}Fe_{0.4}Zr_{0.2}O_{3-δ} and comparison to protonic electrolyte materials," *Solid State Ion.*, vol. 299, pp. 64–69, Jan. 2017, doi: 10.1016/j.ssi.2016.09.012.
- [35] A. Nowick, "High-temperature protonic conductors with perovskite-related structures," *Solid State Ion.*, vol. 77, pp. 137–146, Apr. 1995, doi: 10.1016/0167-2738(94)00230-P.
- [36] H. Dai, H. Kou, H. Wang, and L. Bi, "Electrochemical performance of protonic ceramic fuel cells with stable BaZrO₃-based electrolyte: A mini-review," *Electrochem. Commun.*, vol. 96, pp. 11–15, Nov. 2018, doi: 10.1016/j.elecom.2018.09.001.
- [37] X. Xu and L. Bi, "Proton-conducting electrolyte materials," in *Intermediate Temperature Solid Oxide Fuel Cells*, Elsevier, 2020, pp. 81–111. doi: 10.1016/B978-0-12-817445-6.00003-X.
- [38] E. Fabbri, D. Pergolesi, and E. Traversa, "Materials challenges toward proton-conducting oxide fuel cells: a critical review," *Chem. Soc. Rev.*, vol. 39, no. 11, pp. 4355–4369, 2010, doi: 10.1039/b902343g.
- [39] A. Grimaud *et al.*, "Transport properties and in-situ Raman spectroscopy study of BaCe_{0.9}Y_{0.1}O_{3-δ} as a function of water partial pressures," *Solid State Ion.*, vol. 191, no. 1, pp. 24–31, Jun. 2011, doi: 10.1016/j.ssi.2011.03.020.
-

- [40] L. Bi, Z. Tao, C. Liu, W. Sun, H. Wang, and W. Liu, "Fabrication and characterization of easily sintered and stable anode-supported proton-conducting membranes," *J. Membr. Sci.*, vol. 336, no. 1–2, pp. 1–6, Jul. 2009, doi: 10.1016/j.memsci.2009.03.042.
- [41] K. H. Ryu and S. M. Haile, "Chemical stability and proton conductivity of doped BaCeO₃–BaZrO₃ solid solutions," *Solid State Ion.*, vol. 125, no. 1–4, pp. 355–367, Oct. 1999, doi: 10.1016/S0167-2738(99)00196-4.
- [42] S. Wang *et al.*, "Further optimization of barium cerate properties via co-doping strategy for potential application as proton-conducting solid oxide fuel cell electrolyte," *J. Power Sources*, vol. 387, pp. 24–32, May 2018, doi: 10.1016/j.jpowsour.2018.03.054.
- [43] F. J. A. Loureiro, N. Nasani, G. S. Reddy, N. R. Munirathnam, and D. P. Fagg, "A review on sintering technology of proton conducting BaCeO₃–BaZrO₃ perovskite oxide materials for Protonic Ceramic Fuel Cells," *J. Power Sources*, vol. 438, p. 226991, Oct. 2019, doi: 10.1016/j.jpowsour.2019.226991.
- [44] N. L. R. M. Rashid *et al.*, "Review on zirconate-cerate-based electrolytes for proton-conducting solid oxide fuel cell," *Ceram. Int.*, vol. 45, no. 6, pp. 6605–6615, Apr. 2019, doi: 10.1016/j.ceramint.2019.01.045.
- [45] Q. Ma, R. Peng, Y. Lin, J. Gao, and G. Meng, "A high-performance ammonia-fueled solid oxide fuel cell," *J. Power Sources*, vol. 161, no. 1, pp. 95–98, Oct. 2006, doi: 10.1016/j.jpowsour.2006.04.099.
- [46] K. Xie *et al.*, "An ammonia fuelled SOFC with a BaCe_{0.9}Nd_{0.1}O_{3-δ} thin electrolyte prepared with a suspension spray," *J. Power Sources*, vol. 170, no. 1, pp. 38–41, Jun. 2007, doi: 10.1016/j.jpowsour.2007.03.059.
- [47] N. Bonanos, "Ionic conductivity of gadolinium-doped barium cerate perovskites," *Solid State Ion.*, vol. 35, no. 1–2, pp. 179–188, Aug. 1989, doi: 10.1016/0167-2738(89)90028-3.
- [48] Z. Shi, W. Sun, Z. Wang, J. Qian, and W. Liu, "Samarium and Yttrium Codoped BaCeO₃ Proton Conductor with Improved Sinterability and Higher Electrical Conductivity," *ACS Appl. Mater. Interfaces*, vol. 6, no. 7, pp. 5175–5182, Apr. 2014, doi: 10.1021/am500467m.
- [49] Y. Akimune *et al.*, "Nano-Ag particles for electrodes in a yttria-doped BaCeO₃ protonic conductor," *Solid State Ion.*, vol. 178, no. 7–10, pp. 575–579, Apr. 2007, doi: 10.1016/j.ssi.2007.01.009.
- [50] H. B. Yahia, F. Mauvy, and J. C. Grenier, "Ca_{3-x}La_xCo₄O_{9+δ} (x=0, 0.3): New cobaltite materials as cathodes for proton conducting solid oxide fuel cell," *J. Solid State Chem.*, vol. 183, no. 3, pp. 527–531, Mar. 2010, doi: 10.1016/j.jssc.2009.12.014.
- [51] H. Matsumoto, Y. Kawasaki, N. Ito, M. Enoki, and T. Ishihara, "Relation Between Electrical Conductivity and Chemical Stability of BaCeO₃-Based Proton Conductors with Different Trivalent Dopants," *Electrochem. Solid-State Lett.*, vol. 10, no. 4, p. B77, 2007, doi: 10.1149/1.2458743.
- [52] W. Münch, "Proton diffusion in perovskites: comparison between BaCeO₃, BaZrO₃, SrTiO₃, and CaTiO₃ using quantum molecular dynamics," *Solid State Ion.*, vol. 136–137, no. 1–2, pp. 183–189, Nov. 2000, doi: 10.1016/S0167-2738(00)00304-0.
- [53] D. A. Medvedev, J. G. Lyagaeva, E. V. Gorbova, A. K. Demin, and P. Tsiakaras, "Advanced materials for SOFC application: Strategies for the development of highly conductive and stable solid oxide proton electrolytes," *Prog. Mater. Sci.*, vol. 75, pp. 38–79, Jan. 2016, doi: 10.1016/j.pmatsci.2015.08.001.
- [54] Z. Zhang *et al.*, "High performance In, Ta and Y-doped BaCeO₃ electrolyte membrane for proton-conducting solid oxide fuel cells," *Solid State Ion.*, vol. 323, pp. 25–31, Oct. 2018, doi: 10.1016/j.ssi.2018.04.021.
- [55] Y. Wang, H. Wang, T. Liu, F. Chen, and C. Xia, "Improving the chemical stability of BaCe_{0.8}Sm_{0.2}O_{3-δ} electrolyte by Cl doping for proton-conducting solid oxide fuel cell," *Electrochem. Commun.*, vol. 28, pp. 87–90, 2013.

-
- [56] F. Su, C. Xia, and R. Peng, "Novel fluoride-doped barium cerate applied as stable electrolyte in proton conducting solid oxide fuel cells," *J. Eur. Ceram. Soc.*, vol. 35, no. 13, pp. 3553–3558, Nov. 2015, doi: 10.1016/j.jeurceramsoc.2015.05.016.
- [57] D. Kim, D. Lee, and J. H. Joo, "Effect of Y-doping on the phase relation and electrical properties of Fe-doped BaZrO₃," *J. Eur. Ceram. Soc.*, vol. 38, no. 2, pp. 535–542, Feb. 2018, doi: 10.1016/j.jeurceramsoc.2017.09.019.
- [58] E. Fabbri, L. Bi, D. Pergolesi, and E. Traversa, "Towards the Next Generation of Solid Oxide Fuel Cells Operating Below 600 °C with Chemically Stable Proton-Conducting Electrolytes," *Adv. Mater.*, vol. 24, no. 2, pp. 195–208, Jan. 2012, doi: 10.1002/adma.201103102.
- [59] D. Han and T. Uda, "The best composition of an Y-doped BaZrO₃ electrolyte: selection criteria from transport properties, microstructure, and phase behavior," *J. Mater. Chem. A*, vol. 6, no. 38, pp. 18571–18582, 2018, doi: 10.1039/C8TA06280C.
- [60] J.-H. Kim, Y.-M. Kang, M.-S. Byun, and K.-T. Hwang, "Study on the chemical stability of Y-doped BaCeO₃- δ and BaZrO₃- δ films deposited by aerosol deposition," *Thin Solid Films*, vol. 520, pp. 1015–1021, 2011, doi: 10.1016/j.tsf.2011.08.013.
- [61] Z. Khani, M. Taillades-Jacquín, G. Taillades, M. Marrony, D. J. Jones, and J. Rozière, "New synthesis of nanopowders of proton conducting materials. A route to densified proton ceramics," *J. Solid State Chem.*, vol. 182, no. 4, pp. 790–798, Apr. 2009, doi: 10.1016/j.jssc.2008.12.020.
- [62] P. Babilo and S. M. Haile, "Enhanced Sintering of Yttrium-Doped Barium Zirconate by Addition of ZnO," *J. Am. Ceram. Soc.*, vol. 88, no. 9, pp. 2362–2368, Sep. 2005, doi: 10.1111/j.1551-2916.2005.00449.x.
- [63] H. Wang, R. Peng, X. Wu, J. Hu, and C. Xia, "Sintering Behavior and Conductivity Study of Yttrium-Doped BaCeO₃-BaZrO₃ Solid Solutions Using ZnO Additives," *J. Am. Ceram. Soc.*, vol. 92, no. 11, pp. 2623–2629, Nov. 2009, doi: 10.1111/j.1551-2916.2009.03204.x.
- [64] K.-Y. Park, Y. Seo, K. B. Kim, S.-J. Song, B. Park, and J.-Y. Park, "Enhanced proton conductivity of yttrium-doped barium zirconate with sinterability in protonic ceramic fuel cells," *J. Alloys Compd.*, vol. 639, pp. 435–444, Aug. 2015, doi: 10.1016/j.jallcom.2015.03.168.
- [65] L. Bi and E. Traversa, "Synthesis strategies for improving the performance of doped-BaZrO₃ materials in solid oxide fuel cell applications," *J. Mater. Res.*, vol. 29, no. 1, pp. 1–15, Jan. 2014, doi: 10.1557/jmr.2013.205.
- [66] J. Jiao *et al.*, "Effect of BaOB2O3 composite sintering aid on sinterability and electrical property of BaZr_{0.85}Y_{0.15}O₃- δ ceramic," *Ceram. Int.*, vol. 45, pp. 13679–13684, 2019.
- [67] S. Tao and J. T. S. Irvine, "Conductivity studies of dense yttrium-doped BaZrO₃ sintered at 1325°C," *J. Solid State Chem.*, vol. 180, no. 12, pp. 3493–3503, Dec. 2007, doi: 10.1016/j.jssc.2007.09.027.
- [68] Y. Yamazaki, R. Hernandez-Sanchez, and S. M. Haile, "High Total Proton Conductivity in Large-Grained Yttrium-Doped Barium Zirconate," *Chem. Mater.*, vol. 21, no. 13, pp. 2755–2762, Jul. 2009, doi: 10.1021/cm900208w.
- [69] D. Pergolesi *et al.*, "High proton conduction in grain-boundary-free yttrium-doped barium zirconate films grown by pulsed laser deposition," *Nat. Mater.*, vol. 9, pp. 846–852, 2010.
- [70] P. Babilo, T. Uda, and S. M. Haile, "Processing of yttrium-doped barium zirconate for high proton conductivity," *J. Mater. Res.*, vol. 22, no. 5, pp. 1322–1330, May 2007, doi: 10.1557/jmr.2007.0163.
- [71] K. Katahira, Y. Kohchi, T. Shimura, and H. Iwahara, "Protonic conduction in Zr-substituted BaCeO₃," *Solid State Ion.*, vol. 138, no. 1–2, pp. 91–98, Dec. 2000, doi: 10.1016/S0167-2738(00)00777-3.
-

- [72] Z. Shi, W. Sun, and W. Liu, "Synthesis and characterization of $\text{BaZr}_{0.3}\text{Ce}_{0.5}\text{Y}_{0.2-x}\text{Yb}_x\text{O}_{3-\delta}$ proton conductor for solid oxide fuel cells," *J. Power Sources*, vol. 245, pp. 953–957, Jan. 2014, doi: 10.1016/j.jpowsour.2013.07.060.
- [73] X. Xu, L. Bi, and X. S. Zhao, "Highly-conductive proton-conducting electrolyte membranes with a low sintering temperature for solid oxide fuel cells," *J. Membr. Sci.*, vol. 558, pp. 17–25, Jul. 2018, doi: 10.1016/j.memsci.2018.04.037.
- [74] C. Zuo, S. Zha, M. Liu, M. Hatano, and M. Uchiyama, " $\text{Ba}(\text{Zr}_{0.1}\text{Ce}_{0.7}\text{Y}_{0.2})\text{O}_{3-\delta}$ as an Electrolyte for Low-Temperature Solid-Oxide Fuel Cells," *Adv. Mater.*, vol. 18, no. 24, pp. 3318–3320, Dec. 2006, doi: 10.1002/adma.200601366.
- [75] L. Yang *et al.*, "Enhanced Sulfur and Coking Tolerance of a Mixed Ion Conductor for SOFCs: $\text{BaZr}_{0.1}\text{Ce}_{0.7}\text{Y}_{0.2-x}\text{Yb}_x\text{O}_{3-\delta}$," *Science*, vol. 326, pp. 126–129, 2009.
- [76] T. Shimura, M. Komori, and H. Iwahara, "Ionic conduction in pyrochlore-type oxides containing rare earth elements at high temperature," *Solid State Ion.*, vol. 86–88, pp. 685–689, Jul. 1996, doi: 10.1016/0167-2738(96)00148-8.
- [77] K. E. J. Eurenus, E. Ahlberg, and C. S. Knee, "Proton conductivity in $\text{Ln}_{1.96}\text{Ca}_{0.04}\text{Sn}_2\text{O}_7-\delta$ (Ln=La, Sm, Yb) pyrochlores as a function of the lanthanide size," *Solid State Ion.*, vol. 181, pp. 1258–1263, 2010.
- [78] J. Palisaitis, M. E. Ivanova, W. A. Meulenberg, O. Guillon, and J. Mayer, "Phase homogeneity analysis of $\text{La}_{0.99}\text{Sr}_{0.01}\text{Nb}_{0.99}\text{Al}_{0.01}\text{O}_{4-\delta}$ and $\text{La}_{0.99}\text{Ca}_{0.01}\text{Nb}_{0.99}\text{Ti}_{0.01}\text{O}_{4-\delta}$ proton conductors by high-resolution STEM and EELS," *J. Eur. Ceram. Soc.*, vol. 35, pp. 1517–1525, 2015.
- [79] A. D. Brandão, J. Gracio, G. C. Mather, V. V. Kharton, and D. P. Fagg, "B-site substitutions in $\text{LaNb}_{1-x}\text{M}_x\text{O}_{4-\delta}$ materials in the search for potential proton conductors (M=Ga, Ge, Si, B, Ti, Zr, P, Al)," *J. Solid State Chem.*, vol. 184, no. 4, pp. 863–870, Apr. 2011, doi: 10.1016/j.jssc.2011.02.012.
- [80] R. Haugsrud and T. Norby, "Proton conduction in rare-earth ortho-niobates and ortho-tantalates," *Nat. Mater.*, vol. 5, no. 3, pp. 193–196, Mar. 2006, doi: 10.1038/nmat1591.
- [81] J. Zamudio-García, L. dos Santos-Gómez, J. M. Porras-Vázquez, E. R. Losilla, and D. Marrero-López, "Doping effects on the structure and electrical properties of $\text{La}_2\text{Ce}_2\text{O}_7$ proton conductors," *J. Alloys Compd.*, vol. 816, p. 152600, Mar. 2020, doi: 10.1016/j.jallcom.2019.152600.
- [82] A. K. Lucid, P. R. L. Keating, J. P. Allen, and G. W. Watson, "Structure and Reducibility of CeO_2 Doped with Trivalent Cations," *J. Phys. Chem. C*, vol. 120, no. 41, pp. 23430–23440, Oct. 2016, doi: 10.1021/acs.jpcc.6b08118.
- [83] K. E. J. Eurenus, E. Ahlberg, and C. S. Knee, "Proton conductivity in $\text{Sm}_2\text{Sn}_2\text{O}_7$ pyrochlores," *Solid State Ion.*, vol. 181, no. 35–36, pp. 1577–1585, Nov. 2010, doi: 10.1016/j.ssi.2010.09.008.
- [84] F. He, T. Wu, R. Peng, and C. Xia, "Cathode reaction models and performance analysis of $\text{Sm}_{0.5}\text{Sr}_{0.5}\text{CoO}_{3-\delta}$ – $\text{BaCe}_{0.8}\text{Sm}_{0.2}\text{O}_{3-\delta}$ composite cathode for solid oxide fuel cells with proton conducting electrolyte," *J. Power Sources*, vol. 194, no. 1, pp. 263–268, Oct. 2009, doi: 10.1016/j.jpowsour.2009.04.053.
- [85] H. Uchida, S. Tanaka, and H. Iwahara, "Polarization at Pt electrodes of a fuel cell with a high temperature-type proton conductive solid electrolyte," *J. Appl. Electrochem.*, vol. 15, no. 1, pp. 93–97, 1985, doi: 10.1007/BF00617745.
- [86] K. Thabet, A. Le Gal La Salle, E. Quarez, and O. Joubert, "Protonic-based ceramics for fuel cells and electrolyzers," in *Solid Oxide-Based Electrochemical Devices*, Elsevier, 2020, pp. 91–122. doi: 10.1016/B978-0-12-818285-7.00004-6.
- [87] H. Iwahara, H. Uchida, and S. Tanaka, "High temperature-type proton conductive solid oxide fuel cells using various fuels," *J. Appl. Electrochem.*, vol. 16, no. 5, pp. 663–668, Sep. 1986, doi: 10.1007/BF01006916.
- [88] A. Atkinson *et al.*, "Advanced anodes for high-temperature fuel cells," *Nat. Mater.*, vol. 3, no. 213–223, p. 11, 2004.

-
- [89] H. Bae and G. M. Choi, "Novel modification of anode microstructure for proton-conducting solid oxide fuel cells with BaZr_{0.8}Y_{0.2}O_{3-δ} electrolytes," *J. Power Sources*, vol. 285, pp. 431–438, Jul. 2015, doi: 10.1016/j.jpowsour.2015.03.090.
- [90] N. Nasani, D. Ramasamy, A. D. Brandão, A. A. Yaremchenko, and D. P. Fagg, "The impact of porosity, pH 2 and pH 2 O on the polarisation resistance of Ni–BaZr 0.85 Y 0.15 O 3–δ cermet anodes for Protonic Ceramic Fuel Cells (PCFCs)," *Int. J. Hydrog. Energy*, vol. 39, no. 36, pp. 21231–21241, Dec. 2014, doi: 10.1016/j.ijhydene.2014.10.093.
- [91] N. Nasani, D. Ramasamy, I. Antunes, J. Perez, and D. P. Fagg, "Electrochemical behaviour of Ni-BZO and Ni-BZY cermet anodes for Protonic Ceramic Fuel Cells (PCFCs) – A comparative study," *Electrochimica Acta*, vol. 154, pp. 387–396, Feb. 2015, doi: 10.1016/j.electacta.2014.12.094.
- [92] Z. Liu *et al.*, "A high-performance intermediate-to-low temperature protonic ceramic fuel cell with in-situ exsolved nickel nanoparticles in the anode," *Ceram. Int.*, vol. 46, no. 12, pp. 19952–19959, Aug. 2020, doi: 10.1016/j.ceramint.2020.05.062.
- [93] A. Hagen, J. F. B. Rasmussen, and K. Thydén, "Durability of solid oxide fuel cells using sulfur containing fuels," *J. Power Sources*, vol. 196, no. 17, pp. 7271–7276, Sep. 2011, doi: 10.1016/j.jpowsour.2011.02.053.
- [94] A. Weber, S. Dierickx, A. Kromp, and E. Ivers-Tiffée, "Sulfur Poisoning of Anode-Supported SOFCs under Reformate Operation," *Fuel Cells*, vol. 13, no. 4, pp. 487–493, Aug. 2013, doi: 10.1002/face.201200180.
- [95] A. Hagen, G. B. Johnson, and P. Hjalmarsen, "Electrochemical evaluation of sulfur poisoning in a methane-fuelled solid oxide fuel cell: Effect of current density and sulfur concentration," *J. Power Sources*, vol. 272, pp. 776–785, Dec. 2014, doi: 10.1016/j.jpowsour.2014.08.125.
- [96] D. Papurello, A. Lanzini, S. Fiorilli, F. Smeacetto, R. Singh, and M. Santarelli, "Sulfur poisoning in Ni-anode solid oxide fuel cells (SOFCs): Deactivation in single cells and a stack," *Chem. Eng. J.*, vol. 283, pp. 1224–1233, Jan. 2016, doi: 10.1016/j.cej.2015.08.091.
- [97] M. T. Mehran, M. Z. Khan, S.-B. Lee, T.-H. Lim, S. Park, and R.-H. Song, "Improving sulfur tolerance of Ni-YSZ anodes of solid oxide fuel cells by optimization of microstructure and operating conditions," *Int. J. Hydrog. Energy*, vol. 43, no. 24, pp. 11202–11213, Jun. 2018, doi: 10.1016/j.ijhydene.2018.04.200.
- [98] M. Riegraf, A. Zekri, M. Knipper, R. Costa, G. Schiller, and K. A. Friedrich, "Sulfur poisoning of Ni/Gadolinium-doped ceria anodes: A long-term study outlining stable solid oxide fuel cell operation," *J. Power Sources*, vol. 380, pp. 26–36, Mar. 2018, doi: 10.1016/j.jpowsour.2018.01.067.
- [99] K. S. Blinn and M. Liu, "BaZr 0.9 Yb 0.1 O 3–δ -modified bi-electrode supported solid oxide fuel cells with enhanced coking and sulfur tolerance," *J. Power Sources*, vol. 243, pp. 24–28, Dec. 2013, doi: 10.1016/j.jpowsour.2013.05.177.
- [100] J. Kim, S. Sengodan, S. Kim, O. Kwon, Y. Bu, and G. Kim, "Proton conducting oxides: A review of materials and applications for renewable energy conversion and storage," *Renew. Sustain. Energy Rev.*, vol. 109, pp. 606–618, Jul. 2019, doi: 10.1016/j.rser.2019.04.042.
- [101] N. Q. Minh, "Ceramic Fuel Cells," *J. Am. Ceram. Soc.*, vol. 76, no. 3, pp. 563–588, Mar. 1993, doi: 10.1111/j.1151-2916.1993.tb03645.x.
- [102] G. C. Mather, D. Muñoz-Gil, J. Zamudio-García, J. M. Porras-Vázquez, D. Marrero-López, and D. Pérez-Coll, "Perspectives on Cathodes for Protonic Ceramic Fuel Cells," *Appl. Sci.*, vol. 11, no. 12, p. 5363, Jun. 2021, doi: 10.3390/app11125363.
- [103] G. Fehrer, S. Janes, M. Wildersohn, and R. Clasen, "Proton—conducting ceramics as electrode/electrolyte—materials for SOFCs: Preparation, mechanical and thermal-mechanical properties of thermal sprayed coatings, material combination and stacks," *J.*
-

- Eur. Ceram. Soc.*, vol. 24, no. 5, pp. 705–715, May 2004, doi: 10.1016/S0955-2219(03)00262-0.
- [104] E. Fabbri, L. Bi, D. Pergolesi, and E. Traversa, “High-performance composite cathodes with tailored mixed conductivity for intermediate temperature solid oxide fuel cells using proton conducting electrolytes,” *Energy Environ. Sci.*, vol. 4, no. 12, p. 4984, 2011, doi: 10.1039/c1ee02361f.
- [105] H. Shimada, Y. Yamaguchi, H. Sumi, and Y. Mizutani, “Enhanced $\text{La}_{0.6}\text{Sr}_{0.4}\text{Co}_{0.2}\text{Fe}_{0.8}\text{O}_{3-\delta}$ -based cathode performance by modification of $\text{BaZr}_{0.1}\text{Ce}_{0.7}\text{Y}_{0.1}\text{Yb}_{0.1}\text{O}_{3-\delta}$ electrolyte surface in protonic ceramic fuel cells,” *Ceram. Int.*, vol. 47, pp. 16358–13362, 2021, doi: 10.1016/j.ceramint.2021.02.123.
- [106] H.-I. Ji *et al.*, “Influence of wet atmosphere on electrical and transport properties of lanthanum strontium cobalt ferrite cathode materials for protonic ceramic fuel cells,” *Solid State Ion.*, vol. 249–250, pp. 112–116, Nov. 2013, doi: 10.1016/j.ssi.2013.08.004.
- [107] Y. Bu *et al.*, “A highly efficient composite cathode for proton-conducting solid oxide fuel cells,” *J. Power Sources*, vol. 451, p. 227812, Mar. 2020, doi: 10.1016/j.jpowsour.2020.227812.
- [108] C. Xia, W. Rauch, F. Chen, and M. Liu, “ $\text{Sm}_{0.5}\text{Sr}_{0.5}\text{CoO}_3$ cathodes for low-temperature SOFCs,” *Solid State Ion.*, p. 9, 2002.
- [109] L. Zhao *et al.*, “ $\text{Sm}_{0.5}\text{Sr}_{0.5}\text{CoO}_{3-\delta}$ infiltrated $\text{Ce}_{0.9}\text{Gd}_{0.1}\text{O}_{2-\delta}$ composite cathodes for high performance protonic ceramic fuel cells,” *J. Power Sources*, vol. 333, pp. 24–29, Nov. 2016, doi: 10.1016/j.jpowsour.2016.09.146.
- [110] F. Wang, D. Chen, and Z. Shao, “ $\text{Sm}_{0.5}\text{Sr}_{0.5}\text{CoO}_{3-\delta}$ -infiltrated cathodes for solid oxide fuel cells with improved oxygen reduction activity and stability,” *J. Power Sources*, vol. 216, pp. 208–215, Oct. 2012, doi: 10.1016/j.jpowsour.2012.05.068.
- [111] T. Wu, R. Peng, and C. Xia, “ $\text{Sm}_{0.5}\text{Sr}_{0.5}\text{CoO}_{3-\delta}$ - $\text{BaCe}_{0.8}\text{Sm}_{0.2}\text{O}_{3-\delta}$ composite cathodes for proton-conducting solid oxide fuel cells,” *Solid State Ion.*, vol. 179, no. 27–32, pp. 1505–1508, Sep. 2008, doi: 10.1016/j.ssi.2007.12.005.
- [112] A. S. Habiballah, N. Osman, and A. M. Md Jani, “Microstructural investigation of BSCF-based cathode material for enhanced oxygen reduction reaction performance and electrode stability,” *Ceram. Int.*, vol. 46, no. 14, pp. 23262–23265, Oct. 2020, doi: 10.1016/j.ceramint.2020.06.002.
- [113] Z. Shao and S. M. Haile, “A high-performance cathode for the next generation of solid-oxide fuel cells,” *Nature*, vol. 431, pp. 170–173, 2004, doi: 10.1038/nature02863.
- [114] Y. Lin *et al.*, “Evaluation of $\text{Ba}_{0.5}\text{Sr}_{0.5}\text{Co}_{0.8}\text{Fe}_{0.2}\text{O}_{3-\delta}$ as a potential cathode for an anode-supported proton-conducting solid-oxide fuel cell,” *J. Power Sources*, vol. 180, no. 1, pp. 15–22, May 2008, doi: 10.1016/j.jpowsour.2008.02.044.
- [115] H. An *et al.*, “A $5 \times 5 \text{ cm}^2$ protonic ceramic fuel cell with a power density of 1.3 W cm^{-2} at 600°C ,” *Nat. Energy*, vol. 3, no. 10, pp. 870–875, Oct. 2018, doi: 10.1038/s41560-018-0230-0.
- [116] G. Li, Y. Zhang, Y. Ling, B. He, J. Xu, and L. Zhao, “Probing novel triple phase conducting composite cathode for high performance protonic ceramic fuel cells,” *Int. J. Hydrog. Energy*, vol. 41, no. 9, pp. 5074–5083, Mar. 2016, doi: 10.1016/j.ijhydene.2016.01.068.
- [117] A. J. Abd Aziz, N. A. Baharuddin, M. R. Somalu, and A. Muchtar, “Review of composite cathodes for intermediate-temperature solid oxide fuel cell applications,” *Ceram. Int.*, vol. 46, no. 15, pp. 23314–23325, Oct. 2020, doi: 10.1016/j.ceramint.2020.06.176.
- [118] L. Yang, C. Zuo, S. Wang, Z. Cheng, and M. Liu, “A Novel Composite Cathode for Low-Temperature SOFCs Based on Oxide Proton Conductors,” *Adv. Mater.*, vol. 20, no. 17, pp. 3280–3283, Sep. 2008, doi: 10.1002/adma.200702762.

- [119] B. Wang, L. Bi, and X. S. Zhao, "Liquid-phase synthesis of $\text{SrCo}_{0.9}\text{Nb}_{0.1}\text{O}_{3-\delta}$ cathode material for proton-conducting solid oxide fuel cells," *Ceram. Int.*, vol. 44, pp. 5139–5144, 2018.
- [120] S. Ricote, N. Bonanos, P. M. Rørvik, and C. Haavik, "Microstructure and performance of $\text{La}_{0.58}\text{Sr}_{0.4}\text{Co}_{0.2}\text{Fe}_{0.8}\text{O}_{3-\delta}$ cathodes deposited on $\text{BaCe}_{0.2}\text{Zr}_{0.7}\text{Y}_{0.1}\text{O}_{3-\delta}$ by infiltration and spray pyrolysis," *J. Power Sources*, vol. 209, pp. 172–179, 2012.
- [121] A. Løken, S. Ricote, and S. Wachowski, "Thermal and Chemical Expansion in Proton Ceramic Electrolytes and Compatible Electrodes," *Crystals*, vol. 8, no. 9, p. 365, Sep. 2018, doi: 10.3390/cryst8090365.
- [122] E. Fabbri, I. Markus, L. Bi, D. Pergolesi, and E. Traversa, "Tailoring mixed proton-electronic conductivity of BaZrO_3 by Y and Pr co-doping for cathode application in protonic SOFCs," *Solid State Ion.*, vol. 202, no. 1, pp. 30–35, Nov. 2011, doi: 10.1016/j.ssi.2011.08.019.
- [123] Z. Hui and P. Michèle, "Preparation, chemical stability, and electrical properties of $\text{Ba}(\text{Ce}_{1-x}\text{Bi}_x)\text{O}_3$ ($x = 0.0\text{--}0.5$)," *J Mater Chem*, vol. 12, no. 12, pp. 3787–3791, 2002, doi: 10.1039/B205107A.
- [124] C. Duan *et al.*, "Readily processed protonic ceramic fuel cells with high performance at low temperatures," *Science*, vol. 349, no. 6254, pp. 1321–1326, Sep. 2015, doi: 10.1126/science.aab3987.
- [125] J. Kim *et al.*, "Triple-Conducting Layered Perovskites as Cathode Materials for Proton-Conducting Solid Oxide Fuel Cells," *ChemSusChem*, vol. 7, no. 10, pp. 2811–2815, Oct. 2014, doi: 10.1002/cssc.201402351.
- [126] D. Aymes, M. Ariane, F. Bernard, H. Muhr, and F. Demoisson, "Synthèse de particules par thermohydrolyse de précurseurs minéraux," Patent N° WO2011010056A1, 2011.
- [127] M. François, F. Demoisson, M. Sennour, and G. Caboche, "Continuous hydrothermal synthesis in supercritical conditions as a novel process for the elaboration of Y-doped BaZrO_3 ," *Ceram. Int.*, vol. 47, no. 12, pp. 17799–17803, Mar. 2021, doi: 10.1016/j.ceramint.2021.03.044.
- [128] K. Byrappa and M. Yoshimura, "Hydrothermal Technology—Principles and Applications," in *Handbook of Hydrothermal Technology*, Elsevier, 2013, pp. 1–49. doi: 10.1016/B978-0-12-375090-7.00001-3.
- [129] G. Yang and S.-J. Park, "Conventional and Microwave Hydrothermal Synthesis and Application of Functional Materials: A Review," *Materials*, vol. 12, no. 7, p. 1177, Apr. 2019, doi: 10.3390/ma12071177.
- [130] L. N. Walters, C. Zhang, V. P. Dravid, K. R. Poeppelmeier, and J. M. Rondinelli, "First-Principles Hydrothermal Synthesis Design to Optimize Conditions and Increase the Yield of Quaternary Heteroanionic Oxychalcogenides," *Chem. Mater.*, vol. 33, no. 8, pp. 2726–2741, Apr. 2021, doi: 10.1021/acs.chemmater.0c02682.
- [131] P. Cousin and R. A. Ross, "Preparation of mixed oxides: a review," *Mater. Sci. Eng. A*, vol. 130, no. 1, pp. 119–125, Nov. 1990, doi: 10.1016/0921-5093(90)90087-J.
- [132] D. D. Athayde *et al.*, "Review of perovskite ceramic synthesis and membrane preparation methods," *Ceram. Int.*, vol. 42, no. 6, pp. 6555–6571, May 2016, doi: 10.1016/j.ceramint.2016.01.130.
- [133] O. Kosasang, R. Jareun, S. Phongsathit, and S. Mach-mumas, "Influence of CuO and ZnO additions on grain growth and proton conductivity of Y-doped BaZrO_3 ," *J. Aust. Ceram. Soc.*, vol. 56, no. 2, pp. 441–446, Jun. 2020, doi: 10.1007/s41779-019-00347-1.
- [134] S. Ricote, N. Bonanos, M. C. Marco de Lucas, and G. Caboche, "Ricote 2009 Structural and conductivity study of the proton conductor $\text{BaCe}_{(0.9-x)}\text{Zr}_x\text{Y}_{0.1}\text{O}_{(3-x)}$ at intermediate temperatures," *J. Power Sources*, vol. 193, pp. 189–193, 2009.
- [135] K. Babooram, "Novel solution routes to ferroelectrics and relaxors," in *Handbook of Advanced Dielectric, Piezoelectric and Ferroelectric Materials*, Elsevier, 2008, pp. 852–883. doi: 10.1533/9781845694005.7.852.

-
- [136] A. V. Rane, K. Kanny, V. K. Abitha, and S. Thomas, "Methods for Synthesis of Nanoparticles and Fabrication of Nanocomposites," in *Synthesis of Inorganic Nanomaterials*, Elsevier, 2018, pp. 121–139. doi: 10.1016/B978-0-08-101975-7.00005-1.
- [137] L. Baraket and A. Ghorbel, "Control preparation of aluminium chromium mixed oxides by Sol-Gel process," in *Studies in Surface Science and Catalysis*, vol. 118, Elsevier, 1998, pp. 657–667. doi: 10.1016/S0167-2991(98)80233-4.
- [138] A. Mitra and G. De, "Sol-Gel Synthesis of Metal Nanoparticle Incorporated Oxide Films on Glass," in *Glass Nanocomposites*, Elsevier, 2016, pp. 145–163. doi: 10.1016/B978-0-323-39309-6.00006-7.
- [139] C. B. Carter and M. G. Norton, *Ceramic materials: science and engineering*. New York: Springer, 2007.
- [140] V. G. Kessler, "Pechini Processes: An Alternate Approach of the Sol–Gel Method, Preparation, Properties, and Applications," in *Handbook of Sol-Gel Science and Technology*, L. Klein, M. Aparicio, and A. Jitianu, Eds. Cham: Springer International Publishing, 2016, pp. 1–22. doi: 10.1007/978-3-319-19454-7_123-1.
- [141] K.-Y. Show, Y.-G. Yan, and D.-J. Lee, "Algal biomass harvesting and drying," in *Biofuels from Algae*, Elsevier, 2019, pp. 135–166. doi: 10.1016/B978-0-444-64192-2.00007-X.
- [142] P. K. Mehrotra, "Powder Processing and Green Shaping," in *Comprehensive Hard Materials*, Elsevier, 2014, pp. 213–235. doi: 10.1016/B978-0-08-096527-7.00007-6.
- [143] B. Robertz *et al.*, "Preparation of BaZrO₃ powders by a spray-drying process," *J. Mater. Res.*, vol. 18, no. 6, pp. 1325–1332, Jun. 2003, doi: 10.1557/JMR.2003.0182.
- [144] A. Rabenau, "The Role of Hydrothermal Synthesis in Preparative Chemistry," *Angew. Chem. Int. Ed. Engl.*, vol. 24, no. 12, pp. 1026–1040, Dec. 1985, doi: 10.1002/anie.198510261.
- [145] G. Huang, C.-H. Lu, and H.-H. Yang, "Magnetic Nanomaterials for Magnetic Bioanalysis," in *Novel Nanomaterials for Biomedical, Environmental and Energy Applications*, Elsevier, 2019, pp. 89–109. doi: 10.1016/B978-0-12-814497-8.00003-5.
- [146] Z. Pan, Y. Wang, H. Huang, Z. Ling, Y. Dai, and S. Ke, "Recent development on preparation of ceramic inks in ink-jet printing," *Ceram. Int.*, vol. 41, no. 10, pp. 12515–12528, Dec. 2015, doi: 10.1016/j.ceramint.2015.06.124.
- [147] M. Yoshimura, "Importance of Soft Processing (Low-energy Production) of Advanced Materials for Sustainable Society," *Procedia Eng.*, vol. 171, pp. 40–52, 2017, doi: 10.1016/j.proeng.2017.01.308.
- [148] D. Santos, A. C. Maurício, V. Sencadas, J. D. Santos, M. H. Fernandes, and P. S. Gomes, "Spray Drying: An Overview," in *Biomaterials - Physics and Chemistry - New Edition*, R. Pignatello and T. Musumeci, Eds. InTech, 2018. doi: 10.5772/intechopen.72247.
- [149] E. Lintings, F. Lequeux, L. Talini, and N. Tsapis, "Control of particle morphology in the spray drying of colloidal suspensions," *Soft Matter*, vol. 12, no. 36, pp. 7435–7444, 2016, doi: 10.1039/C6SM01314G.
- [150] X. Zhang *et al.*, "Water's phase diagram: From the notion of thermodynamics to hydrogen-bond cooperativity," *Prog. Solid State Chem.*, vol. 43, no. 3, pp. 71–81, Sep. 2015, doi: 10.1016/j.progsolidstchem.2015.03.001.
- [151] S. Deguchi and K. Tsujii, "Supercritical water: a fascinating medium for soft matter," *Soft Matter*, vol. 3, no. 7, p. 797, 2007, doi: 10.1039/b611584e.
- [152] C. G. Malmberg and A. A. Maryott, "Dielectric constant of water from 0 to 100 C," *J. Res. Natl. Bur. Stand.*, vol. 56, no. 1, p. 1, Jan. 1956, doi: 10.6028/jres.056.001.
- [153] R. Piolet, "Synthèse hydrothermale de nanoparticules de ZnO au-delà du point critique: compréhension des étapes de germination et de croissance," Université de Bourgogne, Dijon, 2014.
-

- [154] K. Karalis, C. Ludwig, and B. Niceno, "Supercritical water anomalies in the vicinity of the Widom line," *Sci. Rep.*, vol. 9, no. 1, p. 15731, Dec. 2019, doi: 10.1038/s41598-019-51843-0.
- [155] F. Demoisson, "Influence of the pH on the ZnO nanoparticle growth in supercritical water: Experimental and simulation approaches," *J. Supercrit. Fluids*, vol. 95, pp. 75–83, 2014, doi: 10.1016/j.supflu.2014.08.007.
- [156] L. Zhang, C. (Charles) Xu, and P. Champagne, "Overview of recent advances in thermo-chemical conversion of biomass," *Energy Convers. Manag.*, vol. 51, no. 5, pp. 969–982, May 2010, doi: 10.1016/j.enconman.2009.11.038.
- [157] D. Aymes, M. Ariane, F. Bernard, H. Muhr, and F. Demoisson, "Counter-current flow reactor with heat transfer for hydrothermolytic synthesis," WO 2011010056A1, 2011
- [158] T. Adschiri, K. Kanazawa, and K. Arai, "Rapid and Continuous Hydrothermal Crystallization of Metal Oxide Particles in Supercritical Water," *J. Am. Ceram. Soc.*, vol. 75, no. 4, pp. 1019–1022, Apr. 1992, doi: 10.1111/j.1151-2916.1992.tb04179.x.
- [159] Y. Zhu *et al.*, "Highly Cr-Substituted CeO₂ Nanoparticles Synthesized Using a Non-equilibrium Supercritical Hydrothermal Process: High Oxygen Storage Capacity Materials Designed for a Low-Temperature Bitumen Upgrading Process," *ACS Appl. Energy Mater.*, vol. 3, no. 5, pp. 4305–4319, May 2020, doi: 10.1021/acs.aem.0c00026.
- [160] A. Yoko, G. Seong, T. Tomai, and T. Adschiri, "Continuous Flow Synthesis of Nanoparticles Using Supercritical Water: Process Design, Surface Control, and Nanohybrid Materials," *KONA Powder Part. J.*, vol. 37, no. 0, pp. 28–41, Jan. 2020, doi: 10.14356/kona.2020002.
- [161] A. Aimable, B. Xin, N. Millot, and D. Aymes, "Continuous hydrothermal synthesis of nanometric BaZrO₃ in supercritical water," *J. Solid State Chem.*, vol. 181, no. 1, pp. 183–189, Jan. 2008, doi: 10.1016/j.jssc.2007.11.015.
- [162] F. Demoisson, M. Ariane, A. Leybros, H. Muhr, and F. Bernard, "Design of a reactor operating in supercritical water conditions using CFD simulations. Examples of synthesized nanomaterials," *J. Supercrit. Fluids*, vol. 58, no. 3, pp. 371–377, Oct. 2011, doi: 10.1016/j.supflu.2011.07.001.
- [163] D. Hennings and S. Schreinemacher, "Characterization of hydrothermal barium titanate," *J. Eur. Ceram. Soc.*, vol. 9, no. 1, pp. 41–46, Jan. 1992, doi: 10.1016/0955-2219(92)90075-O.
- [164] K. M. Sangwan, N. Ahlawat, S. Rani, S. Rani, and R. S. Kundu, "Influence of Mn doping on electrical conductivity of lead free BaZrTiO₃ perovskite ceramic," *Ceram. Int.*, vol. 44, no. 9, pp. 10315–10321, Jun. 2018, doi: 10.1016/j.ceramint.2018.03.039.
- [165] K. Yang, Y. Wang, Z. Yang, Y. Wang, and C. Jin, "Degradation of cobalt-free Ba_{0.95}La_{0.05}FeO_{3-δ} cathode against CO₂-H₂O and Ce_{0.9}Gd_{0.1}O_{2-δ} modification," *Int. J. Hydrog. Energy*, vol. 45, no. 58, pp. 34080–34088, Nov. 2020, doi: 10.1016/j.ijhydene.2020.09.086.
- [166] N. Millot, B. Xin, C. Pighini, and D. Aymes, "Hydrothermal synthesis of nanostructured inorganic powders by a continuous process under supercritical conditions," *J. Eur. Ceram. Soc.*, vol. 25, no. 12, pp. 2013–2016, Jan. 2005, doi: 10.1016/j.jeurceramsoc.2005.03.202.
- [167] T.-M. Usher, B. Kavey, G. Caruntu, and K. Page, "Effect of BaCO₃ Impurities on the Structure of BaTiO₃ Nanocrystals: Implications for Multilayer Ceramic Capacitors," *ACS Appl. Nano Mater.*, vol. 3, no. 10, pp. 9715–9723, Oct. 2020, doi: 10.1021/acsanm.0c01809.
- [168] G. Nuñez, M. J. Balanay, and R. B. M. Cervera, "Preparation of Y-Doped BaZrO₃ Proton Conducting Solid Electrolyte via Modified Low Temperature Pechini Method," *Adv. Mater. Res.*, vol. 1098, pp. 86–91, Apr. 2015, doi: 10.4028/www.scientific.net/AMR.1098.86.

- [169] A. R. Akbarzadeh, I. Kornev, C. Malibert, L. Bellaiche, and J. M. Kiat, "Combined theoretical and experimental study of the low-temperature properties of BaZrO₃," *Phys. Rev. B*, vol. 72, no. 20, p. 205104, Nov. 2005, doi: 10.1103/PhysRevB.72.205104.
- [170] J. Lu, L. Wang, L. Fan, Y. Li, L. Dai, and H. Guo, "Chemical stability of doped BaCeO₃-BaZrO₃ solid solutions in different atmospheres," *J. Rare Earths*, vol. 26, no. 4, p. 505, 2008.
- [171] A. K. Azad and J. T. S. Irvine, "High density and low temperature sintered proton conductor BaCe_{0.5}Zr_{0.35}Sc_{0.1}Zn_{0.05}O_{3-δ}," *Solid State Ion.*, p. 5, 2008.
- [172] A. Lacz, "Effect of microstructure on chemical stability and electrical properties of BaCe_{0.9}Y_{0.1}O_{3-δ}," *Ionics*, vol. 22, pp. 1405–1414, 2016, doi: 10.1007/s11581-016-1665-6.
- [173] D. Medvedev, A. Murashkina, E. Pikalova, A. Demin, A. Podias, and P. Tsiakaras, "BaCeO₃: Materials development, properties and application," *Prog. Mater. Sci.*, vol. 60, pp. 72–129, Mar. 2014, doi: 10.1016/j.pmatsci.2013.08.001.
- [174] E. Fabbri, A. D'Epifanio, E. Di Bartolomeo, S. Licoccia, and E. Traversa, "Tailoring the chemical stability of Ba(Ce_{0.8-x}Zr_x)Y_{0.2}O_{3-δ} protonic conductors for Intermediate Temperature Solid Oxide Fuel Cells (IT-SOFCs)," *Solid State Ion.*, vol. 179, pp. 558–564, 2008, doi: 10.1016/j.ssi.2008.04.002.
- [175] G. K. Williamson and W. H. Hall, "X-ray line broadening from fcc aluminium and wolfram," *Acta Metall.*, vol. 1, no. 1, pp. 22–31, Jan. 1953, doi: 10.1016/0001-6160(53)90006-6.
- [176] R. Sažinas *et al.*, "Surface reactivity and cation non-stoichiometry in BaZr_{1-x}Y_xO_{3-δ} ($x = 0-0.2$) exposed to CO₂ at elevated temperature," *J. Mater. Chem. A*, vol. 7, no. 8, pp. 3848–3856, 2019, doi: 10.1039/C8TA11021B.
- [177] K. D. Kreuer, St. Adams, W. Münch, A. Fuchs, U. Klock, and J. Maier, "Proton conducting alkaline earth zirconates and titanates for high drain electrochemical applications," *Solid State Ion.*, vol. 145, no. 1–4, pp. 295–306, Dec. 2001, doi: 10.1016/S0167-2738(01)00953-5.
- [178] T. Schober, "Water vapor solubility and electrochemical characterization of the high temperature proton conductor BaZr_{0.9}Y_{0.1}O_{2.95}," *Solid State Ion.*, vol. 127, no. 3–4, pp. 351–360, Jan. 2000, doi: 10.1016/S0167-2738(99)00283-0.
- [179] F. Iguchi, N. Sata, T. Tsurui, and H. Yugami, "Microstructures and grain boundary conductivity of BaZr_{1-x}Y_xO₃ ($x = 0.05, 0.10, 0.15$) ceramics," *Solid State Ion.*, vol. 178, no. 7–10, pp. 691–695, Apr. 2007, doi: 10.1016/j.ssi.2007.02.019.
- [180] D. Han, K. Kishida, K. Shinoda, H. Inui, and T. Uda, "A comprehensive understanding of structure and site occupancy of Y in Y-doped BaZrO₃," *J. Mater. Chem. A*, vol. 1, no. 9, pp. 3027–3033, 2013, doi: 10.1039/c2ta00675h.
- [181] M. F. Hoedl, E. Makagon, I. Lubomirsky, R. Merkle, E. A. Kotomin, and J. Maier, "Impact of point defects on the elastic properties of BaZrO₃: Comprehensive insight from experiments and ab initio calculations," *Acta Mater.*, vol. 160, pp. 247–256, Nov. 2018, doi: 10.1016/j.actamat.2018.08.042.
- [182] L. Rioja-Monllor, S. Ricote, C. Bernuy-Lopez, T. Grande, R. O'Hayre, and M.-A. Einaarsrud, "High-Performance La_{0.5}Ba_{0.5}Co_{1/3}Mn_{1/3}Fe_{1/3}O_{3-δ}-BaZr_{1-z}Y_zO_{3-δ} Cathode Composites via an Exsolution Mechanism for Protonic Ceramic Fuel Cells," *Inorganics*, vol. 6, no. 3, p. 83, Aug. 2018, doi: 10.3390/inorganics6030083.
- [183] R. Sažinas, C. Bernuy-López, M.-A. Einaarsrud, and T. Grande, "Effect of CO₂ Exposure on the Chemical Stability and Mechanical Properties of BaZrO₃-Ceramics," *J. Am. Ceram. Soc.*, vol. 99, no. 11, pp. 3685–3695, Nov. 2016, doi: 10.1111/jace.14395.

- [184] Tsvetkov, Ivanov, Malyshkin, Sereda, and Zuev, "Thermoelectric Behavior of BaZr_{0.9}Y_{0.1}O_{3-δ} Proton Conducting Electrolyte," *Membranes*, vol. 9, no. 9, p. 120, Sep. 2019, doi: 10.3390/membranes9090120.
- [185] S. B. C. Duval, P. Holtappels, U. F. Vogt, U. Stimming, and T. Graule, "Characterisation of BaZr_{0.9}Y_{0.1}O_{3-δ} Prepared by Three Different Synthesis Methods: Study of the Sinterability and the Conductivity," *Fuel Cells*, vol. 9, no. 5, pp. 613–621, Oct. 2009, doi: 10.1002/fuce.200800170.
- [186] W. Sun, M. Liu, and W. Liu, "Chemically Stable Yttrium and Tin Co-Doped Barium Zirconate Electrolyte for Next Generation High Performance Proton-Conducting Solid Oxide Fuel Cells," *Adv. Energy Mater.*, vol. 3, no. 8, pp. 1041–1050, Aug. 2013, doi: 10.1002/aenm.201201062.
- [187] A. Aimi, K. Horiuchi, Y. Yamaguchi, S. Ito, and K. Fujimoto, "Disordered off-center direction of Ti⁴⁺ in pseudo-cubic type BaTiO₃ prepared by mixed hydroxide process," *J. Ceram. Soc. Jpn.*, vol. 129, no. 1, pp. 73–78, Jan. 2021, doi: 10.2109/jcersj2.20147.
- [188] E. K. Al-Shakarchi and N. B. Mahmood, "Three Techniques Used to Produce BaTiO₃ Fine Powder," *J. Mod. Phys.*, vol. 02, no. 11, pp. 1420–1428, 2011, doi: 10.4236/jmp.2011.211175.
- [189] N. Yasuda *et al.*, "X-ray diffractometry for the structure determination of a submicrometre single powder grain," *J. Synchrotron Radiat.*, vol. 16, no. 3, pp. 352–357, May 2009, doi: 10.1107/S090904950900675X.
- [190] R. Wäsche and W. Denner, "Influence of high hydrostatic pressure on the crystal structure of barium titanate (BaTiO₃)," vol. 16, no. 5, p. 4.
- [191] Y. V. Baklanova *et al.*, "Synthesis and characterisation of new MO(OH)₂ (M = Zr, Hf) oxyhydroxides and related Li₂MO₃ salts," *Dalton Trans*, vol. 43, no. 7, pp. 2755–2763, 2014, doi: 10.1039/C3DT52929K.
- [192] N. V. Tarakina, A. P. Tyutyunnik, Ya. V. Baklanova, L. G. Maksimova, T. A. Denisova, and R. B. Neder, "Crystal structure of a new HfO(OH)₂ oxyhydroxide," *Powder Diff.*, vol. 28, no. S2, pp. S510–S518, Sep. 2013, doi: 10.1017/S0885715613000791.
- [193] T. Chen, J. Meng, Q. Lin, X. Wei, J. Li, and Z. Zhang, "One-step synthesis of hollow BaZrO₃ nanocrystals with oxygen vacancies for photocatalytic hydrogen evolution from pure water," *J. Alloys Compd.*, vol. 780, pp. 498–503, Apr. 2019, doi: 10.1016/j.jallcom.2018.11.367.
- [194] M. Miodyńska *et al.*, "Preparation and photocatalytic properties of BaZrO₃ and SrZrO₃ modified with Cu₂O/Bi₂O₃ quantum dots," *Solid State Sci.*, vol. 74, pp. 13–23, Dec. 2017, doi: 10.1016/j.solidstatesciences.2017.10.003.
- [195] A. Gauzzi, "AES, XPS and SIMS characterization of YBa₂Cu₃O_{7-x} superconducting high T_c thin films," p. 5.
- [196] F. Werfel, M. Heinonen, and E. Suoninen, "Oxidation States of Cu, Ba and Y in Superconducting YBa₂Cu₃O_{7-x}," p. 6.
- [197] J. F. Moulder, W. F. Stickler, P. E. Sobol, and K. D. Bomben, *Handbook of X-ray Photoelectron Spectroscopy*. USA: Perkin-Elmer Corporation Physical Electronics Division, 1993.
- [198] A. B. Christie, J. Lee, I. Sutherland, and J. M. Walls, "An XPS study of ion-induced compositional changes with group II and group IV compounds," *Appl. Surf. Sci.*, vol. 15, no. 1–4, pp. 224–237, Apr. 1983, doi: 10.1016/0378-5963(83)90018-1.
- [199] A. Gauzzi, "AES, XPS and SIMS characterization of YBa₂Cu₃O_{7-x} superconducting high T_c thin films," *Vacuum*, vol. 41, pp. 870–874, 1990.
- [200] P. J. Schmitz, "Characterization of the Surface of BaCO₃ Powder by XPS," *Surf. Sci. Spectra*, vol. 8, no. 3, pp. 190–194, Jul. 2001, doi: 10.1116/11.20011102.

- [201] O. Karşlıoğlu, L. Trotochaud, I. Zegkinoglou, and H. Bluhm, "X-Ray Spectroscopic Characterization of BaO, Ba(OH)₂, BaCO₃, and Ba(NO₃)₂," *J. Electron Spectrosc. Relat. Phenom.*, vol. 225, pp. 55–61, May 2018, doi: 10.1016/j.elspec.2018.03.008.
- [202] C. Aruta *et al.*, "A-Site Cation Substitutions in Strained Y-Doped BaZrO₃ Multilayer Films Leading to Fast Proton Transport Pathways," *J. Phys. Chem. C*, vol. 120, pp. 8387–8391, 2016, doi: <https://doi.org/10.1021/acs.jpcc.6b01963>.
- [203] I. Gonzalo-Juan, J. A. Escribano, Y. Castro, A. J. Sanchez-Herencia, J. L. G. Fierro, and B. Ferrari, "One-pot manufacture of nanoparticle-based films in aqueous media via an electric field-driven assembly process," *Green Chem.*, vol. 16, no. 6, pp. 3286–3296, 2014, doi: 10.1039/C3GC42539H.
- [204] M. B. Pomfret, C. Stoltz, B. Varughese, and R. A. Walker, "Structural and Compositional Characterization of Yttria-Stabilized Zirconia: Evidence of Surface-Stabilized, Low-Valence Metal Species," *Anal. Chem.*, vol. 77, no. 6, pp. 1791–1795, Mar. 2005, doi: 10.1021/ac048600u.
- [205] F. Parmigiani, L. E. Depero, L. Sangaletti, and G. Samoggia, "An XPS study of yttria-stabilised zirconia single crystals," *J. Electron Spectrosc. Relat. Phenom.*, vol. 63, no. 1, pp. 1–10, Jul. 1993, doi: 10.1016/0368-2048(93)85010-I.
- [206] M. Oishi, Y. Tsutsumi, P. Chen, M. Ashida, H. Doi, and T. Hanawa, "Surface changes of yttria-stabilized zirconia in water and Hanks solution characterized using XPS," *Surf. Interface Anal.*, vol. 50, pp. 587–591, 2017.
- [207] F. Wyrwalski, J. F. Lamonier, S. Siffert, E. A. Zhilinskaya, L. Gengembre, and A. Aboukaï, "Bulk and surface structures of iron doped zirconium oxide systems: Influence of preparation method," *J. Mater. Sci.*, vol. 40, no. 4, pp. 933–942, Feb. 2005, doi: 10.1007/s10853-005-6512-5.
- [208] D. Barreca, G. A. Battiston, D. Berto, R. Gerbasi, and E. Tondello, "Y₂O₃ Thin Films Characterized by XPS," *Surf. Sci. Spectra*, vol. 8, no. 3, pp. 234–239, Jul. 2001, doi: 10.1116/11.20020404.
- [209] T. L. Barr, "An ESCA study of the termination of the passivation of elemental metals," *J. Phys. Chem.*, vol. 82, no. 16, pp. 1801–1810, Aug. 1978, doi: 10.1021/j100505a006.
- [210] T. Sato, S. Imaeda, and K. Sato, "Thermal transformation of yttrium hydroxides to yttrium oxides," *Thermochim. Acta*, vol. 133, pp. 79–85, Oct. 1988, doi: 10.1016/0040-6031(88)87140-5.
- [211] J. Matta, J.-F. Lamonier, E. Abi-Aad, E. A. Zhilinskaya, and A. Aboukaïs, "Transformation of tetragonal zirconia phase to monoclinic phase in the presence of Fe³⁺ ions as probes: an EPR study," *Phys. Chem. Chem. Phys.*, vol. 1, no. 21, pp. 4975–4980, 1999, doi: 10.1039/a904828f.
- [212] T. Sato, "The thermal decomposition of zirconium oxyhydroxide," *J. Therm. Anal. Calorim.*, vol. 69, pp. 255–265, 2002.
- [213] B. Sreedhar, Ch. Satya Vani, D. Keerthi Devi, M. V. Basaveswara Rao, and C. Rambabu, "Shape Controlled Synthesis of Barium Carbonate Microclusters and Nanocrystallites using Natural Polysaccharide – Gum Acacia," *Am. J. Mater. Sci.*, vol. 2, no. 1, pp. 5–13, Feb. 2012, doi: 10.5923/j.materials.20120201.02.
- [214] R. L. Frost, M. Hales, and W. N. Martens, "Thermogravimetric analysis of selected group II carbonate minerals – implication for the geosequestration of greenhouse gases," *J. Therm. Anal. Calorim.*, vol. 95, pp. 999–1005.
- [215] A. Yoko, M. Akizuki, and Y. Oshima, "Formation mechanism of barium zirconate nanoparticles under supercritical hydrothermal synthesis," *J. Nanoparticle Res.*, vol. 16, no. 4, Apr. 2014, doi: 10.1007/s11051-014-2330-5.
- [216] A. Yoko *et al.*, "In situ X-ray diffraction for millisecond-order dynamics of BaZrO₃ nanoparticle formation in supercritical water," *J. Supercrit. Fluids*, vol. 107, pp. 746–752, Jan. 2016, doi: 10.1016/j.supflu.2015.08.002.

- [217] Y. Yamazaki, R. Hernandez-Sanchez, and S. M. Haile, "Cation non-stoichiometry in yttrium-doped barium zirconate: phase behavior, microstructure, and proton conductivity," *J. Mater. Chem.*, vol. 20, pp. 8158–8166, 2010, doi: DOI: 10.1039/c0jm02013c.
- [218] J. Tong, D. Clark, L. Bernau, M. Sanders, and R. O'Hayre, "Solid-state reactive sintering mechanism for large-grained yttrium-doped barium zirconate proton conducting ceramics," *J. Mater. Chem.*, vol. 20, no. 30, p. 6333, 2010, doi: 10.1039/c0jm00381f.
- [219] E. Barsoukov and J. R. Macdonald, Eds., *Impedance spectroscopy: theory, experiment, and applications*, 2nd ed. Hoboken, N.J: Wiley-Interscience, 2005.
- [220] A. Lasia, *Electrochemical impedance spectroscopy and its applications*. New York: Springer, 2014.
- [221] Q.-A. Huang, M. Liu, and M. Liu, "Impedance Spectroscopy Study of a SDC-based SOFC with High Open Cell Voltage," *Electrochimica Acta*, vol. 177, pp. 227–236, 2015, doi: 10.1016/j.electacta.2014.11.065.
- [222] J. R. Macdonald and W. B. Johnson, "Fundamentals of Impedance Spectroscopy," in *Impedance Spectroscopy*, E. Barsoukov and J. R. Macdonald, Eds. Hoboken, NJ, USA: John Wiley & Sons, Inc., 2018, pp. 1–20. doi: 10.1002/9781119381860.ch1.
- [223] L. Khotseng, "Oxygen Reduction Reaction," in *Electrocatalysts for Fuel Cells and Hydrogen Evolution - Theory to Design*, InTech, 2018, p. 27.
- [224] M. S. Markov, "Electric and Magnetic Fields Bioeffects," in *Encyclopedia of Applied Electrochemistry*, G. Kreysa, K. Ota, and R. F. Savinell, Eds. New York, NY: Springer New York, 2014, pp. 379–384. doi: 10.1007/978-1-4419-6996-5_261.
- [225] A. Lasia, "Modeling of Impedance of Porous Electrodes," in *Modern Aspects of Electrochemistry, Number 43*, vol. 43, M. Schlesinger, Ed. New York, NY: Springer New York, 2008, pp. 1–71. doi: 10.1007/978-0-387-49582-8_3.
- [226] J. F. Gómez-Aguilar, J. E. Escalante-Martínez, C. Calderón-Ramón, L. J. Morales-Mendoza, M. Benavidez-Cruz, and M. Gonzalez-Lee, "Equivalent Circuits Applied in Electrochemical Impedance Spectroscopy and Fractional Derivatives with and without Singular Kernel," *Adv. Math. Phys.*, vol. 2016, pp. 1–15, 2016, doi: 10.1155/2016/9720181.
- [227] F. Ciucci and C. Chen, "Analysis of Electrochemical Impedance Spectroscopy Data Using the Distribution of Relaxation Times: A Bayesian and Hierarchical Bayesian Approach," *Electrochimica Acta*, vol. 167, pp. 439–454, Jun. 2015, doi: 10.1016/j.electacta.2015.03.123.
- [228] A. Weiß, S. Schindler, S. Galbiati, M. A. Danzer, and R. Zeis, "Distribution of Relaxation Times Analysis of High-Temperature PEM Fuel Cell Impedance Spectra," *Electrochimica Acta*, vol. 230, pp. 391–398, Mar. 2017, doi: 10.1016/j.electacta.2017.02.011.
- [229] N. Bonanos, "Oxide-based protonic conductors: point defects and transport properties," *Solid State Ion.*, vol. 145, pp. 265–274, 2001, doi: 10.1016/s0167-2738(01)00951-1.
- [230] C. Lefrou, J. Fouletier, and P. Fabry, "Conductivité des électrolytes," *Tech. Ing.*, p. 21, 2010, doi: Reference K840 V1.
- [231] X. Wang, Y. Ma, S. Li, A.-H. Kashyout, B. Zhu, and M. Muhammed, "Ceria-based nanocomposite with simultaneous proton and oxygen ion conductivity for low-temperature solid oxide fuel cells," *J. Power Sources*, vol. 196, no. 5, pp. 2754–2758, Mar. 2011, doi: 10.1016/j.jpowsour.2010.11.033.
- [232] J. C. Díaz and J. Kamcev, "Ionic conductivity of ion-exchange membranes: Measurement techniques and salt concentration dependence," *J. Membr. Sci.*, vol. 618, p. 118718, Jan. 2021, doi: 10.1016/j.memsci.2020.118718.
- [233] K. C. Anjaneya, G. P. Nayaka, J. Manjanna, G. Govindaraj, and K. N. Ganesha, "Preparation and characterization of $\text{Ce}_{1-x}\text{Sm}_x\text{O}_{2-\delta}$ ($x = 0.1-0.3$) as electrolyte

- material for intermediate temperature SOFC,” *Solid State Sci.*, vol. 26, pp. 89–96, Dec. 2013, doi: 10.1016/j.solidstatesciences.2013.09.015.
- [234] G. Balazs, “ac impedance studies of rare earth oxide doped ceria,” *Solid State Ion.*, vol. 76, no. 1–2, pp. 155–162, Feb. 1995, doi: 10.1016/0167-2738(94)00242-K.
- [235] T. Yajima, H. Iwahara, and H. Uchida, “Protonic and oxide ionic conduction in BaCeO₃-based ceramics — effect of partial substitution for Ba in BaCe_{0.9}O_{3-α} with Ca.,” *Solid State Ion.*, vol. 47, pp. 117–124, 1991, doi: 10.1016/0167-2738(91)90189-i.
- [236] E. C. C. de Souza and R. Muccillo, “Properties and applications of perovskite proton conductors,” *Mater. Res.*, vol. 13, no. 3, pp. 385–394, Sep. 2010, doi: 10.1590/S1516-14392010000300018.
- [237] N. Bonanos, “Transport properties and conduction mechanism in high-temperature protonic conductors,” *Solid State Ion.*, vol. 53–56, pp. 967–974, 1993, doi: 10.1016/0167-2738(92)90278-w.
- [238] M. Jovaní, H. Beltrán-Mir, E. Cordoncillo, and A. R. West, “Field-induced p-n transition in yttria-stabilized zirconia,” *Nat. Res.*, vol. 9, pp. 18538–18547, 2019, doi: 10.1038/s41598-019-54588-y.
- [239] M. G. Jung, Y. J. Kim, Y.-G. Jung, and H.-T. Lim, “Measurement of hydrogen and oxygen chemical potential in yttria doped barium cerate (BCY) electrolyte of anode-supported protonic ceramic fuel cells,” *Int. J. Hydrog. Energy*, vol. 39, no. 29, pp. 16576–16584, Oct. 2014, doi: 10.1016/j.ijhydene.2014.04.146.
- [240] F. Iguchi, N. Sata, and H. Yugami, “Proton transport properties at the grain boundary of barium zirconate based proton conductors for intermediate temperature operating SOFC,” *J. Mater. Chem.*, vol. 20, no. 30, p. 6265, 2010, doi: 10.1039/c0jm00443j.
- [241] V. P. Gorelov, V. Balakireva, and A. Kuzmin, “Ionic, proton, and oxygen conductivities in the BaZr_{1-x}Y_xO_{3-α} system (x = 0.02–0.15) in humid air,” *Russ. J. Electrochem.*, vol. 46, pp. 890–895, 2010, doi: 10.1134/S1023193510080057.
- [242] Z. Sun, E. Fabbri, L. Bi, and E. Traversa, “Electrochemical Properties and Intermediate-Temperature Fuel Cell Performance of Dense Yttrium-Doped Barium Zirconate with Calcium Addition,” *J. Am. Ceram. Soc.*, vol. 95, no. 2, pp. 627–635, Feb. 2012, doi: 10.1111/j.1551-2916.2011.04795.x.
- [243] Y. Liu, R. Ran, S. Li, Y. Jiao, M. O. Tade, and Z. Shao, “Significant performance enhancement of yttrium-doped barium cerate proton conductor as electrolyte for solid oxide fuel cells through a Pd ingress–egress approach,” *J. Power Sources*, vol. 257, pp. 308–318, Jul. 2014, doi: 10.1016/j.jpowsour.2014.02.013.
- [244] T. Norby and Y. Larring, “Concentration and transport of protons in oxides,” *Curr. Opin. Solid State Mater. Sci.*, vol. 2, no. 5, pp. 593–599, Oct. 1997, doi: 10.1016/S1359-0286(97)80051-4.
- [245] K. D. Kreuer, “Proton-Conducting Oxides,” *Annu. Rev. Mater. Res.*, vol. 33, no. 1, pp. 333–359, Aug. 2003, doi: 10.1146/annurev.matsci.33.022802.091825.
- [246] D. Pergolesi *et al.*, “High proton conduction in grain-boundary-free yttrium-doped barium zirconate films grown by pulsed laser deposition,” *Nat. Mater.*, vol. 9, no. 10, pp. 846–852, Oct. 2010, doi: 10.1038/nmat2837.
- [247] A. Benes *et al.*, “Proton Conduction in Grain-Boundary-Free Oxygen-Deficient BaFeO_{2.5+d} Thin Films,” *Materials*, vol. 11, pp. 52–73, 2018, doi: 10.3390/ma11010052.
- [248] D. Kek and N. Bonanos, “Investigation of hydrogen oxidation reaction on a metal/perovskite proton conductor interface by impedance spectroscopy,” *Vacuum*, vol. 61, no. 2–4, pp. 453–457, May 2001, doi: 10.1016/S0042-207X(01)00154-3.
- [249] E. Fabbri, T. Oh, S. Licoccia, E. Traversa, and E. D. Wachsman, “Mixed Protonic/Electronic Conductor Cathodes for Intermediate Temperature SOFCs Based

- on Proton Conducting Electrolytes,” *J. Electrochem. Soc.*, vol. 156, no. 1, p. B38, 2009, doi: 10.1149/1.3005781.
- [250] E. Fabbri, D. Pergolesi, S. Licoccia, and E. Traversa, “Does the increase in Y-dopant concentration improve the proton conductivity of $\text{BaZr}_{1-x}\text{Y}_x\text{O}_{3-\delta}$ fuel cell electrolytes?,” *Solid State Ion.*, vol. 181, pp. 1043–1051, 2010, doi: 10.1016/j.ssi.2010.06.007.
- [251] R. M. German, P. Suri, and S. J. Park, “Review: liquid phase sintering,” *J. Mater. Sci.*, vol. 44, no. 1, pp. 1–39, Jan. 2009, doi: 10.1007/s10853-008-3008-0.
- [252] A. Magrez and T. Schober, “Preparation, sintering, and water incorporation of proton conducting $\text{Ba}_{0.99}\text{Zr}_{0.8}\text{Y}_{0.2}\text{O}_{3-\delta}$: comparison between three different synthesis techniques,” *Solid State Ion.*, vol. 175, pp. 585–588, 2004, doi: 10.1016/j.ssi.2004.03.045.
- [253] S. Yamanaka *et al.*, “Thermophysical properties of BaZrO_3 and BaCeO_3 ,” *J. Alloys Compd.*, vol. 359, pp. 109–113, 2003, doi: 10.1016/S0925-8388(03)00214-7.
- [254] H. Yoshida *et al.*, “Densification of Nanocrystalline Ytria by Low Temperature Spark Plasma Sintering,” *J. Am. Ceram. Soc.*, vol. 91, no. 5, pp. 1707–1710, May 2008, doi: 10.1111/j.1551-2916.2008.02337.x.
- [255] T. Norby and P. Kofstad, “PROTON AND NATIVE-ION CONDUCTIVITIES IN Y_2O_3 AT HIGH TEMPERATURES,” *Solid State Ion.*, vol. 20, pp. 169–184.
- [256] R. Gateau, “Comportement vis-à-vis de la corrosion à haute température de métaux (Ti, TA6V) revêtus d’aluminium de titane,” Université de Bourgogne, Dijon, 2010.
- [257] S. Diethelm and J. Van herle, “Ethanol internal steam reforming in intermediate temperature solid oxide fuel cell,” *J. Power Sources*, vol. 196, no. 17, pp. 7355–7362, Sep. 2011, doi: 10.1016/j.jpowsour.2010.11.063.
- [258] J. T. S. Irvine, D. C. Sinclair, and A. R. West, “Electroceramics: Characterization by Impedance Spectroscopy,” *Adv. Mater.*, vol. 2, no. 3, pp. 132–138, Mar. 1990, doi: 10.1002/adma.19900020304.
- [259] L. Rioja-Monllor, C. Bernuy-Lopez, M.-L. Fontaine, T. Grande, and M.-A. Einarsrud, “Compositional Engineering of $\text{aLa}_{1-x}\text{Ba}_x\text{CoO}_{3-\delta}$ -(1-a) $\text{BaZr}_{0.9}\text{Y}_{0.1}\text{O}_{2.95}$ (a=0.6, 0.7, 0.8 and x=0.5, 0.6, 0.7) Nanocomposite Cathodes for Protonic Ceramic Fuel Cells,” *Materials*, vol. 12, pp. 3441–3456, 2019, doi: 10.3390/ma12203441.
- [260] M. Chen, X. Xie, J. Guo, D. Chen, and Q. Xu, “Space charge layer effect at the platinum anode/ $\text{BaZr}_{0.9}\text{Y}_{0.1}\text{O}_{3-\delta}$ electrolyte interface in proton ceramic fuel cells,” *J. Mater. Chem. A*, vol. 8, no. 25, pp. 12566–12575, 2020, doi: 10.1039/D0TA03339A.
- [261] D. Chen, S. R. Bishop, and H. L. Tuller, “Nonstoichiometry in Oxide Thin Films Operating under Anodic Conditions: A Chemical Capacitance Study of the Praseodymium–Cerium Oxide System,” *Chem. Mater.*, vol. 26, pp. 6622–6627, 2014, doi: <https://doi.org/10.1021/cm503440v>.
- [262] J. Jamnik and J. Maier, “Generalised equivalent circuits for mass and charge transport: chemical capacitance and its implications,” *Phys. Chem. Chem. Phys.*, vol. 3, no. 9, pp. 1668–1678, 2001, doi: 10.1039/b100180i.
- [263] M. Riegraf, R. Costa, G. Schiller, K. A. Friedrich, S. Dierickx, and A. Weber, “Electrochemical Impedance Analysis of Symmetrical Ni/Gadolinium-Doped Ceria (CGO10) Electrodes in Electrolyte-Supported Solid Oxide Cells,” *J. Electrochem. Soc.*, vol. 166, no. 13, pp. F865–F872, 2019, doi: 10.1149/2.0051913jes.
- [264] J. Dailly, S. Fourcade, A. Largeteau, F. Mauvy, J. C. Grenier, and M. Marrony, “Perovskite and A_2MO_4 -type oxides as new cathode materials for protonic solid oxide fuel cells,” *Electrochimica Acta*, vol. 55, no. 20, pp. 5847–5853, Aug. 2010, doi: 10.1016/j.electacta.2010.05.034.
- [265] A. Grimaud *et al.*, “Hydration Properties and Rate Determining Steps of the Oxygen Reduction Reaction of Perovskite-Related Oxides as H^+ -SOFC Cathodes,” *J. Electrochem. Soc.*, vol. 159, no. 6, pp. B683–B694, 2012, doi: 10.1149/2.101205jes.

- [266] T. Q. Nguyen and C. Breitkopf, "Determination of Diffusion Coefficients Using Impedance Spectroscopy Data," *J. Electrochem. Soc.*, p. 7, 2018.
- [267] L. Zhang, F. Liu, K. Brinkman, K. L. Reifsnider, and A. V. Virkar, "A study of gadolinia-doped ceria electrolyte by electrochemical impedance spectroscopy," *J. Power Sources*, vol. 247, pp. 947–960, Feb. 2014, doi: 10.1016/j.jpowsour.2013.09.036.
- [268] J. Nielsen and J. Hjelm, "Impedance of SOFC electrodes: A review and a comprehensive case study on the impedance of LSM:YSZ cathodes," *Electrochimica Acta*, vol. 115, pp. 31–45, Jan. 2014, doi: 10.1016/j.electacta.2013.10.053.
- [269] E. P. M. van Westing, G. M. Ferrari, and J. H. W. de Wit, "The determination of coating performance with impedance measurements-I. Coating polymer properties," *Corrion Sci.*, vol. 34, no. 9, pp. 1511–1530, 1993, doi: [https://doi.org/10.1016/0010-938X\(93\)90245-C](https://doi.org/10.1016/0010-938X(93)90245-C).
- [270] B. Hirschorn, M. E. Orazem, B. Tribollet, V. Vivier, I. Frateur, and M. Musiani, "Determination of effective capacitance and film thickness from constant-phase-element parameters," *Electrochimica Acta*, vol. 55, no. 21, pp. 6218–6227, Aug. 2010, doi: 10.1016/j.electacta.2009.10.065.
- [271] C. H. Hsu and F. Mansfeld, "**Technical Note:** Concerning the Conversion of the Constant Phase Element Parameter Y_0 into a Capacitance," *Corrosion*, vol. 57, no. 9, pp. 747–748, Sep. 2001, doi: 10.5006/1.3280607.
- [272] B.-Y. Chang, "Conversion of a Constant Phase Element to an Equivalent Capacitor," *J. Electrochem. Sci. Technol.*, vol. 11, no. 3, pp. 318–321, Aug. 2020, doi: 10.33961/jecst.2020.00815.
- [273] S. B. Adler, "Factors Governing Oxygen Reduction in Solid Oxide Fuel Cell Cathodes," *Chem. Rev.*, vol. 104, no. 10, pp. 4791–4844, Oct. 2004, doi: 10.1021/cr020724o.
- [274] W. Sun, L. Yan, Z. Shi, Z. Zhu, and W. Liu, "Fabrication and performance of a proton-conducting solid oxide fuel cell based on a thin $\text{BaZr}_{0.8}\text{Y}_{0.2}\text{O}_{3-\delta}$ electrolyte membrane," *J. Power Sources*, vol. 195, no. 15, pp. 4727–4730, Aug. 2010, doi: 10.1016/j.jpowsour.2010.02.012.
- [275] Z. Sun, E. Fabbri, L. Bi, and E. Traversa, "Lowering grain boundary resistance of $\text{BaZr}_{0.8}\text{Y}_{0.2}\text{O}_{3-\delta}$ with LiNO_3 sintering-aid improves proton conductivity for fuel cell operation," *Phys Chem Chem Phys*, vol. 13, no. 17, pp. 7692–7700, 2011, doi: 10.1039/C0CP01470B.
- [276] C. Kjøseth *et al.*, "Space-charge theory applied to the grain boundary impedance of protonconducting $\text{BaZr}_{0.9}\text{Y}_{0.1}\text{O}_{3-\delta}$," *Solid State Ion.*, vol. 181, pp. 268–275, 2010, doi: 10.1016/j.ssi.2010.01.014.
- [277] A. Fluri *et al.*, "Enhanced Proton Conductivity in Y-Doped BaZrO_3 via Strain Engineering," *Adv. Sci.*, vol. 4, no. 12, p. 1700467, Dec. 2017, doi: 10.1002/advs.201700467.
- [278] E. Traversa, "Proton conductors for solid oxide fuel cells (SOFCs)," 2012, p. 23.
- [279] H. G. Bohn and T. Schober, "Electrical Conductivity of the High-Temperature Proton Conductor $\text{BaZr}_{0.9}\text{Y}_{0.1}\text{O}_{2.95}$," *J. Am. Ceram. Soc.*, vol. 83, no. 4, pp. 768–772, Dec. 2004, doi: 10.1111/j.1151-2916.2000.tb01272.x.
- [280] T. Yajima and H. Iwahara, "Studies on behavior and mobility of protons in doped perovskite-type oxides: (I) In situ measurement of hydrogen concentration in $\text{SrCe}_{0.95}\text{Y}_{0.05}\text{O}_3$ at high temperature," *Solid State Ion.*, vol. 50, pp. 281–286, doi: 10.1016/0167-2738(92)90230-M.
- [281] L. Bi, E. Fabbri, Z. Sun, and E. Traversa, "A novel ionic diffusion strategy to fabricate high-performance anode-supported solid oxidefuel cells (SOFCs) with proton-conducting Y-doped BaZrO_3 films," *Energy Env. Sci.*, vol. 4, no. 2, pp. 409–412, 2011, doi: 10.1039/C0EE00353K.

- [282] L. Bi, E. Fabbri, and E. Traversa, "Effect of anode functional layer on the performance of proton-conducting solid oxide fuel cells (SOFCs)," *Electrochem. Commun.*, vol. 16, no. 1, pp. 37–40, Mar. 2012, doi: 10.1016/j.elecom.2011.12.023.
- [283] C. Tang *et al.*, "The effect of an anode functional layer on the steam electrolysis performances of protonic solid oxide cells," *J. Mater. Chem. A*, vol. 9, no. 24, pp. 14032–14042, 2021, doi: 10.1039/D1TA02848K.
- [284] E. Ivers-Tiffée, A. Weber, and D. Herbristrit, "Materials and technologies for SOFC-components," *J. Eur. Ceram. Soc.*, vol. 21, no. 10–11, pp. 1805–1811, Jan. 2001, doi: 10.1016/S0955-2219(01)00120-0.
- [285] H. Shi, C. Su, R. Ran, J. Cao, and Z. Shao, "Electrolyte materials for intermediate-temperature solid oxide fuel cells," *Prog. Nat. Sci. Mater. Int.*, vol. 30, no. 6, pp. 764–774, Dec. 2020, doi: 10.1016/j.pnsc.2020.09.003.
- [286] A. Tarutin, N. Danilov, J. Lyagaeva, and D. Medvedev, "One-Step Fabrication of Protonic Ceramic Fuel Cells Using a Convenient Tape Calendering Method," *Appl. Sci.*, vol. 10, no. 7, p. 2481, Apr. 2020, doi: 10.3390/app10072481.
- [287] A. Wain-Martin, R. Campana, A. Morán-Ruiz, A. Larrañaga, and M. I. Arriortua, "Synthesis and processing of SOFC components for the fabrication and characterization of anode supported cells," *Bol. Soc. Esp. Cerámica Vidr.*, p. S0366317520301187, Dec. 2020, doi: 10.1016/j.bsecv.2020.11.008.
- [288] M. Tanhaei and M. Mozammel, "Yttria-stabilized zirconia thin film electrolyte deposited by EB-PVD on porous anode support for SOFC applications," *Ceram. Int.*, vol. 43, no. 3, pp. 3035–3042, Feb. 2017, doi: 10.1016/j.ceramint.2016.11.097.
- [289] R. K. Lenka, P. K. Patro, V. Patel, L. Muhmood, and T. Mahata, "Comparative investigation on the functional properties of alkaline earth metal (Ca, Ba, Sr) doped Nd₂NiO_{4+δ} oxygen electrode material for SOFC applications," *J. Alloys Compd.*, vol. 860, p. 158490, Apr. 2021, doi: 10.1016/j.jallcom.2020.158490.
- [290] C. Jeong *et al.*, "Design and processing parameters of La₂NiO_{4+δ}-based cathode for anode-supported planar solid oxide fuel cells (SOFCs)," *J. Power Sources*, vol. 297, pp. 370–378, Nov. 2015, doi: 10.1016/j.jpowsour.2015.08.023.
- [291] G. Taillades, P. Pers, V. Mao, and M. Taillades, "High performance anode-supported proton ceramic fuel cell elaborated by wet powder spraying," *Int. J. Hydrog. Energy*, vol. 41, no. 28, pp. 12330–12336, Jul. 2016, doi: 10.1016/j.ijhydene.2016.05.094.
- [292] V. Sivasankaran, L. Combemale, and G. Caboche, "Method for preparing a fuel cell" Patent <https://patents.google.com/patent/WO2014057218A2/en>.
- [293] H. Su and Y. H. Hu, "Progress in low-temperature solid oxide fuel cells with hydrocarbon fuels," *Chem. Eng. J.*, vol. 402, p. 126235, Dec. 2020, doi: 10.1016/j.cej.2020.126235.
- [294] Z. Zakaria, Z. Awang Mat, S. H. Abu Hassan, and Y. Boon Kar, "A review of solid oxide fuel cell component fabrication methods toward lowering temperature," *Int. J. Energy Res.*, vol. 44, no. 2, pp. 594–611, Feb. 2020, doi: 10.1002/er.4907.
- [295] Y. Lyu, F. Wang, D. Wang, and Z. Jin, "Alternative preparation methods of thin films for solid oxide fuel cells: review," *Mater. Technol.*, vol. 35, no. 4, pp. 212–227, Mar. 2020, doi: 10.1080/10667857.2019.1674478.
- [296] A. Akbari-Fakhrabadi, R. V. Mangalaraja, F. A. Sanhueza, R. E. Avila, S. Ananthakumar, and S. H. Chan, "Nanostructured Gd–CeO₂ electrolyte for solid oxide fuel cell by aqueous tape casting," *J. Power Sources*, vol. 218, pp. 307–312, Nov. 2012, doi: 10.1016/j.jpowsour.2012.07.005.
- [297] G. Blugan, K. Morawa, S. Koebel, T. Graule, and J. Kuebler, "Development of a tape casting process for making thin layers of Si₃N₄ and Si₃N₄+TiN," *J. Eur. Ceram. Soc.*, vol. 27, no. 16, pp. 4789–4795, Jan. 2007, doi: 10.1016/j.jeurceramsoc.2007.02.211.

- [298] M. Suzuki, H. Sasaki, S. Otsoshi, A. Kajimura, and M. Ippommatsu, "High power density solid oxide electrolyte fuel cells using Ru/Y2O3 stabilized zirconia cermet anodes," p. 6.
- [299] J. Huang, Y. Ma, M. Cheng, and S. Ruan, "Fabrication of integrated BZY electrolyte matrices for protonic ceramic membrane fuel cells by tape-casting and solid-state reactive sintering," *Int. J. Hydrog. Energy*, vol. 43, no. 28, pp. 12835–12846, Jul. 2018, doi: 10.1016/j.ijhydene.2018.04.148.
- [300] K. Bae *et al.*, "Demonstrating the potential of yttrium-doped barium zirconate electrolyte for high-performance fuel cells," *Nat. Commun.*, vol. 8, no. 1, p. 14553, Apr. 2017, doi: 10.1038/ncomms14553.
- [301] M. Arab Pour Yazdi, P. Briois, S. Georges, and A. Billard, "Electrical and structural investigations of perovskite structure reactively sputter deposited coatings," *Solid State Ion.*, vol. 180, no. 23–25, pp. 1246–1251, Oct. 2009, doi: 10.1016/j.ssi.2009.07.008.
- [302] D. R. Biswas, "Influence of porosity on the mechanical properties of lead zirconate--titanate ceramics," LBL-5479, 7110774, Sep. 1976. doi: 10.2172/7110774.
- [303] A. Siad, A. Besnard, C. Nouveau, and P. Jacquet, "Critical angles in DC magnetron glad thin films," *Vacuum*, vol. 131, pp. 305–311, Sep. 2016, doi: 10.1016/j.vacuum.2016.07.012.
- [304] R. N. Tait, T. Smy, and M. J. Brett, "Modelling and characterization of columnar growth in evaporated films," *Thin Solid Films*, vol. 226, no. 2, pp. 196–201, Apr. 1993, doi: 10.1016/0040-6090(93)90378-3.
- [305] Sulhadi *et al.*, "Influence of annealing temperature on the morphology and crystal structure of Ga-doped ZnO thin films," *J. Phys. Conf. Ser.*, vol. 1170, p. 012066, Mar. 2019, doi: 10.1088/1742-6596/1170/1/012066.
- [306] W.-C. Chen, C.-T. Lee, J. Su, and H.-P. Chen, "The Effects of Annealing Temperature on the Structural Properties of ZrB2 Films Deposited via Pulsed DC Magnetron Sputtering," *Coatings*, vol. 9, no. 4, p. 253, Apr. 2019, doi: 10.3390/coatings9040253.
- [307] F. Challali *et al.*, "Effect of RF sputtering power and vacuum annealing on the properties of AZO thin films prepared from ceramic target in confocal configuration," *Mater. Sci. Semicond. Process.*, vol. 118, p. 105217, Nov. 2020, doi: 10.1016/j.mssp.2020.105217.
- [308] G. Zoppi, N. S. Beattie, J. D. Major, R. W. Miles, and I. Forbes, "Electrical, morphological and structural properties of RF magnetron sputtered Mo thin films for application in thin film photovoltaic solar cells," *J. Mater. Sci.*, vol. 46, no. 14, pp. 4913–4921, Jul. 2011, doi: 10.1007/s10853-011-5404-0.
- [309] G. F. Harrington, A. Cavallaro, D. W. McComb, S. J. Skinner, and J. A. Kilner, "The effects of lattice strain, dislocations, and microstructure on the transport properties of YSZ films," *Phys. Chem. Chem. Phys.*, vol. 19, no. 22, pp. 14319–14336, 2017, doi: 10.1039/C7CP02017A.
- [310] R. Peng, T. Wu, W. Liu, X. Liu, and G. Meng, "Cathode processes and materials for solid oxide fuel cells with proton conductors as electrolytes," *J. Mater. Chem.*, vol. 20, no. 30, p. 6218, 2010, doi: 10.1039/c0jm00350f.
- [311] H. Sumi, H. Shimada, Y. Yamaguchi, Y. Mizutani, Y. Okuyama, and K. Amezawa, "Comparison of electrochemical impedance spectra for electrolyte-supported solid oxide fuel cells (SOFCs) and protonic ceramic fuel cells (PCFCs)," *Sci. Rep.*, vol. 11, no. 1, p. 10622, Dec. 2021, doi: 10.1038/s41598-021-90211-9.
- [312] Y. Ling, J. Yu, B. Lin, X. Zhang, L. Zhao, and X. Liu, "A cobalt-free Sm_{0.5}Sr_{0.5}Fe_{0.8}Cu_{0.2}O_{3-d}-Ce_{0.8}Sm_{0.2}O_{2-d} composite cathode for proton-conducting solid oxide fuel cells," *J. Power Sources*, vol. 196, pp. 2631–2634, 2011, doi: 10.1016/j.jpowsour.2010.11.017.
- [313] M. François *et al.*, "Chemical Degradation of the La_{0.6}Sr_{0.4}Co_{0.2}Fe_{0.8}O_{3-δ}/Ce_{0.8}Sm_{0.2}O_{2-δ} Interface during Sintering and Cell

- Operation,” *Energies*, vol. 14, no. 12, pp. 3674–3689, Jun. 2021, doi: 10.3390/en14123674.
- [314] A. Chroneos, B. Yildiz, A. Tarancón, D. Parfitt, and J. A. Kilner, “Oxygen diffusion in solid oxide fuel cell cathode and electrolyte materials: mechanistic insights from atomistic simulations,” *Energy Environ. Sci.*, vol. 4, pp. 2774–2789, 2011, doi: 10.1039/c0ee00717j.
- [315] J. B. Goodenough, “Oxide-Ion Electrolytes,” *Annu. Rev. Mater. Res.*, vol. 33, no. 1, pp. 91–128, Aug. 2003, doi: 10.1146/annurev.matsci.33.022802.091651.
- [316] S. Omar, “Doped Ceria for Solid Oxide Fuel Cells,” in *Cerium Oxide - Applications and Attributes*, S. Bahadar Khan and K. Akhtar, Eds. IntechOpen, 2019. doi: 10.5772/intechopen.79170.
- [317] M. A. Vasiliades, D. Harris, H. Stephenson, S. Boghosian, and A. M. Efstathiou, “A Novel Analysis of Transient Isothermal ^{18}O Isotopic Exchange on Commercial $\text{Ce}_{0.9}\text{Zr}_{0.1}\text{O}_{2-x}$ -Based OSC Materials,” *Top. Catal.*, vol. 62, pp. 219–226, 2019, doi: <https://doi.org/10.1007/s11244-018-1116-x>.
- [318] P. Li, X. Chen, Y. Li, and J. W. Schwank, “A review on oxygen storage capacity of CeO_2 -based materials: Influence factors, measurement techniques, and applications in reactions related to catalytic automotive emissions control,” *Catal. Today*, vol. 327, pp. 90–115, May 2019, doi: 10.1016/j.cattod.2018.05.059.
- [319] Sk. Anirban and A. Dutta, “Structural and ionic transport mechanism of rare earth doped cerium oxide nanomaterials: Effect of ionic radius of dopant cations,” *Solid State Ion.*, vol. 309, pp. 137–145, Oct. 2017, doi: 10.1016/j.ssi.2017.07.020.
- [320] N. Yang *et al.*, “Role of Associated Defects in Oxygen Ion Conduction and Surface Exchange Reaction for Epitaxial Samaria-Doped Ceria Thin Films as Catalytic Coatings,” *ACS Appl. Mater. Interfaces*, vol. 8, no. 23, pp. 14613–14621, Jun. 2016, doi: 10.1021/acsami.6b03909.
- [321] G.-B. Jung, T.-J. Huang, and C.-L. Chang, “Effect of temperature and dopant concentration on the conductivity of samaria-doped ceria electrolyte,” *J. Solid State Electrochem.*, vol. 6, no. 4, pp. 225–230, May 2002, doi: 10.1007/s100080100238.
- [322] S. A. Acharya, V. M. Gaikwad, S. W. D’Souza, and S. R. Barman, “Gd/Sm dopant-modified oxidation state and defect generation in nano-ceria,” *Solid State Ion.*, vol. 260, pp. 21–29, Jul. 2014, doi: 10.1016/j.ssi.2014.03.008.
- [323] H. Yahiro, Y. Eguchi, K. Eguchi, and H. Arai, “Oxygen ion conductivity of the ceria-samarium oxide system with fluorite structure,” *J. Appl. Electrochem.*, vol. 18, no. 4, pp. 527–531, Jul. 1988, doi: 10.1007/BF01022246.
- [324] K. Eguchi, T. Setoguchi, T. Inoue, and H. Arai, “Electrical properties of ceria-based oxides and their application to solid oxide fuel cells,” *Solid State Ion.*, vol. 52, no. 1–3, pp. 165–172, May 1992, doi: 10.1016/0167-2738(92)90102-U.
- [325] K. C. Anjaneya, G. P. Nayaka, J. Manjanna, G. Govindaraj, and K. N. Ganesha, “Preparation and characterization of $\text{Ce}_{1-x}\text{Sm}_x\text{O}_{2-\delta}$ ($x = 0.1-0.3$) as electrolyte material for intermediate temperature SOFC,” *Solid State Sci.*, vol. 26, pp. 89–96, Dec. 2013, doi: 10.1016/j.solidstatesciences.2013.09.015.
- [326] M. Coduri, S. Checchia, M. Longhi, D. Ceresoli, and M. Scavini, “Rare Earth Doped Ceria: The Complex Connection Between Structure and Properties,” *Front. Chem.*, vol. 6, p. 526, Oct. 2018, doi: 10.3389/fchem.2018.00526.
- [327] W. Z. Zhu and S. C. Deevi, “Development of interconnect materials for solid oxide fuel cells,” *Mater. Sci. Eng. A*, vol. 348, no. 1–2, pp. 227–243, May 2003, doi: 10.1016/S0921-5093(02)00736-0.
- [328] A. Giuliano *et al.*, “Infiltration, Overpotential and Ageing Effects on Cathodes for Solid Oxide Fuel Cells: $\text{La}_{0.6}\text{Sr}_{0.4}\text{Co}_{0.2}\text{Fe}_{0.8}\text{O}_{3-\delta}$ versus $\text{Ba}_{0.5}\text{Sr}_{0.5}\text{Co}_{0.8}\text{Fe}_{0.2}\text{O}_{3-\delta}$,” *J. Electrochem. Soc.*, vol. 164, no. 10, pp. F3114–F3122, 2017, doi: 10.1149/2.0161710jes.

- [329] K. C. Anjaneya, G. P. Nayaka, J. Manjanna, G. Govindaraj, and K. N. Ganesha, "Studies on structural, morphological and electrical properties of $\text{Ce}_{0.8}\text{Ln}_{0.2}\text{O}_{2-\delta}$ ($\text{Ln}=\text{Y}^{3+}$, Gd^{3+} , Sm^{3+} , Nd^{3+} and La^{3+}) solid solutions prepared by citrate complexation method," *J. Alloys Compd.*, vol. 585, pp. 594–601, Feb. 2014, doi: 10.1016/j.jallcom.2013.09.101.
- [330] J. Koettgen, S. Grieshammer, P. Hein, B. O. H. Grope, M. Nakayama, and M. Martin, "Understanding the ionic conductivity maximum in doped ceria: trapping and blocking," *Phys. Chem. Chem. Phys.*, vol. 20, pp. 14291–14321, 2018.
- [331] N. S. C. Priya, K. Sandhya, and D. N. Rajendran, "Study on Electrical conductivity and Activation Energy of doped Ceria nanostructures," *Electrochem. Energy Technol.*, vol. 3, no. 1, pp. 49–53, Jan. 2018, doi: 10.1515/eetech-2017-0004.
- [332] C. Fu, K. Sun, N. Zhang, X. Chen, and D. Zhou, "Electrochemical characteristics of LSCF–SDC composite cathode for intermediate temperature SOFC," *Electrochimica Acta*, vol. 52, no. 13, pp. 4589–4594, Mar. 2007, doi: 10.1016/j.electacta.2007.01.001.
- [333] J. Parbey *et al.*, "High-performance solid oxide fuel cells with fiber-based cathodes for low-temperature operation," *Int. J. Hydrog. Energy*, vol. 45, no. 11, pp. 6949–6957, Feb. 2020, doi: 10.1016/j.ijhydene.2019.12.125.
- [334] W. Zhou, R. Ran, and Z. Shao, "Progress in understanding and development of $\text{Ba}_{0.5}\text{Sr}_{0.5}\text{Co}_{0.8}\text{Fe}_{0.2}\text{O}_{3-\delta}$ -based cathodes for intermediate-temperature solid-oxide fuel cells: A review," *J. Power Sources*, vol. 192, pp. 231–246, 2009.
- [335] L.-W. Tai, M. M. Nasrallah, H. U. Anderson, D. M. Sparlin, and S. R. Sehlin, "Structure and electrical properties of $\text{La}_{1-x}\text{Sr}_x\text{Co}_{1-y}\text{Fe}_y\text{O}_3$. Part 2. The system $\text{La}_{1-x}\text{Sr}_x\text{Co}_{0.2}\text{Fe}_{0.8}\text{O}_3$," *Solid State Ion.*, vol. 76, pp. 273–283, 1995.
- [336] S. Ramesh, V. Kumar, P. Kistaiah, and C. Vishnuvardhan Reddy, "Preparation, characterization and thermo electrical properties of co-doped $\text{Ce}_{0.8-x}\text{Sm}_{0.2}\text{Ca}_x\text{O}_{2-\delta}$ materials," *Solid State Ion.*, vol. 181, pp. 86–91, 2010.
- [337] M. Liu, D. Ding, Y. Bai, T. He, and M. Liu, "An Efficient SOFC Based on Samaria-Doped Ceria (SDC) Electrolyte," *J. Electrochem. Soc.*, vol. 159, no. 6, pp. B661–B665, 2012, doi: 10.1149/2.032206jes.
- [338] R. D. Shannon, "Revised Effective Ionic Radii and Systematic Studies of Interatomic Distances in Halides and Chalcogenides," *Acta Cryst.*, vol. A32, pp. 754–767, 1976.
- [339] P. Dutta, S. Pal, M. S. Seehra, Y. Shi, E. M. Eyring, and R. D. Ernst, "Concentration of Ce^{3+} and Oxygen Vacancies in Cerium Oxide Nanoparticles," p. 3.
- [340] Y. Lu, L. Chen, C. Lu, Y. Ni, and Z. Xu, "Effects of oxygen defects on structure and properties of $\text{Sm}_{0.5}\text{Sr}_{0.5}\text{CoO}_{3-\square}$ annealed in different atmospheres," *J. Rare Earths*, vol. 31, pp. 1183–1190, 2013.
- [341] F. Giannici *et al.*, "Cation Diffusion and Segregation at the Interface between Samarium-Doped Ceria and LSCF or LSFCu Cathodes Investigated with X-ray Microspectroscopy," *ACS Appl. Mater. Interfaces*, vol. 9, no. 51, pp. 44466–44477, Dec. 2017, doi: 10.1021/acsami.7b13377.
- [342] H.-C. Chang, D.-S. Tsai, W.-H. Chung, Y.-S. Huang, and M.-V. Le, "A ceria layer as diffusion barrier between LAMOX and lanthanum strontium cobalt ferrite along with the impedance analysis," *Solid State Ion.*, vol. 180, no. 4–5, pp. 412–417, Apr. 2009, doi: 10.1016/j.ssi.2009.01.018.
- [343] N. E. Volkova, L. V. Khvostova, L. Ya. Gavrilova, and V. A. Cherepanov, "Role of Sm content to the crystal structure and properties of $\text{Sr}_{1-x}\text{Sm}_x\text{FeO}_{3-\delta}$," *J. Solid State Chem.*, vol. 267, pp. 113–118, Nov. 2018, doi: 10.1016/j.jssc.2018.08.007.
- [344] F. Zhou *et al.*, "Effects of cerium doping on the performance of LSCF cathodes for intermediate temperature solid oxide fuel cells," *Int. J. Hydrog. Energy*, vol. 43, no. 41, pp. 18946–18954, Oct. 2018, doi: 10.1016/j.ijhydene.2018.08.041.
- [345] B. P. Mandal, V. Grover, and A. K. Tyagi, "Phase relations, lattice thermal expansion in $\text{Ce}_{1-x}\text{Eu}_x\text{O}_{2-x/2}$ and $\text{Ce}_{1-x}\text{Sm}_x\text{O}_{2-x/2}$ systems and stabilization of cubic RE_2O_3

- (RE: Eu, Sm),” *Mater. Sci. Eng. A*, vol. 430, no. 1–2, pp. 120–124, Aug. 2006, doi: 10.1016/j.msea.2006.05.140.
- [346] W. Zhang *et al.*, “La_{0.6}Sr_{0.4}Co_{0.2}Fe_{0.8}O_{3-δ}/CeO₂Heterostructured Composite Nanofibers as a Highly Active and Robust Cathode Catalyst for Solid Oxide Fuel Cells,” *Appl. Mater. Interfaces*, vol. 11, pp. 26830–26841, 2019, doi: 10.1021/acsami.9b06668.
- [347] H. Wang *et al.*, “Enhancing Activity and Durability of A-Site-Deficient (La_{0.6} Sr_{0.4})_{0.95} Co_{0.2} Fe_{0.8} O_{3-δ} Cathode by Surface Modification with PrO_{2-δ} Nanoparticles,” *ACS Sustain. Chem. Eng.*, vol. 8, no. 8, pp. 3367–3380, Mar. 2020, doi: 10.1021/acssuschemeng.9b07354.
- [348] J. S. Hardy, J. W. Templeton, D. J. Edwards, Z. Lu, and J. W. Stevenson, “Lattice expansion of LSCF-6428 cathodes measured by in situ XRD during SOFC operation,” *J. Power Sources*, vol. 198, pp. 76–82, Jan. 2012, doi: 10.1016/j.jpowsour.2011.09.099.
- [349] K. Kuntaiah, P. Sudarsanam, B. M. Reddy, and A. Vinu, “Nanocrystalline Ce₁₂xSm_xO₂₂d (x = 0.4) solid solutions: structural characterization versus CO oxidation,” *RSC Adv.*, p. 11, 2013.
- [350] S. Kundu, N. Sutradhar, R. Thangamuthu, B. Subramanian, A. B. Panda, and M. Jayachandran, “Fabrication of catalytically active nanocrystalline samarium (Sm)-doped cerium oxide (CeO₂) thin films using electron beam evaporation,” *J Nanopart Res*, p. 16, 2012.
- [351] S. Liang, E. Broitman, Y. Wang, A. Cao, and G. Vesper, “Highly stable, mesoporous mixed lanthanum–cerium oxides with tailored structure and reducibility,” *J. Mater. Sci.*, vol. 46, no. 9, pp. 2928–2937, May 2011, doi: 10.1007/s10853-010-5168-y.
- [352] D. Loche, “Determining the maximum lanthanum incorporation in the fluorite structure of La-doped ceria nanocubes for enhanced redox ability,” *RSC Adv.*, p. 7, 2019.
- [353] J.-C. Dupin, D. Gonbeau, P. Vinatier, and A. Levasseur, “Systematic XPS studies of metal oxides, hydroxides and peroxides,” *Phys. Chem. Chem. Phys.*, vol. 2, no. 6, pp. 1319–1324, 2000, doi: 10.1039/a908800h.
- [354] R. D. Feltham and P. Brant, “XPS studies of core binding energies in transition metal complexes. 2. Ligand group shifts,” p. 5.
- [355] C. Drouet, C. Laberty, J. L. G. Fierro, P. Alphonse, and A. Rousset, “X-ray photoelectron spectroscopic study of non-stoichiometric nickel and nickel–copper spinel manganites,” *Int. J. Inorg. Mater.*, vol. 2, no. 5, pp. 419–426, Oct. 2000, doi: 10.1016/S1466-6049(00)00047-7.
- [356] G. C. Allen, S. J. Harris, and L. Jutson, “A study of a number of mixed transition metal oxide spinels using X-ray photoelectron spectroscopy,” p. 24.
- [357] M. M. Natile, A. Galenda, and A. Glisenti, “From La₂O₃ To LaCoO₃: XPS Analysis,” *Surf. Sci. Spectra*, vol. 15, p. 14, 2008.
- [358] J. P. H. Li *et al.*, “Understanding of binding energy calibration in XPS of lanthanum oxide by *in situ* treatment,” *Phys. Chem. Chem. Phys.*, vol. 21, no. 40, pp. 22351–22358, 2019, doi: 10.1039/C9CP04187G.
- [359] L. Zhang, “Integrating the cationic engineering and hollow structure engineering into perovskites oxides for efficient and stable electrocatalytic oxygen evolution,” *Electrochimica Acta*, p. 11, 2019.
- [360] L. Wang *et al.*, “A novel core-shell LSCF perovskite structured electrocatalyst with local hetero-interface for solid oxide fuel cells,” *Int. J. Hydrog. Energy*, vol. 45, no. 20, pp. 11824–11833, Apr. 2020, doi: 10.1016/j.ijhydene.2020.02.130.
- [361] M. F. Sunding, “XPS characterisation of in situ treated lanthanum oxide and hydroxide using tailored charge referencing and peak fitting procedures,” *J. Electron Spectrosc. Relat. Phenom.*, p. 11, 2011.
- [362] A. K. Opitz *et al.*, “The Chemical Evolution of the La_{0.6}Sr_{0.4}CoO_{3-δ} Surface Under SOFC Operating Conditions and Its Implications for Electrochemical Oxygen

- Exchange Activity,” *Top. Catal.*, vol. 61, no. 20, pp. 2129–2141, Dec. 2018, doi: 10.1007/s11244-018-1068-1.
- [363] D. Newby *et al.*, “Surface evolution of lanthanum strontium cobalt ferrite thin films at low temperatures,” *Thin Solid Films*, vol. 589, pp. 655–661, Aug. 2015, doi: 10.1016/j.tsf.2015.06.037.
- [364] J. Oishi, J. Otomo, Y. Oshima, and M. Koyama, “The Effects of Minor Components in LSCF Cathode on Oxygen Reduction Reaction,” *ECS Trans.*, vol. 57, no. 1, pp. 1909–1916, Oct. 2013, doi: 10.1149/05701.1909ecst.
- [365] V. Young and T. Otagawa, “XPS studies on strontium compounds,” *Appl. Surf. Sci.*, vol. 20, pp. 228–248, 1985.
- [366] R. P. Vasquez, “SrCO₃ by XPS,” *Surf. Sci. Spectra*, vol. 1, pp. 112–116, 1992.
- [367] S. P. Simner, M. D. Anderson, M. H. Engelhard, and J. W. Stevenson, “Degradation Mechanisms of La–Sr–Co–Fe–O₃ SOFC Cathodes,” *Electrochem. Solid-State Lett.*, vol. 9, pp. A478–A481, 2006.
- [368] H. Wang *et al.*, “Mechanisms of Performance Degradation of (La,Sr)(Co,Fe)O_{3-δ} Solid Oxide Fuel Cell Cathodes,” *J. Electrochem. Soc.*, vol. 163, no. 6, pp. F581–F585, 2016, doi: 10.1149/2.0031607jes.
- [369] M. Kubicek, A. Limbeck, T. Fromling, and H. Hutter, “Relationship between Cation Segregation and the Electrochemical Oxygen Reduction Kinetics of La_{0.6}Sr_{0.4}CoO_{3.2} Thin Film Electrodes,” *J. Electrochem. Soc.*, p. 8, 2011.
- [370] H. Dai *et al.*, “Optimization of sintering temperature for SOFCs by a co-firing method,” *Ceram. Int.*, vol. 46, no. 5, pp. 6987–6990, Apr. 2020, doi: 10.1016/j.ceramint.2019.11.134.
- [371] M. Li *et al.*, “Mechanism for the enhanced oxygen reduction reaction of La_{0.6}Sr_{0.4}Co_{0.2}Fe_{0.8}O_{3-δ} by strontium carbonate,” *Phys. Chem. Chem. Phys.*, vol. 19, no. 1, pp. 503–509, 2017, doi: 10.1039/C6CP06204K.
- [372] Z. Pan, Q. Liu, L. Zhang, X. Zhang, and S. H. Chan, “Effect of Sr Surface Segregation of La_{0.6}Sr_{0.4}Co_{0.2}Fe_{0.8}O_{3-δ} Electrode on Its Electrochemical Performance in SOC,” *J. Electrochem. Soc.*, vol. 162, no. 12, pp. F1316–F1323, 2015.
- [373] B. Feng, I. Sugiyama, H. Hojo, H. Ohta, N. Shibata, and Y. Ikuhara, “Atomic structures and oxygen dynamics of CeO₂ grain boundaries,” *Sci. Rep.*, vol. 6, no. 1, pp. 20288–20294, Apr. 2016, doi: 10.1038/srep20288.
- [374] M. Izuki *et al.*, “Interfacial stability and cation diffusion across the LSCF/GDC interface,” *J. Power Sources*, vol. 196, no. 17, pp. 7232–7236, Sep. 2011, doi: 10.1016/j.jpowsour.2010.11.013.
- [375] N. W. Kwak, D. Lim, S. J. Jeong, P. Byeon, S. Chung, and W. Jung, “Diffusion of Cation Impurities through Ceria Grain Boundaries,” *Adv. Mater. Interfaces*, vol. 7, no. 20, p. 2000688, Oct. 2020, doi: 10.1002/admi.202000688.
- [376] M. K. Mahapatra and P. Singh, “Fuel Cells,” in *Future Energy*, Elsevier, 2014, pp. 511–547. doi: 10.1016/B978-0-08-099424-6.00024-7.
- [377] J. W. Yun *et al.*, “Modifying the cathodes of intermediate-temperature solid oxide fuel cells with a Ce_{0.8}Sm_{0.2}O₂ sol–gel coating,” *Int. J. Hydrog. Energy*, vol. 34, no. 22, pp. 9213–9219, Nov. 2009, doi: 10.1016/j.ijhydene.2009.08.091.
- [378] M. Morales *et al.*, “Multi-scale analysis of the diffusion barrier layer of gadolinia-doped ceria in a solid oxide fuel cell operated in a stack for 3000 h,” *J. Power Sources*, vol. 344, pp. 141–151, Mar. 2017, doi: 10.1016/j.jpowsour.2017.01.109.
- [379] R. F. Klevtsova and P. V. Klevtsov, “The crystal structure of YOOH,” *J. Struct. Chem.*, vol. 5, no. 6, pp. 795–797, 1965, doi: 10.1007/BF00744232.

Titre : Pile à combustible à céramique protonique : élaboration et caractérisation. Étude de l'électrolyte $\text{BaZr}_{0.8}\text{Y}_{0.2}\text{O}_{3-\delta}$ par spectroscopie d'impédance électrochimique

Mots clés : Pile à combustible à céramique protonique ; $\text{BaZr}_{0.8}\text{Y}_{0.2}\text{O}_{3-\delta}$; spectroscopie d'impédance électrochimique ; conductivité ; synthèse hydrothermale

Résumé : L'un des défis mondiaux actuels consiste à développer des techniques nouvelles, propres et efficaces pour la production d'énergie. L'utilisation de cellules électrochimiques combinées à l'hydrogène est l'une des solutions. Ces cellules permettent de convertir l'excès d'énergie produit par les moyens conventionnels en hydrogène par électrolyse de l'eau. L'hydrogène peut être stocké et transformé en électricité au besoin par les cellules en mode pile à combustible. Parmi les différentes cellules électrochimiques, les cellules à céramiques protoniques attirent grandement l'attention en raison de leur efficacité élevée à température intermédiaire (400 – 600 °C). De plus, ces systèmes offrent l'avantage de ne pas diluer l'hydrogène produit en mode électrolyse. Ce travail de thèse porte sur le mode pile à combustible des cellules à céramique protonique (PCFC). Le matériau conducteur protonique, $\text{BaZr}_{0.8}\text{Y}_{0.2}\text{O}_{3-\delta}$, a été élaboré par le procédé de synthèse hydrothermale à basse température

(400 °C) sous une pression de 300 bars. Deux variantes du procédé ont été utilisées : un système batch et un système continu. En plus de présenter une plus grande productivité (6 g.h⁻¹), le procédé en continu permet l'élaboration d'un matériau de meilleure qualité aussi bien en terme de stabilité et que de conductivité (évaluée par spectroscopie d'impédance électrochimique). Des cellules complètes PCFC ont également été réalisées lors de ce travail. La partie anodique, composée de Ni et $\text{BaZr}_{0.8}\text{Y}_{0.2}\text{O}_{3-\delta}$, a été élaborée par coulage en bande. L'électrolyte ($\text{BaZr}_{0.8}\text{Y}_{0.2}\text{O}_{3-\delta}$) par pulvérisation cathodique réactive. Enfin, la cathode, un composite $\text{BaZr}_{0.8}\text{Y}_{0.2}\text{O}_{3-\delta}$ - $\text{Ba}_{0.5}\text{Sr}_{0.5}\text{Co}_{0.8}\text{Fe}_{0.2}\text{O}_{3-\delta}$, a été déposé par pulvérisation au moyen d'un aérographe. Ce procédé de fabrication permet la production de cellules électrochimiques présentant un électrolyte fin (5 µm) et de microstructure colonnaire, ce qui permet d'abaisser la résistance ohmique à 7 Ω.cm⁻² à 525 °C.

Title: Protonic ceramic fuel cell: elaboration and characterization. Investigation of the $\text{BaZr}_{0.8}\text{Y}_{0.2}\text{O}_{3-\delta}$ electrolyte by electrochemical impedance spectroscopy.

Keywords: Protonic ceramic fuel cell; $\text{BaZr}_{0.8}\text{Y}_{0.2}\text{O}_{3-\delta}$; electrochemical impedance spectroscopy, conductivity; hydrothermal synthesis

Abstract: One of the current global challenges is to find novel, clean and efficient techniques for the energy production. The use of electrochemical cells and hydrogen is one of the solutions. These cells convert the excess energy produced by conventional systems into hydrogen by steam electrolysis. The hydrogen can be stored and transformed into electricity when needed in the fuel cell mode. Among the different electrochemical cells, protonic ceramic electrochemical cells have attracted much attention due to their high efficiency at intermediate temperatures (400 – 600 °C). In addition, these systems offer the advantage of not diluting the fuel in electrolysis mode. This thesis work focuses on the electricity production, i.e., on the protonic ceramic fuel cell (PCFC). The protonic conductor material $\text{BaZr}_{0.8}\text{Y}_{0.2}\text{O}_{3-\delta}$ was produced at low temperature (400 °C) under a pressure of 300 bar by

hydrothermal synthesis. Two variants of the process were evaluated: a batch and a continuous system. In addition to exhibit greater productivity (6 g.h⁻¹), the continuous process allows the elaboration of a better quality material in terms of stability and conductivity (evaluated by electrochemical impedance spectroscopy). PCFCs were also produced during this work. The anode, composed of Ni and $\text{BaZr}_{0.8}\text{Y}_{0.2}\text{O}_{3-\delta}$, was elaborated by tape casting. The electrolyte ($\text{BaZr}_{0.8}\text{Y}_{0.2}\text{O}_{3-\delta}$) by reactive DC sputtering. Finally, the cathode, a $\text{BaZr}_{0.8}\text{Y}_{0.2}\text{O}_{3-\delta}$ - $\text{Ba}_{0.5}\text{Sr}_{0.5}\text{Co}_{0.8}\text{Fe}_{0.2}\text{O}_{3-\delta}$ ceramic composite, was deposited by spray using an airbrush. This manufacturing process allows the production of an electrochemical cell with a thin electrolyte (5 µm) and a columnar microstructure allowing the ohmic resistance to be lowered to 7 Ω.cm⁻² at 525 °C.